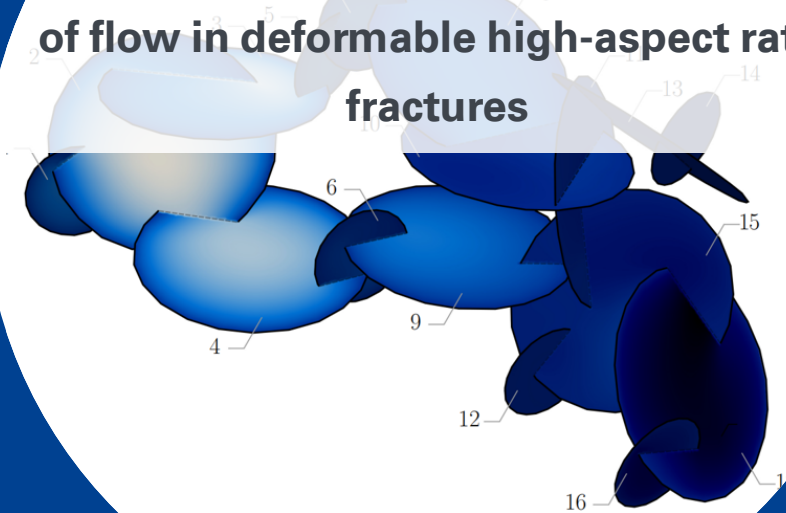




University of Stuttgart
Germany

Patrick
Schmidt

Hydro-mechanical coupling of flow in deformable high-aspect ratio fractures



10

Publication series of the
Institute of Applied Mechanics (IAM)

Hydro-mechanical coupling of flow in deformable high-aspect ratio fractures

Von der Fakultät Bau- und Umweltingenieurwissenschaften
der Universität Stuttgart zur Erlangung der Würde
eines Doktor-Ingenieurs (Dr.-Ing.)
genehmigte Abhandlung

vorgelegt von

Patrick Schmidt

aus

Hagen

Hauptberichter: Prof. Dr.-Ing. Holger Steeb

Mitberichter: Prof. Dr. Jörg Renner

Prof. Dr. Hadi Hajibeygi

Tag der mündlichen Prüfung: 21. Januar 2022

Institut für Mechanik (Bauwesen) der Universität Stuttgart

Lehrstuhl für Kontinuumsmechanik

Prof. Dr.-Ing. H. Steeb

2022

Publication series of the Institute of Applied Mechanics (IAM), Volume 10
Institute of Applied Mechanics
Universität Stuttgart, Germany, 2022

Editors:

Prof. Dr.-Ing. Dr.h.c. W. Ehlers
Prof. Dr.-Ing. Dipl.-Math. techn. F. Fritzen
Prof. Dr.-Ing. M.-A. Keip
Prof. Dr.-Ing. H. Steeb

© Patrick Schmidt
Institute of Applied Mechanics (CE)
Chair of Continuum Mechanics
University of Stuttgart
Pfaffenwaldring 7
70569 Stuttgart, Germany

All rights reserved. No part of this publication may be reproduced, stored in a retrieval system, or transmitted, in any form or by any means, electronic, mechanical, photocopying, recording, scanning or otherwise, without the permission in writing of the author.

ISBN 978-3-937399-58-4
(D 93 – Dissertation, Universität Stuttgart)

Acknowledgements

The work presented in this doctoral thesis was carried out during my time as a research assistant at the Institute of Applied Mechanics (Civil Engineering), Chair of Continuum Mechanics, at the University of Stuttgart. During this time many people positively influenced and contributed in various ways to this work, whom I would like to thank.

First and foremost, I would like to express my deepest appreciation to my supervisor Professor Holger Steeb for introducing me to the field of continuum mechanics, the numerous fruitful scientific discussions, but especially for his human approach to guidance. Furthermore, I am particularly thankful to Professor Jörg Renner for patiently supporting my work throughout countless discussions, helping me to improve my scientific writing and always making me feel welcome. Special thanks also belong to Professor Miriam Schulte, Dr. Alexander Jaust and Dr. Nathan Dutler for the enjoyable and successful work on various scientific questions and Professor Hadi Hajibeygi for accepting the role as a referee for my doctoral thesis.

My colleagues, whom I can proudly call friends, made the time at the Institute of Applied Mechanics special to me. I would like to thank Samaneh Vahid Dastjerdi, Dr. Lukas Eurich, Dominik Fauser, Prof. Dr. Felix Fritzen, Dr. Ehsan Ghobadi, Dr. Said Jamei, Dr. Nikos Karadimitriou, Josef Katzmann, Nadine Kijanski, David Koch, Dongwon Lee, Julian Lissner, Dr. Maria Orsorno, Daniel Rostan, Matthias Ruf, Dr. Malte Sauerwein, Dr. Maik Schenke, Patrick Schröder, Miloš Simeunović, Dr. Rakulan Sivanesapillai, Alixa Sonntag, David Uribe, Paul Voland and Dr. Arndt Wagner for the scientific, but particularly the personal discussions and time we spent together.

Finally, I would like to deeply thank my parents who always gave me the feeling of being understood. My deepest gratitude also belongs to my girlfriend Phuong for being my haven in peace.

Contents

Deutschsprachige Zusammenfassung	VII
Motivation	VII
Stand der Forschung und Zielsetzung	VIII
Gliederung der Arbeit	XII
Nomenclature (Introductory Part)	XIII
Conventions	XIII
Symbols	XIII
1 Introduction and overview	1
1.1 Motivation	1
1.2 State of the art, scope and aims	2
1.3 Outline of the thesis	5
2 Continuum-mechanical modelling of flow in fractured porous media	7
2.1 Flow in deformable fractures - Hybrid-dimensional formulation	8
2.1.1 Conservation of mass	8
2.1.2 Balance of linear momentum	10
2.1.3 Governing equation	14
2.1.4 Weak form of governing equation	15
2.2 Hydro-mechanical formulation for a biphasic poro-elastic medium	17
2.2.1 Balance of momentum of the mixture	17
2.2.2 Constitutive relations	18
2.2.3 Governing equations	19
2.2.4 Weak form of governing equation	21
2.3 Fracture surface boundary conditions	21
2.4 Consideration of fracture normal stiffness	23
2.5 Volumetric split of fracture deformation and fluid compressibility	25
3 Numerical coupling schemes	27
3.1 Monolithic coupling scheme	27
3.1.1 Zero-thickness element	27
3.2 Staggered coupling schemes	28

3.2.1	Fixed-Stress coupling	29
3.2.2	Quasi-Newton coupling	30
4	Publications	33
5	Summary and outlook	161
5.1	Summary	161
5.2	Outlook	162
	Bibliography	164
	Curriculum Vitae	183

List of Figures

2.1	Fractured continuum	7
2.2	Transition from laminar to non-laminar flow	14
2.3	Boundary conditions along fracture surface	22
2.4	In-situ contact model	24

List of Tables

4.1	List of journal publications as a first author.	33
4.2	List of journal publications as a contributing author.	34
4.3	List of contributions to book chapters.	34
4.21	Parameters used for the numerical simulation of periodic hydraulic testing experiments on the two model domains B_1 and B_2	156
4.22	Numerical and experimental characteristic properties. Here, we replace the fracture length l^{Fr} by the more general domain size a and introduce the hydraulic conductivity K_{hyd}	158
4.23	Numerical and experimental dimensionless properties.	159

Deutschsprachige Zusammenfassung

Motivation

Unterirdische Flussvorgänge durch gebrochenes poröses Material haben eine große Bedeutung für die Optimierung der Energiegewinnung von natürlichen Ressourcen. Energieressourcen sind in Form von verschiedenen Liquiden oder Wärme in unterirdischen Reservoiren gespeichert. Ihre Gewinnung ist stark von Diskontinuitäten der Transportcharakteristiken von porösen Medien abhängig, die unter anderem in Verbindung zu diskreten Rissen oder Rissnetzwerken zu bringen sind. Während des Förderprozesses können komplexe Flussprozesse auftreten, da die vorhandenen Risse nicht nur die Permeabilität des porösen Materials erhöhen, sondern auch die Steifigkeit der umgebenden Felsmasse reduzieren. Um die Effizienz der ausgewählten Fördermethode zu steigern ist es daher notwendig ein fundiertes Wissen über die Wechselwirkung von Strömungsprozessen und mechanischer Deformation aufzubauen. Die gewonnenen Erkenntnisse über die während der Förderung von Gas- und Ölvorkommen auftretenden hydromechanischen Effekte haben ebenfalls eine Relevanz im Bereich der Kohlenwasserstoffindustrie [e.g., 49] und können zur Optimierung von Speichermethoden beitragen.

Eine effizientere Gewinnung von Öl, Gas oder Wärme kann durch die Förderung in Gebieten mit einer durch Risse erhöhten Permeabilität erreicht werden. Risse in porösen Medien können bereits existieren oder durch Hydrofracking künstlich erzeugt werden, um die Konduktivität des Reservoirs zu erhöhen [e.g., 85]. Sobald das Equilibrium durch Porendruckvariationen gestört wird erlaubt eine erhöhte Konduktivität des Reservoirs höhere Flussraten. Dieses Phänomen wird genutzt um höhere Förderraten während der Gewinnung von Fluiden, beziehungsweise Gasen zu erzeugen, um das Management von Wasserreservoirs zu optimieren [e.g., 74, 128] oder die Gewinnung von geothermischer Energie zu steigern, bei der die potenzielle Austauschfläche von Felsmasse und Fluid durch die Präsenz von Rissen ebenfalls erhöht wird [e.g., 192]. Im Gegensatz zu den genannten Fördermethoden sollte sich das geologische Umfeld für Abfallagerung und die Speicherung von Kohlenstoff durch eine geringe Permeabilität auszeichnen, um den Massentransport während einer Langzeitlagerung zu minimieren.

Unabhängig von der gewählten Methode ist die hydromechanische Charakterisierung des in Betracht gezogenen geologischen Gebiets für eine große Anzahl von technischen Anwendungen von Relevanz. So ist die Untersuchung der Reservoircharakteristik vor und nach der Stimulation von benachbarten Gebieten von Bedeutung, um mögliche Änderungen der Reservoirreigenschaften zu dokumentieren. Um das Risiko von ungewollten Zwischenfällen zu reduzieren und die Effizienz der gewählten Methode durch die Bestimmung von Parametern, wie dem zu induzierenden Gesamtvolumen oder dem maximalen Fluidruck, zu steigern, ist es notwendig das umliegende Reservoir bestmöglich zu charakterisieren. Betrachtet man exemplarisch die Anwendung des Hydrofrackings, so ist eine erfolgreiche Durchführung stark von dem gewählten Pumpprotokoll abhängig, das basierend auf den Informationen über die Permeabilität und Steifigkeit der umliegenden Felsmasse zusam-

men mit dem Wissen über bereits existierende Risse ausgelegt wird. Die im Anschluss von Bohrlochwendungen durchgeführten Charakterisierungsstudien geben Aufschluss über gewollte und ungewollte Änderungen der Reservoirigenschaften, wie einer erhöhten Permeabilität nach Anwendung von Hydrofracking Stimulationen.

Flussraten in unterirdischen Gebieten werden aufgrund von Informationen über die Permeabilität und Speicherkapazität des gebrochenen porösen Grundmaterials abgeschätzt. Die Charakterisierung basiert auf der Auswertung von Datensätzen, die durch zerstörungsfreie Methoden, beruhend auf der Ausbreitung von mechanischen Wellen [111, 112, 116, 149, 189] oder durch Pumpvorgängen, die transiente Druck- und Flussänderungen induzieren [11, 36, 60, 126], erzeugt werden. Das Repertoire an Pumpvorgängen umfasst Impulstests [35, 99, 101, 191], harmonische [153, 154], beziehungsweise nicht harmonische [157] und Stufentests [59]. Kürzlich konnte während eines Pumpvorgang neben den klassischen Fluss- und Druckdatensätzen ebenfalls ein konsistenter Datensatz für die transiente uniaxiale Änderung der Rissöffnung erzeugt werden [52], der eine genauere Auswertung der hydromechanischen Eigenschaften des Reservoirs ermöglicht. Unabhängig von der Komplexität der gewählten Methode sind die meisten Datensätze räumlich jedoch auf diskrete Positionen des Bohrlochs reduziert und erfordern eine inverse numerische Analyse, um den möglichen Bereich von hydromechanischen Parametern des Reservoirs einzugrenzen.

Stand der Forschung und Zielsetzung

Für die Bestimmung von charakteristischen Eigenschaften, basierend auf der Auswertung von Messdaten, stehen eine Anzahl von verschiedenen Methoden zur Verfügung. Die Auswahl einer geeigneten Methode kann mit Hinblick auf das durchgeführte Experiment, die aufgezeichneten Datensätze und die gesuchten Parameter getroffen werden. Kenntnisse über die treibenden Mechanismen von Flussprozessen in deformierbaren Rissen haben in einer großen Bandbreite von potenziellen Anwendungen, die das harmonische Anregen von Einzelrissen oder Rissnetzwerken zum Bestimmen von Heterogenitäten des Untergrunds [3, 36, 63, 157] oder Studien zur Rissöffnungsevolution während Stufentests umfassen [164], Relevanz und müssen bei der Methodenentwicklung berücksichtigt werden. Im Folgenden wird mit einer auf der vorhandenen Literatur beruhenden Diskussion der bestehenden Analysemethoden von Messdaten, des konsistenten Modellierens von hydromechanisch gekoppelten Flussprozessen in gebrochenen porösen Medien und den verschiedenen Methoden zum Lösen der sich ergebenden partiellen Differenzialgleichungen die Grundlage für ein besseres Verständnis der Problematik gelegt.

Analyse von transienten Messdaten

Die Methoden zur Analyse von Messdaten können grob als analytische und numerische Verfahren kategorisiert werden. Analytische Methoden basieren zumeist auf isotropen Druckdiffusionsmodellen und beschreiben den Fluss in einem starren Einzelriss um dessen charakteristischen Größen zu bestimmen [25, 125]. Numerische Analysemethoden, die den Fluss durch gerissene poröse Medien mit komplexen Geometrien basierend auf Druckdiffusionsmodellen untersuchen, wurden ebenfalls umfangreich in der Literatur diskutiert

[e.g., 19, 62]. Der Nachteil von rein diffusionsbasierten Methoden ist jedoch, dass die getroffenen Annahmen keine hydromechanische Interaktion zulassen und somit bestimmte Phänomene, die während hydraulischer Tests an Rissen auftreten, nicht abgebildet werden können [173]. Bestimmte Beschränkungen können durch eine lokale Anreicherung der Modelle aufgehoben werden, um Risseigenschaften mit einer höheren Genauigkeit abzubilden [e.g., 137, 139]. Die zumeist genutzte konstitutive Beziehung zwischen Fluiddruck und Permeabilität des Risses ermöglicht eine gute numerische Annäherung der Messdaten, sobald transiente Änderungen der Rissöffnung während des Testvorgangs zu erwarten sind [163, 164]. Darüberhinaus wurden experimentelle Untersuchungen bezüglich der Verbindung zwischen der Permeabilität eines Risses und dessen effektiven Spannungszustandes in der Literatur diskutiert und eine Beziehung zwischen dem druckinduzierten Fluss und der geometrischen Änderung des Risses aufgestellt [115, 122, 215, 219]. Diese Beziehung ist in den Bereichen der Seismik [33, 78–80] und während der Korrelation von hydraulischen und mechanischen Rissöffnungen von Interesse [209]. Die diskutierte konstitutive Beziehung zwischen Fluiddruck und Rissöffnung führt jedoch eine lokale Charakteristik ein, die im Kontrast zu experimentellen Beobachtungen steht. Ein bekanntes Szenario, bei dem diese Beziehung nicht ausreichend ist um die experimentellen Beobachtungen zu reproduzieren ist das durch nicht lokale Rissvolumenänderungen induzierte Phänomen von inversen Wasserstandsschwankungen [69, 185, 206, 208]; ein Phänomen, das ebenfalls aus Untersuchungen an intakten porösen Medien als Noordbergum Effekt bekannt ist [107, 162]. Die stark unterschiedlichen Ausbreitungsgeschwindigkeiten von Fluidfluss und Rissdeformation resultieren in volumetrischen Änderungen des Risses in Bereichen, die zu diesem Zeitpunkt noch nicht vom induzierten Fluidvolumen erreicht werden konnten und treten als gemessene Druckabfälle in entfernten Bohrlöchern in Erscheinung. Im Gegensatz zu den bisher diskutierten analytischen und numerischen Methoden im Zeitbereich kann die Effizienz für den Fall von harmonischen Anregungen durch eine Analyse im Frequenzbereich deutlich gesteigert werden. Harmonische Tests an einem Reservoir ermöglichen neben den technischen Vorteilen, wie der Signalbereinigung der Messdaten [154, 157], ebenfalls eine Transformation in den Frequenzbereich, die eine quasistatische Analyse für gegebene Erregungsfrequenzen ermöglicht [39, 153, 157]. Die in der Literatur diskutierten Modelle im Frequenzbereich berücksichtigen jedoch nicht die starke Interaktion von Fluidfluss und Rissdeformation, die in Form von volumetrischen und lokalen geometrischen Änderungen des Risses auftritt.

Modellierung von Fluidfluss in deformierbaren Rissen

Hydromechanische Effekte haben einen großen Einfluss auf den Fluidfluss in deformierbaren Rissen. Relevante Risse im Bereich von geologischen Untersuchungen sind durch ein großes Verhältnis von Risslänge l und Rissöffnung δ charakterisiert $l/\delta > 10^4$ [26]. Ein erster Lösungsansatz um den Fluidfluss in deformierbaren Rissen zu charakterisieren sind direkte numerische Simulationen (DNS), bei denen der Fluidfluss durch die (Navier-) Stokes Gleichung beschrieben wird und mit der poroelastischen Domäne interagiert [21]. Die Qualität von DNS zeigt eine starke Abhängigkeit von der Diskretisierung des Rissgebiets [21], die aufgrund von begrenzten Rechenkapazitäten zu einer Beschränkung mit Hinblick auf die zu untersuchende Gebietsgröße führt. Im Kontext von Rissen mit ho-

hen Seitenverhältnissen kann die Effizienz der numerischen Methode deutlich gesteigert werden, sobald die geometrische Annahme von Fluss zwischen zwei parallelen Platten getroffen wird. Druckgetriebener Fluidfluss zwischen zwei parallelen Platten wurde ausgiebig unter dem Synonym des Poiseuille Flusses diskutiert [e.g., 193], für den unter der Annahme von laminaren Strömungen für viskose Fluide das Geschwindigkeitsfeld analytisch bestimmt werden kann. Die Annahme von Poiseuille Fluss im Bereich von Rissen wurde durch experimentelle Untersuchungen bestätigt [121, 216] und für den Fall von veränderbaren Rissöffnungen als untere Grenze der Fluss-Druck Beziehung identifiziert [146]. Untersuchungen von Fluidfluss in deformierbaren Rissen kann durch eine Erweiterung der getroffenen Annahmen im Rahmen der Kontinuumsmechanik, die Bilanzgleichungen konsultiert [e.g., 88, 91, 123, 194] um einen konsistenten Zusammenhang zwischen Volumenänderungen des Risses und dessen Einfluss auf den Flussprozess herzustellen, durchgeführt werden. Unter der Berücksichtigung eines biphasigen poroelastischen Models [e.g., 20, 54, 158, 190] kann die Interaktion mit der Riss Domäne in Bezug auf volumetrische Änderungen und Fluidaustausch diskutiert werden. Betrachtet man Fluidfluss durch einen deformierbaren Riss kann durch konsistentes Auswerten der Bilanzgleichungen ein in seiner Dimension reduziertes, sogenanntes hybrid-dimensionales Model hergeleitet werden [177, 206–208]. In der Literatur werden vergleichbare Modelle unter dem Aspekt der Schmierströmung eingeführt [16]. Eine Erweiterung des Spannungskonzepts muss in Betracht gezogen werden, sobald mechanische Interaktion durch Rissflächenkontakt das eingeführte hydromechanische Model ergänzt. Eine Anzahl von verschiedenen Ansätzen wurde hierfür in der Literatur diskutiert und umfasst gänzlich empirische Ansätze [e.g., 76], Modelle, die eine nicht veränderliche, konstante Risssteifigkeit annehmen [e.g., 34], diskrete Kontaktmodelle [e.g., 18] und Modelle, die Kontaktmechanismen entkoppelt von der volumetrischen Änderung des Risses betrachten [e.g., 56, 109, 144]. Alternativ dazu kann die Rissöffnung als ein Indikator für das spezifische Equilibrium des Risses betrachtet werden [40, 145, 147]. Die mechanische Interaktion von Rissoberflächen ist durch eine hohe Anzahl von Hertzschen Kontaktzonen charakterisiert. Die durch Oberflächenkontakt induzierten Normalspannungen skalieren mit der akkumulierten Kontaktfläche in einer stark nicht-linearen Beziehung [40, 77, 197]. Das Auftreten von Hysteresen während der zyklischen Belastung eines Einzelrisses auf der Laborskala ist auf die relative Neuausrichtung beider Rissoberflächen zurückzuführen. Der Hystereseneffekt nimmt mit zunehmender Zyklusanzahl ab und konvergiert gegen einen reversiblen Zustand [14]. Risse die bei Felduntersuchungen unter in-situ Bedingungen getestet werden haben bereits eine natürliche Neuausrichtung durchlaufen und zeigen keine Hysteresiseffekte solange die Perturbationen des Equilibriumzustandes unterhalb der Grenze zu seismischen Aktivitäten liegen [14, 147]. Der reversible Charakter der Normalspannungsantwort motiviert die Annahme einer nicht-linear elastischen konstitutiven Beziehung. Modelle, die basierend auf experimentellen Daten Normalspannungsbeziehungen ausnutzen, können in der Literatur gefunden werden [e.g., 12, 70, 75, 181]. Das bereits eingeführte hydromechanische Model ist jedoch sensitiv mit Bezug auf Parameteränderungen [175] und eine Kalibrierung unter in-situ Bedingungen ist eine nicht triviale Aufgabe. Simple Modifikationen eines bestehenden Kontakmodels vereinfachen Untersuchungen unter in-situ Bedingungen durch die Berücksichtigung des initialen Spannungszustandes [173]. Der Einfluss von mechanischer Interaktion zwischen den Rissoberflächen auf den Fluidfluss während harmonischer An-

regung eines Einzelrisses wurde ausgiebig in einer numerischen Studie untersucht. Die Studie konnte einen konsistenten Zusammenhang zwischen nicht konstanten Phasenverschiebungen zwischen Fluiddruck und -fluss, beziehungsweise zusätzlichen Amplituden im Frequenzraum herstellen und mit hydromechanischen Effekten korrelieren [174]. Rissstellungen und damit verbundene Scherspannungsevolutionen [e.g., 201] wurden im Rahmen dieser Arbeit nicht betrachtet, da, wie bereits erwähnt, Pumpvorgänge zum Testen von gerissenen Reservoiren deutlich unterhalb der Grenze zu seismischen Aktivitäten durchgeführt werden.

Numerische Kopplungsverfahren

Bei der Betrachtung von Fluidfluss durch deformierbare Risse, eingebettet in ein poröses Medium, kann das resultierende globale System in die Rissdomäne und die hydromechanische Antwort der poroelastischen Matrix unterteilt werden. Eine konsistente Interaktion zwischen beiden Bereichen wird durch an der Rissoberfläche definierte Übergangsbedingungen sichergestellt [e.g., 177]. Im Zuge dieser Arbeit wird das Feld an potentiellen numerischen Lösungsstrategien auf netzbasierte Methoden, wie das Finite-Volumen-Verfahren (FV) [e.g., 57, 204] oder die Finite-Elemente-Methode (FE) [e.g., 17, 94, 223], beschränkt. Die starke numerische Interaktion zwischen volumetrischer Änderungen des Rissvolumens und der Druckverteilung des Fluids benötigt eine implizite Kopplung beider Bereiche [1, 218], die durch partitionierte oder monolithische Lösungsverfahren eingeführt werden kann. Arbeiten aus dem Forschungsbereich der ungeschädigten porösen Medien diskutieren im Rahmen von volumetrisch gekoppelten Systemen Modifikationen der numerischen Formulierung, um Stabilität eines partitionierten Ansatzes zu gewährleisten [104–106]. Das sogenannte Fixed-Stress basierte Aufspalten des Systems ist ebenfalls für gerissene poröse Medien erweitert worden [72, 73] und ermöglicht stabile numerische Untersuchungen von Fluidfluss durch deformierbare Risse in Form einer vorkondizinierten Richardson-Iteration [38]. Eine Alternative zur Kopplung der poroelastischen Antwort mit der Riss Domäne sind Quasi-Newton-Verfahren [45, 83, 171]. Eine Stabilitätsanalyse für die Quasi-Newton Kopplung im Bereich von gerissenen porösen Medien wurde anhand von Einzelrissen und Rissnetzwerken in drei Dimensionen durchgeführt [176]. Der Vorteil von partitionierten Lösungsverfahren sind Berechnungen auf nicht konformen Diskretisierungen und im Kontext des parallelen Rechnens, das Verwenden von iterativen linearen Lösern. Das Konvergenzverhalten von partitionierten Lösern ist jedoch weniger effizient als das von monolithischen Strategien [177]. Monolithische Verfahren lösen in einem global aufgestellten Gleichungssystem die gesuchten primären Variablen beider Bereiche simultan. Das globale Gleichungssystem kann unter Berücksichtigung verschiedener numerischer Methoden und deren Kombinationen aufgestellt werden. In der Literatur sind FV-FV [e.g., 202], FE-FV [e.g., 183] and FE-FE [e.g., 177, 179–181] Kopplungsansätze dokumentiert. Monolithische Lösungsstrategien sind numerisch robust, benötigen jedoch aufgrund der schlechten Konditionierung des Gleichungssystems vorrangig direkte Löser, die im Rahmen des parallelen Rechnens gewisse Skalierungsgrenzen mit sich bringen.

Gliederung der Arbeit

Der Motivation, der Zielsetzung und dem Stand der Forschung, eingeführt in **Kapitel 1**, folgt eine theoretische Diskussion der erforderlichen Bilanzgleichungen in **Kapitel 2**, um die in dieser Arbeit verwendete Formulierung für den Fluss in deformierbaren Rissen zu motivieren. Das Kapitel beschäftigt sich mit der hydromechanischen Interaktion von Flussprozessen in deformierbaren Rissen, die sich unterhalb der kritischen Grenze zu seismischen Aktivitäten befinden. In diesem Zusammenhang wird ein konsistentes hydromechanisches Flussmodell hergeleitet, eine poroelastische Formulierung eingeführt, um die Antwort des umliegenden Materials abzubilden und Übergangsbedingungen von beiden Gebieten diskutiert, um das globale Gleichungssystem zu schließen. Zusätzlich zu den beschreibenden Gleichungen wird ein konstitutives Modell eingeführt, mit dem Messdaten aus dem Feld unter in-situ Bedingungen analysiert werden können.

Aufgrund der Trennung der Berechnungsgebiete in einen durch das hydromechanische Flussmodell abgebildeten Bereich und einen Bereich, in dem die poroelastische Formulierung gilt, beschäftigt sich **Kapitel 3** mit verschiedenen numerischen Kopplungsstrategien. Dabei wird der Fokus der Diskussion auf die numerische Effizienz und Genauigkeit der möglichen Lösungsansätze gelegt. Neben der Diskussion von partitionierten konstanten Spannungs- und Quasi-Newton Lösungsstrategien wird durch das Mitteln der Bilanzgleichungen eine monolithische Formulierung eingeführt.

Kapitel 4 besteht aus veröffentlichten und eingereichten Publikationen. Die Bereiche der Veröffentlichungen umfasst numerische Studien über das Kopplungsverhalten der eingeführten numerischen Gebiete, Untersuchungen von hydromechanischen Phänomenen, die während harmonischer Anregung von Einzelrissen auftreten und Charakterisierung von Rissen basierend auf in-situ Messdaten aus dem Feld.

Die Dissertation findet dann mit einer Zusammenfassung und Aussicht der Arbeit in **Kapitel 5** einen Abschluss. Im abschließenden Kapitel werden Möglichkeiten zur Erweiterung des eingeführten Modells im Zusammenhang mit zukünftigen Anwendungsgebieten im Bereich der gerissenen porösen Medien diskutiert.

Nomenclature (Introductory Part)

Conventions

Index and suffix conventions

\square^\pm	positive and negative fracture surface
\square^+ / \square_+	positive fracture surface
\square^- / \square_-	negative fracture surface
\square^α	constituent identifier - superscript
\square^l	longitudinal direction
\square^{sol}	numerical solution
\square^t	tangential direction

Symbols

Greek letters

Symbol	Unit	Description
α	[-]	Biot-Willis or effective stress coefficient
β^f	[1/Pa]	fluid compressibility
γ_0^{fR}	[kg]	specific fluid weight
γ_c	[Pa]	fixed-stress convergence estimate
Γ^{Fr}	[-]	fracture domain
Γ^{Pe}	[-]	poro-elastic surface
δ	[m]	fracture aperture
δ_0	[m]	initial fracture aperture
δ_{min}	[m]	minimal mechanical aperture
δ^c	[m]	fracture closure
δ_{max}^c	[m]	maximum fracture closure
ε_r	[m]	absolute roughness
η^{fR}	[m]	effective fluid shear viscosity
κ^{fR}	[Pa]	effective fluid bulk viscosity
λ	[Pa]	first Lamé parameter
ρ^{fR}	[kg/m ³]	effective fluid density
σ_N^{Con}	[Pa]	contact normal stress
σ_M	[Pa]	total mean stress of mixture

ϕ	[-]	porosity
ε	[-]	small strain tensor
σ	[N/m ²]	Cauchy stress tensor
σ_T	[Pa]	total stress tensor
τ	[N/m ²]	deviatoric stress
ξ	[-]	averaging weighting parameter
\mathcal{X}	[-]	unique motion function
Ψ	[-]	dimensionless friction factor

Latin letters

Symbol	Unit	Description
a	[m ²]	actual area
A	[m ²]	referential area
A^{ext}	[m ²]	external Surface
\mathcal{B}^{Pe}	[-]	poro-elastic domain
E^{Fr}	[Pa]	fracture stiffness parameter
$E_{\text{eq}}^{\text{Fr}}$	[Pa]	equilibrium fracture stiffness parameter
G	[Pa]	shear modulus
J	[-]	Jacobian
K	[Pa]	solid skeleton bulk modulus
K^s	[Pa]	solid material bulk modulus
K^f	[Pa]	fluid bulk modulus
$1/M$	[1/Pa]	inverse storage capacity
k_{Fr}^s	[m ²]	effective fracture permeability
l_c	[m]	characteristic length
m^f	[kg]	fluid mass
p	[Pa]	fluid pressure
p_0^{eq}	[Pa]	initial equilibrium fluid pressure
\mathcal{P}	[-]	material point
\hat{P}^l	[Pa]	averaged longitudinal pressure
\hat{P}^t	[Pa]	averaged tangential pressure
Q	[m ³ /s]	volumetric flow rate
q_{lk}	[m/s]	fluid leak-off
Re	[-]	Reynolds number
s^α	[N/m ²]	partial mean stress
s_0	[-]	hydraulic-mechanical aperture parameter
t	[s]	time

V	[m ³]	referential volume
V^{β^f}	[m ³]	fluid compressibility volume
V^δ	[m ³]	fracture aperture volume
V^{Inj}	[m ³]	injected fluid volume
V^{Leak}	[m ³]	leak-off fluid volume
V^{Fr}	[m ³]	referential fracture volume
w	[-]	test function
\mathbf{a}_f	[m/s ²]	fluid acceleration
\mathbf{a}_s	[m/s ²]	solid acceleration
\mathbf{b}	[m/s ²]	body force vector
\mathbf{C}	[Pa]	elasticity tensor
\mathbf{d}_f	[m/s]	symmetric part of spatial fluid velocity gradient
\mathbf{e}_i	[-]	(Cartesian) basis of orthonormal vectors
$\hat{\mathbf{e}}_i$	[-]	local (Cartesian) basis of orthonormal vectors
\mathbf{f}^{ext}	[N]	external force vector
\mathbf{F}	[-]	referential deformation gradient
\mathbf{I}	[-]	identity tensor
\mathbf{l}_f	[m/s]	spatial gradient of the fluid velocity
L^{Fr}	[m]	line segment on fracture boundary
\mathbf{n}^{Fr}	[-]	normal of fracture surface
\mathbf{n}^l	[-]	longitudinal normal of fracture surface
$\hat{\rho}^\alpha$	[N/m ³]	volume-specific direct momentum production
\mathbf{x}	[m]	absolute actual position vector to a material Point
\mathbf{X}	[m]	absolute reference position vector to a material Point
\mathbf{t}	[N/m ²]	surface traction
\mathbf{v}_f	[m/s]	fluid velocity
\mathbf{v}_s	[m/s]	solid velocity
\mathbf{w}_f	[m/s]	relative fluid mean velocity

Calligraphic letters

Symbol	Description
\mathcal{O}	origin of a coordinate system

Acronyms

Acronym	Description
2d	two-dimensional
3d	three-dimensional

DOF	degree of freedom
FE(M)	Finite Element (Method)
FV(M)	Finite Volume (Method)
DNS	direct numerical simulations

Chapter 1:

Introduction and overview

1.1 Motivation

Underground flow processes in fractured porous media possess a great significance regarding the optimization of energy production based on natural resources. Energy is stored in form of liquids, respectively heat in the underground and its excavation is highly impacted by discontinuities of the porous medium's transport characteristics such as induced by discrete fractures or fracture networks. Throughout the exploitation flow processes might become fairly complex, since fractures do not simply increase the permeability and induce preferential flow paths within the reservoir, they also reduce the stiffness of the surrounding rock mass. Hence, optimization of the conducted exploitation procedure requires best understanding of the flow processes in combination with their impact on the mechanical deformation state of the system and vice versa. Better knowledge of the hydro-mechanical effects throughout production of gas and oil from wells are also of great value for the hydrocarbon industry [e.g., 49] to increase the design and efficiency of the applied storage methods.

Improvement of oil, gas or heat production rates might be achieved by exploiting areas of increased permeability introduced by discrete fractures. Fractures embedded in a porous medium might be pre-existing, but can also be artificially induced by hydraulic fracturing operations resulting in a higher conductivity of the reservoir [e.g., 85]. An increased conductivity allows for higher flow rates once the equilibrium state of the reservoir is disturbed by variations of the pore pressure. This phenomenon is exploited to achieve higher production rates throughout fluid and gas exploitation, to optimize the management of water reservoirs [e.g., 74, 128] or to improve the heat excavation where the existence of fractures additionally expand the interaction area of rock mass and fluid throughout geothermal energy production [e.g., 192]. In contrast to regions relevant for exploitation procedures, geological settings appropriate for waste disposal [e.g., 42] and carbon sequestration [e.g., 22, 90] should possess low permeabilities suitable for long-term storage of matter by minimization of transport.

Nevertheless, independent of the field of application, the determination of hydro-mechanical properties of the targeted domain is mandatory for all reservoir-engineering methods. Hence, before and after stimulation of neighbouring reservoirs by pressure variations within boreholes resulting in perturbations of the equilibrium state, the reservoirs characteristic properties are required to be determined for documentation of potential changes of its characteristics. Information of the surrounding reservoir before the pumping operations form the basis to appropriately design quantities such as total injected fluid volume and targeted pressure maxima to optimize the procedure's efficiency and to reduce the risk of unwanted incidents. Considering hydraulic fracturing as an example, information about the to be fractured reservoir in terms of permeability and toughness of the rock

mass along with the knowledge about preexisting fractures are mandatory to achieve a successful and safe execution of the pumping protocols. Investigations of the reservoirs properties after the borehole operations reveal wanted and/or unwanted changes of the documented characteristics, such as an increase in permeability after conducting hydraulic fracturing procedures.

Flow rates in underground settings are estimated based on information about the permeability and storage capacity of the investigated fractured domain. The characterization process analyzes data sets that might be obtained from a number of different testing procedures ranging from non-destructive procedures focusing on the evolution of mechanical waves [111, 112, 116, 149, 189] to pumping operations on boreholes where transient pressure and flow data is interpreted [11, 36, 60, 126]. Pumping operations might be executed and interpreted in terms of transients resulting from pulse tests [35, 99, 101, 191], harmonic [153, 154] and non-harmonic testing [157] or step rate tests [59]. Recently the set of flow and pressure transients has consistently been extended to uni-axial tracking of fracture opening throughout testing procedures [52] to limit the parameter space defining the potential hydro-mechanical reservoir characteristics. Nevertheless, mostly the received data is locally limited to the transients recorded at discrete boreholes and can only be interpreted in combination with inverse analysis by best numerical fits of the measurement data to constrain the space of characteristic properties of hydraulically tested reservoirs.

1.2 State of the art, scope and aims

Throughout the analysis of measurement data a number of different strategies might be conducted to determine characteristic properties of the investigated domain. Requirements to the applied method vary dependent on the conducted experiments, the set of transient data and the properties of interest. Knowledge about the driving mechanisms of flow processes in deformable fractures throughout a broad field of potential applications, ranging from periodic excitation of single or multiple fractures to identify heterogeneities of the subsurface [3, 36, 63, 157] to studies on the permeability evolution throughout step rate tests [164], is required to develop a suitable and efficient method for analysis. The needed understanding is gained by discussion of the analysis strategies of measurement data, the consistent modeling of hydro-mechanical flow in fractured porous media and the different solution strategies for hydro-mechanically coupled partial differential equations based on the existent literature.

Analysis of transient measurement data

Analysis of measurement data might be separated into analytical and numerical solution strategies. Analytical methods are traditionally based on isotropic pressure diffusion assumptions to govern flow processes in a single, rigid fracture to estimate its characteristic properties [25, 125]. Numerical treatment of diffusion based models to predict flow through complex fractured porous media have extensively been studied in the literature [e.g., 19, 62]. Still, due to their limitations on the hydro-mechanical interaction with the surrounding medium diffusion based models fail to reproduce a number of phenomena

recorded during hydraulic testing of fractures [173]. Some limitations might be overcome by locally enhanced numerical models for a better approximation of the fracture properties [e.g., 137, 139]. The consideration of constitutive relations between pore pressure and fracture opening serves well to generate best numerical fits when fracture permeabilities might change throughout perturbations of the fracture's equilibrium state [163, 164]. Experimentally permeability variations related to the effective stress state of a fracture have been studied in the literature to correlate the resulting pressure induced flow rates to transient changes of the fracture geometry [115, 122, 215, 219]. This phenomenon is of interest in the field of fault reactivation, respectively seismicity [33, 78–80] and investigations on the relationship between mechanical and hydraulic fracture opening [209]. Nevertheless, the constitutive relation between fluid pressure and fracture opening introduces a local characteristic to the investigated system which does not translate to experimental findings in the field of fracture flow. One prominent example where such models tend to fail are reverse water-level fluctuations introduced by non-local changes of the fracture volume [69, 185, 206, 208]; a phenomenon which was also observed during pumping operations on unfractured reservoirs and is known as the Noordbergum effect [107, 162]. Pressure drops in distant monitoring wells are triggered by the pronounced difference in characteristic travelling times of the fluid pressure diffusion and almost instantaneous deformation response of the surrounding medium resulting in an opening of fractures in regions which have not been reached by the injected fluid volume. In contrast to the proposed methods which focus on the analysis in the time domain the efficiency of procedures designed for data obtained from harmonic fluid pressure excitation experiments might drastically be increased by calculations in the frequency domain. Besides advantages such as signal separation from ongoing pumping operations or measurement imperfections [154, 157] the cost of numerical simulations is drastically reduced to a single quasi-static solution step to investigate the fracture response for a given excitation frequency [39, 153, 157]. Nevertheless, models known from the literature designed for analysis in the frequency domain lack to consistently consider strict coupling of the fracture flow and deformation state of the rock matrix by means of volumetric changes and local variations of the fracture permeability.

Modeling of flow in deformable fractures

Hydro-mechanical effects have a strong impact on flow processes in deformable fractures. In the geological settings of fractured rock material, the fracture's geometry is characterized by a high ratio between fracture length l and aperture δ defining a high aspect-ratio regime $l/\delta > 10^4$ [26]. A first approach uses direct numerical simulations (DNS) where flow processes in fractures are governed by the Navier-Stokes equation and coupled to the response of the poro-elastic matrix [21]. Nevertheless, direct numerical simulations are computationally expensive resulting in limitations on the investigated domain size, respectively the complexity of the fracture network and might introduce large numerical errors once the discretization is not chosen accordingly [151]; a non-trivial task in the presence of the investigated fracture dimensions. An increase in efficiency can be achieved in the regime of high aspect-ratio fractures by approximation of their geometry assuming two parallel plates. Pressure driven processes for flow between parallel plates have

been extensively studied under the name of Poiseuille's law [e.g., 193] where the velocity profile for viscous fluids under laminar flow conditions can analytically be derived. Studies proved that the introduced assumption closely reproduces flow data obtained from experiments [121, 216] and serves as a lower bound in the presence of fracture opening and closing [146]. Investigations on flow in deformable fractures might be achieved by extension of the introduced assumptions based on the framework of continuum mechanics which postulates a set of balance equations [e.g., 88, 91, 123, 194] to consistently consider changes of the fracture volume and their impact on the flow solution. Considering a biphasic poro-elastic medium [e.g., 20, 54, 158, 190] the hydro-mechanical interaction with the embedded fracture by means of deformation and fluid exchange can be discussed. Consistent evaluation of the balance equations leads to a dimensionally reduced model for flow in deformable fractures and is referred to as the hybrid-dimensional formulation in the context of this work [177, 206-208]. In the literature comparable formulations have been introduced under the name of the lubrication theory [16]. Besides the purely hydro-mechanical interaction of fluid and fracture the acting stresses might be extended by contact induced phenomena once fracture surfaces mechanically interact. Different approaches can be found in the literature to describe the fracture stiffness induced normal stresses including purely empirical models [e.g., 76], models assuming a non-evolving, constant fracture stiffness [e.g., 34], discrete contact models [e.g., 18] or fracture models that are volumetrically decoupled from the flow processes [e.g., 56, 109, 144]. An alternative approach is the consideration of fracture stiffness as an indicator for the fracture's equilibrium state [40, 145, 147]. Mechanical interaction of fracture surfaces is characterized by a high number of Hertzian contact zones. Normal stress response due to surface interaction characteristically scales with the amount of contact zones, respectively total contact surface in a highly non-linear manner [40, 77, 197]. Hysteresis effects regarding the normal stress response during loading and unloading of fractures might be investigated in a laboratory setting since fracture surfaces might relocate, but reaches a state of mated surfaces and reversible responses after a certain number of loading cycles [14]. Under in-situ conditions natural relocation of fractures induces a state of mated surfaces with no hysteresis effects during fracture opening and closing triggered by perturbations of the equilibrium state below the limit of seismic actions [14, 147]. The reversible characteristic motivates a non-linear elastic constitutive relation between the contact induced normal stresses and the fracture opening, respectively closing. A number of partly physics based models capturing the asymptotic closing behaviour can be found in the literature [e.g., 12, 70, 75, 181]. Nevertheless, the proposed hydro-mechanical model is sensitive to parameter changes [175] and configuration of consistent sets of model parameters is a non-trivial task under in-situ conditions. To overcome this burden a newly developed contact model considers the fracture's equilibrium configuration by simple modification of the initial stress state governed by an existent contact model [173]. The influence of fracture stiffness on the hydro-mechanical response of a single fracture throughout harmonic excitation has been investigated throughout numerical experiments. The study consistently correlates the existence of non-constant phase shifts between fluid pressure and flow, respectively additional amplitudes in the frequency domain to hydro-mechanical phenomena and not as previously assumed to measurement imperfections [174]. The treatment of fracture shearing, respectively shear stress evolution [e.g., 201] is not discussed in

the context of this work since hydraulic characterization of fractured reservoirs are below the limit of seismic actions and have a minor contribution throughout the characterization process of fracture properties based on hydraulic testing.

Numerical coupling procedures

In the context of flow through deformable fractures embedded in a poro-elastic medium the resulting global system might be splitted in the fracture flow domain and the response of the poro-elastic matrix. The system is then closed by a set of transition boundary conditions to guarantee consistency of the balance equations throughout interaction of both regions [e.g., 177]. Discussion of the numerical treatment of flow through deformable fractures is limited to the field of mesh-based methods such as the Finite Volume (FV) [e.g., 57, 204] or Finite Element Method (FE) [e.g., 17, 94, 223]. Strong interaction between volumetric changes and pressure state requires implicit coupling of both domains [1, 218] which might be achieved by staggered/partitioned or monolithic schemes. From studies in the field of unfractured porous media it is known that volumetrically coupled systems require special treatment to guarantee numerical stability, respectively efficiency once staggered approaches are applied [104–106]. Extension of the fixed-stress splitting to the field of fractured poro-elastic media [72, 73] introduces a stable numerical scheme for flow processes in deformable fractures in terms of a physics based preconditioned Richardson iteration [38]. Besides fixed-stress or drained splitting techniques coupling of fracture domain and poro-elastic matrix might be realized by advanced quasi-Newton methods [45, 83, 171]. Efficiency and stability of quasi-Newton methods for applications in the context of deformable high-aspect ratio fractures have been studied for single fractures and complex fracture networks in three dimensions [176]. Advantages of staggered algorithms are, amongst others, calculations on non-conforming meshes [177] and the reuse of pre-existing solvers for the different underlying physical problems which discrete global systems can then be solved by efficient iterative methods leading to an optimization of memory utilization and computational performance. Nevertheless, a higher number of iterations is required to reach global equilibrium when compared to the convergence behaviour of monolithic schemes [177]. In contrast to staggered approaches monolithic strategies require assembly of a global system of equations to solve both domains simultaneously. Different strategies to assemble a monolithic system are documented in the literature including FV-FV [e.g., 202], FE-FV [e.g., 183] and FE-FE coupling approaches [e.g., 177, 179–181]. Monolithic schemes are numerically robust, but since the global system is not well-conditioned require the use of direct solvers which are not particularly preferred when it comes to high performance computing.

1.3 Outline of the thesis

Motivation, aim and state of the art presented in **Chapter 1** is followed by a theoretical introduction of the necessary balance equations in **Chapter 2** to motivate the fracture flow formulation used throughout this work. The chapter is concerned with the hydro-mechanical interaction present throughout flow processes in deformable fractures below

the limit of seismic actions. In this context a consistent hybrid-dimensional flow model is derived, a poro-elastic formulation introduced to capture the response of the surrounding bulk matrix and transition boundary conditions discussed to close the global system of equations. Additionally, constitutive relations governing the normal stress evolution initiated by contact of two fracture surfaces are motivated and extended for the case of measurement data analysis under in-situ conditions.

Since the computational domain is separated in a region governed by the hybrid-dimensional flow model and a region described by poro-elastic formulations a number of numerical coupling procedures are examined in **Chapter 3**. Focus of the discussion is on possible solution strategies of the global system in terms of computational efficiency and accuracy. In this context staggered approaches, namely fixed-stress and quasi-Newton techniques are discussed and a monolithic formulation is introduced by averaging of the balance equations.

Chapter 4 consists of published and submitted research articles. The field of publication includes numerical studies on the coupling behaviour of fracture flow and poro-elastic domain, the analysis of hydro-mechanical phenomena found throughout harmonic excitation of single fractures and the characterization of tested fractures under in-situ conditions. The thesis is then closed by a summary and an outlook of the presented work in **Chapter 5**. Extensions of the model will be discussed along with the potential for future investigations in the field of fractured porous media.

Chapter 2: Continuum-mechanical modelling of flow in fractured porous media

Flow through fractured porous media induces strongly coupled hydro-mechanical phenomena by interacting volume changes of the fracture and variations of the fluid pressure state. Investigations conducted on fractured reservoirs proof the evidence of hydro-mechanical responses of the system induced by perturbations of the equilibrium state [e.g., 8, 139, 173, 221]. Hence, a physical sound description of the coupled process requires a consistent consideration of both constituents, namely the solid and the fluid phase [73, 131, 132, 177, 202, 206]. In this chapter the theory of continuum mechanics is conducted to derive a hybrid-dimensional model for flow in deformable fractures by evaluation of the balance equations, to introduce a poro-elastic formulation governing the response of the surrounding matrix and to discuss transition boundary conditions to close the global system.

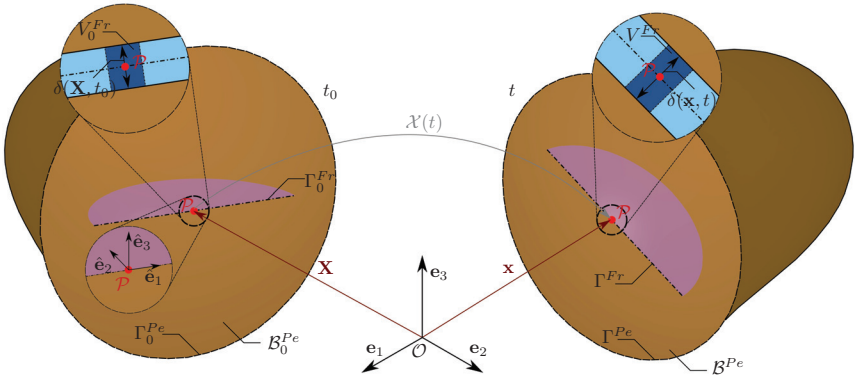


Figure 2.1: Representation of a single fracture Γ^{Fr} embedded in a poro-elastic body B^{Pe} with the surface Γ^{Pe} . Changes of the fracture are considered with respect to the local coordinate system \hat{e}_i where the direction of \hat{e}_3 and the direction of the fracture surface normal \mathbf{n}^{Fr} are aligning. Changes of the fracture volume V^{Fr} induced by changes of the aperture δ defined in the reference configuration \mathbf{X} at time t_0 and spatial configuration \mathbf{x} at time t on material point level \mathcal{P} are coupled to the deformation response of the poro-elastic body in terms of the unique motion function $\mathcal{X}(t)$ [176]

2.1 Flow in deformable fractures - Hybrid-dimensional formulation

Flow processes in deformable fractures are affected by the initial fracture geometry, transient changes of the fracture volume and local permeability variations. Modelling of fractured reservoirs requires an efficient description of the hydro-mechanical processes to resolve the domain of experiments performed on different scales ranging from laboratory to field investigations. Assumptions made about the fracture geometry, respectively velocity profile within the fracture domain allow the derivation of the hybrid-dimensional model and the reduction of the fracture flow domain by one dimension. The model is derived by a consistent evaluation of the conservation of mass and balance of momentum under fully saturated conditions. Since a local coordinate system is introduced for the fracture domain kinematic quantities related to the fracture domain are highlighted by $\hat{\square}$ to avoid confusion with quantities defined in the poro-elastic domain.

2.1.1 Conservation of mass

Conservation of mass describes the classical principal of mechanics which considers mass as a fixed quantity regarding a given system [194]. In the framework of continuum mechanics mass is conserved for a fluid filled fracture once the material time derivative

$$\frac{D}{Dt} \int_V dm^f = \frac{D}{Dt} \int_V \rho^{fR} dv \quad (2.1)$$

is fulfilled for an arbitrarily chosen volume V which is introduced as a subset of the fracture volume V^{Fr} . In eq. (2.1) m^f is the fluid mass and ρ^{fR} the effective fluid density. The fracture volume $V^{Fr}(t)$ is a non-constant property changing in time dependent on the deformation state of the surrounding poro-elastic material. The rate of change of the integral over a subset of the total fracture volume V^{Fr} is defined in local Cartesian coordinates where $dv = d\hat{x}_1 d\hat{x}_2 d\hat{x}_3$ and $d\hat{x}_3$ points in direction of the fracture normal \mathbf{n}^{Fr} in case of a three-dimensional (3d) fracture domain. Taking the pre-known fracture geometry into account and considering negligible changes of the fracture normal (spatial and reference configuration of fracture normal are approximately equivalent $\mathbf{n}^{Fr} \approx \mathbf{N}^{Fr}$) integration in direction of \hat{x}_3 returns the fracture aperture $\delta(\hat{x}_1, \hat{x}_2)$ and the conservation of mass in the spatial description can be rewritten as

$$\frac{D}{Dt} \int_V \rho^{fR} dv = \frac{D}{Dt} \int_A \delta \rho^{fR} da \quad (2.2)$$

considering $a = d\hat{x}_1 d\hat{x}_2$ and A to be a subset of the referential lower dimensional fracture plane Γ^{Fr} . To evaluate the material time derivative the formulation must be transformed to the referential configuration to express the integrands, respectively the integral's domain as a function of \mathbf{X} . Since the integration domain is reduced to two dimensions local changes in area are expressed by the Jacobian of the deformation mapping

$$\hat{J} = \det \hat{\mathbf{F}} = \frac{dA}{dA_0} \quad (2.3)$$

where $\hat{\mathbf{F}} = d\hat{\mathbf{x}}/d\hat{\mathbf{X}}$ is the deformation gradient. Transformation of eq. (2.1) to the referential configuration by using the Jacobian introduced by eq. (2.3) results in

$$\frac{D}{Dt} \int_{A_0} \check{\delta}(\hat{\mathbf{X}}, t) \check{\rho}^{iR}(\hat{\mathbf{X}}, t) \hat{J} da_0 \quad (2.4)$$

where $\check{\delta}(\hat{\mathbf{X}}, t)$ and $\check{\rho}^{iR}(\hat{\mathbf{X}}, t)$ are functions of the reference position vector $\hat{\mathbf{X}}$, the differential is defined as $da_0 = d\hat{X}_1 d\hat{X}_2$ and the integral domain A_0 is a subset of the lower dimensional referential fracture plane Γ_0^{Fr} . In the referential configuration the domain of integration A_0 is a fixed quantity in time. Hence, the differentiation $D/Dt = \square$ is brought inside the integral and applied to the integrands

$$\int_{A_0} \overline{(\check{\delta} \check{\rho}^{iR} \hat{J})} da_0 = \int_{A_0} [\check{\delta} \check{\rho}^{iR} \hat{J} + \check{\delta} \dot{\check{\rho}}^{iR} \hat{J} + \check{\delta} \check{\rho}^{iR} \dot{\hat{J}}] da_0 = \int_{A_0} [\overline{(\check{\delta} \check{\rho}^{iR})} + \check{\delta} \check{\rho}^{iR} \text{div } \check{\mathbf{v}}_f] \hat{J} da_0 \quad (2.5)$$

where $\check{\mathbf{v}}_f$ is the referential velocity of the fluid flow within the fracture plane. Throughout the derivation of eq. (2.5) the following relation for the rate of the Jacobian has been used

$$\dot{\hat{J}} = \overline{\dot{\det} \hat{\mathbf{F}}} = \hat{J} \hat{\mathbf{F}}^{-T} : \dot{\hat{\mathbf{F}}} = \hat{J} \mathbf{I} : \hat{\mathbf{l}}_f = \hat{J} \text{div}(\check{\mathbf{v}}_f) \quad (2.6)$$

considering $\hat{\mathbf{l}}_f = \text{grad}(\check{\mathbf{v}}_f)$ to be the spatial gradient of the fluid velocity. In eq. (2.5) separation of $\hat{J} da_0$ allows a change of variables to rewrite the equation with respect to the spatial configuration

$$\frac{D}{Dt} \int_V \rho^{iR} dv = \int_A [\overline{(\check{\delta} \rho^{iR})} + \delta \rho^{iR} \text{div } \check{\mathbf{v}}_f] da. \quad (2.7)$$

The given relationship in eq. (2.7) is a slightly modified version of the classical Reynolds transport theorem for the specific case of high aspect-ratio fractures which correlates the rate of change of an integral property with the integrands production and net transport over the domain's boundary [194]. When compared to the fluid velocity $\check{\mathbf{v}}_f$, the solid velocity \mathbf{v}_s is found to be negligible ($\mathbf{v}_s \ll \check{\mathbf{v}}_f$) simplifying the formulation by replacing the fluid velocity $\check{\mathbf{v}}_f$ with the relative fluid velocity $\hat{\mathbf{w}}_f$. The conservation of mass in its spatial description reads

$$\frac{D}{Dt} \int_V dm^f = \int_A [\overline{(\check{\delta} \rho^{iR})} + \delta \rho^{iR} \text{div } \hat{\mathbf{w}}_f] da \quad (2.8)$$

and must be pointwise satisfied for any subset of A to be consistent

$$\overline{(\check{\delta} \rho^{iR})} + \delta \rho^{iR} \text{div } \hat{\mathbf{w}}_f = 0. \quad (2.9)$$

Evaluation of the material time derivative results in an equivalent form of eq. (2.9)

$$\frac{\partial}{\partial t} (\delta \rho^{iR}) + \text{div}(\delta \rho^{iR} \hat{\mathbf{w}}_f) = 0 \quad (2.10)$$

which guarantees conservation of fluid mass for an arbitrary change in fracture volume and fluid density.

2.1.2 Balance of linear momentum

The global balance of linear momentum is defined by the product of velocity and mass of a certain volume element. In the following the local form of the balance of linear momentum is derived and evaluated for flow in high aspect-ratio fractures. The derivation is limited to selected steps since, in contrast to the evaluation of the balance of mass, its derivation is a standard procedure in classical continuum mechanics [e.g., 194].

Local form of balance of linear momentum

Starting with the global balance of linear momentum the continuum mechanical description is obtained by the material time derivative of a given domain V^{Fr}

$$\frac{D}{Dt} \int_{V^{Fr}} \rho^{iR} \dot{\mathbf{x}} \, dv = \mathbf{f}^{\text{ext}} \quad (2.11)$$

where the external forces \mathbf{f}^{ext} are composed of body forces \mathbf{b} acting in a volumetric sense and surface traction $\tilde{\mathbf{t}}$ acting on the body's external surface A^{ext}

$$\mathbf{f}^{\text{ext}} = \int_{V^{Fr}} \rho^{iR} \hat{\mathbf{b}} \, dv + \int_{A^{\text{ext}}} \tilde{\mathbf{t}} \, da. \quad (2.12)$$

By replacing the external forces term in eq. (2.11) by the decomposition of such introduced by eq. (2.12) and applying the Reynolds transport theorem in a subsequent step the global balance of momentum is defined by

$$\int_{V^{Fr}} \rho^{iR} \ddot{\mathbf{x}} \, dv = \int_{V^{Fr}} \rho^{iR} \hat{\mathbf{b}} \, dv + \int_{A^{\text{ext}}} \tilde{\mathbf{t}} \, da. \quad (2.13)$$

Since the traction forces $\tilde{\mathbf{t}}$ are exclusively defined on the external surface of the global volume the expression given by eq. (2.13) is limited and not generally applicable to any subset of V^{Fr} . The limitation can be overcome by Cauchy's stress principle which relates traction forces on internal, artificial surfaces $\mathbf{t}(\hat{\mathbf{x}}, \mathbf{n}) = -\mathbf{t}(\hat{\mathbf{x}}, -\mathbf{n})$, defined for a certain combination of position $\hat{\mathbf{x}}$ and surface normal \mathbf{n} , to the externally acting traction forces and proves their equivalence $\mathbf{t} = \tilde{\mathbf{t}}$ on the external surface A^{ext} . Considering the stress state of a given position $\hat{\mathbf{x}}$ to be the set of infinite surface tractions defined by the various surface normals, Cauchy conducted a small tetrahedron to relate the surface tractions to the stress state

$$\mathbf{t}(\mathbf{n}) = \boldsymbol{\sigma} \cdot \mathbf{n} \quad (2.14)$$

by means of the Cauchy stress tensor $\boldsymbol{\sigma}$ [e.g., 194]. The relation given in eq. (2.14) is known as Cauchy's stress theorem and allows in combination with the findings regarding internal surface traction the derivation of the local form of the balance of linear momentum in the spatial configuration

$$\int_V [\text{div}(\hat{\boldsymbol{\sigma}}_{\hat{\mathbf{x}}}) + \rho^{iR} \hat{\mathbf{b}} - \rho^{iR} \hat{\mathbf{a}}_{\hat{\mathbf{x}}}] \, dv \quad (2.15)$$

where V is a subset of V^{Fr} and $\mathbf{a}_f = \ddot{\mathbf{x}}$ the fluid acceleration. For consistency the expression given by eq. (2.15) must be locally satisfied by

$$\operatorname{div}(\hat{\boldsymbol{\sigma}}_f) + \rho^{fR} \hat{\mathbf{b}} - \rho^{fR} \hat{\mathbf{a}}_f = 0 \quad (2.16)$$

considering acceleration and body forces. Evaluation of the material time derivative on the acceleration term \mathbf{a}_f gives the continuity momentum equation

$$\operatorname{div}(\hat{\boldsymbol{\sigma}}_f) + \rho^{fR} \hat{\mathbf{b}} - \rho^{fR} \left[\frac{\partial \hat{\mathbf{v}}_f}{\partial t} + \operatorname{grad}(\hat{\mathbf{v}}_f) \cdot \hat{\mathbf{v}}_f \right] = 0 \quad (2.17)$$

which is used in the following to derive the characteristic velocity profile for flow in high aspect-ratio fractures.

Evaluation of the balance of linear momentum for fracture flow

Flow processes through high aspect-ratio fractures might be best understood when derived from the general assumption of the Navier-Stokes equation. Considering the local form of the balance of momentum given by eq. (2.17), a constitutive relation governing the stress response of a compressible Newtonian fluid [e.g., 194] needs to be introduced assuming constant material parameters

$$\hat{\boldsymbol{\sigma}}_f = -\hat{p}(\rho^{fR}) \mathbf{I} + \left[\kappa^{fR} - \frac{2}{3} \eta^{fR} \right] \operatorname{tr}(\hat{\mathbf{d}}_f) \mathbf{I} + 2\eta^{fR} \hat{\mathbf{d}}_f \quad (2.18)$$

where the fracture fluid pressure $\hat{p}(\rho^{fR})$ is still a function of the fluid density, $\hat{\mathbf{d}}_f = 1/2(\hat{\mathbf{l}}_f + \hat{\mathbf{l}}_f^T)$ is the symmetric part of the spatial fluid velocity gradient, κ^{fR} the effective fluid bulk viscosity and η^{fR} the effective fluid shear viscosity. Inserting the constitutive relation of eq. (2.18) into the local balance of momentum given by eq. (2.17) the Navier-Stokes equation is obtained

$$\underbrace{-\operatorname{grad} \hat{p}}_i + \underbrace{\left[\kappa^{fR} + \frac{1}{3} \eta^{fR} \right] \operatorname{grad} \operatorname{div} \hat{\mathbf{v}}_f + \eta^{fR} \operatorname{div} \operatorname{grad} \hat{\mathbf{v}}_f}_{ii} + \underbrace{\rho^{fR} \hat{\mathbf{b}}}_{iii} = \rho^{fR} \underbrace{\left[\frac{\partial \hat{\mathbf{v}}_f}{\partial t} + \operatorname{grad}(\hat{\mathbf{v}}_f) \cdot \hat{\mathbf{v}}_f \right]}_{iv} \quad (2.19)$$

where the identity $\operatorname{div}(\operatorname{grad}(\hat{\mathbf{v}}_f)^T) = \operatorname{grad}(\operatorname{div}(\hat{\mathbf{v}}_f))$ was used when inserting the given relation for the symmetric part of the velocity gradient $\hat{\mathbf{d}}_f$. The terms of the Navier-Stokes equation introduced by eq. (2.19) might be characterized by pressure gradient forces *i*), viscous forces *ii*), body forces *iii*) and forces related to the fluid acceleration *iv*). Focusing on flow processes in high aspect-ratio fractures eq. (2.19) can be simplified by the following assumptions. Considering relevant fracture geometries, characteristic aperture dimensions are in the micrometer range and prevent fluid particles to flow at

high velocities for a broad range of pressure gradients resulting in laminar flow under stationary conditions motivating neglect of the instationary and non-linear convection parts forming term *iv*). Section 2.1.2 discusses the laminar flow assumption in detail by evaluation of the Reynolds number Re for a set of aperture and pressure gradient combinations. Additionally, the orientation and length of the investigated fractures induce body force differences which are negligible when compared to the pressure variations related to mechanical or hydraulic perturbations of the equilibrium state allowing to simplify eq. (2.19) by disregarding term *iii*). Complexity of the fracture flow model can be reduced once the velocity profile is known a priori. Closed form solutions for flow processes between two parallel plates might be derived under the assumption of parallel flow lines resulting in $\text{div}(\hat{\mathbf{v}}_f) = 0$ and neglect of the first part of term *ii*). The simplified Stokes like equation reads

$$-\text{grad}(\hat{p}) + \eta^{iR} \text{div grad } \hat{\mathbf{v}}_f = 0 \quad (2.20)$$

where velocities within the fracture plane are considered and the velocity component normal to the fracture surface is neglected. Analytical evaluation of eq. (2.19) by assuming no-slip boundary conditions along both parallel plates and separation of variables results in the characteristic parabolic velocity profile known as the Poiseuille's law [e.g., 193]. By integration of the velocity profile in direction of the fracture normal and normalization with respect to the flow cross section area, a relation between the pressure gradient and relative mean velocity

$$\hat{\mathbf{w}}_f = -\frac{\delta^2(\mathbf{x}, t)}{12 \eta^{iR}} \text{grad } \hat{p} = -\frac{k_{Fr}^s(\mathbf{x}, t)}{\eta^{iR}} \text{grad } \hat{p} \quad (2.21)$$

is obtained, where k_{Fr}^s is introduced as the time and space dependent effective fracture permeability. The characteristic proportionality factor $1/12$ might be adapted in case of tortuous fractures or comparable imperfections of the fracture surface [159].

Discussion on the validity of laminar fracture flow

The characteristic of fracture flow has extensively been studied in the literature. Approximation of the fracture geometry by two parallel plates is a fundamental assumption proven to reproduce experimental findings in a fulfilling manner [e.g., 215, 216]. The presence of fracture roughness and tortuosity impact the flow characteristics by variations of flow length and velocity [e.g., 210] justifying the discussion of an effective hydraulic fracture opening. Identification of such has been discussed in a number of works introducing relations between mechanical and effective hydraulic fracture apertures to compensate for geometrical imperfections differing from the parallel plate assumption [e.g., 67, 224]. Nevertheless, independent of the effective aperture choice the considered flow processes are defined in the laminar regime. To avoid incorrect calculations throughout inverse analysis of experiments performed in the turbulent flow regime, a parameter space must be defined in which the proposed model is valid. In case of two smooth parallel plates the different regimes of laminar flow, transition zone and turbulent flow have been identified

[44]. Evaluation of the Reynolds number

$$Re = \frac{\rho^{iR} v_f l_c}{\eta^{iR}} \quad (2.22)$$

where v_f is the fluid velocity in the fracture plane and $l_c = \delta$ the characteristic length, serves to identify the different flow regions. Laminar flow conditions throughout flow between two parallel plates are evident in the range $Re \leq 1440$ followed by a transition zone between $1440 < Re < 2400$ before turbulent flow is fully developed $Re \geq 2400$. Geometrical imperfections of rough fracture surfaces induce Eddies which promote the transition to turbulent flow at lower Reynold numbers. The roughness might be identified by the dimensionless ratio between the absolute roughness ε_r and fracture aperture δ [96]. Expanding the parameter space by the empirical dimensionless friction factor

$$\Psi = \frac{96}{Re} \left(1 + 8.8 \left(\frac{\varepsilon_r}{\delta} \right)^{1.5} \right) \quad (2.23)$$

which was experimentally determined by hydraulic tests on rough fracture surfaces [121], allows the consideration of fracture roughness and its influence on the different flow regimes.

In works concerned with flow through rough fractures, the characteristic length l_c necessary to evaluate eq. (2.22) is not uniquely defined and assumptions of 2δ , δ or $\delta/2$ can be found in the literature [e.g., 43, 136, 147, 225]. In this work δ is considered to be the characteristic length. The Reynolds number Re is then determined by evaluating the fluid velocity v_f by means of eq. (2.21) where the pressure gradient is varied in terms of a discrete value $\Delta\hat{p}$. Discretization of the pressure gradient in space considers two scenarios, namely the field scale where the representative discrete length of a natural fracture is chosen to be $\Delta l = 1\text{m}$ and the laboratory scale where the conducted sample size requires a discrete length of $\Delta l = 1\text{cm}$. Based on the laminar fluid velocity v_f the obtained results characterize the laminar zone correctly, but introduce errors to the size of the transition and turbulent regime. Since this work is exclusively concerned with laminar flow, the graph in figure 2.2 identifies combinations of $\Delta\hat{p}$ and δ valid to conduct the proposed model for inverse analysis of measurement data under laminar conditions and summarizes the transition and turbulent zones to the non-laminar regime.

The parameter study strengthens the laminar flow assumption for investigations on the field scale. The range of relevant parameters are motivated by step rate tests, where pressure differences between steps are in the dimension of $\Delta\hat{p} = 1\text{MPa}$ and fracture apertures are expected to be smaller than $150\ \mu\text{m}$ [e.g., 173]. Considering investigations on the laboratory scale experiments need to be distinguished based on the applied boundary conditions. Experiments with no-flow boundary conditions at the fracture tip, achieved by a shrinking tube isolating the fractured sample from the fluid inducing a confining pressure in a triaxial cell set-up, do not, even under large absolute changes of the applied pressure, allow for large pressure gradients $\Delta\hat{p}$ within the fracture when weakly compressible fluids are used. This can be explained by the low characteristic diffusion time $\Delta t_c = l_c^2/D_\delta$ in the dimension of 10^{-6}s assuming water to be the injected fluid and fracture apertures in the μm range, where the diffusion parameter is $D_\delta = \delta^2/(12.0\ \eta^{iR}\beta^f)$ and β^f the fluid

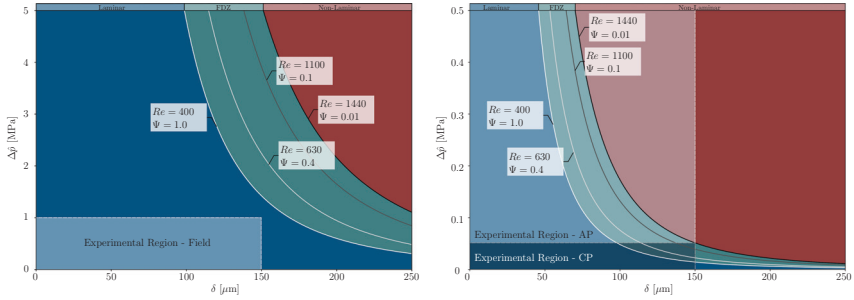


Figure 2.2: Transition from laminar to non-laminar flow regimes based on the effective fracture aperture δ and discrete pressure gradient $\Delta\hat{p}$. The friction dependent zone (FDZ) is evaluated between the lower $\varepsilon/\delta = 0$ ($\Psi = 0.01$) and upper roughness limit $\varepsilon/\delta = 0.4$ ($\Psi = 1$) and defines the transition from laminar to non-laminar flow. **Left:** Flow regimes considering a characteristic length of $l_c = 1\text{m}$ representative for natural fractures tested throughout field investigations. Parameter sets which are of interest in experimental studies are highlighted. **Right:** Flow regimes considering a characteristic length of $l_c = 1\text{cm}$ representative for laboratory studies. Parameter sets which are of interest in experimental studies are highlighted and distinguished between confining pressure (CP) and atmospheric pressure (AP) experiments.

compressibility. Almost instantaneous pressure diffusion has been investigated throughout numerical harmonic testing of a single fracture [e.g., 174]. Pressure gradient changes at such time scales cannot be achieved by experimental devices used to control the pore pressure, resulting in low pressure gradients, respectively fluid velocities and laminar conditions. In contrast, throughout experiments using drained fracture boundary conditions, for instance when a pressure gradient is induced by a rise of fluid pressure at the inlet of a fracture and atmospheric pressure boundary conditions are applied at the outlet, fluid can freely travel through the tested fracture and critical, non-laminar flow inducing velocities can easily be reached. For experiments considering atmospheric/drained boundary conditions the experimental set-up must individually be examined to guarantee laminar flow throughout the testing procedure.

2.1.3 Governing equation

The hybrid-dimensional formulation governing flow processes in deformable fractures is derived by combining the local form of the conservation of mass with the relation obtained from the evaluation of the balance of momentum. Inserting the relative fluid velocity defined by eq. (2.21) into the local conservation of mass introduced by eq. (2.10) results in

$$\frac{\partial}{\partial t}(\delta \rho^{iR}) - \text{div} \left(\rho^{iR} \frac{\delta^3(\hat{\mathbf{x}}, t)}{12 \eta^{iR}} \text{grad } \hat{p} \right) = 0 \quad (2.24)$$

where two independent variables by means of the fluid pressure \hat{p} and the fluid density ρ^{iR} remain unknown. The given system is closed by a linear constitutive relation introducing

proportionality between fluid density ρ^{iR} and fluid pressure \hat{p}

$$\hat{p} = K^f \left[\frac{\rho^{iR}}{\rho_0^{iR}} - 1 \right] \quad (2.25)$$

under a barotropic assumption considering K^f to be the fluid's bulk modulus and ρ_0^{iR} the initial fluid density at $t = 0$. Inserting eq. (2.25) into eq. (2.24) and evaluation of the mathematical operations results in the hybrid-dimensional formulation

$$\underbrace{\frac{\partial \hat{p}}{\partial t}}_{i)} - \underbrace{\frac{\delta^2}{12 \eta^{iR}} \text{grad } \hat{p} \cdot \text{grad } \hat{p}}_{ii)} - \underbrace{\frac{\delta}{12 \eta^{iR} \beta^f} \text{grad } \delta \cdot \text{grad } \hat{p}}_{iii)} - \underbrace{\frac{\delta^2}{12 \eta^{iR} \beta^f} \text{div grad } \hat{p}}_{iv)} + \underbrace{\frac{1}{\delta \beta^f} \frac{\partial \delta}{\partial t}}_{v)} = \underbrace{\frac{\hat{q}_{lk}}{\delta \beta^f}}_{vi)} \quad (2.26)$$

where \hat{q}_{lk} was introduced to account for leak-off governing the fluid exchange with the surrounding rock matrix. The hybrid-dimensional eq. (2.26) is composed of a transient $i)$, a quadratic $ii)$, a convection $iii)$, a diffusion $iv)$, a coupling $v)$ and a leak-off $vi)$ term defined with respect to the normal seepage velocity of the surrounding porous medium $\hat{q}_{lk} = \mathbf{w}_f^N$. Nevertheless, dimensionless analysis of the governing equation motivates neglect of quadratic term $ii)$ and convection term $iii)$ throughout investigations in the high aspect-ratio regime since their contribution to the overall solution is minor [206]. The simplified formulation

$$\frac{\partial \hat{p}}{\partial t} - \frac{\delta^2}{12 \eta^{iR} \beta^f} \text{div grad } \hat{p} + \frac{1}{\delta \beta^f} \frac{\partial \delta}{\partial t} = \frac{\hat{q}_{lk}}{\delta \beta^f} \quad (2.27)$$

is used throughout this work to govern flow processes in deformable fractures under the given assumptions. Since numerical investigations are exclusively concerned with pressure changes relative to the initial equilibrium fluid pressure $\Delta \hat{p} = \hat{p} - \hat{p}_0^{\text{eq}}$ the notation is simplified and \hat{p} is equivalent to pressure changes $\Delta \hat{p}$ in the following.

2.1.4 Weak form of governing equation

Numerical solutions of eq. (2.27) are calculated by means of a classical Bubnov Galerkin finite element scheme. The strong form of equations is not suitable for finite element formulations and a weak form using the principal of virtual work needs to be derived [e.g., 17]. For this purpose a trial function \hat{p}_t is introduced for the fluid pressure \hat{p} which is required to be smooth enough for the applied mathematical operations and to reproduce the considered boundary conditions. The test function $w_{\hat{p}}$ is introduced also required to be smooth enough for the necessary mathematical operations and to vanish in regions where Dirichlet boundary conditions are defined. The weak form is then obtained by multiplying the test function $w_{\hat{p}}$ to eq. (2.27) and integrating such over the fracture volume. Despite the lower dimensional characteristic of eq. (2.27) the domain of integration in

$$\int_{V_{Fr}} w_{\hat{p}} \frac{\partial \hat{p}_t}{\partial t} dv - \int_{V_{Fr}} w_{\hat{p}} \frac{\delta^2}{12 \eta^{iR} \beta^f} \text{div grad } \hat{p}_t dv + \int_{V_{Fr}} w_{\hat{p}} \frac{1}{\delta \beta^f} \frac{\partial \delta}{\partial t} dv = \int_{\Gamma_{Fr}} w_{\hat{p}} \frac{\hat{q}_{lk}}{\delta \beta^f} dv \quad (2.28)$$

is still higher dimensional since the element volume requires to be consistent to the dimension of the surrounding domain. To further reduce the smoothness demand on the trial function \hat{p}_t in the second term of eq. (2.28) Green's first identity

$$\int_{\Gamma^{Fr}} w_{\hat{p}} \text{grad } \hat{p}_t \cdot \mathbf{n}^l da = \int_{V^{Fr}} w_{\hat{p}} \text{div grad } \hat{p}_t dv + \int_{V^{Fr}} \text{grad } w_{\hat{p}} \cdot \text{grad } \hat{p}_t dv, \quad (2.29)$$

obtained from the evaluation of the divergence theorem on the vector field $\text{grad } \hat{p}_t$, is conducted. Green's first identity applied on the weak form of the hybrid-dimensional element formulation differs from the standard formulation in terms of the resulting boundary terms. Assuming continuous pressure fields across the fracture, the pressure gradient in direction of the fracture normal \mathbf{n}^{Fr} vanishes and no contribution to the boundary condition terms is related to tangential flow. This reduces the boundary term to inflow boundary conditions regarding the longitudinal flow direction defined by the outward pointing normal \mathbf{n}^l . In an experimental setting the boundary domain defined by \mathbf{n}^l is considered to be the intersection of borehole and fracture. The assumption of discontinuous pressure jumps across fracture surfaces is discussed in section 3.1.1. Considering the relation given by eq. (2.29) the weak form now reads

$$\begin{aligned} \int_{V^{Fr}} w_{\hat{p}} \frac{\partial \hat{p}_t}{\partial t} dv + \int_{V^{Fr}} \frac{\delta^2}{12 \eta^{lR} \beta^{\bar{f}}} \text{grad } w_{\hat{p}} \cdot \text{grad } \hat{p}_t dv + \int_{V^{Fr}} w_{\hat{p}} \frac{1}{\delta \beta^{\bar{f}}} \frac{\partial \delta}{\partial t} dv \\ = \int_{\Gamma^{Fr}} w_{\hat{p}} \frac{\delta^2}{12 \eta^{lR} \beta^{\bar{f}}} \text{grad } \hat{p}_t \cdot \mathbf{n}^l da + \int_{\Gamma^{Fr}} w_{\hat{p}} \frac{\hat{q}_k}{\delta \beta^{\bar{f}}} dv \end{aligned} \quad (2.30)$$

where the order of derivatives applied on \hat{p}_t is reduced. Conducting the introduced Neumann boundary condition term in its weak form the relative mean velocity introduced by eq. (2.21) can be identified. Analytical integration of the integrals in direction of the fracture normal results in the fracture aperture δ and reduces their integration domain by one, where the integral domain of the boundary condition term simplifies to a line segment

$$\int_{\Gamma^{Fr}} \left[\delta w_{\hat{p}} \frac{\partial \hat{p}_t}{\partial t} + \frac{\delta^3}{12 \eta^{lR} \beta^{\bar{f}}} \text{grad } w_{\hat{p}} \cdot \text{grad } \hat{p}_t + w_{\hat{p}} \frac{1}{\beta^{\bar{f}}} \frac{\partial \delta}{\partial t} \right] da + \int_{L^{Fr}} \frac{\delta}{\beta^{\bar{f}}} w_{\hat{p}} \hat{\mathbf{w}}_f \cdot \mathbf{n}^l dl = \int_{\Gamma^{Fr}} w_{\hat{p}} \frac{\hat{q}_k}{\beta^{\bar{f}}} da. \quad (2.31)$$

Based on the outward pointing normal \mathbf{n}^l the boundary conditions consider outflow to be positive. On a side note, when expressing the boundary term regarding the volumetric flow rate normalized to the applied boundary segment $\hat{Q}/L^{Fr} = \delta \hat{\mathbf{w}}_f \cdot \mathbf{n}^l$ the explicit dependence on the fracture aperture δ moves to the introduced relation and vanishes when discrete values are applied. For instance, considering a cylindrical borehole with a radius of r_b which possesses an orthogonal intersection with a single fracture, the segment of the applied boundary condition would read $L^{Fr} = 2\pi r_b$ and integration of \hat{Q}/L^{Fr} would lead to a constant volumetric flow rate along the discretized intersection boundary segments. The formulation given by eq. (2.31) is used when implementation based on classical finite element formulations of the weak form are used to determine numerical solutions. Specific integration of zero-thickness interface elements are discussed in section 3.1.1.

2.2 Hydro-mechanical formulation for a biphasic poro-elastic medium

Information about the deformation state and fluid exchange with the surrounding bulk matrix are required for the governing equation of flow processes in deformable fractures. In this work the desired information are obtained by a biphasic poro-linear-elastic formulation. Derivation of the governing equations is based on the balance of momentum of the mixture, balance of momentum of the fluid and the linearized conservation of mass. The derivation is limited to the introduction of the local forms since their derivation is a standard procedure in the field concerned with continuum mechanics of mixtures [e.g., 20, 54, 158, 211].

2.2.1 Balance of momentum of the mixture

In the presence of mixtures the balance of momentum introduced by eq. (2.16) for a single phase medium needs to be extended by a term $\hat{\mathbf{p}}^\alpha$ for each constituent α governing the interaction forces between such. Under consideration of negligible inertia forces the local form of the balance of momentum for each constituent reads

$$\operatorname{div} \boldsymbol{\sigma}^\alpha = \rho^\alpha \mathbf{b} + \hat{\mathbf{p}}^\alpha. \quad (2.32)$$

Considering the mixtures theory based on the fundamental assumptions introduced by Truesdell [54, 199], the mixture's balance equations are expressed with respect to the sum of the balance equations of the contributing constituents. Hence, the local form of the balance of momentum of the mixture reads

$$\sum_{\alpha=1}^k [\operatorname{div} \boldsymbol{\sigma}^\alpha + \rho^\alpha \mathbf{b} + \hat{\mathbf{p}}^\alpha] = 0. \quad (2.33)$$

The convention introduced by eq. (2.33) requires constraints on the interaction forces which equate to zero under the assumption of negligible mass production

$$\sum_{\alpha=1}^k \hat{\mathbf{p}}^\alpha = 0. \quad (2.34)$$

Here the balance of momentum of a mixture has been introduced by eq. (2.33) along with a constraint on the interaction forces motivated by negligible mass production between constituents considering eq. (2.34). Applying a tensorial split on the partial stresses they can be rewritten by means of a volumetric and deviatoric contribution

$$\boldsymbol{\sigma}^\alpha = \frac{1}{3} \operatorname{tr}(\boldsymbol{\sigma}^\alpha) \mathbf{I} + \operatorname{dev}(\boldsymbol{\sigma}^\alpha) = s^\alpha \mathbf{I} + \boldsymbol{\tau}^\alpha. \quad (2.35)$$

where s^α is the partial mean stress and $\boldsymbol{\tau}^\alpha$ the deviatoric stress contribution. Considering a biphasic poro-elastic medium the partial stresses are defined with respect to a solid $\boldsymbol{\sigma}^s$

and a fluid σ^f constituent [190]. Referring to eq. (2.33) the total stress of the mixture is then composed of the sum

$$\sigma_{\text{T}} = \sigma_M \mathbf{I} + \boldsymbol{\tau} = (s^s + s^f) \mathbf{I} + \boldsymbol{\tau}^s. \quad (2.36)$$

where the fluid constituent at rest exclusively contributes to the total mean stresses σ_M in terms of the fluid mean stress under equilibrium conditions which is directly proportional to the pore pressure $s^f \propto p$. The explicit form of the partial mean stresses cannot be identified by the equations related to the balance of momentum of the mixture alone, but is introduced in the following section. For a detailed derivation of the balance equations regarding the mixture theory the interested reader is referred to [54].

2.2.2 Constitutive relations

The set of governing equations is closed by introducing constitutive relations for the thermodynamic state variables of the fluid, solid and mixture. Similar to the fracture domain the fluid constituent of the biphasic mixture is considered to be linear barotropic in which case the pore pressure is directly related to the effective fluid density $p(\rho^{fR})$ following the relation introduced by eq. (2.25).

Constitutive relations for a biphasic poro-elastic mixture might be derived based on a general strain energy function introduced by Biot [20] and evaluation of the second law of thermodynamics in terms of the Clausius-Planck inequality in combination with the Coleman-Noll procedure. In this work the partial differentiation of the strain energy function given by Biot [20] is not explicitly executed, but the results are introduced and discussed. For a detailed derivation and discussion of the constitutive relations of porous media the interested reader is referred to [54, 190]. Under consideration of small deformations the isotropic linear-elastic response of the solid constituent is captured by Hooke's law using the set of the solid material bulk modulus K^s and shear modulus G as the elastic constants

$$\boldsymbol{\sigma}^{E,s} = 3 K^s \text{vol}(\boldsymbol{\varepsilon}^{E,s}) + 2 G \text{dev}(\boldsymbol{\varepsilon}^{E,s}) \quad (2.37)$$

which might consistently be derived by implying isothermal conditions for reversible processes to relate the internal energy to the effective elastic Cauchy stress tensor in terms of the strain energy density function

$$W_e = \frac{1}{2} \boldsymbol{\sigma}^{E,s} : \boldsymbol{\varepsilon}^{E,s} = \frac{1}{2} \boldsymbol{\varepsilon}^{E,s} : \mathbf{C} : \boldsymbol{\varepsilon}^{E,s} \quad (2.38)$$

which is valid under the assumption of small deformations, where \mathbf{C} is the elasticity tensor [194]. The concept of effective stress is briefly introduced as an result of the extension of the Clausius-Duhem inequality by the product of the sum of transient volume fraction changes, enforced to result in zero to fulfill the saturation condition, and a Lagrange parameter which can be identified as the pore pressure. Volumetric deformations of the solid skeleton are induced by the weighted interaction of pore pressure p and total mean stress of the mixture σ_M which defines the effective mean stress of the solid constituent

$$\boldsymbol{\sigma}_M^{E,s} = \sigma_M + \alpha p \quad (2.39)$$

where $0 \leq \alpha \leq 1$ is the Biot-Willis or effective stress coefficient relating the volumetric stresses of the solid constituent with the fluid pore pressure by the ratio of the solid skeleton's bulk characteristics obtained under drained conditions and the bulk modulus of the solid material $\alpha = 1 - K/K^s$. Eq. (2.39) explicitly provides the term discussed in eq. (2.36) consisting of the partial mean stresses of the solid s^s and fluid s^f constituent and closes the total stress definition of the mixture. Considering the acting stresses related to the fluid constituent dimensionless analysis motivates the neglect of effective fluid stresses [55] under creeping flow conditions resulting in the following definition of the total fluid stresses

$$\boldsymbol{\sigma}^f = \phi p \mathbf{I} \quad (2.40)$$

where ϕ is the porosity of the porous medium. The remaining unknown expressions required to define the set of governing equations of the biphasic mixture are the momentum interaction terms $\hat{\mathbf{p}}^f = -\hat{\mathbf{p}}^s$, where the constraint defined by eq. (2.34) was used. The missing constitutive relation is introduced based on the results of the formal derivation discussed in [54] under consideration of non-equilibrium conditions due to pressure gradient induced fluid flow through the poro-elastic medium. The interaction forces $\hat{\mathbf{p}}^f$ might be split in an equilibrium and non-equilibrium part first

$$\hat{\mathbf{p}}^f = \hat{\mathbf{p}}_{\text{eq}}^f + \hat{\mathbf{p}}_{\text{neq}}^f, \quad (2.41)$$

where $\hat{\mathbf{p}}_{\text{eq}}^f$ considers the contribution of static porosity variations and the non-equilibrium contribution $\hat{\mathbf{p}}_{\text{neq}}^f$ the influence of viscous drag forces induced by the relative fluid velocity \mathbf{w}_f . Consulting the formal work of [54] the equilibrium and non-equilibrium terms governing the momentum interaction read

$$\begin{aligned} \hat{\mathbf{p}}_{\text{eq}}^f &= p \text{grad } \phi, \\ \hat{\mathbf{p}}_{\text{neq}}^f &= -\frac{\phi_0^2 \gamma_0^{fR}}{k^f} \mathbf{w}_f, \end{aligned} \quad (2.42)$$

where γ_0^{fR} is the specific weight of the fluid and k^f the Darcy permeability of the porous medium. Nevertheless, the equilibrium term introduced in eq. (2.42) is non-linear and can be neglected in the context of linear poro-elasticity simplifying the definition of the interaction forces to

$$\hat{\mathbf{p}}^f = \hat{\mathbf{p}}_{\text{neq}}^f = -\frac{\phi_0^2 \gamma_0^{fR}}{k^f} \mathbf{w}_f \quad (2.43)$$

which provides the missing constitutive relation necessary to close the set of governing equations.

2.2.3 Governing equations

Considering the momentum balance equations for the biphasic poro-elastic medium and fluid constituent defined by eq. (2.33) the set of governing equations is closed by the constitutive relations introduced in section 2.2.2. Special treatment is required once the fluid stresses given by eq. (2.40) are inserted in the balance of momentum of the fluid

by exploiting certain relations between potential primary variables [190] to obtain a formulation governing the fluid behaviour by means of the primary variables fluid pressure p and solid deformation \mathbf{u}_s . The balance of mass of the biphasic poro-elastic mixture is consistently derived by considering the total stresses closed by the effective stress principle introduced by eq. (2.39) and the constitutive relations defined in eq. (2.37) in terms of Hooke's law. The coupled set of equations governing the hydro-mechanical response of a biphasic poro-elastic medium under quasi static conditions neglecting static body forces reads

$$\begin{aligned} \operatorname{div} \boldsymbol{\sigma}_T &= 0 \\ \frac{1}{M} \frac{\partial p}{\partial t} - \frac{k^f}{\gamma_0^f R} \operatorname{div} \operatorname{grad} p &= -\alpha \operatorname{div} \frac{\partial \mathbf{u}_s}{\partial t} \end{aligned} \quad (2.44)$$

where the inverse storage capacity or (local) storativity is introduced by $1/M = \phi/K^f + (\alpha - \phi_0)/K^s$ [211]. Eq. (2.44) is used throughout this work to capture processes where the permeability of the poro-elastic medium allows fluid exchange between the fracture and porous domain within the investigated time frame. Similar to the fluid pressure of the fracture domain the notation is simplified by also using p to express relative changes of the fluid pressure to the initial equilibrium pressure state. Boundary conditions defined on the surface are distinguished in regions Γ_N^α where Neumann boundary conditions are applied in terms of surface traction $\bar{\mathbf{t}}$ defined with respect to the total stresses and flow boundary conditions \bar{w}_f , respectively regions of Dirichlet boundary conditions Γ_D^α constraining the primary variables pore pressure \bar{p} and solid deformation $\bar{\mathbf{u}}_s$

$$\begin{aligned} \mathbf{u}_s &= \bar{\mathbf{u}}_s \quad \text{on} \quad \Gamma_D^s & \text{and} & \quad p = \bar{p} \quad \text{on} \quad \Gamma_D^f, \\ \boldsymbol{\sigma}_T \cdot \mathbf{n} &= \bar{\mathbf{t}} \quad \text{on} \quad \Gamma_N^s & \text{and} & \quad \mathbf{w}_f \cdot \mathbf{n} = \bar{w}_f \quad \text{on} \quad \Gamma_N^f. \end{aligned} \quad (2.45)$$

In the presence of porous media characterized by a low permeability the distinct difference in characteristic diffusion times between flow processes in the fracture and porous domain lead to negligible fluid volume exchange between both domains under consideration of moderate time scales. In these cases eq. (2.44) simplifies to a single phase solid description governed by the momentum balance of the mixture where the total stresses reduce to the solid stress tensor governed by Hooke's law. Consideration of poro-elastic effects by means of effective material parameters are motivated by studies on systems characterized by a low viscosity of the investigated fluid, undrained conditions and low frequency perturbations ($\ll 100\text{Hz}$) of the equilibrium state and are defined by means of Gassmann's low-frequency result [66]

$$\begin{aligned} K_{eff} &= \frac{\phi_0 \left(\frac{1}{K^s} - \frac{1}{K^f} \right) + \frac{1}{K^s} - \frac{1}{K}}{\frac{\phi_0}{K} \left(\frac{1}{K^s} - \frac{1}{K^f} \right) + \frac{1}{K^s} \left(\frac{1}{K^s} - \frac{1}{K} \right)}, \\ \mu_{eff} &= \mu \end{aligned} \quad (2.46)$$

where K_{eff} is the effective bulk and μ_{eff} the effective shear modulus. The numerical treatment is discussed based on the more general case of a biphasic poro-elastic formulation given by eq. (2.44).

2.2.4 Weak form of governing equation

The set of governing equations introduced by eq. (2.44) is numerically evaluated by a Bubnov Galerkin finite element formulation similar to the numerical treatment of the flow processes in deformable fractures discussed earlier. The approximation function spaces introduced with regards to the primary variables, namely pore pressure p and solid deformation \mathbf{u}_s , do not require to be similar, but might vary in their order of approximation. Considering a mixed element formulation for poro-elastic problems in terms of so called Taylor-Hood elements a linear approximation for the pore fluid pressure and quadratic approximation for the solid deformation are introduced to guarantee numerical stability [28]. Note that in this work Taylor-Hood elements have only been used throughout staggered solution schemes since implementation of the monolithic approach did not allow for a technically sound implementation in the presence of the fracture flow domain and the used computational framework. Nevertheless, the choice of linear approximation functions for fluid pressure and solid deformations did not induce any numerical instabilities throughout the conducted studies. In the following the weak form is introduced in its general form by the test functions for the solid deformation $w_{\mathbf{u}_s}$ and pore fluid pressure w_p , respectively the trial functions for the solid deformation $\mathbf{u}_{s,t}$ and the pore fluid pressure p_t . Multiplying the trial functions to the governing equations, inserting the test functions and integrating over the numerical domain results in

$$\int_{V^{Pe}} \operatorname{div} \left(\boldsymbol{\sigma}_t^{E,s} - \alpha p_t \mathbf{I} \right) \cdot w_{\mathbf{u}_s} \, dv = 0, \quad (2.47)$$

$$\int_{V^{Pe}} \left[\frac{1}{M} \frac{\partial p_t}{\partial t} w_p - \frac{k^f}{\gamma_0^f R} \operatorname{div} (\operatorname{grad} p_t) w_p + \alpha \operatorname{div} \frac{\partial \mathbf{u}_{s,t}}{\partial t} w_p \right] \, dv = 0$$

where the approximated effective stress tensor $\boldsymbol{\sigma}_t^{E,s}$ considers the constitutive dependence on the trial functions $\mathbf{u}_{s,t}$. Similar to the derivation of the weak form of the hybrid-dimensional formulation (see eq. (2.29)) the demand on the smoothness of the trial functions is reduced by applying Green's first identity. The implemented weak form of the governing equations for a biphasic poro-elastic medium then reads

$$\int_{V^{Pe}} \left(\boldsymbol{\sigma}_t^{E,s} - \alpha p_t \mathbf{I} \right) : \operatorname{grad} w_{\mathbf{u}_s} \, dv = \int_{\Gamma_N^s} \bar{\mathbf{t}} \cdot w_{\mathbf{u}_s} \, da, \quad (2.48)$$

$$\int_{V^{Pe}} \left[\frac{1}{M} \frac{\partial p_t}{\partial t} w_p - \frac{k^f}{\gamma_0^f R} \operatorname{grad} w_p \cdot \operatorname{grad} p_t + \alpha \operatorname{div} \frac{\partial \mathbf{u}_{s,t}}{\partial t} w_p \right] \, dv = \int_{\Gamma_N^f} \bar{w}_f w_p \, da$$

defining the Neumann boundary conditions of each constituent on the surfaces Γ_N^α . The weak form introduced by eq. (2.48) is considered throughout this work whenever fluid mass exchange between fracture and fluid domain is of importance.

2.3 Fracture surface boundary conditions

The governing equations for flow in deformable fractures introduced by eq. (2.27) and the response of a poro-elastic medium defined by eq. (2.44) consider hydro-mechanical

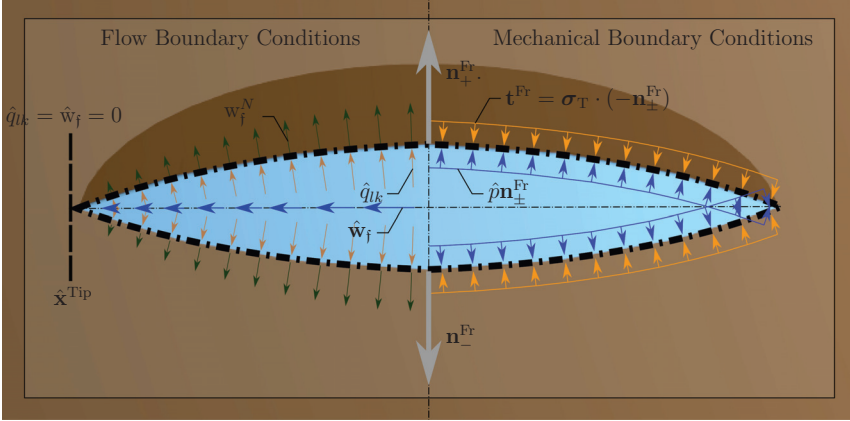


Figure 2.3: Boundary conditions defined along the fracture surface Γ^{Fr} identified by the space dependent fracture normal vectors $\mathbf{n}_{\pm}^{Fr}(\hat{\mathbf{x}})$. Exchange of fluid volume between both domains requires equilibrium of fracture outflow \hat{q}_{lk} and the normal seepage velocity w_f^N defined in the poro-elastic domain. At the fracture tips $\hat{\mathbf{x}}^{Tip}$ no-flow conditions are required to be met. Mechanical equilibrium is enforced regarding the fracture surface traction \mathbf{t}^{Fr} and the acting fluid pressure \hat{p} [176]

effects individually within each domain. Hence, consistent evaluation of the coupled system requires the definition of equilibrium conditions along the fracture surface. Figure 2.3 introduces a visualization of the acting forces, respectively fluxes of both domains. Mechanical equilibrium conditions along the fracture surface are met once the sum of acting fracture fluid pressure $\hat{p} \cdot \mathbf{n}_{\pm}^{Fr}$ and poro-elastic surface traction $\mathbf{t}^{Fr} = \boldsymbol{\sigma}_T \cdot \mathbf{n}_{\pm}^{Fr}$ equates to zero. Flow equilibrium along the fracture surface is reached once the fracture outflow defined by means of the fracture leak-off term \hat{q}_{lk} is balanced with the normal seepage velocity \mathbf{w}_f^N of the biphasic poro-elastic domain and results in zero at the fracture tip. Numerical evaluation of the normal seepage velocity considering a compressible poro-elastic medium requires the use of Green's first identity [198] which is determined by element-wise evaluation using FE discretization

$$\mathbf{w}_f^N = \int_{V^{el}} \left[\frac{1}{M} \frac{\partial p_t}{\partial t} w_p - \frac{k^j}{\gamma_0^{jR}} \text{grad } p_t \cdot \text{grad } w_p + \alpha \text{div} \frac{\partial \mathbf{u}_{s,t}}{\partial t} w_p \right] dv. \quad (2.49)$$

Eq. (2.49) is of relevance when staggered schemes are applied to define the leak-off Neumann boundary conditions of the fracture domain. Here it is of importance to mention that eq. (2.49) is evaluated in a post-processing procedure based on the solution obtained for the primary variables fluid pressure \hat{p}^{sol} and solid deformation \mathbf{u}_s^{sol} of a certain iteration step. The monolithic scheme used in this work does not require special treatment of the outflow conditions since they are intrinsically met by the formulation. Despite the definition of the coupling conditions along the fracture surface the physical characteristic of the coupling is volumetric considering the contribution of the fracture pressure \hat{p}

which explicitly depends on the volumetric coupling term v). The boundary conditions required to be met along the fracture surface to guarantee consistent evaluation of the global equilibrium are summarized below

$$\begin{aligned} \hat{q}_{lk} &= \mathbf{w}_f^N & \text{on } \Gamma^{\text{Fr}} & \quad \text{and} \quad \hat{q}_{lk} = 0 & \text{at } \hat{\mathbf{x}}^{\text{Tip}}, \\ \mathbf{t}^{\text{Fr}} &= -\hat{p}\mathbf{n}_{\pm}^{\text{Fr}} & \text{on } \Gamma^{\text{Fr}}. \end{aligned} \quad (2.50)$$

2.4 Consideration of fracture normal stiffness

The proposed model introduced to govern flow through deformable fractures embedded in a biphasic poro-elastic medium forms the basis to consider the interdependence of fluid pressure and porous deformation. Nevertheless, interaction of both fracture surfaces is not limited to mechanically induced fluid pressure variations within the fracture domain, but might be extended by mechanical interaction in terms of fracture surface contact. In this work the contact mechanism is limited to induce normal fracture stresses only, neglecting the existence of shear stresses and irreversible processes related to fracture shearing. This assumption is valid in the context of a model derived to investigate pumping operations which induce perturbations well below the limit of seismic actions [14, 147]. To relate normal stresses induced by mechanical contact to the deformation state of fractures this work consults the effective fracture aperture δ to define a partly physics based constitutive relation. Thinking of rough fracture surfaces the leading mechanism of normal stress evolution is the large number of Hertzian contact zones requiring highly non-linear relations due to a constantly varying total contact surface [40, 77, 197]. Considering field settings it is known that natural fractures are in a state of so called mated fracture surfaces, characterized by a reversible response of the normal stresses to moderate perturbations of the equilibrium state [14, 147]. In a laboratory setting the state of mated fracture surfaces is achieved by applying cycling loading until hysteresis effects vanish [14]. These findings motivate the derivation of a non-linear elastic model to govern the asymptotic fracture closing characteristic under in-situ conditions. Normal fracture stiffness evolution has been topic of several research contributions [e.g., 12, 75]. In this work the basis of the derived model is motivated by the formulation introduced by [70, 181] defining the contact related normal stresses

$$\sigma_N^{\text{Con}} = E^{\text{Fr}} \frac{1}{\delta_{\text{max}}^c - \delta^c} \delta^c \quad (2.51)$$

by means of the fracture closure δ^c with the initial value $\delta_0^c = 0$, the maximum fracture closure δ_{max}^c and the fracture stiffness E^{Fr} . The formulation introduced by eq. (2.51) has been considered in a slightly modified form throughout studies on the laboratory scale [174] where the fracture stiffness E^{Fr} and maximum fracture closure were fitted to reproduce the contact behaviour obtained from experimental investigations [145]. Nevertheless, considering field studies determination of the microstructure of the fracture surface is not a trivial task and is mostly unknown throughout the inverse analysis of pumping operations. Hence, numerical investigations of field data based on the proposed constitutive relation given by eq. (2.51) requires to explicitly model the fracture depth along with acting gravity forces to reproduce the in-situ conditions regarding an initial effective fracture

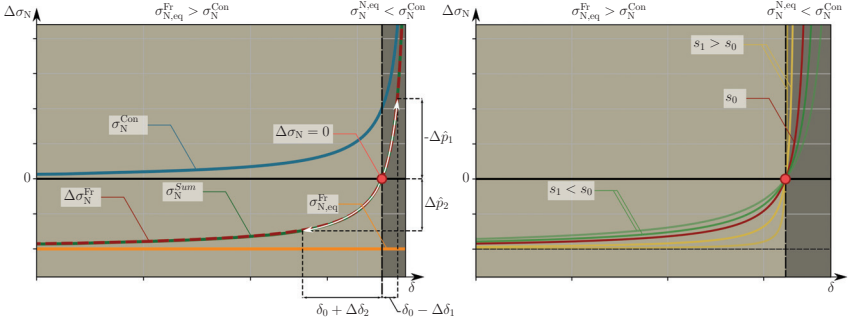


Figure 2.4: **Left:** Relative normal stress changes $\Delta\sigma_N$ as a function of the effective fracture aperture δ evaluated at \hat{p}_0^{eq} . Normal stress changes are expressed relative to the acting normal equilibrium stress state $\Delta\sigma_N = 0$ which is equivalent to the sum σ_N^{sum} of induced contact forces σ_N^{con} and the constant equilibrium normal stress state $\sigma_{N,eq}^{Fr}$ and is recovered by the constitutive in-situ normal stress law σ_N^{Fr} . Effective aperture fluctuations $\delta = \delta_0 + \Delta\delta$ are induced by perturbations of the equilibrium state by means of fluid pressure changes $\Delta\hat{p}$ or vice versa. **Right:** Consideration of the fracture's microstructure in terms of a contact factor s_0 , respectively s_1 controlling the difference between initial hydraulic and mechanical opening [175]

aperture δ_0 which is a delicate task in the context of hydro-mechanical simulations. Identifying the initial effective aperture δ_0 as a parameter characterizing the hydro-mechanical in-situ state of a fracture in terms of transmissivity and acting normal stresses allows a shift of the equilibrium state like proposed in the context of this work [175]. Evaluation of the fracture equilibrium state determines pore pressure, surface traction, normal contact stresses and normal stresses induced by gravitational effects to be the driving forces. Since pore pressure and surface traction are accounted for in the proposed hybrid-dimensional model the constitutive relation is derived by the sum of acting normal contact stresses in terms of eq. (2.51) and a constant acting normal stress related to the orientation and position of the fracture like shown in figure 2.4. The constitutive relation to study fracture stiffness under in-situ conditions is obtained by considering normal stress changes with respect to the unperturbed in-situ stress state $\sigma_{N,eq}^{Fr}$

$$\Delta\sigma_N^{Fr} = \sigma_N^{Fr} - \sigma_{N,eq}^{Fr} = -E_{eq}^{Fr} \frac{\Delta\delta}{\left(\frac{\delta_0}{s_0} + \Delta\delta\right) - \delta_{min}} \quad (2.52)$$

where $\Delta\delta$ is the relative change of the fracture aperture, δ_{min} the minimal mechanical fracture aperture, $s_0 \geq 1$ is a dimensionless parameter introducing a ratio between the initial hydraulic and mechanical fracture aperture and E_{eq}^{Fr} the in-situ normal stiffness parameter. The interested reader is referred to [175] for a detailed derivation and discussion of the proposed in-situ normal stiffness model.

2.5 Volumetric split of fracture deformation and fluid compressibility

The proposed model for flow in deformable fractures accounts for compressibility effects of the fluid and changes of the fracture volume. This does not imply that both effects equally contribute, but that their contribution highly depends on the acting normal stresses, the geometrical stiffness of the fracture and the characteristics of the present fluid. Better understanding of the leading mechanisms is obtained once both phenomena are separated to study the influence of fracture deformation, respectively fluid compressibility on the flow process in deformable fractures. Introducing the difference of injected fluid volume and volume related to leak-off flow, the change of total volume within the fracture domain is defined by

$$\Delta V^{\text{Fr}} = \Delta V^{\text{Inj}} - \Delta V^{\text{Leak}} \quad (2.53)$$

where the difference of injected fluid volume ΔV^{Inj} and leak-off volume ΔV^{Leak} are expressed with respect to a certain time step size Δt . The total change of volume introduced by eq. (2.53) must be compensated by a combination of fracture ΔV^δ and fluid volume ΔV^{β^f} changes within the fracture domain

$$\Delta V^{\text{Fr}} = \Delta V^\delta + \Delta V^{\beta^f}. \quad (2.54)$$

Considering a FE discretization the introduced volumetric changes of injection, leak-off, fracture and fluid can be calculated in a post-processing step. The leak-off volume ΔV^{Leak} is obtained by integration over the fracture surface by means of the normal seepage velocity \mathbf{w}_f^N determined by eq. (2.49). In case of Neumann boundary conditions, prescribing the flow, calculation of the injected fluid volume is straight forward by considering the time step size Δt . In contrast, once Dirichlet boundary conditions are introduced by prescribing the fluid pressure \hat{p} the corresponding injection flow is required to be determined similarly to the procedure conducted when deriving the leak-off flow (see eq. (2.49)) into the poro-elastic domain. Introducing the isothermal compressibility condition for a barotropic fluid, volume changes of fracture and fluid within the fracture domain are calculated by means of

$$\Delta V^\delta = \int_{\Gamma^{\text{Fr}}} \Delta \delta^{\text{sol}} \, da \quad \text{and} \quad \Delta V^{\beta^f} = \int_{\Gamma^{\text{Fr}}} (\delta_0 + \Delta \delta^{\text{sol}}) \beta^f \Delta \hat{p}^{\text{sol}} \, da \quad (2.55)$$

where the integrals might be solved by introducing the same finite element approximations used to determine the solution of the fracture deformation $\Delta \delta^{\text{sol}}$ and fluid pressure $\Delta \hat{p}^{\text{sol}}$. Solutions can be crosschecked by inserting the calculated terms into eq. (2.54). The split of volumetric responses in terms of fracture deformation and fluid volume defined by eq. (2.54) has been used in this work to identify the driving mechanisms throughout hydro-mechanical testing of fractures on the field and laboratory scale [173–175].

Chapter 3:

Numerical coupling schemes

Implementation of the governing equations introduced in terms of the biphasic poro-elastic (2.44) and hybrid-dimensional flow model (2.27) might be distinguished regarding the chosen coupling scheme. Coupling procedures are distinguished in terms of the strategy used to reach global equilibrium. In this work staggered, respectively partitioned schemes and a monolithic approach are considered. Staggered or partitioned schemes treat both domains individually by conducting separate solvers for each problem and perform communication via boundary conditions and by introducing certain constraints to guarantee numerical stability throughout the global equilibrium iterations. In this work the wording of staggered and partitioned coupling are used interchangeably. In contrast monolithic strategies build a single global assembly matrix which is then solved to obtain solutions for both domains simultaneously. The implemented strategies are discussed in the following.

3.1 Monolithic coupling scheme

Monolithic coupling implies the assembly of a global matrix consisting of the discretized contributions of both domains including their coupling. In this work monolithic coupling is realized in terms of zero-thickness elements [177, 179–181]. The weak form obtained for the interface elements are briefly introduced in the following. For a detailed derivativation the interested reader is referred to [177].

3.1.1 Zero-thickness element

Monolithic coupling of fracture and poro-elastic domain requires a discussion of the balance equations introduced to govern hydro-mechanical flow processes within the fracture domain. Considering the fracture aperture to be a design parameter constructed by the normal deformation of both fracture surfaces

$$\delta(\mathbf{x}, t) = \mathbf{u}_s^+ \cdot \mathbf{n}_+^{\text{Fr}} + \mathbf{u}_s^- \cdot \mathbf{n}_-^{\text{Fr}} \quad (3.1)$$

where \mathbf{u}_s^\pm are the deformations and $\mathbf{n}_\pm^{\text{Fr}}$ the normal vectors defined on facing fracture surfaces. Identifying the primary variables of both domains in terms of solid deformation of the poro-elastic medium \mathbf{u}_s and fluid pressure p/\hat{p} computational efficiency is increased by sharing such between the fracture and poro-elastic domain. This is achieved by averaging the balance equations regarding mass and momentum [124]. Throughout the averaging procedure tangential and longitudinal fracture flow is distinguished, meaning that pressure discontinuities along the fracture surfaces are accounted for in the formulation [177]. Variables and mathematical operations related to longitudinal flow is highlighted by \square' and

tangential flow by \square^t . Throughout the averaging procedure the stability limit considering a weighting parameter of $\xi = 1/2$ has been used which might induce numerical instabilities, but has a high solution quality for most cases. For a detailed derivation including the averaging of the balance equations the interested reader is referred to [124, 177]. Nevertheless, by adapting the tangential permeability parameter to introduce continuous flow across the fracture surfaces throughout the investigated boundary value problems no stability issues arose. The averaged pressure in longitudinal, respectively the discrete gradient of the tangential pressure difference result in

$$\hat{P}^l = \frac{\hat{p}^+ + \hat{p}^-}{2} \quad \text{and} \quad \hat{P}^t = \frac{\hat{p}^- - \hat{p}^+}{\delta} \quad (3.2)$$

where \hat{p}^\pm defines the pressure on the positive and negative fracture surface at aligning positions. Considering FE approximations in terms of zero-thickness elements the averaging introduced by eq. (3.2) allows to perform integration on lower dimensional auxiliary elements without introducing additional DOF. The averaging is then performed on values of aligning element nodes and the weak form might be introduced with regards to the auxiliary, lower-dimensional test functions $w_{a,\hat{p}}$ and the auxiliary, lower-dimensional trial functions of the longitudinal pressure $\hat{P}_{a,t}^l$. The weak form then reads

$$\int_{\Gamma_{\pm}^{Fr}} \left[\delta w_{a,\hat{p}} \frac{\partial \hat{P}_{a,t}^l}{\partial t} + \frac{\delta^3}{12 \eta^{iR} \beta^f} \text{grad } w_{a,\hat{p}} \cdot \text{grad } \hat{P}_{a,t}^l + w_{a,\hat{p}} \frac{1}{\beta^f} \frac{\partial \delta}{\partial t} \pm w_{a,\hat{p}} \frac{k_{Fr,t}^s}{\delta \eta^{iR} \beta^f} \hat{P}_{a,t}^l \right] da \quad (3.3)$$

$$+ \int_{LFr} \frac{\delta}{\beta^f} w_{a,\hat{p}} \hat{\mathbf{w}}_f \cdot \mathbf{n}^l dl = 0.$$

where tangential flow within the fracture domain is evaluated regarding the discrete derivative $1/\delta$ and introduction of an intrinsic tangential permeability $k_{Fr,t}^s$. The proposed monolithic solution scheme considers leak-off into the surrounding poro-elastic matrix implicitly, since the primary variables pore-pressure and deformation are shared between both domains. Nevertheless, assembly of both computational regions in a single matrix requires dimensional compatibility of eqs. (3.3) and (2.48) which is achieved by appropriately adjusting their prefactors. The distinct difference in discretized contributions of the fracture and poro-elastic domain to the global assembly matrix does not allow to increase the computational performance by using standard linear iterative solvers in parallel and would require a physics based pre-conditioning to guarantee numerical stability like discussed in the literature for flow in non-deformable fractures embedded in a porous medium [e.g., 169]. In this work, to avoid specific pre-conditioning, a sequential assembly method is conducted and the resulting set of equations is solved in parallel by the direct sparse matrix solver PARDISO [170] embedded in a modified DUNE-pdelab framework [15]. In this work the introduced weak form given by eq. (3.2) is consulted for monolithic investigations of flow processes in deformable fractures.

3.2 Staggered coupling schemes

In contrast to the proposed monolithic coupling scheme partitioned coupling strategies solve the introduced governing equations of both domains using individual solvers. Equilibrium conditions are then enforced by coupling boundary conditions in an iterative

process, required to reach convergence for a given time step by fulfilling a defined solution accuracy, before the simulation proceeds in time. Considering the case of individual solver implementations for the hybrid-dimensional fracture flow and homogeneous bi-phasic poro-elastic medium formulation, solutions for the discretized set of equations are determined by linear iterative solvers in parallel to increase the overall computational efficiency. Besides the use of iterative solvers computational performance might be additionally increased by non-conformal meshing [177]. Nevertheless, coupling of fracture flow and poro-elastic domain results in a numerically stiff [1] system and naive coupling approaches such as introducing the unchanged individual solutions as the other problem's boundary conditions throughout the equilibrium iterations do not guarantee convergence and might diverge for most relevant combinations of material parameters. Two different staggered coupling procedures have been considered throughout this work to gain numerical stability, namely a fixed-stress [72, 73, 177] and a quasi-Newton implementation [176]. For the considered partitioned approaches both, the hybrid-dimensional flow and poro-elastic solver, have been implemented using the FEniCS computing platform [5]. The numerical, respectively technical realization of the quasi-Newton based scheme is built around the coupling library preCICE [32]. In the following both staggered implementations are briefly introduced. For a detailed discussion the interested reader is referred to [176, 177].

3.2.1 Fixed-Stress coupling

Considering intact porous media different strategies to reach global equilibrium based on an implicit coupling scheme have been proposed in the literature. Decoupling of the mechanical and flow processes might be achieved by either fixed-stress/strain strategies, where the flow problem is solved before the solution is evaluated on the mechanical problem or the drained/undrained schemes where the sequence of solutions is reversed [104–106]. In the presence of fractured porous media the fixed-stress strategy has consistently been extended to account for the characteristics of both domains [72, 73] and is introduced as the first of two staggered coupling strategies proposed in this work to guarantee numerical stability throughout equilibrium iterations. Physics based pre-conditioning of the governing equations results from a fixed-stress assumption, meaning that the stress rate throughout calculations in the flow domain is enforced to be constant. Evaluation of the stress restriction results in the following strong form of the governing equations in its local form

$$\frac{\partial \hat{p}^{k+1}}{\partial t} - \frac{\gamma_c}{\gamma_c + \beta^f} \frac{\partial \hat{p}^k}{\partial t} - \frac{\delta^2 \beta^f}{12 \eta^{fR} (\gamma_c + \beta^f)} \operatorname{div} \operatorname{grad} \hat{p}^{k+1} + \frac{1}{\delta (\gamma_c + \beta^f)} \frac{\partial \delta}{\partial t} = \frac{\hat{q}_{tk}}{\delta (\gamma_c + \beta^f)} \quad (3.4)$$

where $\gamma_c = M \beta^f \alpha^2 / (\lambda + M \beta^f \lambda \phi)$ is an estimate to achieve convergence, λ the first Lamé parameter, \hat{p}^{k+1} the solution of the current iteration step and \hat{p}^k the solution of the previous iteration step. The transients of \hat{p}^{k+1} and \hat{p}^k are evaluated regarding the converged solution of the previous time step. Once the solution converges $\hat{p}^{k+1} \approx \hat{p}^k$ the additionally introduced transient stabilization term including \hat{p}^k vanishes, which can be seen once eq. (3.4) is multiplied by $\gamma_c + \delta \beta^f$. The equilibrium iteration using the strong form given by eq. (3.4) might mathematically be classified as a preconditioned Richardson iteration

[38] resulting from the physics based assumption of fixed-stress rates throughout the flow calculations. Clarification concerning the numerical coupling of both domains requires a brief discussion of the applied boundary conditions. Considering the hybrid-dimensional flow domain, Neumann conditions are applied in terms of the transient coupling of the fracture volume $\partial\delta/\partial t$ and the fluid exchange between both domains governed by leak-off \hat{q}_{lk} . Both can be constructed using the poro-elastic solution by applying eq. (3.1), respectively eq. (2.49). The fluid pressure solution \hat{p} of the hybrid-dimensional flow model is considered throughout the poro-elastic calculations by means of a Dirichlet boundary condition prescribing the fluid pressure and a Neumann boundary condition representing the pressure induced surface traction; both applied along the fracture surfaces. For a detailed study of the implemented fixed-stress scheme derived to investigate hydro-mechanical phenomena throughout equilibrium perturbations of the deformable fractured porous media, the interested reader is referred to [177]. For the sake of completeness the implemented weak form of eq. (3.4) is derived similar to the procedure discussed in section 2.1.4 and reads

$$\int_{\Gamma^{Fr}} \left[\delta w_{\hat{p}} \frac{\partial \hat{p}_t^{k+1}}{\partial t} - \frac{\delta \gamma_c}{\gamma_c + \beta^f} w_{\hat{p}} \frac{\partial \hat{p}_t^k}{\partial t} + \frac{\delta^3}{12 \eta^{IR} (\gamma_c + \beta^f)} \text{grad } w_{\hat{p}} \cdot \text{grad } \hat{p}_t + w_{\hat{p}} \frac{1}{\gamma_c + \beta^f} \frac{\partial \delta}{\partial t} \right] da + \int_{L^{Fr}} \frac{\delta}{\gamma_c + \beta^f} w_{\hat{p}} \hat{\mathbf{w}}_f \cdot \mathbf{n}^l dl = \int_{\Gamma^{Fr}} w_{\hat{p}} \frac{\hat{q}_{lk}}{\gamma_c + \beta^f} da. \quad (3.5)$$

3.2.2 Quasi-Newton coupling

Implementation of a quasi-Newton scheme to implicitly couple fracture and poro-elastic domain is a general approach to introducing a partitioned solution strategy. The quasi-Newton scheme approximates the required coupling entries of the Jacobian based on the communicated residua of the individual problems to increase the numerical stability of the global problem. In the scope of this work Quasi-Newton schemes have not explicitly been implemented, but the coupling library preCICE has been consulted [32]. Besides less advanced coupling strategies such as the dynamic Aitken scheme [114], preCICE offers a number of quasi-Newton implementations being the frequently used interface quasi-Newton scheme IQN-ILS which calculates its Jacobian based on a least square model [45, 46] or the more sophisticated multi-vector update based quasi-Newton variant IQN-IMVJ [171]. Quasi-Newton coupling is frequently used in the field of multiphysics problems such as fluid solid interaction (FSI). Nevertheless, in the known literature no contributions could be found which is concerned with flow processes in deformable fractures introducing a strict split of fracture and poro-elastic domain. Besides numerical coupling schemes, preCICE offers an interface for parallelized communications of defined properties between the implemented solvers. In this work, considering a biphasic poro-elastic in its weak form given by eq. (2.48) and the implementation of eq. (2.31) in a hybrid-dimensional flow solver, communicated properties are the fluid pressure solution \hat{p} of the fracture domain, the fracture aperture δ constructed from the deformations obtained by solving the poro-elastic problem and the normal relative velocity \mathbf{w}_f^N obtained by evaluation of eq. (2.49). Determining the Jacobian based on the fracture aperture δ rather than the individual deformation states of both fracture surfaces is motivated by

the outcome of a convergence study that indicates increased performance and numerical stability of the aperture constructed Jacobian over the one based on the individual deformations of the fracture surfaces [176]. The improved convergence behaviour might be related to the implicit consideration of additional coupling terms throughout the Jacobian calculations, numerically connecting both fracture surfaces under consideration of relative fracture aperture changes like proposed in eq. (3.1). The applied coupling boundary conditions introduced for the fixed-stress strategy remain unchanged for the quasi-Newton scheme. The quasi-Newton based implementation is capable of considering complex fracture networks in three dimensions, flow processes through the poro-elastic medium and fracture domain, respectively their hydro-mechanical interaction and allows for parallel computing [176].

Chapter 4:

Publications

This chapter consists of the journal publications written in the course of this work and is summarized in the table below. The filled in status is with regards to the present date (April 2021).

Table 4.1: List of journal publications as a first author.

Title	Authors	Journal	status
Numerical aspects of hydro-mechanical coupling of fluid-filled fractures using hybrid-dimensional element formulations and non-conformal meshes [177]	P. Schmidt, H. Steeb	GEM ¹	published
Investigations into the opening of fractures during hydraulic testing using a hybrid-dimensional flow formulation [175]	P. Schmidt, H. Steeb, J. Renner	EES ²	published
Importance of fracture deformation throughout hydraulic testing under in-situ conditions [173]	P. Schmidt, N. Dutler, H. Steeb	GJI ³	published
Simulation of flow in deformable fractures using a quasi-Newton based partitioned coupling approach [176]	P. Schmidt, A. Jaust, H. Steeb, M. Schulte	CG ⁴	published
Assessing the role of non-linear contact mechanics for flow in fractures [174]	P. Schmidt, H. Steeb, J. Renner	Geophys. Res. Lett. ⁵	submitted

¹ International Journal on Geomathematics

² Environmental Earth Sciences

³ Geophysical Journal International

⁴ Computational Geosciences

⁵ Geophysical Research Letters

Table 4.2: List of journal publications as a contributing author.

Title	Authors	Journal	status
GeomInt - Geomechanical integrity of host and barrier rocks - experiment, modeling and analysis of discontinuities [110]	O. Kolditz et al.	EES ¹	published

¹ Environmental Earth Sciences

Table 4.3: List of contributions to book chapters.

Title	Authors	Publisher	status
GeomInt-Mechanical Integrity of Host Rocks	O. Kolditz et al.	TTS ¹	published

¹ Terrestrial Environmental Sciences - Springer

Numerical aspects of hydro-mechanical coupling of fluid-filled fractures using hybrid-dimensional element formulations and non-conformal meshes

Patrick Schmidt, Holger Steeb, GEM - International Journal on Geomathematics (10), February 2019, DOI: 10.1007/s13137-019-0127-5

Abstract In the field of porous and fractured media, subsurface flow provides insight into the characteristics of fluid storage and properties connected to underground matter and heat transport. Subsurface flow is precisely described by many diffusion based models in the literature. However, diffusion-based models lack to reproduce important hydro-mechanical coupling phenomena like inverse water-level fluctuations (Noordbergum effect). In theory, contemporary modeling approaches, such as Direct Numerical Simulations (DNS) of surface-coupled fluid-solid (fracture) interactions or coarse-grained continuum approaches like Biot's theory, are capable of capturing such phenomena. Nevertheless, during modeling processes of fractures with high aspect ratios, DNS methods with the explicit discretization of the fluid domain fail, and coarse-grained continuum approaches require a non-linear formulation for the fracture deformation since large deformation can be reached easily within fractures. Hence a hybrid-dimensional approach uses a parabolic velocity profile to avoid an explicit discretization of the fluid domain within the fracture. For fracture flow, the primary variable is the pressure field only, and the fracture domain is reduced by one dimension. The interaction between the fracture and the surrounding matrix domain, respectively, is realized by modified balance equations. The coupled system is numerically stiff when fluids are described with a low compressibility modulus. Two algorithms are proposed within this work, namely the weak coupling scheme, which uses an implicit staggered-iterative algorithm to find the residual state and the strong coupling scheme which directly couples both domains by implementing interface elements. In the course of this work, a consistent implementation scheme for the coupling of hybrid-dimensional elements with a surrounding bulk matrix is proposed and validated and tested throughout different numerical experiments.

1 Introduction

Underground fluid flow in fractured and porous media exhibits a variety of hydro-mechanical phenomena, which have been intriguing the research community for several decades [54, 135]. The long-established research interest in subsurface flow, such as studies of reservoir storage capacities, is regarding both theoretical/numerical and experimental investigations. Various hydro-mechanical coupling phenomena, like inverse pumping or Noordbergum effect [107, 161], are observed in fracture networks, and apparently, affect the reservoir behavior during fluid pressure or deformation fluctuations. For fractures with a high aspect-ratio (length l vs. aperture δ , i.e. $l/\delta > 10^4$) filled by viscous fluids with low compressibility these effects become evident.

A considerable number of theoretical and numerical studies of subsurface flow in frac-

tured media can be found in the literature. The first solution strategy to mention is the so-called diffusion-based approach. This approach uses the poroelastic framework with slight modifications to the diffusion formulation within the fracture and assumes that the mechanical response of the surrounding rock (bulk) material is decoupled from the governing equation of fluid flow. For specific combinations of material parameters or a constant mean stress [158], this decoupling assumption is valid and has successfully been applied in several investigations, to study pressure diffusion effects along fractures [138, 140]. Nevertheless, phenomena due to a strong hydro-mechanical coupling, such as the earlier mentioned Noordbergum effect, cannot be captured by even extended diffusion formulations.

Further strategies to describe hydro-mechanical phenomena are based on partly-analytical solutions. In a first approach, Sneddon [187] introduced a plane strain crack solution to find deformation states for various fluid pressure conditions. Based on Sneddon's formulation further models evolved such as the PK-model by Perkins and Kern [142], the PKN model by Nordgren [134] which takes fluid loss effects into account or the penny-shaped KGD model independently developed by Geertsma and de Klerk [68] and Khristianovic and Zheltov [222]. All models provide further insights on phenomena related to hydro-mechanical coupling. However, the pressure state described in all models is not associated with the deformation response of the surrounding bulk matrix, and furthermore, only relatively simple geometries can be analyzed. Partly-analytical formulations serve for a better understanding of the physics but are not suitable for fully coupled formulations and/or complex fracture geometries.

Most promising with regards to hydro-mechanical investigations of complex fracture networks are fully coupled numerical strategies. In Direct Numerical Simulation (DNS), the fracture domain is explicitly discretized, e.g., with finite elements, and the inherent fluid is modeled by the Navier-Stokes equations, coupled to the deformation of the surrounding rock. Thus hydro-mechanical phenomena can be reproduced using different coupling algorithms, such as staggered or fully coupled schemes. However, in the case of creeping flow conditions, i.e., Poiseuille-type flows a specific discretization over the fracture height is required to reproduce the parabolic velocity field. Having in mind fractures with high aspect ratios, the total number of elements increases drastically, and DNS are finally applicable to fracture ratios of $l/\delta < 10^4$ only due to technical limitations.

For fractures with higher aspect ratios than $l/\delta > 10^4$ and low Reynolds numbers, viscous shear stresses in the bulk fluid can be neglected and creeping flow conditions can be assumed. Coarse-grained continuum approaches like Biot's quasi-static poroelastic theory [20], take these assumptions into account and couple fluid pressure to solid deformation in a smeared continuum-based formulation at the local material point. The set of governing equations are based on volume-averaged quantities [41] and treats materials homogeneous if inhomogeneities occur at the length scale of the averaged pore size. The classical poroelastic formulation relates the specific storage capacity as an inherent material property to each material point which is not valid anymore for structural properties with finite extensions like fractures. By exchanging the solid with the fracture surface deformation, this limitation can be circumvented. Still, an explicit discretization of the fracture domain is required. Since poroelastic formulations are designed explicitly for hydro-mechanical problems, the number of elements needed decreases compared to DNS strategies. Never-

theless, the explicit discretization of the fracture domain constrains the method to aspect ratios of $l/w < 10^5$.

Concerning numerical efficiency, subsurface flow for conduits with aspect ratios of $l/\delta > 10^5$ demands a different numerical treatment, other than an explicit discretization of the fracture domain. The efficiency of the procedure can significantly be increased by using hybrid-dimensional formulations [72, 73, 104, 105, 206, 208]. Hybrid-dimensional approaches allow for a lower-dimensional discretization of fracture flow which reduces the discretization space of the fracture domain's dimension by assuming a priori parabolic velocity profiles of Poiseuille-type. Besides a storage analysis of fracture networks, comparable strategies have been used in the field of hydro-mechanical coupling [86, 180, 181, 183, 195]. Hybrid-dimensional approaches have been used in the past often for purely hydraulic problems related to fracture flow. Authors focused on non-conformal techniques [200], the formulation of discontinuous pressure at fracture interfaces [27, 124] and the improvement of performance and stability [168].

Another important limiting factor for numerical treatments of hydro-mechanical coupling is the stiffness of the overall coupled system. Contributions of Adachi [1] and Yew [218] study the hydro-mechanical coupling by investigating high aspect-ratio fractures using a staggered coupling scheme. Nevertheless, it has been stated that the introduced scheme should preferably be used for fluids with low or moderate compressibility parameters otherwise the scheme requires high numbers of iterations or non-practical small time steps. In unfractured porous media different staggered schemes have been introduced to solve such stiff systems in a stable fashion. Kim et al. [104, 105] proposed the drained/undrained (modifications throughout mechanical calculations) and the fixed-strain/fixed-stress (modifications throughout flow calculations) in their work. The fixed-stress scheme achieves numerical stability by varying the strain rate throughout the flow problem to fix the stress state, whereas stability is reached using the drained scheme by enforcing a constant fluid mass per element in each iteration step [38]. The fixed-stress scheme has been extended by Girault et al. [72, 73] for coupling flow in deformable fractures embedded in a biphasic porous medium.

Deformation dependent permeability changes within fractures influence the pressure prediction, particularly when high aspect ratios are investigated. In the literature mentioned above, a constant aperture is assumed for the calculations of the fracture permeability [72, 73]. Fixed fracture permeabilities might lead to incorrect predictions of the pressure state. This work will take permeability changes due to local deformations of the fracture into account and show the importance based on a three-dimensional boundary value problem. Furthermore, staggered algorithms are used in the literature to solve the coupled set of governing equations; hence iterations are needed even for linear problem formulations. Mathematically it has been shown, that a fully coupled, monolithically solved scheme is unconditionally stable [72], but has not been investigated concerning efficiency yet. Since no iterations are needed the performance of a monolithic scheme is potentially higher than a staggered scheme. Nevertheless, by using non-conformal discretizations for porous and fracture domain, the performance of a staggered algorithm can be increased. This work will investigate the performance improvement by reducing the total number of degrees of freedom (DoF) taking the loss of accuracy of the solution into account. Based on the number of iterations needed in combination with the reduced number of DoF the

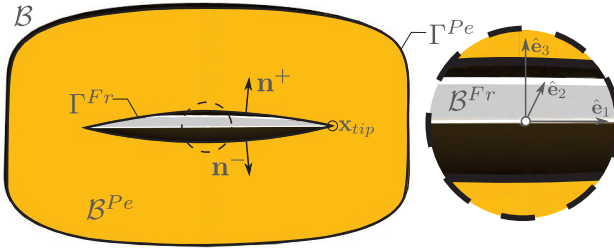


Figure 1: Subsurface domain \mathcal{B} including poroelastic subdomain \mathcal{B}^{Pe} , the fracture subdomain \mathcal{B}^{Fr} and boundaries.

efficiency of the staggered will be compared to a fully coupled monolithic scheme.

2 Model Formulation

This section introduces the continuum based mathematical continuum-based model for underground flow in fractured porous media. The bounded subsurface domain will be denoted as \mathcal{B} and includes the poroelastic subdomain \mathcal{B}^{Pe} with its outer boundary surface Γ^{Pe} and the embedded deformable fracture subdomain \mathcal{B}^{Fr} . The domain of the fracture is defined through its exterior outer normal vectors \mathbf{n}^\pm , cf. Fig. 1.

2.1 Partial Differential Equations in the poroelastic subdomain \mathcal{B}^{Pe}

The subdomain \mathcal{B}^{Pe} is described as a linear biphasic poroelastic medium, see [20] or e.g. [211]. The leading set of Partial Differential Equations (PDEs) of poroelasticity consists of the balance of momentum of the mixture and the balance of momentum of the fluid combined with the linearized form of the balance of mass. The system of equations is closed by constitutive assumptions for the extra stresses of the solid phase denoted as $\boldsymbol{\sigma}_E^s$, the momentum interaction between the viscous pore fluid and the solid matrix $\hat{\mathbf{p}}^s$, and an equation of state for the compressible pore fluid.

2.1.1 Balance of momentum of the mixture

The local form of the balance of linear momentum for a biphasic mixture with the solid constituent φ^s and the pore fluid φ^f reads

$$-\operatorname{div}(\boldsymbol{\sigma}) = \rho \mathbf{b} \quad (4.1)$$

in its (quasi-static) local form if inertia forces are neglected. The total stresses are denoted as $\boldsymbol{\sigma}$ and the body forces as $\rho \mathbf{b}$. The density of the mixture reads $\rho = \rho^s + \rho^f$. The partial densities are introduced as $\rho^s = dm^s/dv$ and $\rho^f = dm^f/dv$, respectively. Here, the mass elements of the constituents are denoted as dm^s and dm^f . The volume element of the mixture is denoted as dv . Effective densities are given by $\rho^{sR} = dm^s/dv^s$ and

$\rho^{fR} = dm^f/dv^f$. Partial and effective densities are related through the porosity $\phi = dv^f/dv$, i.e. $\rho^s = (1 - \phi)\rho^{sR}$ and $\rho^f = \phi\rho^{fR}$. In poroelasticity, the total stresses split into the effective stress and the pore pressure. Following Biot [20], we assume compressible constituents (i.e. a compressible skeleton with dry bulk modulus K , compressible grains which are composing the skeleton with bulk modulus K^s , and a compressible pore fluid with bulk modulus K^f). Thus, the effective stress principle composes the total stresses additively into the effective stresses and the pore pressure p

$$\boldsymbol{\sigma} = \boldsymbol{\sigma}_E^s - \alpha p \mathbf{I}. \quad (4.2)$$

The Biot parameter is related to the bulk moduli by $\alpha = 1 - K/K^s$. Thus, in case of $K^s \gg K$, the effective stress principle reduces to Terzaghi's effective stress principle with $\alpha = 1$. The effective stresses of the solid constituents are given by

$$\boldsymbol{\sigma}_E^s = 3K \text{vol}(\boldsymbol{\varepsilon}_s) + 2G \text{dev}(\boldsymbol{\varepsilon}_s) + (1 - \alpha)p \mathbf{I}. \quad (4.3)$$

Here, we split the solid strain tensor $\boldsymbol{\varepsilon}_s = 1/2(\text{grad } \mathbf{u}_s + \text{grad}^T \mathbf{u}_s)$ into its volumetric and deviatoric part. Further, the dry shear modulus of the skeleton is given by G .

2.1.2 Balance of mass and balance of momentum of the fluid

Two constitutive assumptions are inherent in the second PDE of poroelasticity. A linear equation of state for the barotropic pore fluid is introduced

$$p = K^f \left[\frac{\rho^{fR}}{\rho_0^{fR}} - 1 \right]. \quad (4.4)$$

The effective density in the initial configuration at time $t = t_0$ is introduced as $\rho^{fR}(t_0) =: \rho_0^{fR}$.

The viscous momentum interactions between the solid and fluid constituent $\hat{\mathbf{p}}^f = -\hat{\mathbf{p}}^s$, or drag forces, are modeled as

$$\hat{\mathbf{p}}^f = p \text{grad} \phi - \frac{\phi_0^2 \gamma_0^{fR}}{k^f} \mathbf{w}_f. \quad (4.5)$$

The first (equilibrium) term on the right hand side of Eq. 4.5 is a nonlinear equilibrium term which is vanishing in linear poroelasticity. The second non-equilibrium term describes the viscous momentum exchange and contains the initial porosity $\phi(t_0) =: \phi_0$, the effective weight of the fluid γ_0^{fR} at $t = t_0$ and the Darcy permeability k^f sometimes also denoted as hydraulic conductivity. Thus, the non-equilibrium momentum exchange is proportional to the seepage velocity $\mathbf{w}_f = \dot{\mathbf{u}}_f - \dot{\mathbf{u}}_s$. The solid and fluid displacements are given by \mathbf{u}_s and \mathbf{u}_f . The hydraulic conductivity k^f [m/s] can be related to the intrinsic permeability k^s [m²] by $k^f = \rho^{fR} g k^s / \eta^{fR}$. Here, η^{fR} [Pa s] is the effective dynamic viscosity of the pore fluid and g is the gravitational constant. The constitutive equations (4.4) and (4.5) can be inserted into the balance of mass of the fluid and the balance of momentum of the fluid. The derivation of the resulting equations is straightforward but needs a proper

linearization. We would therefore refer to the literature (e.g. the review [158]) and present the resulting pressure diffusion equation with the coupling term on the right hand side

$$\frac{\dot{p}}{M} - \frac{k^f}{\gamma_0^{fR}} \operatorname{div} \operatorname{grad} p = -\alpha \operatorname{div} \dot{\mathbf{u}}_s \quad (4.6)$$

Here, we have introduced the (local) storativity or inverse storage capacity $1/M = \phi_0/K^f + (\alpha - \phi_0)/K^s$, cf. [211]. Furthermore, it should be noted that in linear poroelasticity, the “dot” derivative is identical to the partial time derivative.

2.1.3 Resulting set of PDEs

The resulting set of PDEs for the poroelastic domain is then summarized $\forall \mathbf{x} \in \mathcal{B}^{Pe}$ as equations (4.1) and (4.6)

$$\begin{aligned} -\operatorname{div}(\boldsymbol{\sigma}_E^s - \alpha p \mathbf{I}) &= \rho \mathbf{b}, \\ \dot{p} - \frac{k^f M}{\gamma_0^{fR}} \operatorname{div} \operatorname{grad} p &= -\alpha M \operatorname{div} \dot{\mathbf{u}}_s, \end{aligned} \quad (4.7)$$

with Dirichlet boundary conditions for the solid displacement $\bar{\mathbf{u}}_s$ and the pore pressure \bar{p} . Neumann boundary conditions are described for the fluxes of the total stresses $\bar{\mathbf{t}}$ and the pore fluid \bar{w}_f

$$\begin{aligned} \mathbf{u}_s &= \bar{\mathbf{u}}_s & \text{on } \Gamma_D^s & & \text{and} & & p &= \bar{p} & \text{on } \Gamma_D^f, & & (4.8) \\ \boldsymbol{\sigma} \cdot \mathbf{n} &= \bar{\mathbf{t}} & \text{on } \Gamma_N^s & & \text{and} & & \mathbf{w}_f \cdot \mathbf{n} &= \bar{w}_f & \text{on } \Gamma_N^f. & & (4.9) \end{aligned}$$

The set of PDEs is formulated in a weak format as the basis for subsequent finite element investigations. Primary variables are then solid displacements and pore pressure. Note that we multiply the pressure diffusion equation with the storativity M . This guarantees consistency in dimensions with the governing equations of the fracture flow model (introduced in the following section) and holds for a monolithic assembly covering both domains.

2.2 Equations in \mathcal{B}^{Fr} - Hybrid-Dimensional Fracture Flow Model

The hybrid-dimensional approach recently introduced by Vinci et al. [206] has specifically been designed to investigate high aspect ratio fractures. In order to avoid an explicit discretization of the fracture domain \mathcal{B}^{Fr} , equilibrium conditions with respect to a deformable fracture are imposed on the fluid phase to derive the governing equations of fluid flow. The model for a biphasic porous medium introduced in section 2.1 provides the local aperture from which the local fracture permeability is calculated; hence fluid flow and solid deformation are coupled by means of the fracture aperture δ . Later in this work numerical coupling schemes for solving the governing equations are introduced.

2.2.1 Balance of Momentum of the Fluid - Fracture Flow

The hybrid-dimensional approach is based on the hydraulic description for flow of compressible and viscous fluids ($Re \ll 1$) with compressibility $\beta^f = 1/K^f$, where K^f denotes the fluid's bulk modulus and η^{fR} is the fluid's effective dynamic viscosity. Fluid flow is investigated for high aspect, hydraulic transmissive fracture domains possessing low contact areas; hence the pressure-driven Poiseuille-type flow between two plates is a valid assumption. Due to its geometrical nature the flow process is predominant within the plane defined by the normal vector \mathbf{n}^+ of the fracture surface. For a planar fracture geometry with basis vector $\hat{\mathbf{e}}_1$ and $\hat{\mathbf{e}}_2$ and normal $\hat{\mathbf{e}}_3 = \mathbf{n}^+$ (fig. 1), the parabolic velocity profile results in a relative fluid velocity

$$\hat{\mathbf{w}}_f = -\frac{\delta^2(\mathbf{x}, t)}{12\eta^{fR}} \text{grad } \hat{p} = -\frac{k_{Fr}^s(\mathbf{x}, t)}{\eta^{fR}} \text{grad } \hat{p}, \quad (4.10)$$

where the pressure of the fluid within the fracture is \hat{p} in order to avoid confusion with the pore pressure p that has been introduced in course of the poroelastic formulation. Dependent on fracture surface roughness or in case of mechanically-closed fractures the proportionality factor $1/12$ might be adapted [159]. Since the relative velocity $\hat{\mathbf{w}}_f$ is space-resolved for coordinate \mathbf{x} , the local and time-dependent effective fracture permeability $k_{Fr}^s(\mathbf{x}, t)$ for high aspect ratio fractures is introduced. Finally, a hydraulic formulation for a pressure driven flow that allows for varying local permeabilities has been introduced.

2.2.2 Balance of Mass of the Fluid - Fracture Flow

The derivation of the balance of mass requires consideration of the fluid compressibility along with a varying aperture $\delta(\mathbf{x}, t)$ of a single fracture. Evaluation of the mass balance yield relations between fluid velocity, fluid density changes, injected fluid volume and fracture volume. Fulfilment of condition

$$(\rho^{fR} \delta) + \text{div} (\hat{\mathbf{w}}_f \rho^{fR} \delta) = 0 \quad (4.11)$$

guarantees conservation of mass in a fluid-filled fracture. For investigations where leak-off is of interest the system needs to be modified by simply extending the right hand side of eq. (4.11) by a source term that will be explained in section 2.2.3.

2.2.3 Governing Equations

The governing equation are derived by evaluating the balance of mass eq.(4.11) and the balance of momentum eq. (4.10) with respect to the fluid within the deformable fracture. Assuming proportionality between the fluid pressure and the effective fluid density given by eq. (4.4) finally leads to the governing scalar PDE

$$\begin{array}{ll}
\text{(i)} & \dot{p} & \text{Transient} \\
\text{(ii)} & -\frac{\delta^2}{12 \eta^{rk}} \text{grad } \hat{p} \cdot \text{grad } \hat{p} & \text{Quadratic} \\
\text{(iii)} & -\frac{\delta}{12 \eta^{rk} \beta f} \text{grad } \delta \cdot \text{grad } \hat{p} & \text{Convection} \\
\text{(iv)} & -\frac{1}{12 \eta^{rk} \beta f} \text{div} \left(\delta^2 \text{grad } \hat{p} \right) & \text{Diffusion} \\
\text{(v)} & +\frac{1}{\delta \beta f} \dot{\delta} & \text{Coupling} \\
\text{(vi)} & = \frac{w_f^N}{\delta \beta f} & \text{Leak-Off}
\end{array} \tag{4.12}$$

where divergence $\hat{\text{div}}$ and gradient $\hat{\text{grad}}$ are evaluated with respect to the lower dimensional fracture domain \mathcal{B}^{Fr} . The non-linear storage eq. (4.12) consists of a transient term i), a quadratic term ii), a convection term iii), a diffusion term iv) and a hydro-mechanical coupling term which takes into account the transient evolution of the fracture's aperture v). In the present case we are focusing on high aspect ratio fractures. Thus, based on the results of a dimensional analysis of eq. (4.12) [205], the quadratic and the convection term can be neglected due to their minor contribution to the solution.

An initial pressure of $\hat{p}(\hat{\mathbf{x}}, t_0) = 0$ relative to the confining pressure and an undrained (non-flux) condition at the fracture tip $q(\hat{\mathbf{x}}_{tip}, t) = 0$ (where $\hat{\mathbf{x}}_{tip}$ denotes the fracture tip position) define the Dirichlet and Neumann boundary conditions. In case of applications related to borehole investigations, the related pressure or flux can additionally be prescribed at the borehole intersection.

For a surrounding poroelastic matrix material, an exchange of mass occurs between the fracture and the surrounding matrix which is taken into account by a non-zero right-hand-side in eq. (4.11). The sink or source term is considered by

$$q_{lk} = \frac{w_f^N}{\delta \beta f}, \tag{4.13}$$

where w_f^N is the leak-off induced seepage velocity determined by Darcy's law of the poroelastic matrix. In the course of this work, the leak-off treatment differs for the coupling strategies and is individually derived for each scheme in section 3.

3 Numerical Schemes for Hybrid-Dimensional Formulations

Consistent implementation of the governing equations describing fluid flow, deformation and the possible exchange of fluid from the fracture to a poroelastic matrix material, require an implicitly coupled system of both domains, the fracture, and the matrix material. Suitable algorithms to solve the discrete system for pressure \hat{p} and fracture width δ will be discussed in this section.

3.1 Weak Form of the Governing Equations

In the course of this work, a classical Bubnov Galerkin finite element formulation for poroelasticity will be applied to the surrounding matrix material with domain \mathcal{B}^{Pe} . Analysis of the coupled response inside the fracture, i.e., the fluid pressure \hat{p} - fracture aperture δ interplay is analyzed. The numerical formulation for the biphasic porous matrix is based on the weak form of the set of governing equations (4.7) and reads

$$\int_{\mathcal{B}^{Pe}} (\boldsymbol{\alpha} \boldsymbol{\epsilon}_E^s - \alpha p \mathbf{I}) : \text{grad } w_{\mathbf{u}} \, dv = \int_{\Gamma_N^s} \bar{\mathbf{t}} \cdot w_{\mathbf{u}} \, da, \quad (4.14)$$

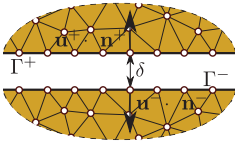
$$\int_{\mathcal{B}^{Pe}} \left[\frac{\dot{p}}{M} w_p + \frac{k^f}{\gamma^f R} \text{grad } p \cdot \text{grad } w_p + \alpha \text{div } \dot{\mathbf{u}}_s w_p \right] dv = \int_{\Gamma_N^f} \bar{w}_f w_p \, da.$$

Note that the test functions of the balance of momentum of the mixture $w_{\mathbf{u}}$ and the balance of mass of the fluid w_p are introduced. To investigate pressure fluctuations related to aperture changes, the poroelastic eqs. (4.14) of the surrounding matrix (domain \mathcal{B}^{Pe}) medium are coupled to the modified hybrid-dimensional formulation (domain \mathcal{B}^{Fr}) in its weak form

$$\int_{\mathcal{B}^{Fr}} \left[\dot{p} w_{\hat{p}} + \frac{\delta^2}{12 \eta^i R \beta^f} \text{grad } \hat{p} \cdot \text{grad } w_{\hat{p}} + \frac{1}{\delta} \frac{\partial \delta}{\beta^f \partial t} w_{\hat{p}} \right] dv = 0. \quad (4.15)$$

Note that advection and quadratic terms are neglected based on the dimensional analysis evaluated in [205]. The test functions for the hybrid-dimensional problem are given by $w_{\hat{p}}$.

In section 2.2, the fracture width δ has already been introduced as the hydro-mechanical coupling parameter. By assuming predominant deformation normal to the fracture surface the local fracture aperture

$$\delta = \mathbf{u}^+ \cdot \mathbf{n}^+ - \mathbf{u}^- \cdot \mathbf{n}^- \quad (4.16)$$


can be rewritten with respect to the fracture normal surface displacements \mathbf{u}^+ and \mathbf{u}^- which are primary variables of the solid formulation (eq. (4.14a)).

3.2 Characteristic of the Coupled System

To obtain a deeper understanding of the coupled system, Adachi et al. [1] studied the characteristic of hydro-mechanical coupled systems by assuming a 1D penny-shaped Kristianovich-Geertsma-de Klerk (KGD) fracture width description coupled to the Reynold's equation modified for the fluid flow in deformable fractures. Based on linear elastic solid mechanics coupled to a diffusive process, Adachi's simplified system is equivalent to a highly permeable poroelastic drained medium, since the deformation of the surrounding

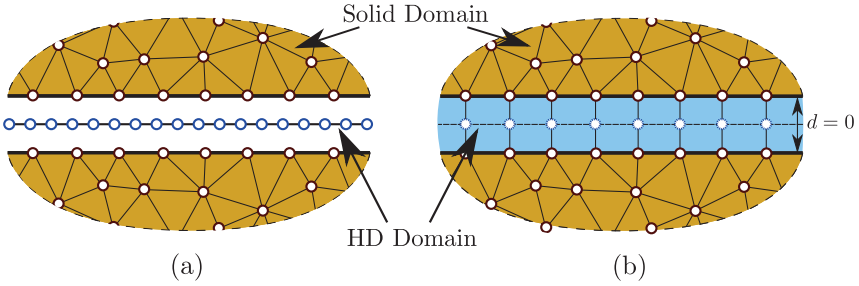


Figure 2: Comparison of a weak coupling scheme using non-conformal meshes (a) and a strong coupling scheme with implemented interface elements (here interface elements, and auxiliary nodes are explicitly shown for presentation purposes only; in final discretization fracture surfaces align with $d = 0$) (b).

matrix is not damped by the pore pressure evolution; hence it represents the stiffest case of the coupled system due to possibly large fracture deformations. By analyzing the eigenvalues of the coupled matrices [141] it has been shown that the stability is guaranteed if the Courant-Friedrichs-Lewy (CFL) condition

$$\Delta t < \frac{\Delta x^3}{E' D} \quad (4.17)$$

is fulfilled. Eq. (4.17) does not only clarify that explicit time-stepping using the explicit Euler method is not suitable due to inadequate small time steps, but also the extreme stiffness of the coupled system that requires an implicit coupling procedure. In the following an implicit time discretization in form of a backward Euler method will be used throughout this work. In eq. (4.17) Δx denotes the element length, E' the elastic plane-strain modulus and D the conductivity.

3.3 Weak Coupling - Staggered Coupling Scheme

Non-conformal meshes and computations on two different domains (\mathcal{B}^{Pe} and \mathcal{B}^{Fr}) are the motivation for the first proposed strategy, namely a staggered coupling scheme. Besides the reduction of DoFs by the lower-dimensional elements for pressure diffusion in the fracture, computational time can potentially be reduced by using an individual discretization for both domains. In the numerical study section an investigation of the error evolution for different numerical resolution combinations of the fracture (pressure diffusion) and poroelastic matrix domains will provide further insights of increasing computational efficiency based on non-conformal meshes (reduction of DoF). Schematically the idea of non-conformal meshing using hybrid-dimensional elements is shown in fig. 2 (a).

3.3.1 Coupling Algorithm

In the field of non-fractured porous media different sequential implicit strategies for solving biphasic mixtures have been proposed. Depending on the sequence both problems are solved Kim et al. [104, 105] differentiate between drained/undrained (mechanical followed by flow problem) and fixed-stress/fixed-strain splits (flow followed by the mechanical problem). The drained and undrained split differ concerning the consideration of the applied pressure within the mechanical problem. The drained split treats the pressure constant throughout the mechanical calculations, unlike the undrained split where the pressure can vary with the volumetric deformation enforcing a constant fluid mass in each element. In contrast, the fixed-strain and fixed-stress split differ concerning the consideration of the applied strain used in the flow calculations. For the fixed-strain split, the applied strain rate stays constant in contradistinction to the fixed-stress split where the strain rate can vary depending on the calculated fluid pressure enforcing a constant stress rate throughout the flow calculations. Girault et al. [72] modified the fixed-stress method to achieve convergence and stability for fractured porous media applications.

In the course of this work, the staggered scheme implicitly couples the fracture with the porous domain allowing non-conformal numerical discretizations of the porous and lower dimensional fracture domain. Nevertheless, the porous domain does not explicitly discretize the fracture volume, and volumetric changes of the fracture throughout porous matrix calculations are not accessible. Hence the fixed-stress and fixed-strain algorithms suit the described discretization strategy best since no volumetric change information are required. An algorithm comparable to the fixed-strain scheme and the modified fracture formulation of the fixed-stress scheme is implemented and tested with regards to stability and convergence. In case of the fixed-stress algorithm the simplified governing equations (quadratic and convection terms are neglected; high aspect ratio assumption) eq. (4.12) is extended to achieve constant stress rates throughout the flow problem

$$\dot{\hat{p}}^{new} - \frac{\gamma_c}{\gamma_c + \delta \beta^f} \dot{\hat{p}}^{old} - \frac{\delta^3 \beta^f}{12 \eta^{IR} (\gamma_c + \delta \beta^f)} \hat{\text{div}} \hat{\text{grad}} \hat{p} - \frac{1}{\gamma_c + \delta \beta^f} \dot{\delta} = q_{lk}. \quad (4.18)$$

Note that a term has been consistently added to the governing equation to fix the stress rate without limiting the functions, where $\gamma_c = M \beta^f \alpha^2 / (\lambda + M \beta^f \lambda \phi)$ is an estimate to achieve convergence, $\hat{p}^{new} = \hat{p}_{k+1}^t$ is the solution of the current and $\hat{p}^{old} = \hat{p}_k^t$ the solution of the former iteration (the interested reader is referred to [72]). Since the time derivative is evaluated with respect to the fixed pressure \hat{p}^{t-1} of the former time step the introduced term vanishes once the problem converges ($\hat{p}_{k+1}^t \approx \hat{p}_k^t$). The fixed-stress formulation can be classified as a preconditioned Richardson iteration [38].

$$\delta_{k+1}^t = \bar{\alpha} \delta_{k+1/2}^t + (1 - \bar{\alpha}) \delta_k^t \quad 0 < \bar{\alpha} < 1 \quad (4.19)$$

updates the fracture width to δ_{i+1}^t , where δ_i^n is the fracture width of the prior iteration step, $\delta_{k+1/2}^t$ an intermediate value and $\bar{\alpha}$ the Picard update constant. In case of the fixed-stress strategy the update constant is equal to one $\bar{\alpha} = 1$. Convergence of the procedure is checked by the error measure

$$\epsilon = \frac{\sum_{n=1}^{n_{total}} |\delta_{k+1,n}^t - \delta_{k,n}^t|}{\sum_{n=1}^{n_{total}} |\delta_{k+1,n}^t|}, \quad (4.20)$$

which is calculated by iterating over all nodes n , where n_{total} denotes the total number of nodes.

The algorithm 1 schematically shows the implemented coupling scheme and is valid for

Algorithm 1: Staggered Coupling Procedure

```

while  $t \leq t_{end}$  do
  while  $k < k_{max}$  do
    # Update pressure state dependent on fracture width changes
     $\hat{p}_{k+1}^t = \text{eq. (4.15)}$  using  $\delta_k^t$ 
    # Update deformation for new pressure state
     $\mathbf{u}_{k+1}^t = \text{eq. (4.14)}$  using  $\hat{p}_{k+1}^t$ 
    # Intermediate fracture width for
     $\delta_{k+1/2}^t = \text{eq. (4.16)}$  using  $\mathbf{u}_{k+1}^t$ 
    # Use Picard update to calculate new fracture width
     $\delta_{k+1}^t = \text{eq. (4.19)}$  using  $\delta_{k+1/2}^t$  and  $\delta_k^t$ 
    # Calculate Error
     $\epsilon = \text{eq. (4.20)}$ 
    if  $\epsilon < \epsilon_{max}$  then
      # Update solutions for time-step
       $\hat{p}_{k+1}^{t+1} = \hat{p}_{k+1}^t$ 
       $\delta_{k+1}^{t+1} = \delta_{k+1}^t$ 
      # Break iteration loop
      break
    else
      # Set pressure values to values of prior time-step
       $\hat{p}_{k+1}^t = \hat{p}^{t-1}$ 
      # Continue
      continue
    end
  end
end
end

```

both strategies. The numerical scheme contains two major loops; one time-stepping loop due to the transient (diffusive) nature of the problem and a second one for the residuum iterations of every time-step. For a better understanding the main steps of the algorithm are summarized below.

Residuum Iterations

1. The iteration procedure starts with an update of the pressure to \hat{p}_{k+1}^t based on the fracture width of the prior iteration step δ_{k-1}^t . During the first iteration the initially calculated value δ_0^t is used. Further, to guarantee consistency, the discrete form of fracture change velocity $\dot{\delta} = \frac{\delta_{k-1}^t - \delta^{t-1}}{\Delta t}$ is related to the fixed fracture width δ^{t-1} of the previous time-step.

2. With pressure \hat{p}_{k+1}^t all necessary boundary conditions are provided to determine deformation \mathbf{u}_{k+1}^t .
3. In the following step the intermediate fracture width $\delta_{k+1/2}^t$ is obtained from deformation \mathbf{u}_{k+1}^t .
4. The new fracture width δ_{k+1}^t (using the Picard update) can be considered as the result of each iteration step.
5. Error ϵ is calculated using fracture width δ_{k+1}^t . If the error is less than a predefined maximum error convergence is reached and the pressure \hat{p}^t and fracture width δ^t of the active time-step t are updated by the values \hat{p}_c^t and δ_c^t , where index c denotes the convergence iteration step. If the error criterion is not fulfilled the pressure \hat{p}_{k+1}^t is set back to the fixed pressure \hat{p}^{t-1} of the previous time-step to avoid transient artifacts and guarantee consistency, before the process is repeated within the next iteration.

In case of a low fluid compressibilities $\beta^f < 10^{-6} \text{ GPa}^{-1}$ it is expected that the fixed-strain scheme requires small values for the Picard update constant (approx. $\bar{\alpha} < 5.0e^{-3}$) to reach convergence. Small values for $\bar{\alpha}$ result in an inadequate high number of iteration steps and reasonable values for $\bar{\alpha}$ in inadequate small time steps [184], respectively. Nevertheless, for moderate up to high compressibilities $\beta^f > 10^{-6} \text{ GPa}^{-1}$, the scheme converges in a low number of iterations. In contrast the fixed-stress approach is supposed to converge even for a low compressibility in an adequate number of iterations. For both schemes it is intuitive to implement non-conformal mesh coupling in order to gain an advantage with respect to computation times.

3.3.2 Leak-Off - Weak Coupling

Leak-off in the weak coupling scheme is related to the normal seepage velocity determined by the poroelastic problem and is captured by an extension of the fracture flow formulation by source term q_{lk} . In order to determine q_{lk} in eq. (4.12) the seepage velocity w_{Γ}^N normal to the fracture surface Γ^{Fr} must be calculated based on Darcy's law

$$w_{\Gamma}^N(\mathbf{x}) = -\frac{k_{Fr}^s}{\eta_{Fr}^s} \text{grad} p \cdot \mathbf{n}^{\pm} \quad (4.21)$$

where \mathbf{n}^{\pm} denotes the top and bottom normal vector. Once source term q_{lk} is calculated it is applied in the form of a Neumann boundary condition to the fracture flow problem. The pore pressure p on the fracture surfaces is obtained by the pressure state \hat{p} of the fracture flow problem, and no discontinuities of the pressure state between both fracture surfaces are taken into account. Nevertheless, the leak-off into the porous medium can differ on both surfaces due to possibly varying permeabilities of the surrounding matrix and also allows fluid flow across the fracture. Throughout the equilibrium iterations of the staggered algorithm, the leak-off term is updated for every iteration step. The interaction procedure throughout the calculations is schematically shown in fig. 3 (a).

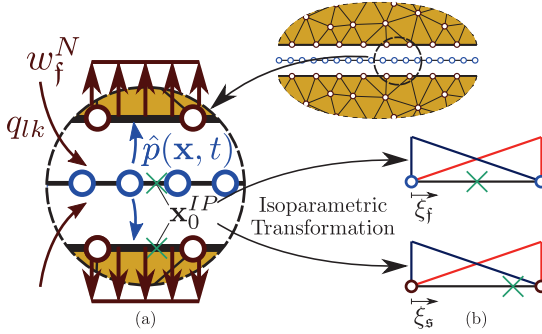


Figure 3: Leak-off interaction of the poroelastic and fracture flow domain (a) by using a consistent interpolation scheme (b).

3.3.3 Consistent Interpolation

Information of all primary variables \mathbf{u} , p and \hat{p} are required for element integration on integration point level of both problems. Since the lower dimensional elements are geometrically aligning with the fracture surfaces of the poroelastic problem the global coordinates of the integration points \mathbf{x}^{IP} can be transformed to the isoparametric element representation of both domains. In fig. 3 (b) the transformation is arbitrarily shown for an integration point \mathbf{x}_0^{IP} and linear element formulations in both domains. Note, that the element order can independently be chosen for the fracture flow and poroelastic domain discretization.

3.4 Strong Coupling - Interface Elements

Especially for fluids with a low compressibility $\beta^f < 10^{-6} \text{ GPa}^{-1}$, the system of equations becomes extremely stiff. Besides the already proposed weakly coupled fixed-stress strategy an implicitly coupled formulation will be proposed to model such stiff systems. In the present approach, the strong coupling is realized by zero-thickness interface elements based on the work of Segura and Carol [180, 181] which will be applied to the proposed hybrid dimensional formulation.

3.4.1 Strong Coupling - Interface Element Formulation

This section will introduce zero-thickness interface elements to build up a global assembly matrix concerning only two primary variables, namely pressure p and deformation \mathbf{u} , for both domains. The resulting global system is then monolithically solved. For linear cases, no iterations are needed, and convergence is always guaranteed [72]; for non-linear cases, the Newton-Raphson scheme is implemented. In general interface elements possess no thickness, meaning that facing nodes are aligning. In the case of fracture flow the

volume of the fracture is not captured geometrically, but through integration by using the fracture aperture to determine the fracture volume. Different interface elements have been proposed in the literature such as single node - interface elements [217] that capture longitudinal fracture flow only, doubled node - interface elements [181] with two aligning nodes where the element-integration takes place on mid-plane auxiliary nodes allowing transversal and longitudinal flow and triple node - interface elements [81] where a third aligning node is introduced in order to separate the transversal from the longitudinal flow. This work exclusively focuses on the double node - interface element since no additional DoF are introduced and flow in both directions is captured.

In contrast to the weak coupling scheme where only longitudinal flow was described in the lower dimensional elements and transversal flow captured by leak-off only, the proposed interface elements directly model longitudinal and transversal flow concerning the pressure state on the fracture surfaces of the porous matrix and allows a discontinuous pressure jump regarding both fracture surfaces. Modeling of fracture pressure \hat{p} in direct relation to pressure p obtained on the fracture surface of the porous matrix requires an averaging across the fracture as proposed in [124]. Martin et al. treat the fracture as an interface separating two connected domains and is employed to derive the proposed interface elements. By averaging the conservation equation, a formulation governing the flow into, across and along the fracture is obtained. Both equations are then closed by boundary conditions for the pressure along the fracture surfaces.

3.4.2 Averaging of Balance of Mass of the Fluid - Fracture Flow

An extension of the mentioned work of Martin et al. to capture deformable fractures is derived in the following. Balance of mass, given by eq. (4.11), is rewritten by inserting the pressure density relationship for a barotropic fluid of eq. (4.4)

$$\frac{\delta}{K^f} \dot{\hat{p}} + \dot{\delta} + \hat{\text{div}}(\hat{\mathbf{w}}_f \delta) = 0. \quad (4.22)$$

In order to capture a pressure jump along the fracture surfaces the seepage velocity $\hat{\mathbf{w}}_f$ is decomposed into a longitudinal $\hat{\mathbf{w}}_f^l$ and a transversal $\hat{\mathbf{w}}_f^t$ component

$$\hat{\mathbf{w}}_f = \hat{\mathbf{w}}_f^l + \hat{\mathbf{w}}_f^t. \quad (4.23)$$

Note that the transversal component is defined concerning the seepage velocity normal to the fracture interface $\hat{\mathbf{w}}_f^t = \hat{\mathbf{w}}_f \cdot \mathbf{n}$ with $\mathbf{n} = \mathbf{n}^+ = -\mathbf{n}^-$. Since two flow directions are taken into account divergence $\hat{\text{div}}_l$ and gradient $\hat{\text{grad}}_l$ in longitudinal and divergence $\hat{\text{div}}_t$ and gradient $\hat{\text{grad}}_t$ in transversal direction are introduced. By inserting these in eq. (4.22) the decomposed balance of mass of the fluid within the fracture

$$\frac{\delta}{K^f} \dot{\hat{p}} + \dot{\delta} + \hat{\text{div}}_l(\hat{\mathbf{w}}_f \delta) + \delta \hat{\text{div}}_t(\hat{\mathbf{w}}_f) = 0 \quad (4.24)$$

is derived. In order to formulate the fracture flow with respect to a line segment an averaging in transversal direction is necessary. Note that only pressure \hat{p} and seepage

velocity $\hat{\mathbf{w}}_f$ vary in tangential direction. The averaging results in

$$\frac{\delta}{K^\dagger} \dot{\hat{P}} + \dot{\delta} + \hat{\text{div}}_l \left(\hat{\mathbf{W}}_f \delta \right) = -\hat{\mathbf{w}}_f \cdot \mathbf{n}|_{\Gamma_+^{Fr}} + \hat{\mathbf{w}}_f \cdot \mathbf{n}|_{\Gamma_-^{Fr}} \quad (4.25)$$

where $\hat{P} = \int_{-\delta/2}^{\delta/2} \hat{p} \, d\mathbf{n}$ defines the integral value of the fracture fluid pressure and $\hat{\mathbf{W}}_f = \int_{-\delta/2}^{\delta/2} \hat{\mathbf{w}}_f^t \, d\mathbf{n}$ the integral value of the longitudinal seepage velocity. Continuity between the fluxes of the porous medium and the fracture domain on the fracture surfaces Γ_{\pm}^{Fr} is introduced by

$$w_f^\pm \cdot \mathbf{n} = \hat{\mathbf{w}}_f \cdot \mathbf{n}. \quad (4.26)$$

Inserting the continuity condition formulated in eq. (4.26) in the averaged mass balance of eq. (4.25)

$$\frac{\delta}{K^\dagger} \dot{\hat{P}} + \dot{\delta} + \hat{\text{div}}_l \left(\hat{\mathbf{W}}_f \delta \right) = \mathbf{w}_f^+ \cdot \mathbf{n}^+ + \mathbf{w}_f^- \cdot \mathbf{n}^- \quad (4.27)$$

combines the surrounding matrix and the fracture domain, where the source term on the right hand side governs the leak-off into the surrounding matrix and across the fracture.

3.4.3 Averaging of Balance of Momentum of the Fluid - Fracture Flow

In longitudinal direction eq. (4.10) defines the relative fluid velocity. By integration over the aperture δ the averaged expression for the seepage velocity reads

$$\hat{\mathbf{W}}_f = -\frac{k_{Fr,l}^s(\mathbf{x}, t)}{\eta^{lR}} \hat{\text{grad}}_l \hat{P}. \quad (4.28)$$

The averaged mass balance given by eq. (4.27) combined with the averaged seepage velocity defined by eq. (4.28) provides a formulation for the flow within the fracture including leak-off. Pressure differences on both fracture surfaces are modelled by introducing another governing equation for the transversal flow. In transversal direction a Darcy type flow is introduced by

$$\hat{\mathbf{w}}_f^t = -\frac{k_{Fr,t}^s}{\eta^{tR}} \hat{\text{grad}}_t \hat{p} \quad (4.29)$$

where $k_{Fr,t}^s$ defines the permeability in transversal direction. Integration over the aperture results in

$$\int_{-\delta/2}^{\delta/2} \hat{\mathbf{w}}_f^t \cdot \mathbf{n} \, d\mathbf{n} = -\frac{k_{Fr,t}^s}{\eta^{tR}} \left(-\hat{p}|_{\Gamma_+^{Fr}} + \hat{p}|_{\Gamma_-^{Fr}} \right). \quad (4.30)$$

Integration of the left hand side $\int_{-\delta/2}^{\delta/2} \hat{\mathbf{w}}_f^t \cdot \mathbf{n} \, d\mathbf{n}$ is not carried out explicitly, but approximated by the trapezoidal rule

$$\int_{-\delta/2}^{\delta/2} \hat{\mathbf{w}}_f^t \cdot \mathbf{n} \, d\mathbf{n} \approx \frac{\delta}{2} \left(\hat{\mathbf{w}}_f \cdot \mathbf{n}|_{\Gamma_+^{Fr}} + \hat{\mathbf{w}}_f \cdot \mathbf{n}|_{\Gamma_-^{Fr}} \right) = \frac{\delta}{2} \left(-\mathbf{w}_f^+ \cdot \mathbf{n}^+ + \mathbf{w}_f^- \cdot \mathbf{n}^- \right). \quad (4.31)$$

where continuity of fluid flow on the fracture surfaces is assumed. Finally, the approximation given in eq. (4.31) is inserted in eq. (4.30) to define the relation of pressure and

flow in transversal direction

$$\frac{1}{2}(-\mathbf{w}_f^+ \cdot \mathbf{n}^+ + \mathbf{w}_f^- \cdot \mathbf{n}^-) = -\frac{k_{Fr,t}^s}{\eta^{iR}} \frac{-p^+ + p^-}{\delta}. \quad (4.32)$$

Note that eq. (4.32) made use of the continuity of the pressure on the fracture surface $p^\pm = \hat{p}|_{\Gamma_\pm}$. The formulation depends on parameters that can be expressed by the primary variables of the porous domain.

3.4.4 Interface Element Formulation

To close the system of equations and to derive the interface element formulation, a boundary condition for the averaged fracture domain pressure \hat{P} is introduced. In contrast to the weak coupling scheme where no discretization of the surrounding matrix governs the fracture domain, the constitutive modelling of solid behaviour, such as closing and opening of rough fracture surfaces [180] can be realized within the framework of interface elements if needed. Extension of the existing set of governing equations by a formulations of the fracture surface interaction allows i.e. modelling of hydraulically open and mechanically closed fractures and motivates a discontinuous pressure assumption for the transversal fracture flow which is also valid for investigations on open fractures by choosing a suitable value for $k_{Fr,t}^s$. Throughout the averaging process of the fracture pressure \hat{P} different domain decompositions are possible [124] leading to a general set of balance equations at both fracture surfaces

$$\begin{aligned} -\xi \mathbf{w}_f^+ \cdot \mathbf{n}^+ + \frac{2k_{Fr,t}^s}{\delta \eta^{iR}} p^+ &= -(1-\xi) \mathbf{w}_f^- \cdot \mathbf{n}^- + \frac{2k_{Fr,t}^s}{\delta \eta^{iR}} \hat{P} \\ -\xi \mathbf{w}_f^- \cdot \mathbf{n}^- + \frac{2k_{Fr,t}^s}{\delta \eta^{iR}} p^- &= -(1-\xi) \mathbf{w}_f^+ \cdot \mathbf{n}^+ + \frac{2k_{Fr,t}^s}{\delta \eta^{iR}} \hat{P} \end{aligned} \quad (4.33)$$

where weighting parameter ξ is a positive real number within the range $\xi \in]1/2, 1]$. In this work ξ is chosen to be the stability limit $\xi = 1/2$ [179] which despite a high solution quality for most cases might lead to numerical instabilities for some numerical set ups where ξ needs to be adjusted [124]. No such numerical instabilities occurred throughout the performed numerical studies. Hence the averaged fracture domain pressure \hat{P} and the pressure difference along δ read

$$\begin{aligned} \hat{P} &= \frac{p^+ + p^-}{2} \\ \mathbf{w}_f^- \cdot \mathbf{n}^- - \mathbf{w}_f^+ \cdot \mathbf{n}^+ &= 2k_{Fr,t}^s \frac{p^- - p^+}{\delta} \end{aligned} \quad (4.34)$$

where the transversal discontinuous pressure assumption is introduced by $\hat{P}^t = (p^- - p^+)/\delta$. By summation/subtraction of eq. (4.34) and eq. (4.25) a formulation governing longitudinal and transversal flow depending only on the primary variables of the porous

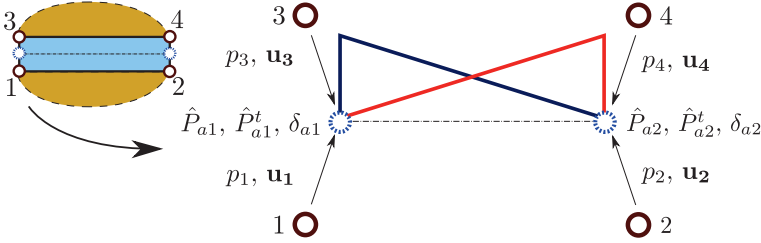


Figure 4: Integration of linear auxiliary element, including the contribution of interface element nodes to averaged pressure \hat{P}_{ai} , pressure difference \hat{P}_{ai}^t and aperture δ_{ai} on auxiliary element nodes.

matrix is found for the upper and lower fracture surface

$$\begin{aligned} \frac{1}{2} \left[\frac{1}{K^f} \dot{\hat{P}} + \delta + \hat{\text{div}}_l (\hat{\mathbf{W}}_f \delta) \right] - k_{Fr,t}^s \hat{P}^t &= \mathbf{w}_f^+ \cdot \mathbf{n}^+ \quad \text{on } \Gamma_+^{Fr}, \\ \frac{1}{2} \left[\frac{1}{K^f} \dot{\hat{P}} + \delta + \hat{\text{div}}_l (\hat{\mathbf{W}}_f \delta) \right] + k_{Fr,t}^s \hat{P}^t &= \mathbf{w}_f^- \cdot \mathbf{n}^- \quad \text{on } \Gamma_-^{Fr}. \end{aligned} \quad (4.35)$$

The weak form of the governing set of equations given by 4.35 are simplified and evaluated for the case of high aspect ratio fractures similar to the derivation of the hybrid dimensional formulation used for the weak coupling scheme

$$\begin{aligned} \int_{\Gamma_+^{Fr}} \left[\frac{1}{2} \left(\dot{p} w_a + \frac{\delta^2}{12 \eta^{fR} \beta^f} \hat{\text{grad}}_l \hat{P} \cdot \hat{\text{grad}}_l w_a + \frac{1}{\delta \beta^f} \frac{\partial \delta}{\partial t} w_a \right) - \frac{1}{\delta \beta^f} k_{Fr,t}^s \hat{P}^t w_a \right] dv &= \frac{1}{\delta \beta^f} \mathbf{w}_f^+ \cdot \mathbf{n}^+, \\ \int_{\Gamma_-^{Fr}} \left[\frac{1}{2} \left(\dot{p} w_a + \frac{\delta^2}{12 \eta^{fR} \beta^f} \hat{\text{grad}}_l \hat{P} \cdot \hat{\text{grad}}_l w_a + \frac{1}{\delta \beta^f} \frac{\partial \delta}{\partial t} w_a \right) + \frac{1}{\delta \beta^f} k_{Fr,t}^s \hat{P}^t w_a \right] dv &= \frac{1}{\delta \beta^f} \mathbf{w}_f^- \cdot \mathbf{n}^-. \end{aligned} \quad (4.36)$$

where w_a denotes the lower dimensional test functions used for the auxiliary element.

3.4.5 Leak-Off - Strong Coupling

Leak-off in the strong coupling scheme is described by the right-hand side of eqs. (4.36). Nevertheless, the boundary term is naturally covered by the pore pressure evolution within the surrounding poroelastic matrix since the fluid pressure \hat{p} within the fracture is calculated based on the pore pressure p of the fracture boundary. Leak-off from the fracture into the porous matrix can vary concerning to the upper and lower fracture surface Γ_{\pm}^{Fr} .

3.4.6 Interface Element Integration

Integration of auxiliary elements requires the averaged pressure \hat{P} , pressure difference \hat{P}^t and aperture δ on auxiliary node level. The values are calculated from the pressure p

and deformation state \mathbf{u} of aligning nodes of the interface element which is exemplarily shown for a linear element formulation in fig. 4. Note that the upper surface (node 3 and 4) is governed by the first equation and the lower surface (node 1 and 2) by the second equation of eq. (4.36). The governing equations and boundary conditions are summarized in the following.

Governing Equations

Surrounding matrix - \mathcal{B}^{Pe}

$$\text{Solid equilibrium: } -\operatorname{div}(\tilde{\omega}\boldsymbol{\varepsilon}_E^s - \alpha p \mathbf{I}) = \rho \mathbf{b} \quad \text{in } \mathcal{B}^{Pe}$$

$$\text{Fluid equilibrium: } \dot{p} - \frac{Mk^f}{\gamma^f R} \operatorname{div} \operatorname{grad} p + M\alpha \operatorname{div} \dot{\mathbf{u}}_s = M\bar{w}_f \quad \text{in } \mathcal{B}^{Pe}$$

$$\text{with: } \boldsymbol{\sigma}_E^s = 3K \operatorname{vol}(\boldsymbol{\varepsilon}_s) + 2G \operatorname{dev}(\boldsymbol{\varepsilon}_s) + (1 - \alpha) p \mathbf{I} \quad \text{in } \mathcal{B}^{Pe}$$

$${}''_s = \frac{1}{2} (\operatorname{grad} \mathbf{u} + \operatorname{grad}^T \mathbf{u})$$

Fluid filled fracture - \mathcal{B}^{Fr} (high aspect ratio simplification)

$$\text{Fracture flow: } \dot{p} - \frac{\delta^2}{12\eta^f R} \hat{\operatorname{div}} \operatorname{grad} \dot{p} + \frac{1}{\delta \beta^f} \dot{\delta} = q_{lk} \quad \text{in } \mathcal{B}^{Fr}$$

Initial, boundary and coupling conditions

$$\text{Fracture surface force equilibrium: } \mathbf{t}^\pm = -\dot{p} \cdot \mathbf{n}^\pm \quad \text{on } \Gamma_\pm^{Fr}$$

$$\text{Fracture tip no flux condition: } \hat{q} = 0 \quad \text{at } \Gamma_{tip}^f$$

$$\text{Fracture surface flux equilibrium: } q_{lk} = \frac{w_i^N}{\delta \beta^f} \quad \text{on } \Gamma_\pm^{Fr}$$

$$\text{Seepage velocity porous matrix: } w_i^N(\mathbf{x}) = -\frac{k^s}{\eta^f R} \operatorname{grad} p \cdot \mathbf{n}^\pm \quad \text{on } \Gamma_\pm^{Fr}$$

Notation

Poro-elastic domain \mathcal{B}^{pe}					
φ	- constituent	ρ^φ [kg/m ³]	- partial density		
φ^s	- solid constituent	ρ^{φ^R} [kg/m ³]	- effective density		
φ^f	- fluid constituent	k^f [m/s]	- Darcy permeability		
n^φ [-]	- volume fraction	k^s [m ²]	- intrinsic permeability		
α [-]	- Biot-Willis parameter	M [Pa]	- Biot's coupling parameter		
ϕ [-]	- porosity	σ_E^s [Pa]	- Cauchy extra stress		
σ [Pa]	- mixture stress tensor	K^s [Pa]	- grain bulk modulus		
p [Pa]	- pore pressure	K^f [Pa]	- fluid bulk modulus		
γ^{fR} [kg]	- effective fluid weight	\mathbf{w}_f [m/s]	- relative fluid flow		
K [Pa]	- dry frame bulk modulus	G [Pa]	- shear modulus		
\mathbf{u}_s [m]	- deformation				
Fracture Domain \mathcal{B}^f					
δ [m]	- fracture aperture	η^{fR} [Pa·s]	- effective fluid viscosity		
β^f [1/Pa]	- fluid compressibility	\hat{p} [Pa]	- fracture fluid pressure		

4 Numerical Studies

Quantity	Value	Unit	Quantity	Value	Unit
Poroelastic domain \mathcal{B}^{Pe}					
dry frame bulk modulus K	$8.0 \cdot 10^9$	[Pa]	grain bulk modulus K^s	$3.0 \cdot 10^{10}$	[Pa]
shear modulus μ	$1.54 \cdot 10^{10}$	[Pa]	porosity ϕ	$1.0 \cdot 10^{-2}$	[-]
intrinsic permeability k^s	<i>varies</i>	[m ²]	fluid compressibility β^f	<i>varies</i>	[1/Pa]
Fracture domain \mathcal{B}^{Fr}					
effective fluid viscosity η^{fR}	$1.0 \cdot 10^{-3}$	[Pa·s]	initial fracture aperture δ_0	<i>varies</i>	[m]
fluid compressibility β^f	<i>varies</i>	[1/Pa]			

Table 4.4: Collection of required modelling parameters in the poroelastic domain \mathcal{B}^{Pe} and fracture domain \mathcal{B}^f .

The derived hybrid model for fractured porous media is applied to several numerical studies in order to validate the implemented schemes and to investigate hydro-mechanical phenomena. The weak and strong coupling approaches are validated based on solutions obtained by Biot's poroelastic formulation using an explicit discretization (equidimensional model) of the fracture geometry. Since the weak coupling scheme allows for non-conformal meshes of the fracture and the surrounding porous domain, the error evolution for different discretization combinations is studied once the method is verified. Local permeability changes due to fracture aperture fluctuations influence the pressure state; hence a third study simplifies the problem assuming a rigid fracture to investigate the pressure deviations due to a globally applied constant fracture change. For small fracture deformations (constant permeability) the hydro-mechanically triggered inverse pressure response is investigated for fractures embedded in different permeable porous matrices in two dimensions. Finally, the influence of local permeability changes is investigated by simulations of a three-dimensional fracture network. The decisive material parameters

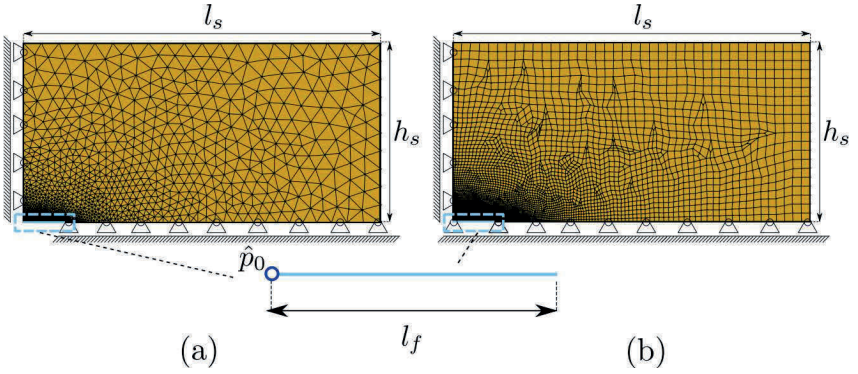


Figure 5: Discretization and boundary conditions used for the weak coupling (a) and strong coupling scheme (b) throughout the validation.

used throughout the simulations are given in table 4.4. Note that varying material and numerical parameters along with values for boundary conditions are introduced for each study individually. The two-dimensional boundary value problems use a radial symmetric formulation of the governing equations.

4.1 Validation and Efficiency Comparison of Weak and Strong Coupling Schemes

The analysis of hydro-mechanical phenomena requires a validation of the weak and strong coupling scheme implementations. Reduction of the boundary value problem's geometrical complexity is achieved by using a single fracture shown in fig. 5. The applied material and numerical parameters are given in table 4.5 and chosen to reproduce the porous material behavior of sandstone. Symmetry for both directions is used to model only a quarter of the actual problem. Influence of the domain's boundary to the fracture zone is avoided by choosing reasonable high dimensions for its height and length.

4.1.1 Validation

Throughout the validation calculations the fracture permeability is constant; hence it is valid to use an equidimensional Biot model to govern the behavior of the surrounding matrix and the flow within the fracture. The reference Biot simulation requires an explicit discretization of the fracture geometry in which the intrinsic permeability of fracture elements is set equal to the permeability $k_{Fr}^s(\delta_0)$ calculated for the hybrid model. The numerically converged (deviation between results $1.0 \cdot 10^{-4}$ by almost doubling the number of DoFs along the fracture; element size 0.0055 m) poroelastic solution serves as a reference for the hybrid-dimensional implementations. Assessing convergence of the weak coupling scheme iterations is based on the error measure ϵ given in eq. (4.20) with the condition $\epsilon \leq \epsilon_{max} = 1.0 \cdot 10^{-6}$. The results are validated at $t_0 = 10.0$ s (1000 time steps) at position

Quantity	Value	Unit	Quantity	Value	Unit
Poroelastic domain \mathcal{B}^{Pe}					
intrinsic permeability k^s	$1.1 \cdot 10^{-19}$	$[m^2]$	min fluid comp. β_{min}^f	$4.5 \cdot 10^{-10}$	$[1/Pa]$
max fluid comp. β_{max}^f	$4.5 \cdot 10^{-4}$	$[1/Pa]$	sample length l_{Pe}	$1.0 \cdot 10^3$	$[m]$
sample height h_{Pe}	$5.0 \cdot 10^2$	$[m]$			
Fracture domain \mathcal{B}^{Fr}					
min fluid comp. β_{min}^f	$4.5 \cdot 10^{-10}$	$[1/Pa]$	max fluid comp. β_{max}^f	$4.5 \cdot 10^{-4}$	$[1/Pa]$
fracture aperture δ_0	$5.0 \cdot 10^{-3}$	$[m]$	fracture length l^{Fr}	$1.0 \cdot 10^2$	$[m]$
pumping pressure p_0	$2.0 \cdot 10^4$	$[Pa]$			
Numerical Parameter					
time step size Δt	$1.0 \cdot 10^{-2}$	$[s]$	fracture discret. in \mathcal{B}^{Fr} Δx_{Fr}^{Fr}	$1.0 \cdot 10^{-1}$	$[m]$
fracture discret. in \mathcal{B}^{Pe} Δx_{Pe}^{Fr}	$1.0 \cdot 10^{-1}$	$[m]$	evaluation time t_0	$1.0 \cdot 10^1$	$[s]$
evaluation position x_0	$1.0 \cdot 10^1$	$[m]$	error tolerance ϵ_{max}	$1.0 \cdot 10^{-6}$	$[-]$
number of DoF	$1.4 \cdot 10^5$	$[-]$			

Table 4.5: Collection of parameters used for validation of the weak and strong coupling schemes.

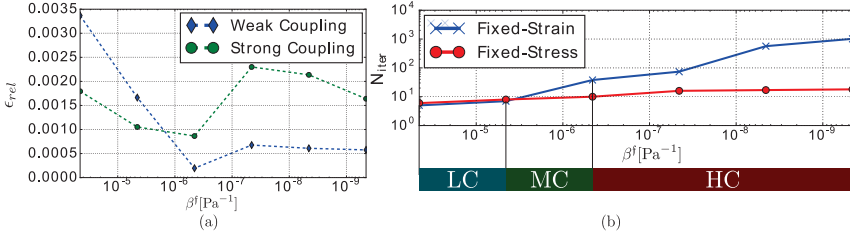


Figure 6: Plot of the relative error ϵ_{rel} for the strong and weak coupling schemes (a) and recommended compressibility range of application for both methods based on the necessary number of iterations N_{iter} of the fixed-strain and fixed-stress scheme for Low Compressibilities, Moderate Compressibilities and High Compressibilities of the fluid (b).

$x_0 = 10.0$ m using conformal meshes with element sizes of $\Delta x_{Fr}^{Fr} = \Delta x_{Pe}^{Fr} = 0.01$ m along the fracture for both domains. The varying fluid compressibility β^f is investigated within the limits of $4.5 \cdot 10^{-5}$ Pa⁻¹ to $4.5 \cdot 10^{-10}$ Pa⁻¹ (compressibility of water at 25°C). The relative error

$$\epsilon_{rel} = \frac{\hat{p}(x_1, t_1) - \hat{p}_{cb}(x_1, t_1)}{\hat{p}_{cb}(x_1, t_1)}, \quad (4.37)$$

shown in fig. 6 (a) is continuously below 0.0035 for both schemes within the investigated limits. Note that in eq. (4.37) \hat{p}_{cb} is the pressure of the converged poroelastic solution and \hat{p} the pressure solution obtained by either weak or strong coupling. The errors calculated for the fixed-strain and fixed-stress split are identical since the same convergence criterion is used. Such small errors do confirm not only the correct implementation of the introduced schemes but also their suitability for such strong hydro-mechanically coupled problems. The implementation of the proposed weak and strong coupling procedures reproduce the results obtained by Biot's poroelastic formulation like expected earlier in this work and can equivalently be applied for fracture flow analysis in the field of hydromechanics.

4.1.2 Efficiency Comparison

Since the weak coupling scheme relies on a staggered coupling of both domains, the number of iterations to reach a converged state is varying with the system's stiffness. Regarding the hybrid-dimensional formulation, the stiffness of the system varies with the fluid compressibility β^f . Hence ranges need to be defined in which the non-conformal mesh strategy has computational advantages over the strong formulation using interface elements and vice versa. The regions are defined based on the number of iterations (fig. 6 (b)) necessary for the weak-coupling scheme to converge. The number of iterations varies throughout the simulation since the convergence behavior is influenced by the pressure gradient between two time steps. In the current boundary value problem, an initial constant pressure \hat{p}_0 is applied. The first time step will require the most iterations to reach equilibrium due to the highest pressure gradient; hence it is adducted throughout the evaluation process as a numerical effort indicator. The number of iterations required for the fixed-strain algorithm to reach convergence correspond to the compressibility of the fluid. For fluid compressibilities between $\beta^f = 4.5 \cdot 10^{-4} \text{ Pa}^{-1}$ and $\beta^f = 4.5 \cdot 10^{-5} \text{ Pa}^{-1}$ the number of iterations is below 7. The low number of iterations in combination with the potentially reduced number of global DoFs guarantees high performance of the fixed-strain scheme for low fluid compressibilities. Within the range of moderate compressibilities $\beta^f = 4.5 \cdot 10^{-5} \text{ Pa}^{-1}$ and $\beta^f = 4.5 \cdot 10^{-6} \text{ Pa}^{-1}$ the number of iterations increases to 38. For any fluid compressibility lower than $\beta^f = 4.5 \cdot 10^{-6} \text{ Pa}^{-1}$ the fixed-strain scheme is not suitable due to an unreasonably high number of iterations (1018 iterations for $\beta^f = 4.5 \cdot 10^{-10} \text{ Pa}^{-1}$). In contrast, the convergence of the fixed-stress scheme is reached within a low number of iterations throughout the whole range of fluid compressibilities with a maximum of 18 iterations in case of β_{min}^f .

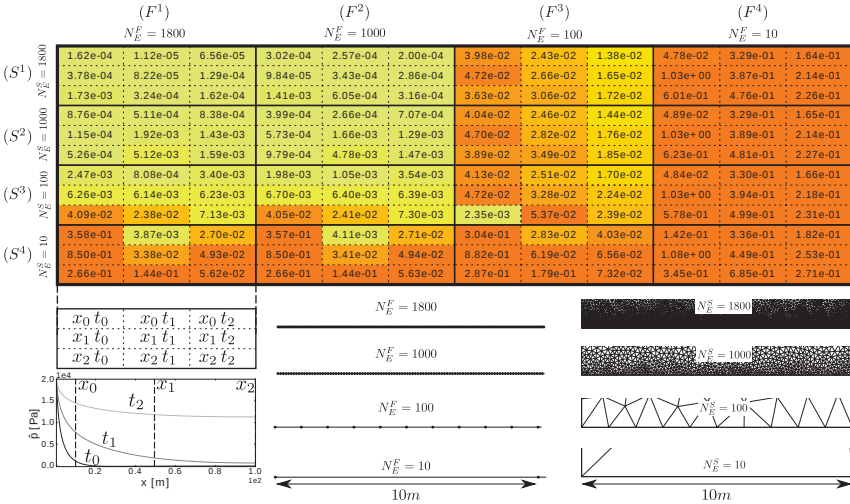
For stiff systems, the strong coupling scheme and fixed-stress algorithm are recommended to solve the coupled system of governing equations. Still, to compete with a directly solved strong coupling formulation concerning computational efficiency the fixed-stress algorithm must take advantage of the non-conformal mesh option to compensate the efficiency loss due to additional iterations.

4.2 Non-Conformal Mesh Study - Sensitivity Analysis of Varying Discretization for Fluid and Porous Domain

In section 4 the potential computational performance increase of the weak coupling scheme based on the reduction of the global number of DoF by non-conformal meshing of the fluid \mathcal{B}^{Fr} and porous domain \mathcal{B}^{Pe} was mentioned. Nevertheless, the quality of the obtained solution for the primary variables should not decrease. This numerical study investigates the solution quality dependence on different discretization combinations. The aim is to define combinations that allow a reduction of the system's number of DoF while maintaining a high solution quality. Within the study two parameters vary to identify the error evolution, namely the fracture discretization for the hybrid, one-dimensional model Δx_{Fr}^{Fr} and the mesh density for the higher dimensional porous matrix Δx_{Pe}^{Fr} along the fracture. For investigations of the error evolution of different discretization combinations, the already introduced boundary value problem shown in fig. 5 (a) is adducted with a

Quantity	Value	Unit	Quantity	Value	Unit
Poroelastic domain \mathcal{B}^{Pe}					
intrinsic permeability k^s	$1.1 \cdot 10^{-19}$	[m ²]	fluid comp. β^f	$4.5 \cdot 10^{-6}$	[1/Pa]
sample length l^s	$1.0 \cdot 10^3$	[m]	sample height l^s	$5.0 \cdot 10^2$	[m]
Fracture domain \mathcal{B}^{Fr}					
fluid comp. β_{min}^f	$4.5 \cdot 10^{-6}$	[1/Pa]	fracture aperture δ_0	$5 \cdot 10^{-3}$	[m]
fracture length l^{Fr}	$1.0 \cdot 10^2$	[m]	pumping pressure p_0	$2.0 \cdot 10^4$	[Pa]
Numerical Parameter					
time step size Δt	$1.0 \cdot 10^{-2}$	[s]	fracture discret. in \mathcal{B}^{Fr} $\Delta x_{Fr,min}^{Fr}$	$5.5 \cdot 10^{-2}$	[m]
fracture discret. in \mathcal{B}^{Pe} $\Delta x_{Fr,max}^{Fr}$	$1.0 \cdot 10^1$	[m]	fracture discret. in \mathcal{B}^{Fr} $\Delta x_{Pe,min}^{Fr}$	$5.5 \cdot 10^{-2}$	[m]
fracture discret. in \mathcal{B}^{Pe} $\Delta x_{Pe,max}^{Fr}$	$1.0 \cdot 10^1$	[m]	error tolerance ϵ_{max}	$1.0 \cdot 10^{-6}$	[-]

Table 4.6: Collection of parameters used throughout numerical studies on non-conformal meshes.

Figure 7: Error matrix for discretization combinations with legend and visualized mesh densities for an interval of 10 m. The error is evaluated for three positions x_0 , x_1 and x_2 at three time-steps t_0 , t_1 and t_2 .

moderate fluid compressibility of $\beta^f = 4.5 \cdot 10^{-6} \text{ Pa}^{-1}$. The material parameters used for the non-conformal mesh study are given in table 4.6. The mesh-dependent error is calculated on the basis of the aforementioned numerically converged poroelastic solution shown in eq. (4.37). The mesh density varies between $N_E^{min} = 10$ and $N_E^{max} = 1800$ elements along the fracture. Calculated errors and discretization of the used meshes are displayed in fig. 7. Note that the solutions obtained with the fixed-strain and fixed-stress approach are identical since the same convergence criterion is applied $\epsilon \leq \epsilon_{max} = 1.0 \cdot 10^{-6}$ and results of this study are valid for both schemes. Combinations involving coarse meshes ($N_E \leq 100$) produce large errors if both domains are coarse $\epsilon_{rel}^{S^4 F^4} = 1.08$. An improve-

ment of the error throughout the solution domain is investigated for a fine discretization of the fluid domain S^3F^1 more evidently than for a fine discretization of the porous domain S^1F^3 . In case of first approximations of the exact solution combination S^3F^2 and S^3F^1 provide an opportunity to give a reasonable prediction with a low number of DoF. For a fine discretization of the domains ($N_E \geq 1000$) all possible combinations provide solutions with a high quality $\epsilon_{err} < 0.006$.

The weak coupling scheme has an advantage over the strong coupling whenever a first prediction of a boundary value problem is of interest. It is possible to reduce the number of DoFs in the surrounding matrix domain \mathcal{B}^{Pe} by a factor of 10 compared to the discretization of the fracture domain \mathcal{B}^{Fr} along the fracture surface which directly leads to a reduction of computational effort. Nevertheless, for precise solutions, the discretization of both domains must be adapted to the boundary value problem. Adaption of just one domain does not lead to satisfactory results. The weak and strong coupling schemes provide solutions of the same quality once similar discretizations of the domain are used throughout simulations. Similar discretizations lead to a comparable number of DoF, and effectively the non-conformal meshing strategy provides no advantage to the weak coupling. Hence the strong coupling scheme is chosen for the following numerical studies based on the efficiency of the method.

4.3 Influence of Aperture Change on Fracture Permeability

In case of hydro-mechanical investigations, the evolution of fracture aperture in time and space is directly related to the deformation state of the surrounding poroelastic matrix material and the effective permeability of the fracture domain. Since the aperture change δ_c varies with time throughout the simulation, the effective permeability of the fracture $k_{Fr}^s(\mathbf{u}(\mathbf{x}, t))$ varies accordingly, see equation (4.10). Besides the negligible convective and quadratic terms of the hybrid-dimensional formulation in the present case [208], it is of interest in which ranges it is valid to reduce the non-linear diffusion term iv) (changing fracture permeability $\delta(\mathbf{u}(\mathbf{x}, t))$ and pressure \hat{p}) to a purely linear expression by assuming a constant permeability. Reducing the model premising a rigid fracture ($\partial\delta/\partial t = 0$

Quantity	Value	Unit	Quantity	Value	Unit
Fracture domain \mathcal{B}^{Fr}					
fluid comp. β_{min}^f	$4.5 \cdot 10^{-10}$	[1/Pa]	fracture aperture δ_0	$5.0 \cdot 10^{-3}$	[m]
fracture length l^{Fr}	$1.0 \cdot 10^2$	[m]	pressure boundary posit. \hat{x}_0	0.0	[m]
pumping pressure p_0	$2.0 \cdot 10^4$	[Pa]	min. aperture change δ_{min}	$5.0 \cdot 10^{-10}$	[m]
max. aperture change δ_{max}	$5.0 \cdot 10^{-3}$	[m]			
Numerical Parameter					
time step size Δt	$1.0 \cdot 10^{-5}$	[s]	fracture discret. in \mathcal{B}^{Fr} Δx_{Fr}^{Fr}	$1.0 \cdot 10^{-2}$	[m]
evaluation time t_0	$1.0 \cdot 10^{-2}$	[s]	evaluation position \hat{x}_1	$1.0 \cdot 10^2$	[m]
number of DoF	$1.0 \cdot 10^4$	[-]			

Table 4.7: Collection of parameters used throughout numerical aperture change studies for a rigid fracture.

and $\delta(\mathbf{u}(\mathbf{x}, t)) = \delta_0$) simplifies the system of governing equations to a one-dimensional

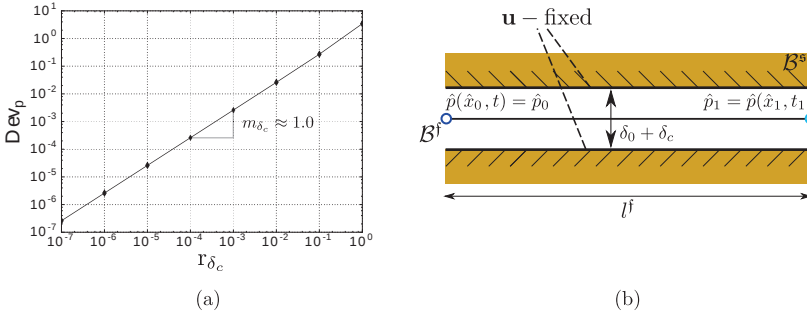


Figure 8: Investigation of fracture change influence on diffusion process in a radial fracture; (a) double logarithmic plot of pressure deviation Der_p with respect to fracture aperture change ratio r_{δ_c} , (b) model parameters and sketch of simulation domain with boundary conditions and investigation position p_1 .

decoupled problem and the hybrid-dimensional formulation is governed by terms i) and the linear formulation of term iv). The boundary value problem is displayed in fig. 8. A single fracture with a length of $l^f = 100$ m is stimulated by a pumping pressure $\hat{p} = 20$ kPa at position $\hat{x}_0 = 0.0$ m. The fracture aperture change δ_c is applied globally as $\delta = \delta_0 + \delta_c$ and deviation

$$Dev_p = \frac{\hat{p}(a, t_1, \delta_0 + \delta_c) - \hat{p}(a, t_1, \delta_0)}{\hat{p}(a, t_1, \delta_0)}, \quad (4.38)$$

is determined concerning the solution obtained with $\delta = \delta_0$. The applied numerical and material parameters are given in table 4.7. Fracture aperture changes in the limits of δ_c^{min} and δ_c^{max} are conducted to investigate their influence on the resulting pressure deviation. Eq. (4.38) is evaluated after 1000 timesteps at $t_0 = 0.01$ s and position \hat{x}_1 concerning the fracture change ratio $r_{\delta_c} = \delta_c/\delta$. The results are plotted with a double logarithmic scale shown in fig. 8 (a). As highlighted in the graph, the pressure deviation increases linearly (slope $m_{\delta_c} = 1$) with the fracture change ratio. Nevertheless, for ratios $r_{\delta_c} \leq 0.01$ the deviation is smaller than 2% when compared to the reference solution received with aperture $\delta = \delta_0$.

To strengthen the reduced prediction model a second boundary value problem is conducted using the set up introduced for validation in section 4 with identical parameters given in table 4.5 and a fluid compressibility of $\beta^f = 4.5 \cdot 10^{-10}$ Pa $^{-1}$. In contrast to the simplified rigid fracture assumption, the complexity is increased by assuming a deformable fracture and requires the hybrid dimensional formulation defined by terms i), iv) and v), coupled to the poroelastic domain. The reference case is modeled with the linear formulation of term iv) assuming a constant permeability $k_{fr}^s(\delta_0)$ throughout the simulation. This solution is then compared after 1000 time steps at $t_2 = 10.0$ s to the results calculated with the non-linear form of term iv) by assuming a aperture dependent permeability $k_{fr}^s(\mathbf{u}(\mathbf{x}, t))$. At time t_2 the maximum local aperture change within the fracture is $\delta_c^{max} = 1.81 \cdot 10^{-5}$ m which is equivalent to a ratio of 0.004. Based on the introduced prediction

model a deviation of approximately $\text{Dev}_p \approx 0.0092$ is expected. Like stated above, the conservative assumptions result in an overestimation of the aperture change influence which is confirmed by the deviation $\text{Dev}_p = 0.0039$ obtained with the hydro-mechanical model. Still, the conservative prediction model gives deviations in the same order of magnitude and is a sufficient estimator to determine whether fracture aperture changes are relevant for calculations regarding the change of fracture permeability. For small deformations ($r_{\delta_c} < 0.01$), it is reasonable to assume constant permeabilities throughout the following two-dimensional hydro-mechanical simulations. In case of large fracture deformations ($r_{\delta_c} > 0.01$) permeability changes need to be considered to reproduce the pressure state correctly.

4.4 Pressure Induced Hydro-Mechanical Response - Fracture Stimulation

Hydro-mechanical coupling of fluid-filled fractures in deformable poroelastic media includes pressure induced phenomena like the Noordbergum effect [107]. Throughout fracture stimulations, the mechanical response in the form of non-local deformations is faster than the pressure diffusion within the fracture. The volumetric change of the fracture influences the pressure state, e.g., in a borehole during well testing where inverse pressure responses can be measured. Calculating accurately the inverse pressure response poses high demands on numerical simulation techniques and will therefore be investigated in further detail to demonstrate the efficiency and accuracy of the proposed algorithms. The

Quantity	Value	Unit	Quantity	Value	Unit
Poroelastic domain \mathcal{B}^{Pe}					
intrinsic permeability k_1^s	$1.1 \cdot 10^{-19}$	[m ²]	intrinsic permeability k_2^s	$1.1 \cdot 10^{-5}$	[m ²]
fluid comp. β^f	$4.5 \cdot 10^{-10}$	[1/Pa]	sample length l^{pe}	$1.5 \cdot 10^3$	[m]
sample height h^{pe}	$1.0 \cdot 10^3$	[m]			
Fracture domain \mathcal{B}^{Fr}					
fluid comp. β_{min}^f	$4.5 \cdot 10^{-10}$	[1/Pa]	fracture aperture δ_0	$5.0 \cdot 10^{-4}$	[m]
fracture <i>A</i> length $l_{A,l}^{Fr}$	$7.0 \cdot 10^2$	[m]	fracture <i>B</i> length $l_{B,l}^{Fr}$	$2.0 \cdot 10^2$	[m]
fracture <i>B</i> height $l_{B,h}^{Fr}$	$1.0 \cdot 10^2$	[m]	fracture discret. Δx^{fr}	$1.0 \cdot 10^{-2}$	[m]
Numerical Parameter					
time step size Δt	$1.0 \cdot 10^{-2}$	[s]	number of DoF	$2.3 \cdot 10^5$	[-]

Table 4.8: Collection of parameters used throughout hydro-mechanical response studies.

validated strongly coupled hydro-dimensional formulation is applied to a fracture stimulation problem with the boundary conditions shown in fig. 9. Corresponding material parameters are given in table 4.8. Two different phenomena are investigated. Besides the fluid pressure evolution within the main fracture *A* (inverse pressure response), shown in fig. 9 (b), the pressure response within T-shape fracture *B* induced by the deformation of the surrounding medium, displayed in fig. 10, are analyzed. Note that the pressure \hat{p} in the graphs correspond to a pressure difference concerning an initial geostatic pressure. The fluid within the surrounding porous rock matrix \mathcal{B}^{Pe} and fracture \mathcal{B}^{Fr} possesses a compressibility of $\beta^f = 4.5 \cdot 10^{-10} \text{ Pa}^{-1}$. A high aspect fracture with an aperture of

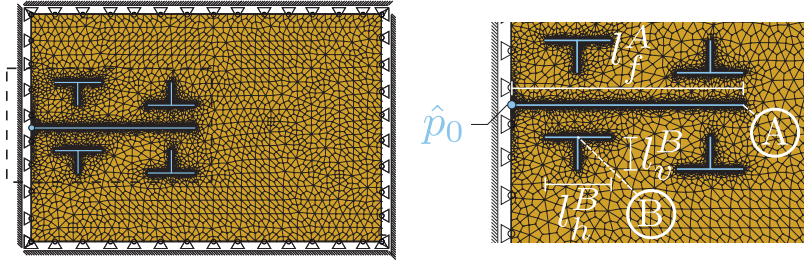


Figure 9: Discretization and boundary conditions used for the hydro-mechanical response studies.

$\delta_0 = 5.0 \cdot 10^{-4}$ m is modeled. Examination of leak-off and its influence on the pressure response within the fluid-filled fracture is studied by assuming two different extreme cases of permeabilities $k_1^s = 1.1 \cdot 10^{-19}$ m² and $k_2^s = 1.1 \cdot 10^{-5}$ m² for the surrounding poroelastic matrix.

Focusing on the pressure distribution along fracture *A* the inverse pressure is evident at time step t_0 . For both permeabilities of the surrounding poroelastic matrix, the pressure decreases when compared to the initial geostatic pressure due to non-local deformation of the fracture. For permeability k_2^s the inverse response is less strong since the leak-off into the surrounding high-permeable medium leads to a smearing effect on the pressure distribution within the fluid filled fracture and is noticeable for an advanced time step t_1 where both pressure distributions differ evidently. The pressure state within a fracture surrounded by a medium with a lower permeability k_1^s is ahead of the fluid pressure within a fracture surrounded by more permeable (permeability k_2^s) porous matrix. Leak-off harms the diffusion process within the fracture which results in a lower pressure state. Pressure changes in the T-shape fracture *B* are not directly induced by the pressure Dirichlet boundary conditions, but mainly through the deformation triggered by the pressure change within fracture *A*. Most interesting is that the Noordbergum effect causes a local closing of main fracture *A* at t_0 that translates in an opening of the horizontal part of T-Shape fracture *B*. The volume change of the horizontal fracture induces a negative pressure response. Due to the geometrical nature of a T-shape fracture, once the horizontal part opens up, the vertical fracture part closes, and a pressure rise along its direction is notable. At time t_1 the advanced fluid pressure along main fracture *A* leads to an opening orthogonal to its direction that causes a closing of the horizontal part of T-shape fracture *B*. Due to the negative volume change a pressure rise results. The vertical part is influenced by the pressure rise and opens up slightly. The positive volume change harms the pressure diffusion process along the vertical direction. Hence the pressure level is lower than its counterpart in horizontal direction. Again for different permeabilities the pressure levels differ for t_1 . The leak-off into the surrounding medium reduces the pressure within fracture *B*.

Reproduction of the pressure-induced hydro-mechanical phenomena within a fluid-filled fracture through passive (deformation) and active (pumping) stimulation using the hybrid-

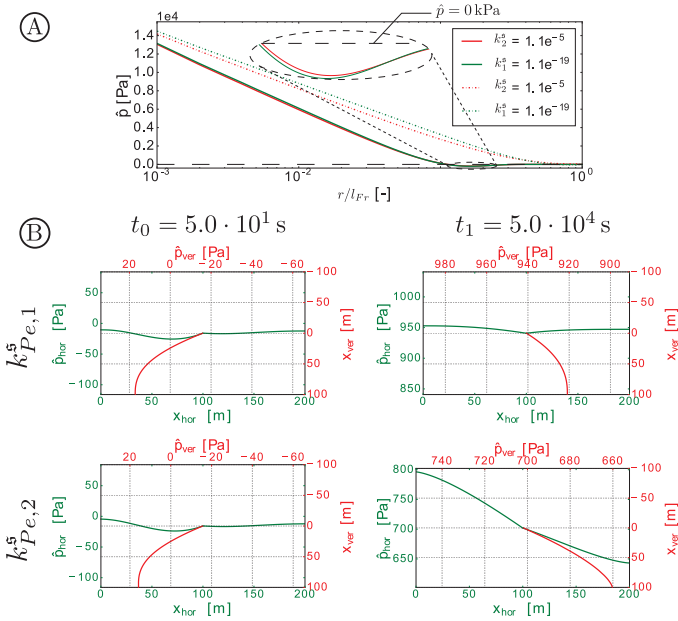


Figure 10: Semi-logarithmic pressure distribution along fracture A for time steps $t_0 = 5.0 \cdot 10^1$ s and $t_1 = 5.0 \cdot 10^4$ s are displayed along with pressure distributions in horizontal (green) and vertical (red) direction within T-shape fracture B for two differing permeabilities of the surrounding matrix. The pressure solutions in fracture A obtained at time t_0 are plotted with plane lines and solutions obtained at t_1 with dashed lines.

dimensional formulation has been numerically investigated by the introduced boundary value problem. The formulation is capable to model pumping experiments and to reproduce the key phenomena concerning hydro-mechanical coupling induced by pressure fluctuations for radial symmetric three-dimensional geometries.

4.5 Deformation Dependent Permeability - Three-Dimensional Fracture Stimulation

Large relative aperture changes in high aspect ratio fractures occur even for small absolute deformations. It is recommended to take aperture dependent permeabilities into account throughout pressure diffusion simulations once $r_{\delta_c} > 0.01$ (see 4). The aperture change is directly related to the pressure state and the geometrical stiffness of the fracture. Especially in three dimensions, the stiffness of fractures influences their opening and closing during pressure stimulations resulting in preferential flow paths due to inhomogeneous permeabilities. This numerical study investigates the deviation of pressure solutions of a

Quantity	Value	Unit	Quantity	Value	Unit
Poroelastic domain \mathcal{B}^{Pe}					
intrinsic permeability k_{pe}^s	$1.1 \cdot 10^{-19}$	$[\text{m}^2]$	fluid comp. β^f	$4.5 \cdot 10^{-10}$	$[\text{1/Pa}]$
poroel. domain length in l_{e_1}	$4.0 \cdot 10^2$	$[\text{m}]$	poroel. domain length in l_{e_2}	$2.0 \cdot 10^2$	$[\text{m}]$
poroel. domain length in l_{e_3}	$4.0 \cdot 10^2$	$[\text{m}]$	cross-section area $A_{\Gamma_1^{con}}$	$4.2 \cdot 10^{-4}$	$[\text{m}^2]$
connection cross-section $A_{\Gamma_2^{con}}$	$2.5 \cdot 10^{-5}$	$[\text{m}^2]$			
Fracture domain \mathcal{B}^{Fr}					
fluid comp. β_{min}^f	$4.5 \cdot 10^{-10}$	$[\text{1/Pa}]$	fracture aperture δ_0	$5.0 \cdot 10^{-4}$	$[\text{m}]$
fracture domain length $l_{e_1}^{Fr}$	$2.0 \cdot 10^2$	$[\text{m}]$	fracture domain length $l_{e_1}^{Fr}$	$1.6 \cdot 10^2$	$[\text{m}]$
fracture center height $c_{e_1}^{Fr}$	$2.0 \cdot 10^2$	$[\text{m}]$	fracture center distance $c_{e_3}^{Fr}$	$2.0 \cdot 10^2$	$[\text{m}]$
Numerical Parameter					
time step size Δt	$5.0 \cdot 10^3$	$[\text{s}]$	error tolerance ϵ_{max}^{NL}	$1.0 \cdot 10^{-6}$	$[-]$
DoF	$4.3 \cdot 10^5$	$[-]$			

Table 4.9: Collection of parameters used throughout deformation dependent permeability studies. Note that the cross-sections $A_{\Gamma_1^{con}}$ and $A_{\Gamma_2^{con}}$ were determined based on the initial fracture aperture δ_0 . ϵ^{NR} defines the error between iterations of the Newton-Raphson scheme and $\epsilon^{NR} < \epsilon_{max}^{NR}$ convergence criterion throughout the non-linear simulation.

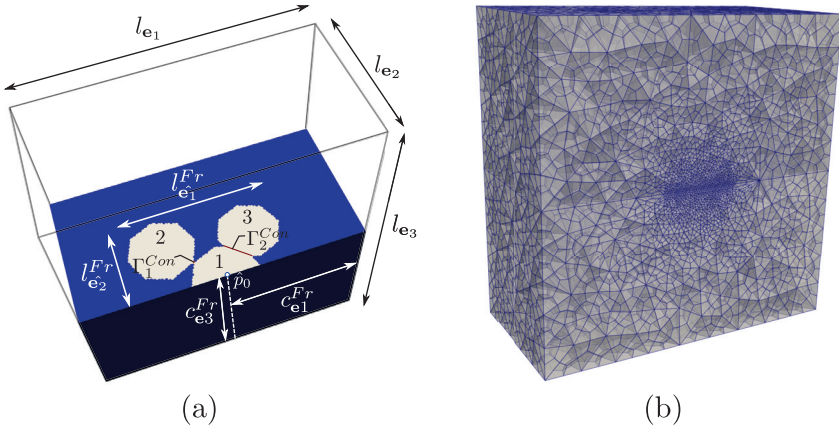


Figure 11: Sketch of fracture (white) and porous domain (blue) is displayed in (a). Discretization of the three-dimensional geometry is shown in (b).

constant compared to an aperture dependent permeability for three connected fractures in three dimensions. Parameters of the simulation are given in table 4.9, and the geometry along with the discretization of the boundary value problem is shown in fig. 11. The fractures are placed in the same plane, where fracture 1 is connected to fracture 2 and 3 via cross-sections Γ_1^{Con} and Γ_2^{Con} .

The displacement DoF on the poroelastic domain's boundaries are fixed in the direction normal to its surface and pressure \hat{p}_0 is induced in the center of fracture 1 on a length of 1.5 m. It is supposed that the apparent difference between cross-section areas $A_{\Gamma_1^{con}}$

and $A_{\Gamma_2^{Con}}$ initiates a dominant flow from fracture 1 into fracture 3 rather than into fracture 2. Additionally, since cross-section Γ_2^{Con} weakens the surrounding geometric stiffness stronger than Γ_1^{Con} higher aperture changes and hence higher permeabilities in the direction of fracture 3 are expected.

The pressure states at times $t_0 = 7.5 \cdot 10^5$ s, $t_1 = 4.0 \cdot 10^6$ s and $t_2 = 8.25 \cdot 10^6$ s for pressure values \hat{p} obtained by a constant and an aperture dependent permeability along with the permeability distribution are given in fig. 12. For t_1 the pressure evolution takes mainly place within fracture 1. For both pressure distributions the inverse pressure response can be examined; for the deformation dependent permeability stronger than for the constant permeability solution. Even at an early stage, an apparent difference between both solutions can be found due to much higher permeabilities close to the pressure stimulation point. The constant permeability measures $k_c^s = 8.3 \cdot 10^{-12}$ m² calculated based on δ_0 and is by the factor of approx. 10 lower than the deformation dependent permeability $k_{Fr,up}^s = 8.2 \cdot 10^{-11}$ m² around the point of pressure initiation. Nevertheless, at t_0 no statement about the influence of the permeability distribution on the flow direction towards one of the connected fractures can be made since the pressure solution evolved radially within fracture 1. For time t_2 the pressure solutions differ vastly. The deformation dependent permeability already shows a clear trend towards a higher permeability in the direction of fracture 3. This might influence the flow path decisively. Nevertheless, since the pressure evolution for the constant permeability calculations is still limited to the region of fracture 1, no statement about the influence of the aperture dependent permeability on the effective flow is possible. The maximum permeability value is approx. 40 times higher than the constant permeability. For time t_3 the pressure diffusion advanced far into fracture 3 and barely into fracture 2 for the non-linear case. The solutions obtained with a constant permeability shows a slightly faster pressure distribution into fracture 3, but the difference is not evident. The difference of the pressure state of fracture 2 and fracture 3 is much higher for the calculations using a deformation-dependent permeability than for calculations with constant permeability and shows its influence on the pressure evolution. The absolute pressure difference between both solutions is explicit since the maximum permeability value is 60 times higher for the aperture dependent compared to the constant permeability value. A maximum number of 6 iterations were needed for the Newton-Raphson scheme to converge for the non-linear case in the first two time-steps. Throughout the rest of the simulation, convergence was reached within 3 to 5 iterations. This study has shown the influence of aperture dependent permeabilities for the case of substantial aperture changes. Strongly differing solutions in the diffusion time and for the diffusion direction motivate the non-linear formulation of the permeability throughout simulations containing large aperture changes.

5 Technical Details

Implementation work of the strong coupling scheme includes the extension of the Dune-PDELab package to lower dimensional element integrations within the DUNE framework [15]. Slight modifications to the assembly procedure of the global system and introduction of new local operators on element level guarantee the maintenance of the high computa-

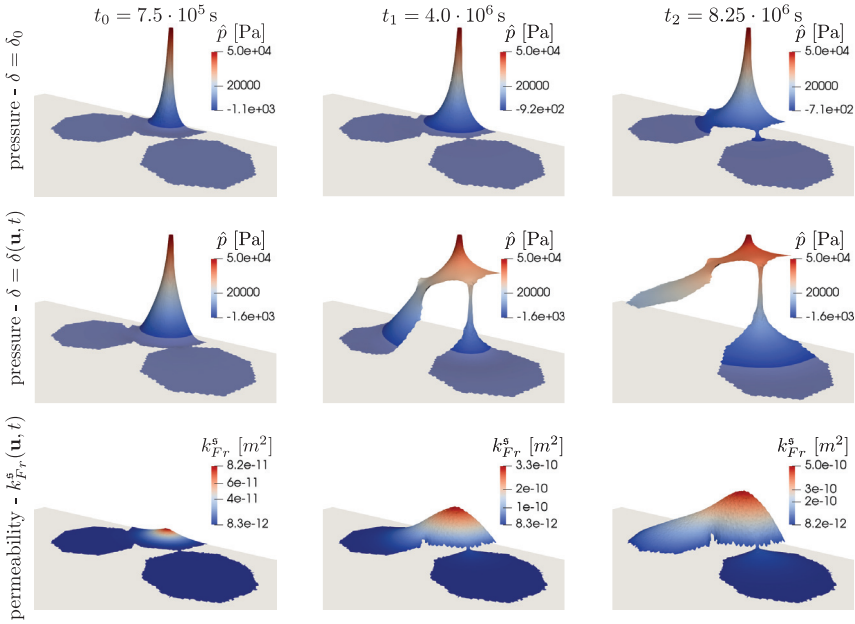


Figure 12: Plots of the pressure \hat{p} obtained with a constant and a deformation dependent permeability along with a distribution of the displacement dependent permeability are shown for three different times. Pressure \hat{p} is the pressure difference concerning an initial geostatic pressure. Note that the grey isosurface in the pressure plot represents the pressure difference $\hat{p} = 0$ Pa and in the permeability plots the initial permeability obtained with δ_0 .

tional efficiency of the C++ (template metaprogramming) based package. Non-conformal mesh calculations have been implemented into the FEniCS environment [6]. Both weak coupling schemes, namely the fixed-strain and fixed-stress strategy have been embedded in a flexible Python-based framework that allows interaction of discretizations of different dimensions.

Fracture discretization is challenging especially when interface elements are introduced. Hence the GMSH API [71] has been consulted to generate an environment that allows mesh creation of fracture networks including the generation of interface elements.

6 Conclusions

This work focused on the numerical formulation and validation of methods suitable to solve hydro-mechanical phenomena of compressible fluids using the proposed hybrid-dimensional formulation. An implicit weak coupling scheme, naturally able to perform

non-conformal mesh calculations and a strong coupling scheme in the form of interface elements were introduced. Validation of both methods based on Biot's formulation showed the ability to reproduce hydro-mechanical phenomena of interest like the Noordbergum effect. Further advantages and disadvantages of both methods were studied. The fixed-strain scheme has been proven to be effective for high fluid compressibilities only. An error evolution for different fine discretization of fluid and porous domain has been investigated, and references for the preferred coupling scheme based on the relative error were given. The strong coupling and fixed-stress scheme were able to solve stiff systems with low fluid compressibility. Implementation of the strong coupling scheme is intuitive since an existent FEM framework requires small modifications for the integration of interface elements only. Since a displacement-pressure-formulation of the surrounding poroelastic material has been conducted, the same global assembly matrix is used for the hybrid-dimensional interface elements. The weak coupling and especially implementation of non-conformal mesh coupling requires more implementation work.

Pressure induced boundary value problems have been performed for different material parameters of the surrounding porous matrix in two and three dimensions. Both stimulation types showed the ability of the strong coupling scheme to solve research questions in the field of fractured porous media even for complex fracture geometries such as well testing and non-linear three-dimensional simulations. For large changes of the aperture, the importance of a deformation-dependent permeability throughout simulations have been shown. Both proposed methods in combination with the hybrid-dimensional formulation are capable of modeling high aspect ratio fractures and reproduce hydro-mechanical effects including leak-off where modeling approaches, that neglect the influence of fracture deformation would fail.

Investigations into the opening of fractures during hydraulic testing using a hybrid-dimensional flow formulation

Patrick Schmidt, Holger Steeb, Jörg Renner, EES - Environmental Earth Sciences, August 2021, DOI: 10.1007/s12665-021-09767-4

Abstract We applied a hybrid-dimensional flow model to pressure transients recorded during pumping experiments conducted at the Reiche Zeche underground research laboratory to study the opening behavior of fractures due to fluid injection. Two distinct types of pressure responses to flow-rate steps were identified that represent radial-symmetric and plane-axisymmetric flow regimes from a conventional pressure-diffusion perspective. We numerically modelled both using a radial-symmetric flow formulation for a fracture that comprises a non-linear constitutive relation for the contact mechanics governing reversible fracture surface interaction. The two types of pressure response can be modelled equally well. A sensitivity study revealed a positive correlation between fracture length and normal fracture stiffness that yield a match between field observations and numerical results. Decomposition of the acting normal stresses into stresses associated with the deformation state of the global fracture geometry and with the local contacts indicates that geometrically induced stresses contribute the more the lower the total effective normal stress and the shorter the fracture. Separating the contributions of the local contact mechanics and the overall fracture geometry to fracture normal stiffness indicates that the geometrical stiffness constitutes a lower bound for total stiffness; its relevance increases with decreasing fracture length. Our study demonstrates that non-linear hydro-mechanical coupling can lead to vastly different hydraulic responses and thus provides an alternative to conventional pressure-diffusion analysis that requires changes in flow regime to cover the full range of observations.

1 Introduction

Estimation of a reservoir's effective hydraulic properties requires a consistent analysis of experimentally determined pressure and flow transients [60, 133]. For individual fractures, simple analytical models for pressure-diffusion have been applied when their intersection with boreholes classified them as axial or radial [25, 92, 125, 126]. Analytical models based on solutions of the diffusion equation for constant flow-rate tests document distinct differences in pressure response for one-dimensional and radial flow associated with axial and radial fractures, respectively. Rocks with a dense array of randomly oriented fractures may justify their treatment as porous media, leading to radial flow, too. Mathematically, the full range of responses can be addressed by regarding the dimension of the flow to be a parameter [13]. However, hydro-mechanical phenomena, such as reverse water-level fluctuations in distant monitoring wells [107, 162] or insensitivity of pressure responses to increases in flow-rates, so called jacking [152], cannot be reproduced by pressure diffusion models and result in inaccurate approximations of the effective fracture characteristics [33,

131, 206]. Despite the growing number of treatments of hydro-mechanical coupling [38, 72, 73, 131, 177], the understanding of the influence of basic geometrical and mechanical properties of fractures on their hydraulic response to flow-rate or pressure perturbations remains limited; a critical obstacle to, e.g., the development of geothermal energy provision from petrothermal reservoirs.

Non-local fracture deformations triggered by perturbations of the fluid pressure along a fracture induce changes in permeability and volume of fractures with a direct impact on flow and storage characteristics and therefore on how the perturbations evolve with time and spread in space [19, 151, 206, 207]. Accounting for hydro-mechanical interaction throughout numerical fitting of pressure and flow-rate transients is a non-trivial task and requires consistent evaluation of the balance equations in an efficient manner. Evaluation of fracture opening or closing in response to a perturbation of the equilibrium state requires considering the acting normal stresses owing to their control on the mechanical interaction between the fracture surfaces in contact. For example, large numbers of single Hertzian contacts have been invoked to characterize the mechanical interaction of two mated fracture surfaces [40, 77, 197]. Responses of these contacts to changes in shear and normal stress result in changes of the effective fracture aperture [12, 75]. Fracture opening does not depend on local contact mechanics alone but also on the geometrical stiffness of the fracture [131]. Despite the importance of fracture stiffness for the interpretation of pumping operations, little work has been devoted to decompose these two contributions.

Here, we analyze pressure transients from pumping tests conducted at the Reiche Zeche underground research laboratory, where the injection borehole penetrates a fractured rock. From a classical pressure-diffusion perspective, the hydraulic responses of the tested intervals mimic that of either radial-symmetric (positive-tangent group) or axial-symmetric (pressure-plateau group) fractures. Yet, logging and impression-packer results do not support this simple association of fracture geometry and hydraulic response. We employ a hydro-mechanical model considering radial-symmetric conditions, as applying for a radial fracture following a monolithic numerical implementation [177] to study the origin of the distinct pressure transients. Specifically, we studied the sensitivity of the hydro-mechanical model to the variation of characteristic fracture properties to identify best fits to the field data and the interdependence between the characteristic fracture properties.

2 Test site and experimental approach

2.1 The Reiche Zeche underground research laboratory

As part of the research program of STIMTEC, a cooperative project investigating the creation and growth of fractures in crystalline rocks to develop and optimise hydraulic STIMulation TECHniques [50, 156], we performed hydraulic tests in the research mine Reiche Zeche (Rich Mine), Freiberg (Germany). The average depth below surface is about 130 m at the test site. The foliation of the fine- to medium-grained biotite gneiss dips 5 to 15° in south-east-direction. The gneiss is penetrated by fairly randomly oriented joints with an average separation of several decimeters. Fracture counting on retrieved cores yield 4.4 ± 2.5 1/m, but intact sections with a length of 1 to 2 m occur. In the test volume

of about $40 \text{ m} \times 50 \text{ m} \times 20 \text{ m}$, two to three steeply dipping, east-west trending damage zones were identified with a variable width between decimeters and a few meters.

The injection borehole BH10 with a length of 63 m and a radius of 0.038 m has a strike of N31°E and a dip of 15° from the horizontal and thus the borehole axis intersects the foliation at an angle of 20 to 30°. Ultrasonic transmission of the test volume as well as laboratory experiments on cores revealed a pronounced anisotropy in elastic parameters. Ultrasonic velocities are up to 20 % faster in the direction of the foliation than perpendicular to it. Dynamic and static Young's moduli in the two directions differ by 10 to 15 %, with the low modulus observed for loading perpendicular to the foliation [2].

2.2 Experimental procedure

Experiments were performed with a double-packer probe of Solexperts GmbH, Bochum, Germany, consisting of two inflatable packers isolating an injection interval of about 0.7 m length. The probe is equipped with uphole and downhole pressure gauges, and an uphole flowmeter, all sampled with 0.2 s. Flowrates measured uphole, i.e., outside of the borehole at the pump, were corrected for the storage capacity of the injection system to derive the true flow into the rock. The storage capacity was determined in a calibration experiment, for which the probe was inserted in a hollow steel cylinder.

The uniformly applied pumping protocol comprised a sequence consisting of a) injection (with rates of 2–10 l/min) until breakdown pressure was reached, the fracking, and subsequent shut-in phase, b) three repeat injections, the refracs, with moderate rates of 3 l/min at maximum, each again followed by a shut-in phase, and c) step-rate tests involving several phases of injection with constant flow rates, successively increased from below 1 l/min to about 5 l/min. The pressure response in these step-rate tests constrains the jacking pressure, the fluid pressure at which the fracture(s) intersecting the borehole wall open. Opening is indicated by a significant increase in injectivity, the ratio between flow-rate and pressure. Impression-packer tests were performed after the entire pumping sequence to document fracture traces on the borehole wall.

2.3 Intervals and selected data sets

The data used here represent part of the results of the step-rate tests performed in six intervals at depths of 24.6 m, 40.6 m, 49.7 m, 51.6 m, 55.7 m, and 56.5 m. Logging before and after fluid injection with an acoustic televiewer and the impression-packer tests revealed pre-existing and induced fractures with a range of orientations (Table 4.10). We consider the circumferential fracture traces to represent radial fractures even though they do not intersect the borehole axis at a right angle as strictly required. In addition, the traces classified as “axial” do not match this end-member geometry in a strict sense but their tilt to the borehole axis is typical of en-echelon hydro-fractures occurring in boreholes that do not follow a principal stress axis [226]. Actually, the short traces of interval 51.6 m are not well constrained at all. Furthermore, it is impossible to associate the observed pressure transients with a specific fracture trace when intervals exhibit multiple traces. This situation is not unusual but representative of what an interpreter typically faces

when tests are performed in crystalline rocks.

Table 4.10: Interval characteristics.

depth (m)	label [†]	$t_{1/3}^p$ ‡ (s)	$t_{1/2}^{si}$ † (s)	orientation of fracture traces
24.6	M_a^t	$\gtrsim 433$	$\gg 226$	1 parabola-shaped, induced
40.6	M_b^t	10	>170	1 pre-existing circumferential; 2 axial, induced
49.7	M_b^p	24	8	1 pre-existing, circumferential; 2 parabola-shaped, pre-existing; 1 pair axial, induced
51.6	M_a^p	7	3	several short axial
55.7	M_c^t	6	28	1 pre-existing circumferential; 1 pair axial, induced
56.5	M_c^p	3	33	1 pre-existing circumferential; 1 axial, induced

† classification of data set (Figure 1)

‡ time it took for a pressure pulse to decay by 1/3 before the stimulation phase

† time it took for pressure to decay by 1/2 during the shut-in phase after the step-rate test

We selected three to five of the first low flow-rate steps for the six intervals (Table 4.10, Figure 1). The selection aimed to restrict to pressure and flow-rate couples, for which the proposed elastic model most likely applies. For some intervals, seismic activity was observed and therefore its absence during flow-rate steps could be used as criterion for “elastic” response. The pressure transients induced by the step-wise increase of flow rate differ for the six intervals. We distinguish two groups of pressure evolution during a step. Pressure responses with flat tangents are evident in data sets M_a^p to M_c^p , a subset of our data that we will address as “pressure-plateau group”. In contrast, the data sets M_a^t to M_c^t exhibit continuously increasing pressure, the “positive-tangents group”. For either group, however, the sensitivity of pressure level to flow rate diminishes with increasing flow rate, the observation interpreted as jacking.

3 Numerical method

When the aim is characterization rather than modification, hydraulic testing of fractures is performed below critical pressures for fracture extension, e.g., indicated by a decrease in injection pressure during constant-rate pumping. Breakdown is often related to tensile hydro-fracturing or when occurring over extended time periods or in a succession of small drops probably related to shearing events, either possibly accompanied by characteristic seismic activity. For tests performed at moderate injection pressures, fracture length can thus be treated constant and effects of changes in shear stress and therefore shear stiffness can be neglected. Fractures induced by hydraulic fracturing are expected to be oriented normal to the direction of the least principal (compressive) stress [93] so that they intrinsically fulfill the assumption of negligible shear stress. In the context of hydraulic characterization of fractures, their contact mechanics may thus be reduced to an account of their normal stiffness [145]. Hence, we apply a hydro-mechanical model considering the constitutive relation of normal contact following a monolithic numerical implementation

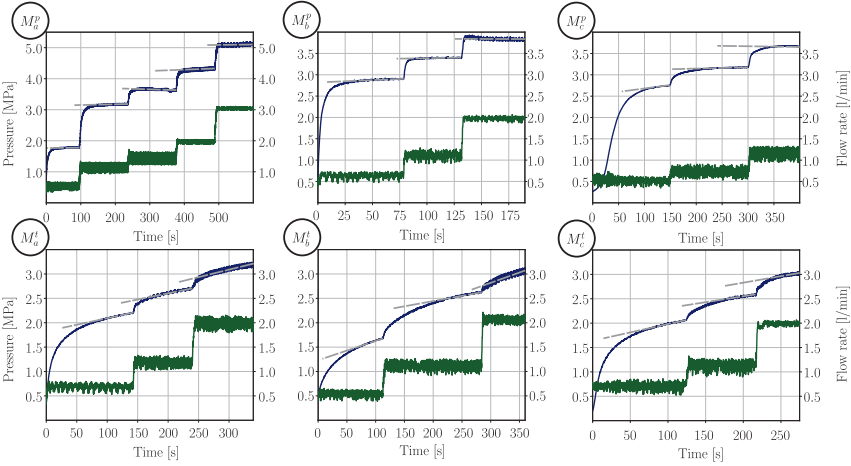


Figure 1: The step-rate test data selected from the six intervals is divided in the pressure-plateau group labeled with M^p and the positive-tangent group labeled with M^t . The dark blue lines represent the recorded pressure data, the dark green lines the step-wise increasing flow-rate, and the dotted grey lines represent tangents to the pressure transient at the end of a flow-rate step.

[177] for the numerical determination of characteristic fracture parameters, initial width or aperture δ_0^{hyd} and normal stiffness parameter E_{Fr} . The third characteristic parameter, the fracture length l_{Fr} , is an element of the modelled fracture-domain discretization. The model's central aspects are recapitulated in the following, before details of the performed parameter search are presented.

3.1 Governing equations

Flow processes of weakly-compressible, viscous fluids in high-aspect ratio fractures motivate the assumption of creeping flow conditions between two locally parallel plates, for which the balance of momentum reduces to a Poiseuille-type formulation [206, 216], i.e., the relative fluid velocity \mathbf{w}_f is proportional to the pressure gradient $\text{grad } p$. In our continuum description, the associated cubic law

$$\mathbf{w}_f = -\frac{(\delta^{\text{hyd}}(\mathbf{u}))^2}{12 \eta^{lR}} \text{grad } p =: -\frac{k_{Fr}^5}{\eta^{lR}} \text{grad } p \quad (4.39)$$

is locally evaluated in the fracture domain Γ^{Fr} , i.e., on the level of a material point $\mathcal{P}(\mathbf{x}, t)$, where \mathbf{x} denotes its position vector, $\mathbf{u}(\mathbf{x}, t) = \mathbf{x} - \mathbf{X}$ the fracture deformation relative to the reference position vector \mathbf{X} , t time, and η^{lR} the dynamic fluid viscosity. The locally evaluated, deformation-dependent permeability is identified as $k_{Fr}^5(\mathbf{x}, t) = (\delta^{\text{hyd}})^2/12$ considering $\delta^{\text{hyd}}(\mathbf{u}(\mathbf{x}, t))$ to be the local effective hydraulic fracture aperture.

The hybrid-dimensional formulation is obtained by inserting the balance of momentum into the balance of mass, derived for a deformable fracture. The outcome of a dimensional analysis of the resulting partial differential equations suggests that quadratic and convective terms are negligible [206–208]; the accordingly reduced hydro-mechanical governing equation reads

$$\underbrace{\frac{\partial p}{\partial t}}_{\text{i)}} - \underbrace{\frac{(\delta^{\text{hyd}})^2}{12 \eta^{\text{fR}} \beta^{\text{f}}}}_{\text{ii)}} \text{div}(\text{grad } p) + \underbrace{\frac{1}{\delta^{\text{hyd}} \beta^{\text{f}}}}_{\text{iii)}} \frac{\partial \delta^{\text{hyd}}}{\partial t} = \underbrace{\frac{q_{lk}}{\delta^{\text{hyd}} \beta^{\text{f}}}}_{\text{iv)}}, \quad (4.40)$$

comprising a transient i), a diffusion ii), a coupling iii), and a leak-off term iv), where β^{f} denotes the fluid compressibility, and q_{lk} leak-off, i.e., the flow-rate from the fracture into the surrounding rock mass. The deformation dependent effective fracture aperture $\delta^{\text{hyd}}(\mathbf{u}(\mathbf{x}, t))$ contributes to the characteristic diffusion process by term ii) and to volume changes of the fluid domain by term iii), which strongly couples the solution of the fracture-flow domain to the deformation state of the surrounding matrix.

The rock matrix surrounding the fracture might be treated by purely elastic or by biphasic poro-elastic, e.g., Biot’s theory [20], formulations depending on the application in mind. For the typically substantial difference in the characteristic times of pressure diffusion in the fracture and in a surrounding crystalline rock, a biphasic description results in oscillations of the pore-pressure solution, when time discretization and material properties are chosen in the relevant range to model the conducted field experiments. Hence, this work refrains from treating the matrix by Biot’s coupled poro-elastic theory but approximates the material behavior with Gassmann’s low-frequency result [66, 127].

The intact gneiss exhibits a permeability $< 10^{-20} \text{ m}^2$ [2]. Thus, leak-off from a fracture, into which fluid is injected from a borehole, into the “surrounding” is controlled by its intersection with other fractures. The hydraulic testing in BH10 revealed that the pre-existing fractures in the gneiss exhibit vastly variable hydraulic properties, as for example evidenced by the results of the pressure-pulse tests (Table 4.10). We thus face a range of possible scenarios for the induced or pre-existing fractures intersecting the borehole. They may intersect only poorly permeable pre-existing fractures or linking up with a highly permeable pre-existing fracture. We consider either scenario to be suitable for an approximate description that neglects leak-off. For the second scenario, our modeling will simply gain the equivalent properties of a single fracture, since a variation of properties along a fracture is not tackled and thus a distinction of “individual” fracture segments composing a conduit is not possible. Neglecting leak-off likely overestimates “effective” length because all of the injected fluid volume has to be stored in the fracture. Applying a single fracture model with fixed geometry to the encountered spectrum of fractures (Table 4.10) intends to test the versatility of the model and to determine equivalent fracture properties in a consistent way.

3.2 Constitutive relations

Traditionally, normal contact models are expressed in terms of fracture deformation relative to the position corresponding to the first, stress-free contact of the two fracture

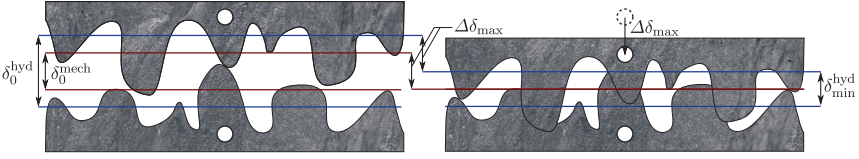


Figure 2: Initial and maximum deformation state of two fracture surfaces in contact for $s_0 > 1$ and $\delta_{\min}^{\text{mech}} = 0$. The preferential direction of the flow q is assumed to be normal to the sketched cross section of the fracture. Effective hydraulic and mechanical aperture represent the averaged local quantities on the continuum scale.

surfaces, describing fracture closing by positive deformation values [12, 70]. For the response of the fracture to changes in normal stress, we use a modified non-linear elastic constitutive relation based on the model proposed by Gens *et al.* (1990) and Segura & Carol (2008)

$$\sigma_N^{\text{FR}} = E^{\text{FR}} \frac{U^e}{U^{\text{max}} - U^e}, \quad (4.41)$$

that characterizes the normal elastic deformation U^e of an interface with two parameters, the initial stiffness at vanishing normal stress, E^{FR} , and the maximum displacement for infinite stress U^{max} . To be consistent with the governing flow eq. (4.12), we formulate (4.41) in terms of relative aperture changes

$$\begin{aligned} U^e &= -(\delta^{\text{hyd}} - \delta_0^{\text{hyd}}) = -(\delta^{\text{mech}} - \delta_0^{\text{mech}}) = -\Delta\delta, \\ U^{\text{max}} &= -\Delta\delta_{\text{max}} = -(\delta_{\min}^{\text{mech}} - \delta_0^{\text{mech}}), \end{aligned} \quad (4.42)$$

where the fracture deformation U^e is defined as changes of the effective hydraulic and mechanical aperture δ^{hyd} and δ^{mech} relative to their initial values δ_0^{hyd} and δ_0^{mech} , respectively. The maximal deformation U^{max} is defined with respect to the difference between the minimal mechanical fracture $\delta_{\min}^{\text{mech}}$, approached for infinite normal stress, and the initial mechanical aperture $\delta_0^{\text{mech}} > \delta_{\min}^{\text{mech}}$ (Figure 2). Neither absolute values of nor changes in mechanical and hydraulic apertures of fractures do have to coincide; particularly true once contact is established and the effective values of these aperture measures strongly depend on contact details and percolation characteristics in the fracture plane [146]. To account for differences in deformation-induced changes of the mechanical and hydraulic fracture properties, we introduce the dimensionless parameter s_0 . The parameter defines a relative deviation $\delta_0^{\text{mech}} = \delta_0^{\text{hyd}}/s_0$ of the initial mechanical aperture δ_0^{mech} from the initial hydraulic aperture δ_0^{hyd} . For $s_0 = 1$ the initial hydraulic aperture coincides with the initial mechanical aperture, $\delta_0^{\text{mech}} = \delta_0^{\text{hyd}}$ and the minimal mechanical aperture becomes equivalent to the minimal hydraulic aperture $\delta_{\min}^{\text{mech}} = \delta_{\min}^{\text{hyd}}$. Requiring $s_0 > 1$ ensures $\delta_{\min}^{\text{hyd}} > \delta_{\min}^{\text{mech}}$. The resulting hydraulic and mechanical fracture apertures are then expressed as

$$\begin{aligned} \delta^{\text{hyd}} &= \delta_0^{\text{hyd}} + \Delta\delta, \\ \delta^{\text{mech}} &= \delta_0^{\text{hyd}}/s_0 + \Delta\delta. \end{aligned} \quad (4.43)$$

Inserting (4.43) into (4.42) and then into (4.41) gives

$$\sigma_{\text{N}}^{\text{Fr}} = -E^{\text{Fr}} \frac{\Delta\delta}{\left(\frac{\delta_0^{\text{hyd}}}{s_0} + \Delta\delta\right) - \delta_{\text{min}}^{\text{mech}}} . \quad (4.44)$$

In principle, coupled hydro-mechanical simulations of deformable fractures require to numerically determine the equilibrium state of a fracture before the perturbation of its mechanical state, here associated with the pumping operations. Instead, we reformulate (4.44) using the aperture $\delta_{\text{eq}}^{\text{mech}} = \delta_{\text{eq}}^{\text{hyd}}/s_0$ that reflects the unperturbed in-situ normal stresses $\sigma_{\text{N,eq}}^{\text{Fr}}$, where $\delta_{\text{eq}}^{\text{hyd}}$ is the hydraulic equilibrium aperture:

$$\begin{aligned} \Delta\sigma_{\text{N}}^{\text{Fr}} &= \sigma_{\text{N}}^{\text{Fr}} - \sigma_{\text{N,eq}}^{\text{Fr}} \\ &= -E^{\text{Fr}} \left[\frac{\Delta\delta}{\left(\frac{\delta_0^{\text{hyd}}}{s_0} + \Delta\delta\right) - \delta_{\text{min}}^{\text{mech}}} - \frac{\left(\delta_{\text{eq}}^{\text{mech}} - \frac{\delta_0^{\text{hyd}}}{s_0}\right)}{\left(\delta_{\text{eq}}^{\text{mech}} - \frac{\delta_0^{\text{hyd}}}{s_0}\right) - \delta_{\text{min}}^{\text{mech}}} \right] , \quad (4.45) \end{aligned}$$

i.e., we shift the reference state of the fracture to the in-situ stress level, the mechanical equilibrium state. Simple manipulations yield the relation in its implemented form by introducing the normal stiffness parameter of the equilibrium state $E_{\text{eq}}^{\text{Fr}}$ in a second step

$$\begin{aligned} \Delta\sigma_{\text{N}}^{\text{Fr}} &= - \left[E^{\text{Fr}} \frac{\frac{\delta_0^{\text{hyd}}}{s_0} - \delta_{\text{min}}^{\text{mech}}}{\delta_{\text{eq}}^{\text{mech}} - \delta_{\text{min}}^{\text{mech}}} \right] \frac{\Delta\delta_{\text{eq}}}{\left(\delta_{\text{eq}}^{\text{mech}} + \Delta\delta_{\text{eq}}\right) - \delta_{\text{min}}^{\text{mech}}} , \\ &= -E_{\text{eq}}^{\text{Fr}} \frac{\Delta\delta_{\text{eq}}}{\left(\frac{\delta_{\text{eq}}^{\text{hyd}}}{s_0} + \Delta\delta_{\text{eq}}\right) - \delta_{\text{min}}^{\text{mech}}} \end{aligned} \quad (4.46)$$

where $\Delta\delta_{\text{eq}} = \delta^{\text{mech}} - \delta_{\text{eq}}^{\text{mech}}$ defines the change in aperture from its equilibrium value.

The reduction of the numerical model to a single fracture embedded in the effectively impermeable surrounding gneiss results in negligible fluid exchange between fracture and solid domain similar to undrained conditions. Furthermore, the contribution of shear forces is negligible due to the low viscosity of the pore fluid, water, and the low frequency of the perturbations induced by the step-rate tests ($\ll 100$ Hz). Therefore, we treat the surrounding matrix by a single phase formulation and neglect the leak-off term iv) in eq. (4.12). The deformation state of the linear-elastic rock matrix, embedding the fracture, is then characterized by effective bulk modulus K_{eff} and shear modulus μ_{eff}

$$\begin{aligned} K_{\text{eff}} &= \frac{\phi_0 \left(\frac{1}{K^s} - \frac{1}{K^s}\right) + \frac{1}{K^s} - \frac{1}{K}}{\frac{\phi_0}{K} \left(\frac{1}{K^s} - \frac{1}{K^s}\right) + \frac{1}{K^s} \left(\frac{1}{K^s} - \frac{1}{K}\right)} \\ \mu_{\text{eff}} &= \mu \end{aligned} \quad (4.47)$$

representing Gassmann's low frequency result [66, 127]. In eq. (4.47), ϕ_0 denotes the initial porosity of the porous matrix, K^s the (average) modulus of the compressible grains composing the matrix, K and μ the bulk and the shear modulus of the dry skeleton, and K^s the bulk modulus of the fluid.

3.3 Model parameters

The flow model requires input values for the elastic parameters of the matrix, K and μ , the fluid bulk modulus K^f , the equilibrium fracture opening $\delta_{\text{eq}}^{\text{hyd}}$, the minimal mechanical fracture opening $\delta_{\text{min}}^{\text{mech}}$, the equilibrium-normal stiffness parameter $E_{\text{eq}}^{\text{Fr}}$, the dimensionless contact parameter s_0 , and flow-boundary conditions for the intersection of the fracture plane with the borehole, as prescribed by the individual experimental protocols followed for the tests in the six intervals. The chosen parameters are listed in Table 4.11; while Freiberg gneiss is anisotropic, see Adero (2020), for simplicity, we rely on representative isotropic material parameters. We employ a constant value of 4 for the parameter s_0 , determined from exploratory calculations. The chosen value leads to changes in hydraulic aperture that are larger than the ones in mechanical aperture, addressing decreasing percolation in the fracture plane with increasing contact area. Fractures are assumed to be mechanically closed once δ^{mech} approaches $\delta_{\text{min}}^{\text{mech}} = 0$. The remaining model parameters, the hydraulic equilibrium fracture aperture $\delta_{\text{eq}}^{\text{hyd}}$ and the equilibrium fracture normal stiffness $E_{\text{eq}}^{\text{Fr}}$, along with the geometrical fracture property, its numerically discretized length l_{Fr} , determine the effective hydraulic conductivity and the storage capacity of the fractures. The initial normal stress is determined by equilibrium aperture and initial stiffness via the constitutive relation. We seek optimized values for these three parameters by analysing the misfit between numerical pressure transients and observed pressure transients.

Table 4.11: Parameters of the matrix and the fracture domain used for the numerical fitting of characteristic fracture properties.

Quantity	Value	Unit	Quantity	Value	Unit
Rock parameters					
dry skeleton bulk modulus K	$2.75 \cdot 10^1$	(GPa)	grain bulk modulus K^s	$6.0 \cdot 10^1$	(GPa)
shear modulus μ	$1.7 \cdot 10^1$	(GPa)	initial porosity ϕ_0	$1.0 \cdot 10^{-2}$	(-)
fluid compressibility β^f	$4.17 \cdot 10^{-1}$	(1/GPa)	effective bulk modulus K_{eff}	$4.25 \cdot 10^1$	(GPa)
effective shear modulus μ_{eff}	$1.7 \cdot 10^1$	(GPa)			
Fracture parameters					
contact characteristic s_0	4.0	(-)	fluid compressibility β^f	$4.17 \cdot 10^{-1}$	(1/GPa)
minimal mechanical opening $\delta_{\text{min}}^{\text{mech}}$	0.0	(μm)			

The assumption of a radial-symmetric fracture geometry and a linear-elastic response of the poro-elastic matrix reduces the total number of degrees of freedom (DoF). This reduction of DoF results in a high efficiency of the method; simulations of transients require just several minutes on a standard desktop PC with the used numerical discretization corresponding to around 20 000 DoF for the whole set of modelled fractures.

3.4 Quantification of misfit

Identifying “the” best numerical fit requires examination of the evolution of the misfit between experimentally observed transients \mathbf{p}_{exp} and the numerically modeled transients \mathbf{p}_{num} . We quantify misfit by a normalized L_2 -error norm

$$e_{L_2} = \frac{\|\mathbf{p}_{\text{num}} - \mathbf{p}_{\text{exp}}\|_2}{\|\mathbf{p}_{\text{exp}}\|_2}, \quad (4.48)$$

i.e., misfit is reduced to a single scalar value for each considered parameter combination. Iso-surfaces of misfit in the three-dimensional space of the model parameters $\{\delta_{\text{eq}}^{\text{hyd}}, E_{\text{eq}}^{\text{Fr}}, l_{\text{Fr}}\}$ were gained from interpolation between the discrete values of actually performed calculations.

3.5 Strategy of parameter search

The sensitivity of the model to its parameters was studied in a total of 1144 and 735 simulations for the pressure-plateau and the positive-tangent group, respectively. Numerical fits with a normalized error of approximately $e_{L_2} \leq 0.055$ correspond to absolute deviations between observed and modelled pressure continuously below 0.2 MPa and are considered matches of the experimental observations in the light of the subsumed effects of flow-rate fluctuations due to irregularities of the pump, intrinsic accuracy of pressure sensors, and the correction of flow rate for storage capacity of the injection system. The investigated ranges of the individual parameters (Table 4.12) were defined based on an exploratory analysis starting from educated guesses. This exploratory search indicated the existence of a misfit minimum below the defined error of $e_{L_2} \leq 0.055$ whose location we then investigated further. For the subsequent analysis of the remaining sets of measurement data, knowledge about the existence of a local minimum motivated the direct search for parameter combinations resulting in an error of $e_{L_2} \leq 0.055$, corresponding to fits within uncertainty.

Table 4.12: Parameter ranges (min, max) and increment (inc) for the studies of the model sensitivity for the pressure-plateau and pressure-tangent group.

Group	$E_{\text{eq}}^{\text{Fr}}$ (MPa)			$\delta_{\text{eq}}^{\text{hyd}}$ (μm)			l_{Fr} (m)		
	min	max	inc	min	max	inc	min	max	inc
pressure-plateau group	4.0	6.4	0.2	30.0	39.0	1.0	20.0	90.0	10.0
positive-tangent group	2.4	3.6	0.2	33.0	47.0	1.0	2.4	16.0	2.5

4 Results

The parameter study aimed at the identification of parameter combinations yielding a match between field data and numerical simulations to understand the characteristics of

fractures responsible for the two distinct groups of pressure transients. In a first step, we focused on one data set of each group, the transient pressure response M_a^p obtained from hydraulic tests at 51.6 m borehole depth, representing the pressure-plateau group, and M_a^t corresponding to tests conducted at a borehole depth of 24.6 m, representative for the pressure-tangent group, before we used the gained knowledge about the existence of a local error minimum to reduce the computational costs of the numerical fitting procedure for the remaining data sets by focusing on parameter combinations resulting in low error values.

4.1 Parameter study

4.1.1 Pressure-plateau group

The error surfaces of the pressure-plateau group possess an ellipsoid-like shape (Figure 3); the surface enclosing numerical solutions with $e_{L_2} = 0.0275$, representing matches of the observed transients within the estimated uncertainty, indicates the existence of an error minimum. The error evolution with fracture length (A_I to H_I in Figure 3) is consistent with the iso-surface plot since the error reaches a minimum at an intermediate fracture length of $l_{Fr} = 50.0$ m. The error evolution is asymmetric around this minimum, it increases less steep for fractures with an increasing than for fractures with a decreasing length. The corresponding unique error minimum in the parameter space occurs for the parameter combination D_I , which consists of an hydraulic equilibrium fracture aperture $\delta_{eq}^{hyd} = 36.0 \mu\text{m}$, an equilibrium fracture normal stiffness parameter of $E_{eq}^{Fr} = 5.6$ MPa, and a fracture length of $l_{Fr} = 50.0$ m. The model shows higher sensitivity to the equilibrium-fracture normal stiffness parameter and the hydraulic equilibrium aperture than to fracture length. Individual variations of the fracture stiffness and hydraulic equilibrium aperture relative to the values obtained for the identified minimum (exemplified by D_I^d to D_I^f in Figure 3) result in pronounced under- and overestimation of the measured transients, respectively.

4.1.2 Positive-tangents group

For the positive-tangent group, the misfit surface identifying relevant parameter combinations with absolute differences to the measured data consistently below 0.2 MPa, defined by $e_{L_2} \leq 0.055$, consists of two connected ellipsoidal shapes with different axis-orientations. A single potential minimum is indicated by the closed iso-surface with $e_{L_2} \leq 0.03$. The error evolution with fracture length (A_{II} to G_{II} in Figure 4) confirms the existence of a minimum for the parameter set B_{II} , consisting of an equilibrium-fracture normal stiffness parameter $E_{eq}^{Fr} = 2.8$ MPa, an equilibrium aperture of $\delta_{eq}^{hyd} = 42.0 \mu\text{m}$, and a fracture length of $l_{Fr} = 4.75$ m. Large misfits result when fracture length decreases below 4.75 m; however, misfit is less sensitive to variations in fracture length above this value. Variation of the equilibrium-fracture normal stiffness parameter E_{eq}^{Fr} and the hydraulic equilibrium aperture δ_{eq}^{hyd} relative to the parameter set B_{II} (i.e., parameter sets B_{II}^a to B_{II}^d in Figure 4) reveals a higher sensitivity of the model to changes of the stiffness parameter than the hydraulic equilibrium aperture.

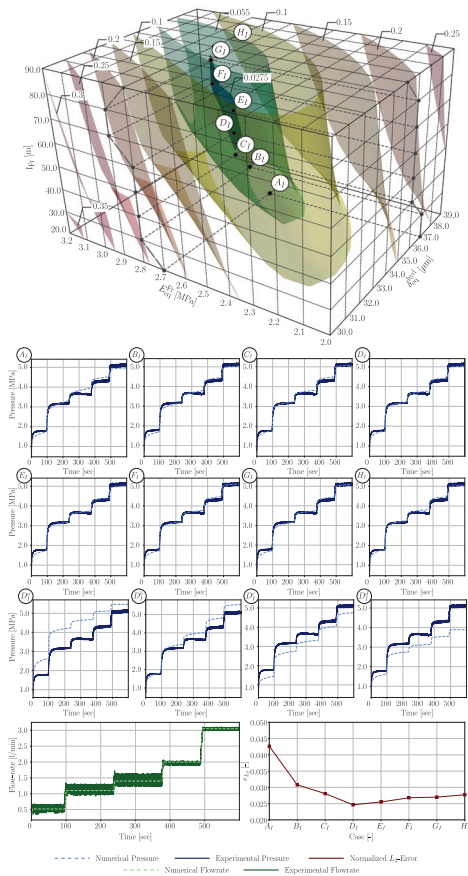


Figure 3: Top: Visualization of iso-surfaces of misfit between observed and calculated pressure transients for the parameter study conducted on the experimental data set M_a^p representative for the pressure-plateau group. Error surfaces are marked with the associated e_{L_2} -errors and parameter combinations relevant for detailed analysis of the error evolution are highlighted by labels A_I to H_I . **Bottom:** Comparison of observed and numerical pressure transients for the parameter combinations A_I to H_I . (left) The flow-rate boundary conditions are well matched by the numerical approach. (right) The errors of the numerical fits for parameter sets A_I to H_I exhibit a minimum. The legend at the bottom applies to all plots.

4.2 Characteristic fracture properties

For each of the further pressure-plateau and pressure-tangent data, parameter sets were found that result in fits with error values close to those obtained for the local minima in

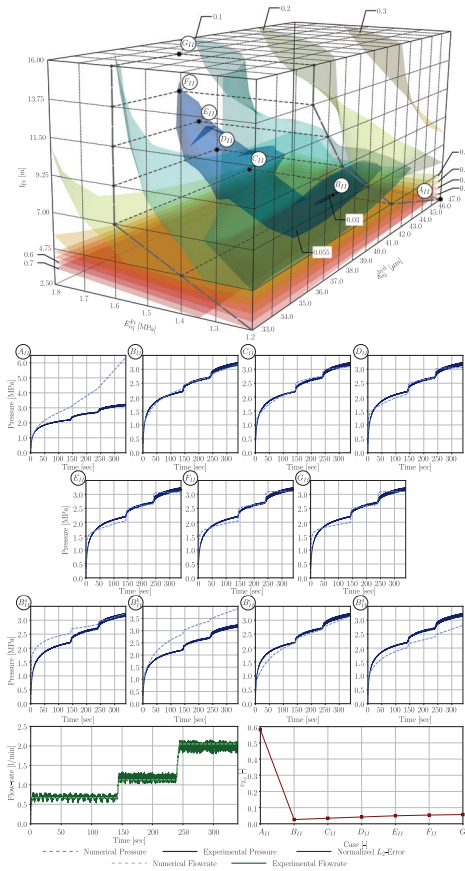


Figure 4: Top: A visualization of error surface plots corresponding to the parameter study conducted on the experimental data set M_{II}^t representative for the positive group is presented. Error surfaces are marked with the associated e_{L_2} -errors and parameter combinations relevant for detailed analysis of the error evolution are highlighted by labels A_{II} to G_{II} . **Bottom:** Numerical fits of the measured pressure transients corresponding to the highlighted parameter combinations A_{II} to G_{II} along with the corresponding fit of flow-rate boundary conditions are introduced. Errors of the numerical fits for parameter sets A_{II} to G_{II} are presented by means of a line plot. A legend introduces the corresponding quantities to the used line types at the bottom of the figure.

the two examples above (Figure 5, Table 4.13). The error for data set N_6^e is exceptionally high compared to that of other sets when we do not neglect the first pumping step (Table

4.13) that involves a delayed pressure increase (Figure 1). This interval loses water when isolated and has to be refilled after an extended shut-in period.

The elongated enclosing hull of the determined parameter combinations for the pressure-plateau group visualizes the recognized bias of fracture stiffness and equilibrium fracture aperture with fracture length. For the positive-tangent group, we observed bias of the fracture stiffness with fracture length, but no correlation between equilibrium aperture and fracture length (Figure 5, Table 4.13). Optimal parameters of the two groups occupy distinctly different volumes of the misfit space. Parameters determined for the pressure-plateau group corresponds to long and stiff fractures whereas the parameters determined for the pressure-tangent group coincide with short and compliant fractures.

Table 4.13: Material parameters gained from numerical fitting of the measured pressure transients.

Depth	Fracture label	Equ. fracture normal stiffness par. E^{FP}	Equilibrium aperture δ_{eq}^{nsd}	fracture length l_F	error ϵ_{L_2}
<i>pressure-plateau group</i>					
51.6 m	N_a^p	5.6 MPa	36.0 μm	50.0 m	0.024
55.7 m	N_b^p	3.5 MPa	26.5 μm	10.0 m	0.048
56.5 m	N_c^p	3.8 MPa	28.0 μm	15.0 m	0.184/0.024 ¹
<i>positive-tangent group</i>					
24.6 m	N_a^t	2.8 MPa	42.0 μm	4.75 m	0.026
40.6 m	N_b^t	2.13 MPa	55.0 μm	3.7 m	0.063
49.7 m	N_c^t	2.95 MPa	46.0 μm	5.4 m	0.046

1: including/excluding the first injection step biased by the necessity to refill the injection interval

5 Discussion

The numerical fitting of pressure transients identified a unique minimum corresponding to an optimal parameter combination in the range of investigated material parameters. The sensitivity analysis proofed increasing errors for changes of parameters relative to the set D_I , which indicates that no further minima exist within realistic limits of the parameters. The model exhibits a high sensitivity to the equilibrium fracture normal stiffness and the equilibrium fracture aperture, whereas simulated pressures are relatively insensitive to changes in fracture length.

5.1 Characteristics of pressure groups

The proposed hydro-mechanical model results in vastly different pressure transients depending on parameter choice and thus either group of observed transients, those with nearly constant pressures and those with continuously increasing pressure at constant flow rate, could be modelled equally well. For both pressure-transient groups, values of equilibrium aperture and equilibrium-normal stiffness parameter determined by the numerical fitting fall well within the range of previously discussed values [108, 178, 219]. The different pressure transients of the two groups require distinctly different length and stiffness to match the measurement data. The fracture lengths of meter-scale derived for the positive-tangent group are consistent with the spatial scale of the test volume and

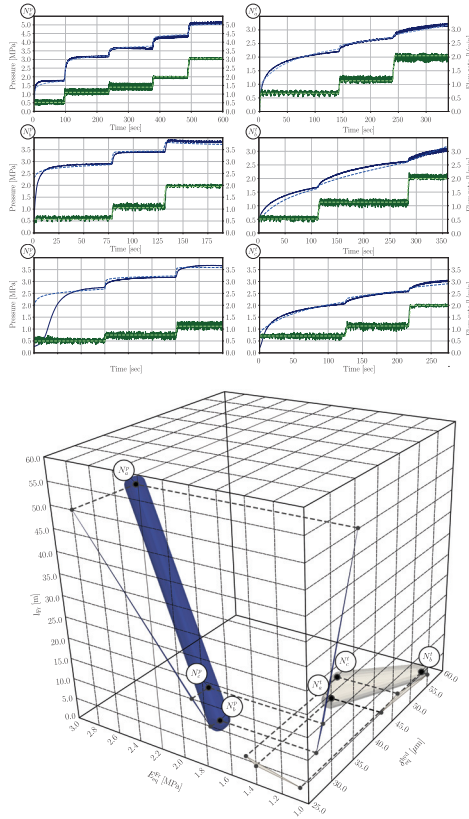


Figure 5: Top: Comparison of numerical flow and pressure transients, corresponding to the set of parameter fits determined throughout the numerical fitting, to the experimentally recorded pressure and flow transients. **Bottom:** Visualization of the determined parameter sets in a three dimensional parameter space. The space spanned by parameter combinations associated to the pressure-plateau group is introduced by a blue hull and the space resulting from parameter sets of the positive-tangent group is limited by a grey hull.

the dimensions of seismicity clouds observed during the corresponding stimulations. The decameter-scale fracture lengths modelled for the pressure-plateau group appear long at first glance. Yet, considering the shape of the misfit iso-surface of this group that documents an insensitivity of the model to changes in fracture length beyond a critical lower bound, fracture lengths barely exceeding 10 m cannot be excluded per-se. Furthermore, the model involves only a single fracture, neglecting leak-off into intersecting fracture systems and thus its application to data determines properties of an equivalent fracture

potentially subsuming pre-existing fractures with a comparable or higher conductivity than that of the fracture intersecting the borehole. The interpretation that the distinct difference in effective fracture length derived for the two pressure-transient groups is an expression of the extent to which the fracture intersecting the borehole connected to pre-existing fractures and thus became an element of a larger conduit network qualitatively agrees with the pressure decay rates during shut-in after the step-rate tests (Table 1)

5.2 Distribution of pressure along the fracture

Knowing the distribution of fluid pressure along the fracture is a crucial pre-requisite for substantial stimulation modeling. Since our hydro-mechanical model includes the entire fracture, we can use the determined parameter sets to investigate the pressure distribution in the fracture at any point during the step-rate tests. We focus on the pressure states at the end of each applied flow-rate step for data sets N_a^p and N_b^t , representative for their corresponding group, to examine whether the characteristics of the transients observed in the borehole bear information on the pressure distribution along the fracture.

For N_a^p , the representative of the pressure-plateau group, pressure gradients along the fracture are higher than for N_b^t of the positive-tangent group, for which the pressure profile is almost flat, i.e., the pressure in the fracture is equilibrated during every stage of the pumping (Figure 6). Thus, the shape of the transients of the injection pressure is opposite to the spatial variation of pressure in the fracture, constant injection pressures are associated with significant pressure gradients while injection pressures increasing with time are associated with momentarily constant pressures in the fractures. The significant difference in pressure distribution reflects the critical interrelation between local deformation and its consequences for local flow and storage. For the long fractures of the pressure-plateau group, the local deformation and thus permeability decrease with distance from the injection point, but storage of fluid is promoted close to the borehole where the fracture is already less stiff than at its end due to the increased fluid pressure. While constant along the relatively short fractures, the pressure increases during each flow-rate step and from step to step for the positive tangent group. The close to constant pressures document that pressure is not controlled by transport restrictions in the fractures but by their storage capacity, which is limited owing to the direct effect of fracture length on fracture volume and also on geometrical fracture stiffness, as detailed in the next section.

5.3 Specific normal stiffness

The contact mechanics of the six investigated fractures is uniquely determined by the parameters constrained by the modeling. Evaluating the constitutive relation (4.46) with the found equilibrium-fracture normal stiffness parameter $E_{\text{eq}}^{\text{Fr}}$ and the hydraulic equilibrium fracture width $\delta_{\text{eq}}^{\text{hyd}}$ yields their opening and closure behavior when subjected to normal stresses deviating from the equilibrium stress (Figure 7). The corresponding specific contact stiffnesses reflect the strong non-linearity of the constitutive relation; close to the equilibrium stress specific stiffness varies between 10^2 and 10^3 MPa/mm and thus falls well within the range of representative previous in-situ observations and laboratory

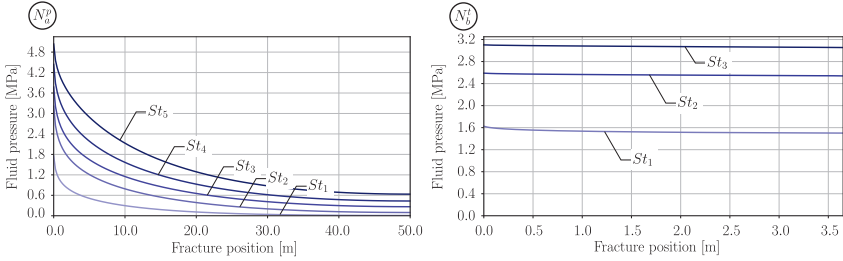


Figure 6: Evolution of pressure distribution along the fractures at the end of each flow-rate step, represented by increasing line thickness with increasing step number St_i , for numerical data set N_a^p of the pressure-plateau group (left) and data set N_b^t of the positive-tangent group (right).

studies [145, 178, 219]. When extended towards increasing fracture contact, i.e., when effective normal stresses exceed the equilibrium in-situ stresses, the stiffness of all tested fractures converge to a narrow range of $2 \cdot 10^3$ MPa/mm to $4 \cdot 10^3$ MPa/mm.

The equilibrium-fracture normal stiffness parameter $E_{\text{eq}}^{\text{Fr}}$ provides a constraint on the equilibrium stress that the fractures experience in-situ. Since the obtained equilibrium-fracture normal stiffness parameters of the pressure-plateau group are higher than the ones of the positive-tangent group, the predicted equilibrium normal stresses for fractures of the plateau group, ranging between 3.5 MPa and 5.6 MPa, are larger than the ones for fractures of the positive-tangent group, ranging from 2.1 MPa to 2.8 MPa. Magnitude and range of these predictions are consistent with the stress state inferred for the test volume at Reiche Zeche, where the overburden corresponds to a vertical stress of about 3.5 MPa [2].

The contribution of the elastic medium, in which the fractures are embedded, to the stiffness of the entire system is conventionally addressed as geometrical stiffness [131, 206]. We evaluated the balance between contact stiffness and geometrical stiffness by numerical evaluation of constant fluid pressures in the range of the experimental pressure levels with an increment of 0.5 MPa for the two “equivalent” fractures found by the modeling for intervals 51.6 m (M_a^p) and 40.6 m (M_b^t), representing the two pressure-transient groups and constituting the upper and lower bounds of the parameter space of optimal fits in terms of fracture length and normal stiffness parameter, respectively.

The prescribed levels of fluid pressure lead to local deformations according to the constitutive relation (4.46) and associated local normal contact stresses σ_N^{Fr} , which we integrate over the fractures’ lengths. Mechanical equilibrium across the fracture requires changes in fluid pressure and total normal stress to hold $\Delta p = \Delta \sigma_N^{\text{Tot}}$. Thus, the mismatch between the applied fluid pressure and the numerically integrated normal contact stresses corresponds to the normal stress exerted on the fracture by the deformation of the surrounding material, here addressed as geometrical normal stress σ_N^{G} . The decomposition

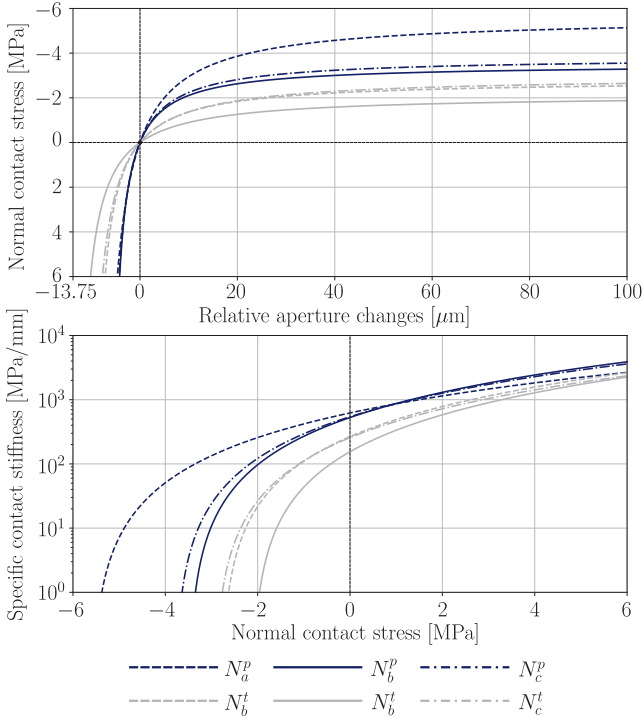


Figure 7: Top: Normal contact stress σ_N^{Fr} as a function of relative aperture changes $\Delta\delta$ gained from evaluating eq. (4.46) with the best fit parameters for the investigated pressure transients (Table 4.13). **Bottom:** Semi-logarithmic representation of the specific contact stiffness K_N^{Fr} as a function of the acting normal contact stresses. Positive values indicate compressive stresses (relative to the equilibrium stress). The legend applies to top and bottom, specifically dark blue lines represent data sets of the pressure-plateau group and grey lines that of the positive-tangent group.

of the changes in total acting normal stress

$$\Delta\sigma_N^{\text{Tot}} = \Delta\sigma_N^{\text{Fr}} + \Delta\sigma_N^{\text{G}} \quad (4.49)$$

gives changes in the geometrical stress as

$$\Delta\sigma_N^{\text{G}} = \Delta p - \Delta\sigma_N^{\text{Fr}}. \quad (4.50)$$

The stress balance differs for the two investigated fractures and varies with fluid pressure for an individual fracture (Figure 8). For the long (50 m) fracture of the pressure-plateau group, force balance across the fracture is dominated by contact stresses, while the contribution of geometrical normal stress is significant for the short (3.7 m) fracture of the

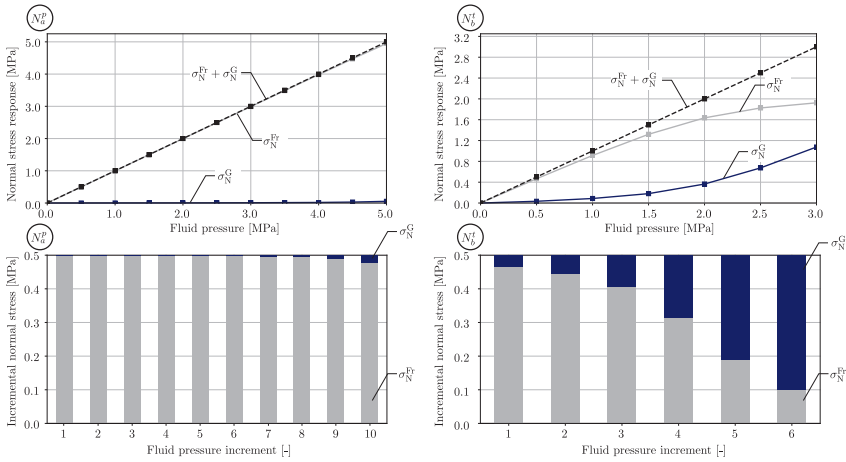


Figure 8: Top: Decomposition of the total acting normal stresses into geometrical σ_N^{G} and normal contact stress σ_N^{Fr} contributions as a function of the acting constant fluid pressure for numerical parameter sets obtained from numerical fits N_p^a , representative for the pressure plateau, and N_b^t , representative for the positive-tangent group. **Bottom:** Contribution of geometrical and normal contact stresses for each incremental pressure increase.

positive-tangent group, the more the higher the fluid pressure. The changing relative contributions result from the non-linearity of the normal-contact stress formulation introduced by eq. (4.46).

We transfer the findings for the normal-stress decomposition (Figure 8) to a corresponding decomposition of specific normal stiffness. The fracture contact normal stiffness is obtained by analytical evaluation of $K^{\text{Fr}} = \partial\sigma_N^{\text{Fr}}/\partial\delta^{\text{Fr}}$ considering the fitted parameters. In a subsequent step, we separated the geometrical stiffness of the two investigated fractures by conducting a numerical analysis of their opening behaviour under the assumption of negligible contact normal stresses, which results in $p = \sigma_N^{\text{G}}$. The discretized geometrical stiffness is then evaluated by calculating an averaged aperture and the discretized normal stress change, i.e., $K^{\text{G}} = \Delta\sigma_N^{\text{G}}/\Delta\delta^{\text{G}}$. The combined stiffness is numerically determined by $K^{\text{Com}} = \Delta\sigma_N^{\text{Tot}}/\Delta\delta^{\text{Com}}$. Since the relation between $\sigma_N^{\text{Tot}} = p$, σ_N^{G} , and σ_N^{Fr} is known from the stress decomposition (Figure 8), the resulting stiffness components can be combined to express the stiffness of the combined model for a uniform fluid pressure.

The sum of transformed geometrical and contact normal stiffness agrees with the combined stiffness (Figure 9) lending support to the assumptions made regarding the transformation of different stress states to the acting effective normal stress. Geometrical stiffness is found to be negligible for data set N_p^a of the pressure-plateau group, for which the combined specific stiffness is well approximated by the contact stiffness, i.e., fluid pressure and acting contact stresses balance (Figure 7). In contrast, the combined specific stiffness for data set N_b^t , the representative of the positive-tangent group, is a superposition of both

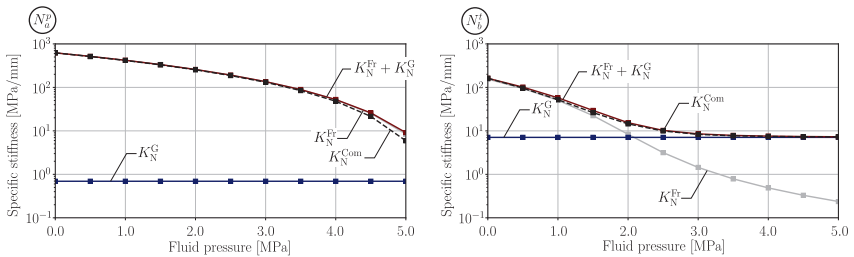


Figure 9: Combined (K_N^{Com}) specific fracture stiffness, i.e., the sum of decomposed geometrical K_N^G and normal contact stiffness K_N^{Fr} , as a function of fluid pressure calculated from results of the proposed hydro-mechanical modelling of data sets N_a^b and N_b^t .

stiffness components converging towards the geometrical stiffness with increasing fluid pressure. In fact, the geometrical stiffness forms the lower bound for combined stiffness. The contribution of the geometrical stiffness to the total fracture stiffness is highest for fluid pressures above the identified asymptotic stress values of the contact model, i.e., at the onset of separation of the fracture halves.

6 Conclusions

We numerically modeled the opening characteristics of fractures during in-situ hydraulic tests using a hydro-mechanical flow model implemented for radial fractures with non-linear contact mechanics and without leak-off. Systematic variations of experimentally observed pressure transients lead us to distinguish two groups, with continuously (positive-tangent) and step-wise rising (pressure-plateau) pressure response to stepwise increases in flow rate. Our parameter study unveiled the role of fracture length, equilibrium-normal stiffness parameter, and equilibrium fracture aperture for borehole-pressure transients. The proposed hydro-mechanical coupling can explain the strikingly different pressure transients within experimental uncertainty and thus provides a perspective to the response of fractures to pumping operations alternative to the traditional pressure-diffusion analyses, which relate the distinct pressure groups to differences in flow regime associated with differences in the orientation of the fracture relative to the borehole. This alternative explanation bears significant consequences for the modeling of energy provision from perthrothermal reservoirs, in which the fractures constitute the prime conduits for the transport agent of the heat.

The identified minima in mismatch between observed and calculated pressure transients correspond to different fracture properties for the two groups. We noticed a bias between fracture length and fracture normal stiffness resulting in a specific mismatch for the positive-tangent group. Pressure plateaus are characteristic of relatively long and stiff fractures, while relatively short and compliant fractures lead to continuously increasing injection pressures. equilibrium fracture apertures do not differ significantly between the two groups, a plausible result considering that the tested fractures are embedded in the

same host rock. The pressure distribution along the fractures differs significantly for the two groups of pressure transients; pronounced non-linear pressure distributions develop in the long fractures of the pressure-plateau group during injection, while the pressure in the short fractures of the positive-tangent group remains close to the injection pressure along their entire length. Our observations on pressure distribution motivate to investigate the validity of the common practices of normal stress estimation from shut-in and jacking pressures. The stress balance across fractures and its relation to fluid distribution in them is central for modeling failure and seismicity. A full analysis of the potential for shear failure will require to expand our model by shear stresses and associated stiffness.

Throughout the performed step-rate tests, fluid injection results predominantly in opening of fractures. Evaluation of the constitutive relation with the determined fracture parameters allowed us to investigate the contributions of local contacts and overall fracture geometry to stress balance and thus bulk stiffness. With decreasing effective stress, the role of the contacts diminishes and total stiffness approaches the lower bound constituted by the geometrical stiffness.

The proposed hydro-mechanical model exhibits diminished sensitivity to fracture length when a flow-rate step results in a constant injection pressure. Thus, extending the pumping duration will not only help to discriminate between the alternatives of flow regime vs. hydro-mechanical effects, but may also reduce uncertainty of model parameters in case pressure ultimately deviates from an early plateau, an observation that could not be explained by the diffusion approaches. Future numerical work should explore different scenarios for the relation between mechanical and hydraulic apertures and its evolution with changes in effective normal stresses.

7 Acknowledgement

Jörg Renner is indebted to Felix Becker, Gerd Klee, and Florian Seebald of Solexperts GmbH for the collegial atmosphere during the field testing. Thomas Grelle and Carlos Lehne, and Katja Hesse of LIAG, Hannover, are thanked for performing the televiewer logging and processing the log data, respectively.

Importance of fracture deformation throughout hydraulic testing under in-situ conditions

Patrick Schmidt, Nathan Dutler, Holger Steeb, GJI - Geophysical Journal International, August 2021, DOI: 10.1093/gji/ggab354

Abstract

In this work, we propose a hydro-mechanical simulation model to study the strong interaction of fluid flow and fracture deformation under in-situ stress conditions. The general model is reduced under physics-based assumptions to provide an efficient numerical approach for inverse analysis of experimental studies and is applied to experimental field data obtained from hydraulic tests conducted at the Grimsel Test Site (GTS), Switzerland. The present set of hydro-mechanical measurement data provides not only valuable information about the transient pressure and flow evolution but also the transient change of fracture deformation. We aim to introduce a strongly-coupled hydro-mechanical model to numerically characterize the fractured reservoir based on experimental data below the limit of hydraulically induced irreversible changes of the reservoir's properties. Insights into the leading mechanisms of flow processes throughout hydraulic testing under in-situ conditions are then gained by best numerical fits of the measurement data. Based on the experimental and numerical findings, this study emphasizes the importance of a consistent consideration of local and non-local fracture deformation throughout inverse analysis of hydraulic testing data to a) better understand hydro-mechanical flow processes in fractured reservoirs and b), to increase the estimation quality of hydraulic properties of tested fractures.

1 Introduction

Traditionally, effective hydraulic characterization of fractured reservoirs are primarily determined by a consistent analysis of pressure and flow transients [60, 133], which are induced by perturbations of the fracture's in-situ state throughout pumping operations by means of constant flow rates or harmonic variations of such [89, 157]. In contrast to conventional procedures [48], hydro-mechanical measurements consistently extend the set of pressure and flow data by information about the fracture deformation in terms of aperture changes [53].

Transient information about fracture aperture changes might not only increase the quality of effective hydraulic parameters but also provides valuable information about the storativity of a tested fracture to further study the interaction of hydraulics and mechanics throughout hydraulic testing of fractures under in-situ conditions. Therefore Fibre-Bragg Grating (FBG) sensors were grouted in a borehole near the injection location, which was placed in intact rock or intersected by pre-existing, natural fractures [52]. The relationship between pressure and uniaxial strain records measuring fracture opening and closing relative to the borehole direction allows investigations on the hydro-mechanical

interaction of tested fractures and fracture networks. The uniaxial strain data indicates non-negligible, reversible changes of the fracture volume throughout injection steps below the jacking pressure. Reversible fracture deformation cannot consistently be accounted for by pressure diffusion based models, but requires a hydro-mechanical formulation for flow in deformable fractures to ensure a reliable characterization of the tested region.

Commonly, sets of pressure and flow transients obtained from hydraulic field tests are analyzed by isotropic pressure diffusion models [25, 125]. Nevertheless, such relatively simple models reach their limits once phenomena related to transient hydraulic changes induced by mechanical responses of the fracture to an in- or decrease of fluid pressure occur in the measurement data [164, 165, 206, 208]. The hydro-mechanical interaction influences the transient pressure, respectively flow evolution, and might introduce inaccuracies throughout the calculations of effective reservoir parameters when not taken into consideration [207]. Mechanical and hydraulic effects act on different time-scales. Instantaneous non-local deformations induced by pressure perturbations potentially lead to a local volume increase in regions of the fracture that have not been reached by pressure diffusion resulting in a pressure drop and reverse water-level fluctuations in distant monitoring wells. In unfractured poro-elastic media, this prominent phenomenon is known as the Noordbergum effect [107, 162]. The findings indicate the dependency of the fracture deformation on the acting stress state that is known to be also composed of normal stresses induced by fracture surface contact [12, 75]. Studies on the relation of fluid flow under varying acting normal stress conditions show a direct relationship between the specific fracture stiffness, respectively total fracture contact surface and flow rates on laboratory scale [145] and have successfully been upscaled to larger scales [143, 148]. Besides the discussed non-local effects, these investigations indicate local mechanical responses of the system that might result in effective hydraulic property changes such as transient variations of the fracture's permeability [115, 122, 209, 215]. Thus, it is essential to study the importance of fracture deformation and its influence on the transient flow process throughout fracture testing. Nevertheless, inverse analysis of consistent hydro-mechanical data sets obtained from hydraulic field tests using implicitly coupled hydro-mechanical simulation models to determine effective fracture properties cannot be found in the literature.

Consistent hydro-mechanical numerical modeling of flow processes in deformable, high-aspect-ratio (length \gg aperture) fractures require tight coupling of the deformation state of the surrounding rock matrix with the resulting fluid flow field in the fracture. In the context of flow processes in fractured porous media, flow within the fracture domain is characterized by low Reynold numbers and creeping flow conditions, which motivates the assumption of a Poiseuille-type description [121, 216]. Taking fracture deformation into consideration by consistently extending the governing equations, an implicitly coupled hybrid-dimensional flow model [208] can be derived, which is closely related to the lubrication equation [16]. Consideration of the low compressibility of water which serves as the injection medium throughout the conducted hydraulic fracture testing results in a numerically stiff system of partial differential equations [1, 184, 218]. Numerical stability for the stiff system can be achieved by physics-based preconditioning of implicitly coupled staggered algorithms [38, 72, 73] which originate from strategies applied in the field of unfractured poro-elastic media [104, 105]. For highly fractured domains staggered algorithms might face numerical difficulties once rigid body movements occur. In

such cases numerical stability is guaranteed by a robust monolithic coupling using zero-thickness interface element formulations [177, 180, 181]. Besides the framework used in this study [177] a number of different mesh-based frameworks are documented in the literature that also provide solution strategies for flow processes in deformable fractures [10, 86, 129, 183, 188, 196]. Contrary to the mentioned approaches, the present numerical model discussed in this work is extended by a lately introduced constitutive relation for normal contact-induced stresses under in-situ conditions [175] obtained by slight modifications of an existing fracture contact formulation [70, 181] to better approximate the initial stress state of in-situ fractures.

In contrast to the rising awareness of strong hydro-mechanical interaction throughout hydraulic stimulation of fractured and/or unfractured reservoirs, its role throughout hydraulic testing below jacking pressures remains subordinate. To emphasize the importance of fracture deformation throughout hydraulic testing of fractures under in-situ conditions, we numerically studied the occurrence of hydro-mechanical interaction based on experimental data. Measurement data obtained from experiments carried out at the Grimsel Test Site (GTS), Switzerland, provide unique hydro-mechanically consistent sets of pressure, flow, and fracture opening data, which are analyzed by a fully coupled, non-linear numerical model to gain a better understanding of the testing process. In particular, we applied the model to study measurement data consisting of pressure steps below the limit of irreversible transient changes of the fracture properties, relevant for the characterization of hydraulically induced and/or preexisting fractures. Analysis of the numerical data set includes a split of the total flow into flow attributed to fluid compressibility and flow triggered by fracture deformation. Concluding, the importance of hydro-mechanical coupling and limitations of purely diffusion-based and locally extended models throughout inverse analysis of experimental hydro-mechanical data sets is discussed based on numerical and experimental findings.

2 Experimental Description

We conduct a time series of flow, pressure and two Fibre-Bragg Grating (FBG) sensors obtained from a pressure-controlled step test to determine characteristic properties of a fractured region. The investigated region includes a hydraulic fracture which was induced throughout the first of two proppant-free hydraulic fracturing cycles. Thereafter a bleed-off phase took place to depressurize the rock volume of interest and sampling the back flow in the open intervals. Then, the characterization of the newly created fracture was done by a pressure-controlled step test. The experiment was performed in two inclined boreholes in a decameter scale, moderately fractured, well-characterized crystalline rock mass at the Grimsel Test Site (GTS), Switzerland. The experiments are part of the in-situ Stimulation and Circulation (ISC) project executed between 2015 and 2018 [9]. The presented experiments are known as HF2, and the data set is presented in Dutler *et al.* 2019.

Within the tested region two natural fractures intersected the FBG sensor at $\delta_{33.0}^{exp} = 33.0$ m ($177/61^\circ$), and a quartz vein crosses the one at $\delta_{31.8}^{exp} = 31.8$ m ($163/57^\circ$). The injection interval has a steeply incomplete axial trace measuring $049/89^\circ$ and $022/69^\circ$

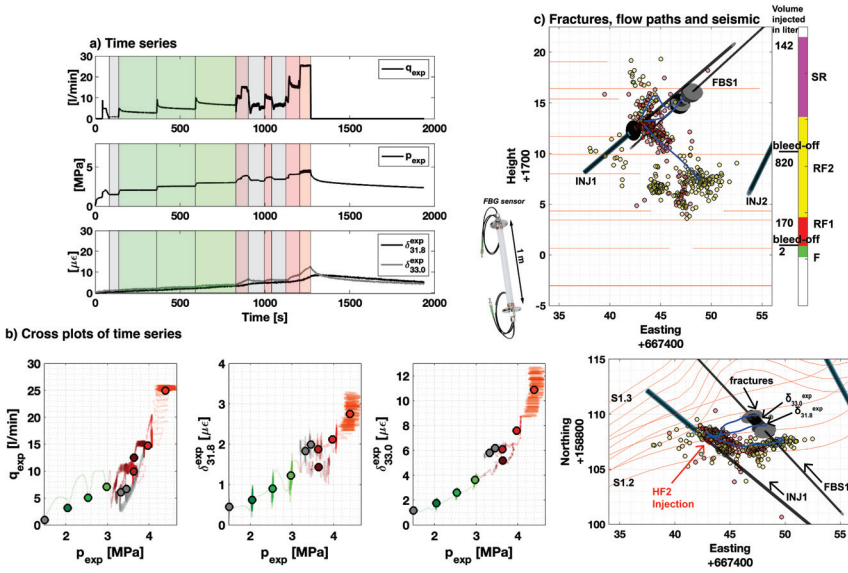


Figure 1: a) The time series of the step test is presented for the flow rate, the pressure, and two FBG strain records in the surrounding of the injection interval, and each valid step is colored with red or green. The cross plot are presented to estimate jacking pressure using flow rate q_{exp} , strain records $d_{31.8}^{exp}$ and $d_{33.0}^{exp}$ versus pressure. The circles indicate the mean of the corresponding colored sections. c) The setup of the experiment HF2 in-plane and map view shows the open injection interval (red cylinder), the fractures (grey discs) with the FBG sensors, the seismic cloud depending on time/volume of injection fluid and the flow paths (adapted by Dutler et al. 2020)

(given in azimuth/dip). The axial trace of the newly created hydraulic fracture at the injection interval represents the primary fracture and is oriented differently than the two natural fractures at the FBG sensors. They agree better with the seismic plane fit for the refracturing cycle RF2 with a cloud-oriented steeply inclined towards South ($175/46^\circ$), which agrees well with the fluid flow along the natural, pre-existing fractures [53]. The two natural fractures intersecting the FBG sensors deviate from the seismic by an angle of 15.2° and 14.7° respectively. Figure 1c) displays the boreholes with the strain and injection intervals, the located microseismic events, and the most relevant flow paths for the step test.

Throughout our study, we focus on pressure steps between 2 to 3 MPa (color-coded with greenish colors) to determine characteristic properties of the tested region. The defined pressure range is below the jacking pressure which was estimated to be 3.7 MPa [52], with a range between 3.3 and 4.2 MPa, depending on the chosen method [48, 87, 164]. The

behaviour of the greenish point in the flow versus pressure plot is slightly non-linear and the greenish points used in the strain record versus pressure plot indicates a pronounced non-linear behavior of fracture deformation (Figure 1 b). During fracture opening, the area of contact of two fracture surfaces decrease until a critical fracture aperture is reached, and the flow rate sharply increases. To visualize the distinct response for high pressure levels, data regarding the open primary fracture is color-coded by reddish colors and ambiguous steps by greyish colors, where fracture opening is taking place at 3.5 MPa [53]. The pronounced difference in hydraulic and mechanical response motivates the split into investigated, reversible pressure steps (greenish colors) and pressure regions which might induce irreversible changes to the fracture properties (reddish; greyish). Pressure levels beyond the reversible region induce highly non-linear and irreversible hydro-mechanical effects and, therefore, exceed the scope of this work (Fig. 1). In this context, we refer to Dutler *et al.* 2020 where shear reactivation induced irreversible effects for injection pressures beyond the jacking pressure are discussed.

The moderately non-linear region chosen for the numerical characterization helps to understand the importance of hydro-mechanical interaction below the limit of fracture separation throughout the determination of reliable effective properties of a hydraulically tested region. For the investigated pressure range no evidence for hydraulically induced permanent changes of the fracture properties, such as shearing or fracture propagation, can be found in the data.

3 Numerical Method

Consistent hydro-mechanical measurement data allows for a higher accuracy throughout the inverse numerical analysis of the tested fractures but also increases the requirements for the applied model drastically since tight coupling of mechanical fracture fluctuations and fracture flow is necessary to provide best numerical fits. Simulations throughout this work are based on a general hybrid-dimensional flow model [177, 206] to capture non-linear hydro-mechanical phenomena in a deformable fracture domain \mathcal{B}^{Fr} embedded in a poro-elastic medium \mathcal{B}^{Pe} . The model approach will be extended to reproduce the full set of measurement data under field conditions aiming to provide an efficient framework for the characterization of hydro-mechanically tested fractures.

3.1 Flow Processes in a Deformable Fracture \mathcal{B}^{Fr}

Fluid volume induced fluctuations around the in-situ equilibrium state of a fracture \mathcal{B}^{Fr} result in mechanical deformation and fluid flow. The caused interaction of the fluid pressure state and the volumetric deformation changes of the fracture need to be consistently taken into account throughout the derivation of the governing equations in order to guarantee a globally mass preserving formulation. For each change in fluid volume an equilibrium state for the biphasic poro-elastic medium \mathcal{B}^{Pe} and the fracture domain \mathcal{B}^{Fr} must be determined with respect to the fluid pressure and the local fracture aperture $\delta(\mathbf{x}, t)$, which is constructed from the normal fracture surface deformation $\mathbf{u}^{\text{Fr}}(\mathbf{x}, t)$. The equilibrium conditions are derived in the following by means of the balance of mass and

linear momentum for a deformable fracture.

3.1.1 Balance of Momentum

Based on experimental investigations of creeping-flow processes within fractures filled by a compressible fluid [216], pressure-driven Poiseuille-type flow assumptions are valid for hydraulically-transmissible fractures. The characteristic parabolic velocity profile for flow between two parallel plates assuming no-slip boundary conditions at the fracture surfaces is obtained by separation of variables and the relative mean fluid velocity

$$\hat{\mathbf{w}}_f = -\frac{\delta^2(\mathbf{x}, t)}{12 \eta^{iR}} \hat{\text{grad}} \hat{p} = -\frac{k_{Fr}^s(\mathbf{x}, t)}{\eta^{iR}} \hat{\text{grad}} \hat{p}, \quad (4.51)$$

by integration of the velocity profile over the fracture aperture normalized to the flow area. In eq. (4.51) $k_{Fr}^s(\mathbf{x}, t)$ is the time and space dependent effective fracture permeability and η^{iR} the effective dynamic viscosity of the fluid. The proportionality factor $1/12$ might be adapted to capture deviations of the fracture geometry such as varying asperities [159]. Confusion with quantities defined in the biphasic porous domain \mathcal{B}^{Pe} is prevented by marking variables and mathematical operations defined within the fracture domain \mathcal{B}^{Fr} by $\hat{\square}$. Thus, $\hat{\text{grad}} \hat{p}$ is the pressure gradient within the fracture and $\hat{\mathbf{w}}_f$ is the fracture's seepage velocity.

3.1.2 Balance of Mass

Perturbations of the balance of mass causes transient changes in fluid pressure and fracture volume, but might also lead to fluid leak-off into the surrounding porous rock. Enforcing global mass conservation implies that changes of the total fluid volume in the fracture domain \mathcal{B}^{Fr} are compensated by a combination of fluid density ρ^{iR} changes of the compressible fluid, where the fluid compressibility $\beta^f = 1/K^f$ is introduced by means of the fluid's bulk modulus K^f and volumetric changes in terms of the local fracture aperture $\delta(\mathbf{x}, t)$. By relating fluid compressibility, volumetric changes and leak-off, the balance of mass finally reads

$$\frac{\partial(\rho^{iR} \delta)}{\partial t} + \hat{\text{div}}(\hat{\mathbf{w}}_f \rho^{iR} \delta) = w_f^N \quad (4.52)$$

in its local form, where the component of the seepage velocity normal to the fracture surface into the porous domain \mathcal{B}^{Pe} is denoted by w_f^N . In eq. (4.52) we consider hydraulically open, proppant-free fractures in mechanical contact; i.e., the fracture surfaces are mechanically interacting, but still allow the fluid to travel through the fracture domain.

3.1.3 Governing Equations

The governing equation for fluid flow in deformable fractures is obtained by inserting the relative mean velocity $\hat{\mathbf{w}}_f$ provided by eq. (4.10) into the local form of the balance of mass given by eq. (4.11). Nevertheless, since fluid pressure \hat{p} and fluid density ρ^{iR} remain as

unknowns, a linear equation of state introduces a proportionality between both

$$\hat{p} = K^f \left[\frac{\rho^{fR}}{\rho_0^{fR}} - 1 \right] \quad (4.53)$$

by assuming a barotropic fluid with initial density ρ_0^{fR} at $t = 0$. Evaluation of the balance of mass and momentum combined with the density-pressure proportionality provided by eq. (4.53) finally leads to the governing equation for fluid flow and transport in the deformable fracture

$$\underbrace{\delta \frac{\partial \hat{p}}{\partial t}}_{\text{i)}} - \underbrace{\frac{\delta^3}{12 \eta^{fR}} \text{grad} \hat{p} \cdot \text{grad} \hat{p}}_{\text{ii)}} - \underbrace{\frac{\delta^2}{12 \eta^{fR} \beta^f} \text{grad} \delta \cdot \text{grad} \hat{p}}_{\text{iii)}} - \underbrace{\frac{\delta^3}{12 \eta^{fR} \beta^f} \text{div} (\text{grad} \hat{p})}_{\text{iv)}} + \underbrace{\frac{1}{\beta^f} \frac{\partial \delta}{\partial t}}_{\text{v)}} = \underbrace{\frac{\hat{q}_{lk}}{\beta^f}}_{\text{vi)}} \quad (4.54)$$

The scalar fluid pressure $\hat{p}(\mathbf{x}, t)$ defines the primary variable and reduces the dimension of the flow within the fracture by one. Within the hybrid dimensional formulation the fracture aperture $\delta(\mathbf{x}, t)$ depends on the deformation state of the surrounding poro-elastic bulk material and is a function of space and time. In eq. (4.54) the sum of the transient term i), quadratic term ii), convection term iii), diffusion term iv), volumetric coupling term v) and leak-off term vi) forms the general non-linear partial differential equation (PDE) for mass preserving fluid flow in a deformable fracture. Dimensionless analysis showed that the non-linear diffusion term ii) scales inversely with the fracture's aspect ratio (l^{Fr}/δ) and, considering its dependence on the aperture gradient, convection term iii) is of importance in limited regions close to the fracture tip once fracture surfaces are separated [206]. For the present study of high aspect ratio fractures below the limit of fracture surface separation terms ii) and iii) have a minor contribution to the overall solution and are neglected throughout the following numerical investigations. The leak-off term \hat{q}_{lk} is directly related to the normal seepage velocity $w_k^N = \hat{q}_{lk}$.

3.2 Hydro-Mechanical Processes in a Biphase Poro-Elastic Medium \mathcal{B}^{Pe}

The equations governing the flow processes in the fracture domain \mathcal{B}^{Fr} require information about the deformation state of the surrounding matrix \mathcal{B}^{Pe} to capture changes in volume and permeability based on the fracture aperture $\delta(\mathbf{u}^{\text{Fr}}(\mathbf{x}, t))$. The deformation state of the surrounding bulk material is obtained through a linear biphase poro-elastic formulation [20, 158, 190, 211] that will be introduced in the following. For a detailed derivation of the governing equations, the interested reader is referred to Schmidt & Steeb 2019.

3.2.1 Governing Equations

Let us assume, that the rock matrix can be described with a poro-elastic approach [20]. The phase index \mathfrak{s} denotes the solid phase, while \mathfrak{f} describes the fluid constituent. Quasi-static conditions are assumed. The compressibility of the mixture is taken into consideration by the dry solid skeleton K , the compressible grains bulk modulus $K^{\mathfrak{s}}$ of the solid constituent and the bulk modulus $K^{\mathfrak{f}}$ of the pore fluid constituent. The fluid-solid interaction is introduced by means of the additive split of the effective stress principle

$\boldsymbol{\sigma} = \boldsymbol{\sigma}_E^s - \alpha p \mathbf{I}$, where $\boldsymbol{\sigma}$ are the total stresses, $\boldsymbol{\sigma}_E^s = 3K \text{vol}(\boldsymbol{\varepsilon}_s) + 2\mu \text{dev}(\boldsymbol{\varepsilon}_s)$ are the effective stresses, $\alpha = 1 - K/K^s$ the Biot parameter and \mathbf{I} is the second order unity tensor [190, 211]. To close the coupled formulation for a biphasic poro-elastic medium the viscous momentum interaction of the fluid is assessed, stresses and strains are related by a linear-elastic constitutive law to evaluate the balance of momentum of the mixture and the already introduced barotropic assumption of eq. (4.53) is made, resulting in

$$\begin{aligned} -\text{div}(\boldsymbol{\sigma}_E^s - \alpha p \mathbf{I}) &= \rho \mathbf{b}, \\ \frac{\dot{p}}{M} - \frac{k^s}{\eta^{fR}} \text{div grad } p &= -\alpha \text{div } \dot{\mathbf{u}}_s, \end{aligned} \quad (4.55)$$

with the effective dynamic viscosity of the fluid η^{fR} , the intrinsic permeability k^s , the pore-fluid pressure p , the solid displacement \mathbf{u}_s , the body forces \mathbf{b} , the elastic strains $\boldsymbol{\varepsilon}_s$, the skeleton's (dry) shear modulus μ and the inverse storage capacity or (local) storativity $1/M = \phi_0/K^f + (\alpha - \phi_0)/K^s$ [211]. The fracture domain \mathcal{B}^{Fr} and the porous domain \mathcal{B}^{Pe} are defined by sets of leading equations (4.54) and (4.55). For a consistent, volume preserving formulation for embedded deformable fractures in a porous domain, the boundary conditions along the fracture surface will be discussed in detail.

3.3 Leading Interaction Boundary Conditions of Poro-Elastic \mathcal{B}^{Pe} and Fracture Domain \mathcal{B}^{Fr}

Along the fracture surface Γ^{Fr} , an implicit coupling of the fracture domain \mathcal{B}^{Fr} and the biphasic poro-elastic domain \mathcal{B}^{Pe} requires fulfillment of the strongly interdependent mechanical and flow equilibrium conditions at any time. Fig. 2 presents the mandatory mechanical and flow boundary conditions at the interface of the fracture. Mechanical equilibrium is enforced by a state of balanced fluid pressure $\hat{p} \mathbf{n}_{\pm}^{\text{Fr}}$ and surface traction $\mathbf{t}^{\text{Fr}} = -\boldsymbol{\sigma} \cdot \mathbf{n}_{\pm}^{\text{Fr}}$, where both are acting normal to the fracture surface. Flow equilibrium is met once no-flow boundary conditions at the fracture tip $\hat{\mathbf{x}}^{\text{Tip}}$ are fulfilled and the exchange flow between the poro-elastic and fracture domain is equivalent. The exchange flow terms are defined by means of the normal seepage velocity $\mathbf{w}_f^N = \mathbf{w}_f^N \cdot \mathbf{n}_{\pm}^{\text{Fr}}$ within the biphasic porous matrix and leak-off flow \hat{q}_{lk} in the fracture domain. Based on the governing equations of the poro-elastic formulation given by the set of eqs. (4.7) the normal seepage velocity \mathbf{w}_f^N is determined by consistent evaluation of the governing equation considering volumetric changes of the poro-elastic domain and compressibility effects of the conducted fluid. Assuming finite element discretizations the boundary term might be identified by applying Green's first identity [198]. Nevertheless, the characteristic of the domain coupling is still volumetric since the fracture fluid pressure \hat{p} , which evolution still depends on governing eq. (4.54) and volumetric coupling term v , is explicitly involved in the flow and mechanical Neumann boundary conditions. Finally, the coupling conditions along the intersection defined by fracture surface Γ^{Fr} are summarized below

$$\begin{aligned} \hat{q}_{lk} = \mathbf{w}_f^N / (\delta \beta^f) \quad \text{on } \Gamma^{\text{Fr}} \quad \text{and} \quad \hat{q}_{lk} = \hat{w}_f = 0 \quad \text{at } \hat{\mathbf{x}}^{\text{Tip}}, \\ \mathbf{t}^{\text{Fr}} = -\hat{p} \mathbf{n}_{\pm}^{\text{Fr}} \quad \text{on } \Gamma^{\text{Fr}}. \end{aligned} \quad (4.56)$$

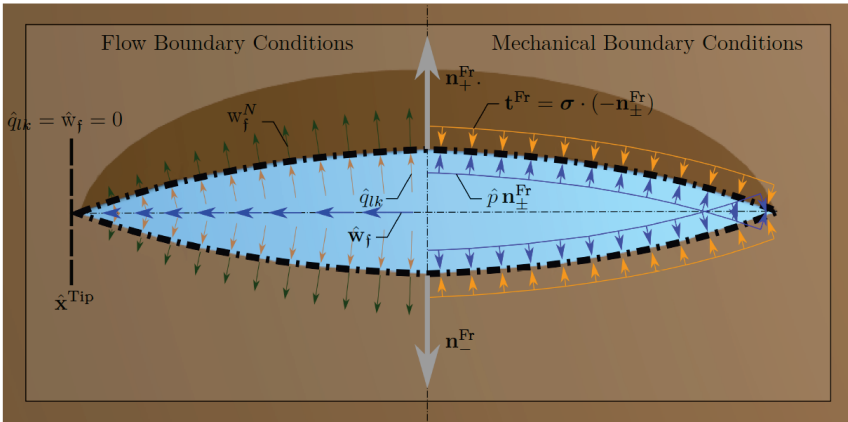


Figure 2: [

] Visualization of required mechanical and flow boundary conditions defined on the intersection surface Γ^{Fr} and the space dependent fracture normal vectors $\mathbf{n}_{\pm}^{\text{Fr}}(\hat{\mathbf{x}})$. Flow between both domains is described by means of the outflow \hat{q}_{lk} and normal seepage velocity $w_f^N = \mathbf{w}_f^N \cdot \mathbf{n}_{\pm}^{\text{Fr}}$ and no-flow requirements are introduced at the fracture tips $\hat{\mathbf{x}}^{\text{Tip}}$. The acting fluid pressure \hat{p} and the fracture surface traction \mathbf{t}^{Fr} define the mechanical boundary conditions.

3.4 Model for Field Scale Fracture Characterization Including an in-Situ Hydro-Mechanical Fracture Stiffness Formulation

Throughout the numerical, data-based characterization of fractures, the efficiency of the applied numerical model is of great importance. Physics-based reduction of the model introduced in section 4 is carried out to increase its performance while still governing the key physical phenomena. Additionally, a recently introduced fracture stiffness model [175] based on perturbations of the in-situ equilibrium state is discussed and motivated by investigations of acting forces on the micro- and macroscale.

3.4.1 Model Reduction Based on Characteristics of the Fracture Geometry and Porous Bulk Material

Numerical analysis of transient flow processes in hydraulically tested fractures is consulted to gain information about fracture characteristics such as the aperture dependent storage capacity S . In contrast, geometrical information about the fracture orientation and the relative intersection of the borehole with the fracture plane can be determined without the need for numerical calculations and might contribute to increase the quality of the deterministic model reduction. In this study, fracture orientation and positioning of the borehole motivate the assumption of a vertically oriented, circular fracture like proposed many times in the literature for different studies on fracture properties, e.g. [82, 157].

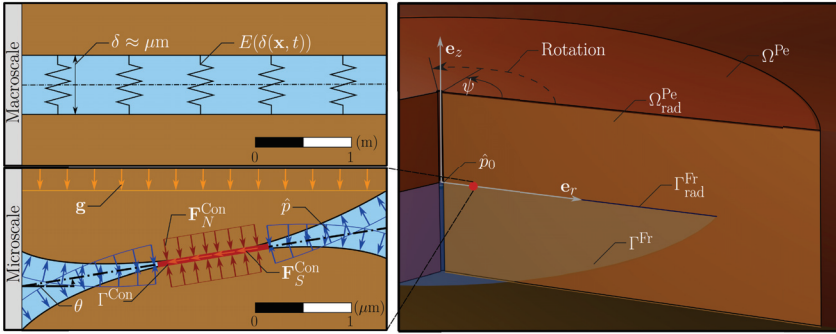


Figure 3: Right: Visualization of the three dimensional poro-elastic \mathcal{B}^{Pe} and the two dimensional fracture \mathcal{B}^{Fr} domain and its reduction to a two dimensional radial-symmetric poro-elastic \mathcal{B}_{rad}^{Pe} and one dimensional fracture domain \mathcal{B}_{rad}^{Fr} concerning rotation angle ψ and basis vectors \mathbf{e}_r and \mathbf{e}_z . The fracture possesses symmetry regarding the borehole which orientation might vary. **Left Top:** Approximation of fracture stiffness by non-linear elastic springs with an aperture dependent stiffness $E(\delta(\mathbf{x}, t))$ on the macroscale. **Left Bottom:** Representation of acting gravitational forces \mathbf{F}^g , fluid pressure \hat{p} , surface \mathbf{t}^{Fr} , contact induced normal \mathbf{t}_N^{Con} and shear \mathbf{t}_S^{Con} traction, contact Γ^{Con} and fracture mean surface Γ^{Fr} and deflection angle θ on the microscopic level for a specific contact point (marked in red) of the reduced fracture domain \mathcal{B}_{rad}^{Fr} .

Fig. 3 illustrates the computational domain for the surrounding biphasic porous matrix \mathcal{B}^{Pe} and the lower dimensional circular fracture domain \mathcal{B}^{Fr} in three, respectively two dimensions. Assuming that material properties and boundary conditions are independent of the rotation angle ψ , radial symmetry of the boundary value problem can be assumed which reduces the computational domains by one spatial dimension. The reduced model is defined by means of the two-dimensional area \mathcal{B}_{rad}^{Pe} for the poro-elastic formulation and the one-dimensional line segment \mathcal{B}_{rad}^{Fr} for the hybrid-dimensional flow model in combination with the cylindrical coordinate system spanned by the basis vectors \mathbf{e}_r and \mathbf{e}_z originated at the rotation center. Besides simplifications made with respect to the fracture's geometry, the time scale of the conducted step tests allows for decoupling of flow processes within the porous matrix and fracture domain in case of intact crystalline rocks with low permeabilities such as e.g. granite, since leak-off has a minor contribution to the total flow volume. Furthermore, the consideration of outflow into low permeable surrounding bulk material would lead to numerical instabilities due to the pronounced difference in characteristic pressure-diffusion times of the poro-elastic and fracture domain. Based on these investigations, the surrounding bulk matrix is simply treated as a linear-elastic material in the following numerical studies where Gassmann's effective low-frequency result [66, 127] is used to capture the effective poro-elastic response according to the modified linear-elastic material constants.

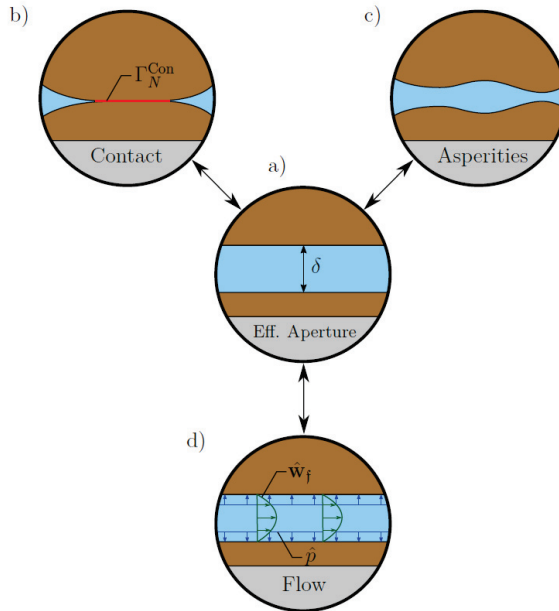


Figure 4: The effective fracture aperture δ a) is identified as a key parameter that explicitly connects mechanical phenomena such as fracture surface contact b) with geometrical aspects such as asperities c) and flow processes d) in the proposed model.

3.4.2 In-Situ Hydro-Mechanical Normal Fracture Stiffness Model

Fracture stiffness has been treated as a constant parameter, e.g., Cappa *et al.* 2006, is captured by empirically motivated formulations, e.g., Gothäll & Stille 2010, or expressed by a function of normal stresses acting on a volumetrically decoupled fracture surface [56, 109, 144] in the literature. In contrast to these concepts, we follow the approach of Pyrak-Nolte, Morris and Cook [40, 145, 147], and consider the fracture stiffness to be a parameter that identifies the equilibrium state of a fracture. The equilibrium state varies with hydro-mechanical perturbations of the in-situ conditions and results in a time and space-dependent non-linear fracture stiffness. The main processes involved in the characterization are introduced in Fig. 4 emphasizing the strong interaction between mechanical and hydraulic flow processes. In this context, aperture δ a) is identified as an effective property that interconnects the driving hydro-mechanical processes and geometrical properties of a fracture, namely the contact mechanism b), the asperities c) and the flow processes d). Its connecting characteristic implies that information about the initial effective fracture aperture $\delta_0(\mathbf{x})$ provides insights about the hydro-mechanical in-situ

state of a fracture. It might be calculated based on low-amplitude flow/pressure controlled (harmonic) field testing protocols to minimize the effect of mechanical fluctuations. Concluding, fracture stiffness and aperture equally depend on the hydro-mechanical state of a fracture, e.g. [89, 153, 157, 176]. Nevertheless, the fracture aperture is an effective geometric property that explicitly contributes to both, the mechanical and flow processes, which motivates the constitutive formulation of the fracture stiffness as a function of the fracture aperture $\delta(\mathbf{x}, t)$. This assumption is studied by a balance of acting forces on the microscopic fracture scale.

Equilibrium Conditions of Acting Forces on the Microscopic Level The constitutive normal stiffness model is motivated by an analysis of the acting forces on the microscale which are visualized in Fig. 3. Investigations of its characteristics are studied by means of the equilibrium condition in direction normal to the fracture's mean surface Γ^{Fr}

$$\sum F_i^N = \int_{\Gamma^{\text{Fr}}} \hat{p} \, da - \int_{\Gamma^{\text{Fr}}} \mathbf{t}^{\text{Fr}}(F^{\text{ext}}, F^{\mathbf{g}}) \cdot \mathbf{n}_{\pm}^{\text{Fr}} \, da + \int_{\Gamma^{\text{Con}}} \mathbf{t}_N^{\text{Con}} \cdot \mathbf{n}_{\pm}^{\text{Fr}} \, da = 0 \quad (4.57)$$

where $\mathbf{t}_N^{\text{Con}}$ is the contact induced surface traction, $\mathbf{t}^{\text{Fr}}(F^{\text{ext}}, F^{\mathbf{g}})$ the surface traction induced by external and gravitational forces, Γ^{Con} the varying contact surface and θ the deflection angle. For simplification the fluid pressure \hat{p} and the surface traction \mathbf{t}^{Fr} are assumed to act normal to the fracture mean plane Γ^{Fr} in eq. (4.57). Previous studies on the fracture stiffness decomposition into geometrical and contact induced stiffness during hydraulic testing identified the geometrical stiffness to be negligible under the limit of fracture separation [175]. Hydraulic characterization of tested fractures fulfills this criterion considering that applied fluid pressures are below the determined jacking pressure. To reduce complexity, we therefore neglected stresses which contribute to the geometrical stiffness, such as characteristic fracture tip stress fields, in eq. (4.57). The driving forces of the normal equilibrium are then identified as the fluid pressure \hat{p} , the normal surface traction induced by external forces $\mathbf{t}^{\text{Fr}}(F^{\text{ext}})$, the normal surface traction induced by gravitational forces $\mathbf{t}^{\text{Fr}}(F^{\mathbf{g}})$, the normal contact surface traction $\mathbf{t}_N^{\text{Con}}$ and the gravitational forces $F^{\mathbf{g}}$ as well as the fracture orientation defined by the deflection angle θ . The investigated excerpt of the measurement data does not indicate any pressure, flow or deformation responses characteristic for major shear events. The absence of significant fracture shearing indicates the minor contribution of shear induced fracture dilation to the total normal fracture deformation and motivates the neglect of the contact-induced shear surface traction $\mathbf{t}_S^{\text{Con}}$.

Macroscopic Constitutive Normal Stiffness Model Throughout studies on the field scale, fracture length might vary between tenth to hundreds of meters, and information about the explicit microscopic structure of the fracture surface with variations on the micrometer scale is not available. Upscaling of the flow processes in deformable fractures to the continuum level result in governing eq. (4.54), but requires a sufficient approximation of the effective fracture aperture change. Analysis of the acting normal forces on the microscale then found the normal traction \mathbf{t}^{Fr} , the normal contact traction $\mathbf{t}_N^{\text{Con}}$ and

the fluid pressure $\hat{p} \mathbf{n}^{\text{Fr}}$ to be the driving mechanisms throughout the identification of the fracture's equilibrium state. From governing eqs. (4.54) and (4.7) the fluid pressure \hat{p} and fracture surface traction $\mathbf{t}^{\text{Fr}}(F^{\text{ext}})$ induced by external forces can be determined, but the consideration of gravity-induced surface traction and contact on the continuum level need to be discussed. Contact between two fracture surfaces with a given roughness results in the deformation of a high number of contact zones of single asperities as (non-linear) Hertzian contact [40, 77, 197]. Contact behavior of mated/matching fracture samples and the resulting normal fracture stiffness variation might empirically be expressed as a function of the effective fracture aperture $\delta(\mathbf{x}, t)$ to correlate the acting normal stresses and total contact surface [12, 75]. In-situ fractures are in a state of mated surfaces responding with reversible deformation to perturbations of the equilibrium state below the limit of fracture surface separation and motivate the consideration of a non-linear elastic constitutive law [14, 147]. In this work, normal contact stress evolution within the fracture domain \mathcal{B}^{Fr} is captured by

$$\sigma_{\text{N}}^{\text{Con}} = E^{\text{Fr}} \frac{1}{\delta_{\text{max}}^{\text{c}} - \delta^{\text{c}}} \delta^{\text{c}} \quad (4.58)$$

where E^{Fr} is a parameter defining the fracture stiffness, δ^{c} the fracture closure which is initially zero and $\delta_{\text{max}}^{\text{c}}$ the maximum fracture closure [70, 181]. Contrary to most fracture stiffness studies under compression, hydro-mechanical testing on the field scale results primarily in opening of the hydraulically tested fracture. Determination of the fracture's in-situ state would require numerical approximations under consideration of the normal stress introduced by eq. (4.58) and gravitational body force effects. In strongly coupled hydro-mechanical simulations this procedure has a number of drawbacks such as, among others, the complex determination of the initial fracture aperture δ_0 obtained from fluid pressure - flow measurement data and explicit geometrical consideration of the fracture depth as a property closely related to the fracture's normal stiffness [97]. To overcome these difficulties the interpretation of the initial equilibrium fracture opening δ_{eq} as an parameter characterizing the fracture's in-situ state is conducted. Like proposed in [175] a shift of the acting normal stresses to the in-situ stress state is introduced by means of

$$\begin{aligned} \Delta \sigma_{\text{N}}^{\text{Fr}} &= \sigma_{\text{N}}^{\text{Fr}} - \sigma_{\text{N,eq}}^{\text{Fr}} \\ &= -E^{\text{Fr}} \left[\frac{\Delta \delta}{\left(\frac{\delta_0}{s_0} + \Delta \delta\right) - \delta_{\text{min}}} - \frac{\left(\frac{\delta_{\text{eq}}}{s_0} - \frac{\delta_0}{s_0}\right)}{\left(\frac{\delta_0}{s_0} + \left(\frac{\delta_{\text{eq}}}{s_0} - \frac{\delta_0}{s_0}\right) - \delta_{\text{min}}\right)} \right], \end{aligned} \quad (4.59)$$

where $\sigma_{\text{N,eq}}^{\text{Fr}}$ represents the acting in-situ stresses dependent on the initial equilibrium fracture aperture δ_{eq} , δ_0 is the initial fracture aperture under stress-free contact initiation and $s_0 \geq 1$ is a dimensionless parameter controlling the difference between the initial hydraulic and mechanical fracture aperture [175]. In eq. (4.59) consistency with the governing eq. (4.54) has been achieved by inserting the relations

$$\begin{aligned} \delta^{\text{c}} &= -(\delta - \delta_0) = -\Delta \delta, \\ \delta_{\text{max}}^{\text{c}} &= -\Delta \delta_{\text{max}} = -(\delta_{\text{min}} - \delta_0) \end{aligned} \quad (4.60)$$

to reformulate the constitutive normal-stress model given by eq. (4.58) with respect to the change in fracture aperture $\Delta \delta$, where δ_{min} denotes the minimal mechanical fracture

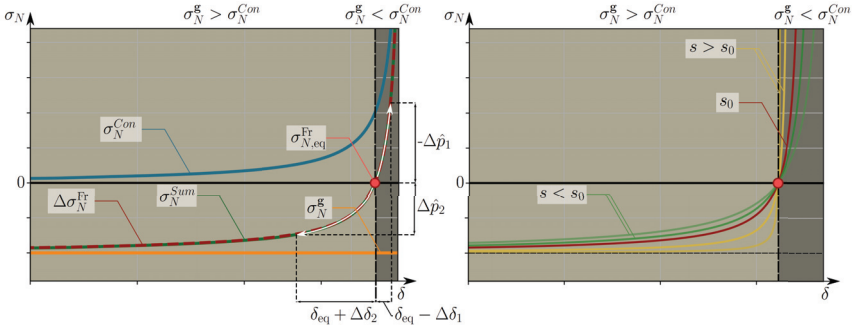


Figure 5: **Left:** Plot of relative normal stress changes $\Delta\sigma_N$ in dependence of the effective fracture aperture $\delta(\mathbf{x}, t)$ on the material point level for the case $\hat{p}_0 = 0$. Normal stresses are captured by the normal contact stress σ_N^{Con} , the normal equilibrium stresses $\sigma_N^{Fr,eq}$, the sum of contact and equilibrium stresses σ_N^{Sum} and the constitutive normal stress law $\Delta\sigma_N^{Fr}$ curves. Perturbations of the equilibrium state σ_N^{eq} caused by pressure fluctuations $\Delta\hat{p}$ result in changes of the effective aperture $\delta = \delta_{eq} + \Delta\delta$. **Right:** Modification of the contact characteristic by means of factor s leading to a softer contact for $s < s_0$ and a more discrete (stiffer) contact for $s > s_0$ when compared to the initial normal stress curve with $s = s_0$.

aperture. Mathematical manipulation of eq. (4.60) results in a formulation describing normal stress changes relative to the in-situ state

$$\Delta\sigma_N^{Fr} = -E_{eq}^{Fr} \frac{\Delta\delta}{\left(\frac{\delta_{eq}}{s_0} + \Delta\delta\right) - \delta_{min}} \quad (4.61)$$

and is closely related to eq. (4.58), where E_{eq}^{Fr} is the normal stiffness parameter of the equilibrium state. Fig. 5 shows the alignment of normal stresses σ_N^{Fr} calculated based on the proposed model defined by eq. (4.61) and the curve constructed by the sum of the on the normal equilibrium stresses $\sigma_N^{Fr,eq}$ and the by eq. (4.58) introduced contact related σ_N^{Con} normal stresses. Perturbations of the equilibrium state by pressure fluctuations around the in-situ pressure state result in a redistribution of the stress state and aperture changes. For instance, an increase of fluid pressure by $\Delta\hat{p}$ reduces the total contact surface, which translates to a decrease in normal contact stresses σ_N^{Con} and an opening of the effective fracture aperture by $\Delta\delta$. In case of fracture surface separation the proposed model reproduces the acting normal stress $\sigma_N^{Fr,eq}$. Dependent on the correlation of fracture surfaces the evolution of fracture stiffness might differ [145]. Alteration of normal contact stresses around a fixed equilibrium state are captured by an increase ($s > s_0$) or decrease ($s < s_0$) of the characteristic stiffness response to deformation. Nevertheless, to reduce the influence of additional fitting parameters on the pressure - flow relations in this work, the dimensionless parameter is considered to be $s_0 = 1$, introducing an equivalence of initial hydraulic and mechanical fracture aperture. For the sake of completeness, it should be noted that despite being negligible under the limit of hydraulic induced fracture separation, embedding of the fracture geometry in the poro-elastic domain results in implicit

consideration of the geometrical stiffness.

In this section a consistent formulation for flow in deformable fractures has been introduced by the governing equations eqs. (4.54) and (4.7). Further, it is reduced to a computationally efficient radial-symmetric, linear-elastic formulation. The physics-based constitutive eq. (4.61) captures the fracture stiffness and is strongly coupled to the deformation state by means of the effective aperture $\delta(\mathbf{x}, t)$ within the fracture domain \mathcal{B}^{fr} .

3.4.3 Applicability of the Proposed Model

The proposed model is specifically tailored to the numerical analysis of hydro-mechanical measurement data containing no evidence of irreversible fracture property changes. Despite introducing a high numerical efficiency, the model reduction is accompanied by a loss of general validity considering its insufficient complexity for investigations in the range of irreversible, hydro-mechanically induced changes of the tested region, such as a potential gain of permanent fracture volume; e.g., relevant for hydraulic stimulation strategies, being hydraulic shearing and/or fracturing. The applied radial symmetric formulation is prone to inaccurate predictions of heterogeneous flow phenomena and the neglect of shear induced fracture dilations leads to a slight overestimation of the dominant normal stiffness contribution to fracture opening. Previous studies investigated an insensitivity throughout the determination of an upper limit to the fracture length once flux/pressure transients converge towards a constant value [175]. This insensitivity is not specific to the proposed model, but arises from a lack of transient information caused by constant flux/pressure plateaus in the measurement data.

Despite the discussed limitations, the proposed model captures key mechanisms expected throughout hydraulic testing when considering the occurrence/absence of specific hydro-mechanical indicators in the present measurement data. Nevertheless, attention needs to be drawn to the necessity of a careful inspection of the experimental data sets to guarantee the absence of irreversible effects and to ensure the applicability of the present model. Once applicable, the combination of numerical analysis and hydro-mechanical measurement data provides valuable insights into the importance of hydro-mechanical interaction during hydraulic testing of fractures.

3.5 Model Parameters and Processing of Hydro-Mechanical Simulation Data

The material parameters of the surrounding bulk material are defined in Table 4.14 to describe the mechanical behaviour of a granitic rock where the effective parameters of the linear-elastic material formulation are calculated based on the introduced Gassmann's effective low-frequency result [66, 127]

$$K_{eff} = \frac{\phi_0 \left(\frac{1}{K^s} - \frac{1}{K^f} \right) + \frac{1}{K^s} - \frac{1}{K}}{\frac{\phi_0}{K} \left(\frac{1}{K^s} - \frac{1}{K^f} \right) + \frac{1}{K^s} \left(\frac{1}{K^s} - \frac{1}{K} \right)} \quad (4.62)$$

$$\mu_{eff} = \mu$$

The resulting numerical effective properties (Table 4.14) are closely related to the characteristic properties of Grimsel granite found in the literature [172, 182, 213]. The injected

Table 4.14: Parameters of the surrounding bulk matrix to model granite rock material

Quantity	Value	Unit	Quantity	Value	Unit
<i>Rock parameters</i>					
dry frame bulk modulus K	20.0	(GPa)	grain bulk modulus K^s	50.0	(GPa)
shear modulus μ	17.0	(GPa)	initial porosity ϕ_0	0.01	(-)
intrinsic permeability k^s	$5.0 \cdot 10^{-19}$	(m ²)	fluid compressibility β^f	0.417	(1/GPa)
effective bulk modulus K_{eff}	42.5	(GPa)	effective shear modulus μ_{eff}	17.0	(GPa)

water is treated as a slightly compressible fluid with bulk modulus $K^f = 1/\beta^f$. Fracture aperture changes $\Delta\delta$ are evaluated at a distance of 7 m to the injection borehole similar to the experimental set up and simulations are performed under pressure boundary conditions $\hat{p}_0(t)$ applied at the fracture-borehole intersection, matching the measurement protocol. Volumetric fracture changes and compressibility of the fluid prevent the calculation of the injected fluid flow based on the pressure \hat{p} - flow \hat{q} relationship defined by eq. (4.10) for results obtained from hydro-mechanical simulations. Governing equation (4.54) enforces global preservation of volume within the fracture domain \mathcal{B}^{Fr} and compensates injected fluid by a combination of fluid compression and volumetric fracture deformations. The total change in fluid volume ΔV_f within the fracture domain \mathcal{B}^{Fr} with respect to an equilibrium in-situ stage is equivalent to

$$\Delta V_f = \Delta V_f^c + \Delta V \quad (4.63)$$

once outflow into the surrounding matrix is negligible, where ΔV_f^c is the volume regarding to the compression of the fluid and ΔV is related to the volumetric deformation of the fracture. Volume changes related to the fluid compressibility $\Delta V_{\beta_f} = -V_0\beta_f\Delta\hat{p}$ are calculated based on isothermal compressibility assumptions using the updated element volume to determine volumetric fracture changes $\Delta V = \Delta\delta A_{El}$ based on the discretized, lower-dimensional fracture surface area of a single element $A_{El} = \int_{A_{El}} \det(\mathbf{J}_{El}) da_0$ where $\det(\mathbf{J}_{El})$ is the determinant of the Jacobian which arises when integration is performed with respect to the reference element area a_0 . Evaluation of the fluid flux considering a discrete time step is captured by $\hat{Q} = (\Delta V_f^1 - \Delta V_f^0)/\Delta t$ where ΔV_f^0 and ΔV_f^1 are the total injected volumes for two consecutive time steps and Δt the time step size. The representation of total injected volume by means of volume fractions helps to increase the understanding of driving hydro-mechanical mechanisms within fluid-filled, deformable fractures by an individual visualization of their contribution to the solution. The performed studies assume intact rock material and no connection between the tested and other pre-existing fractures which might lead to inaccuracies regarding the tested fracture system's capacity S , but serves best to determine leading mechanisms throughout hydraulic testing of single fractures. Parameters that are modified for each simulation will be introduced accordingly.

4 Results

Numerical fits of the consistent set of pressure \hat{p} , flow \hat{q} and deformation $\Delta\delta$ data provide insights into the initial equilibrium δ_{eq} and evolving effective fracture aperture $\delta = \delta_{\text{eq}} + \Delta\delta$. Based on the numerically determined aperture evolution, characteristic parameters such as the fracture's storage capacity S might be resolved by additional post-processing steps. Nevertheless, this work focuses on best numerical fits of the measurement data for the evaluation of the proposed model and investigations of hydro-mechanical fracture phenomena on the field scale rather than the determination of fracture parameters. Despite the intersection of two fractures with the borehole located within the region framed by the installed packers, the simulation is conducted on a single fracture first, and results are compared with a classical diffusion-based approach, before the outcome of simulations considering two parallel, interacting fractures will be discussed.

4.1 Comparison of the Fully-Coupled with a Diffusion-Based Model

Table 4.15: Parameters of the hydro-mechanical a) and diffusion-based model b).

Quantity	Value	Unit	Quantity	Value	Unit
Hydro-Mechanical Model a)					
initial equ. aperture δ_{eq}	62.5	(μm)	effective fluid viscosity η^{fR}	0.001	(Pa-s)
fluid compressibility β^f	0.417	(1/GPa)	fracture stiffness $E_{\text{eq}}^{\text{Fr}}$	2.1	(MPa)
contact characteristic s_0	1	(-)			
Diffusion Based Model b)					
initial equ. aperture δ_{eq}	80.0	(μm)	effective fluid viscosity η^{fR}	0.001	(Pa-s)
fluid compressibility β^f	0.417	(1/GPa)			
Geometrical Parameters					
domain length l	500.0	(m)	domain height h	100.0	(m)
hyd.-mech. fracture length a) $l_{\text{HM}}^{\text{Fr}}$	80.0	(m)	dif. fracture length b) l_{D}^{Fr}	320.0	(m)

Investigations of a single fracture are conducted to compare results obtained from a conventional, diffusion-based model b) to the results of the proposed hydro-mechanically model a) and to study their capability of gaining knowledge about flow processes based on hydro-mechanical measurement data. Assuming the existence of a single fracture allows the investigation of both models without any side effects triggered by the mechanical interaction of tested fractures. The governing equation of the diffusion-based approach b) is obtained by reducing eq. (4.54) to terms i) and iv) under the assumption of a rigid (undeformable) fracture saturated with a compressible viscous fluid. Parameters completing the set of model properties are introduced in Table 4.15. Approximately 15 000 degrees of freedom (DoF) were used for the hydro-mechanical model and 3 500 DoF for the pressure diffusion based model to achieve feasible computational times considering the necessity of multiple simulations throughout the parameter fitting procedure. The difference in DoF between both models arises from the neglect of deformation in the pressure diffusion model.

A comparison of the experimental data to the numerical results obtained by simulations

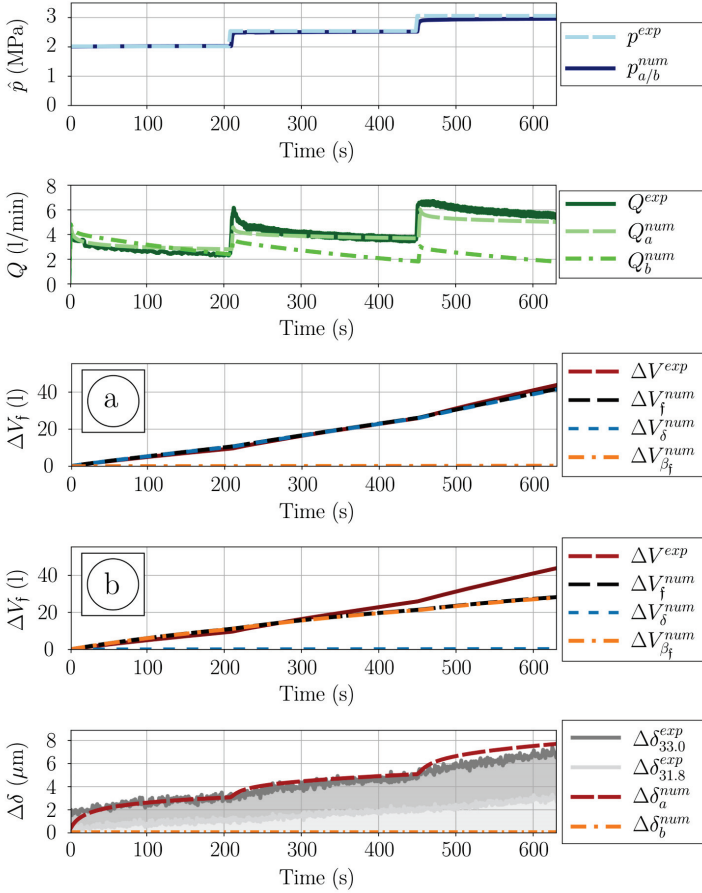


Figure 6: Comparison of numerical fits of the experimentally measured transients calculated by the proposed hydro-mechanical a) and a diffusion-based model b). **Top to bottom:** Injection fluid pressure \hat{p} , injection flux Q , total injected fluid volume ΔV_f decomposed into volume compensated by the compressibility of the fluid ΔV_f and volume compensated by fracture deformation ΔV for the hydro-mechanical model a) and diffusion based model b) and relative fracture deformation changes $\Delta\delta$.

based on the fully coupled model a) and pressure diffusion model b) are displayed in Fig. 6. Dirichlet pressure boundary conditions are applied in both simulations reproducing the experimentally controlled pressure steps by numerically increasing the applied pressure in three steps considering the maximum value of each recorded pressure level. Flux

results obtained by evaluating eq. (4.63) show slight deviations in the first and third step, but an overall close match to the measurement data for the fully coupled model a) and high deviations throughout the second and third injection step for results obtained with the diffusion model b). Fracture deformations obtained from the hybrid-dimensional implementation a) are aligning with the field measurements for the first two pressure steps and overestimate the volumetric change slightly for the third step. Based on the assumptions made, the diffusion-based model b) is not capable of taking any volumetric fracture changes into consideration and underestimates the transient volumetric fracture change drastically. This trend is also evident in the transient change of total injected fluid volume where the estimation based on the coupled formulation a) is in the range of the measured injection volume, whereas the diffusion-based model b) underestimates the total injection volume thoroughly. In order to numerically approximate the first pressure step, the diffusion-based model b) requires a numerical fracture length of $l_D^{\text{Fr}} = 320$ m which largely differs from the fracture length approximated by the hydro-mechanical model a) of $l_{\text{HM}}^{\text{Fr}} = 80$ m.

4.2 Modelling of Two Parallel Fractures

Table 4.16: Parameters of the hydro-mechanical model used throughout calculations made for two parallel fractures.

Quantity	Value	Unit	Quantity	Value	Unit
<i>Hydro-Mechanical Model</i>					
initial equ. aperture $\delta_{\text{eq}}^{31.8}$	46.5	(μm)	initial equ. aperture $\delta_{\text{eq}}^{33.0}$	54.5	(μm)
fluid compressibility β^f	0.417	(1/GPa)	effective fluid viscosity η^{fR}	0.001	(Pa·s)
fracture stiffness $E_{31.8}^{\text{Fr}}$	5.75	(MPa)	fracture stiffness $E_{33.0}^{\text{Fr}}$	4.5	(MPa)
contact characteristic $s_0^{31.8}$	1	(-)	contact characteristic $s_0^{33.0}$	1	(-)
<i>Geometrical Parameters</i>					
domain length l	500.0	(m)	domain height h	100.0	(m)
fracture length $l_{31.8}^{\text{Fr}}$	80.0	(m)	fracture length $l_{33.0}^{\text{Fr}}$	80.0	(m)

The simulation of flow processes in two parallel fractures is carried out by applying the proposed hydro-mechanical simulation model with parameters given in Table 4.16. The field measurements indicate that the previously introduced hydraulic fracture is connected to two natural fractures with similar orientation, intersecting the FBG sensor at 33.0 m borehole depth and a quartz vein which deformation was tracked by a FBG sensor at 31.8 m borehole depth. Throughout the hydraulic fracture procedure the region between the quartz vein and the host rock has been opened and can therefore be treated as a fracture in the numerical model. Since a single, superimposed set of strain transients is available for the two natural fractures, we incorporate both fractures into a single effective fracture in the numerical model. The quartz vein and both natural fractures are oriented normal to the acting principal normal stress motivating a parallel fracture assumption. The fracture length of each numerical fracture is equivalent to the fracture length of the single fracture considered in the previous study. This has mainly three reasons; a) the initial apertures of

both fractures are individually smaller than the one chosen for the single fracture study, b) the fractures are considered to be stiffer and additionally compete against each other in terms of dominant opening behaviour and c) the presence of flux convergence towards constant values in the investigated measurement data induces the discussed numerical insensitivity during fracture length analysis. To compensate for effects related to a) and b), the initial fracture volumes are chosen to be slightly higher. Due to the numerical insensitivity c), an increase in model complexity by individual variation of the fractures' length would lead to nondeterministic numerical results; i.e., different fracture length combinations result in similar numerical transients. This has been investigated during exploratory numerical simulations where we accounted for relative fracture length variations. Hence, we model the numerically investigated fractures by assuming equivalent fracture lengths. The numerical discretization of the boundary value problem results in a total of 36 000 DoF. Fracture deformations are evaluated for both fractures, namely $\Delta\delta_{31.8}^{\text{num}}$ and $\Delta\delta_{33.0}^{\text{num}}$, and compared to the experimentally obtained deformation data $\Delta\delta_{31.8}^{\text{exp}}$ and $\Delta\delta_{33.0}^{\text{exp}}$, whereas the combined numerical flux of both fractures is plotted in comparison to the total flux injected in the region framed by the installed packers during field measurements. A comparison of the experimental and numerical data is shown in Fig. 7. Throughout the numerical simulation of the investigated fractures, the applied pressure boundary conditions capture the measurement protocol by constant pressure increases considering the upper limit of each experimentally applied step. The resulting flux slightly overestimates the first flow-rate step, matches the second and slightly underestimates the experimental flow-rate for the third pressure level. A comparison of the transient fracture deformations shows close alignment with the measurement data for both fractures. Similar to the results shown in section 4 injected fluid volume is almost entirely compensated by volume changes of the fracture, whereas the contribution of the fluid's compressibility is negligible, resulting in a total injected fluid volume that approximates the field data well. In addition to the already introduced quantities flux, pressure, and deformation, the fracture stiffness is evaluated numerically to capture its transient evolution like displayed in Figs. 8 and 9. Best fits of the total flux and deformation data are obtained for fracture stiffness parameters of $E_{31.8}^{\text{Fr}} = 5.75 \text{ MPa}$ and $E_{33.0}^{\text{Fr}} = 4.5 \text{ MPa}$ respectively. For the limiting case of separated fracture surfaces, the model converges towards the normal stresses $\sigma_{N,31.8}^{\text{Fr}} = 5.75 \text{ MPa}$ and $\sigma_{N,33.0}^{\text{Fr}} = 4.5 \text{ MPa}$. The transient evolution of the local specific fracture stiffness shows a decrease with increasing injected fluid volume, and with increasing fluid pressure for both fractures. Close to the injection zone, mechanical interaction prevents a faster opening of fracture $\Gamma_{31.8}^{\text{Fr}}$ resulting in a decreased evolution velocity of its fracture stiffness.

5 Discussion

The results obtained from the comparisons conducted in section 4 proof the capability of the proposed hydro-mechanical model to reproduce consistent sets of pressure, fluxes, and deformation data. The strong coupling of local, respectively, global volume changes of the fracture to the fracture flow reproduces the non-linear pressure-flow relationship throughout increasing pressure steps below the limit of fracture surface separation. The tendency to slightly overestimate the first and underestimate the change in fluxes cor-

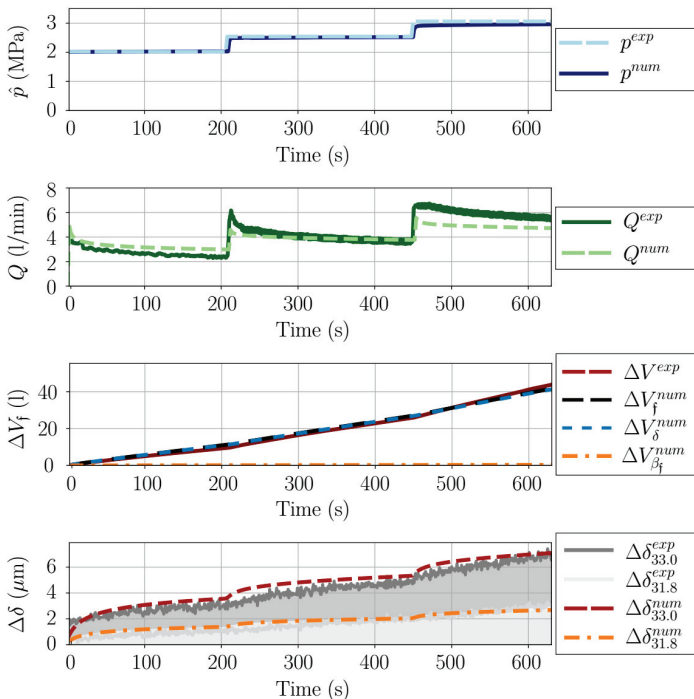


Figure 7: Numerical fits of the experimentally measured transients calculated by the proposed hydro-mechanical model for two parallel fractures. **Top to bottom:** Injection fluid pressure \hat{p} , injection flux Q , total injected fluid volume ΔV_f decomposed into volume compensated by the compressibility of the fluid ΔV_δ and volume compensated by fracture deformation ΔV and relative fracture deformation changes $\Delta\delta$.

responding to the highest pressure level might be caused by the absence of a profound constitutive relationship between hydraulic and mechanical effective fracture aperture that has been discussed in the literature [147, 155]. Still, the proposed model relies on the permeability/volumetric evolution based on the cubic law which serves as an upper bound for the pressure-flow relation [146]. This conservative approach avoids potential overestimation of volumetric changes corresponding to the fitting of additional modeling parameters. Once priorities shift towards higher accuracies of numerical fits to determine characteristic fracture properties, it is straight forward to extend the proposed model by a preferred constitutive relationship for the hydraulic aperture in future works. The derived contact-related normal stress evolution for in-situ conditions given by eq. (4.46) provides high accuracy throughout the reproduction of the measured fracture deforma-

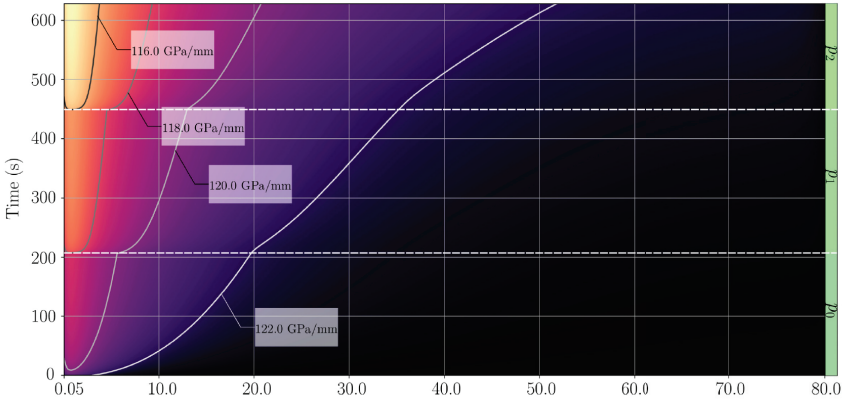


Figure 8: The specific fracture stiffness $\partial\sigma_{N,31.8}^{Fr}/\partial\Delta\delta_{31.8}^{sum}$ of fracture $\Gamma_{31.8}^{Fr}$ is plotted over the local fracture coordinate x^{Fr} and the investigated time range t . The color-map indicates lower values of the specific fracture stiffness by yellow and high values by black. Isolines introduce absolute values of the specific stiffness and visualize the evolution in time.

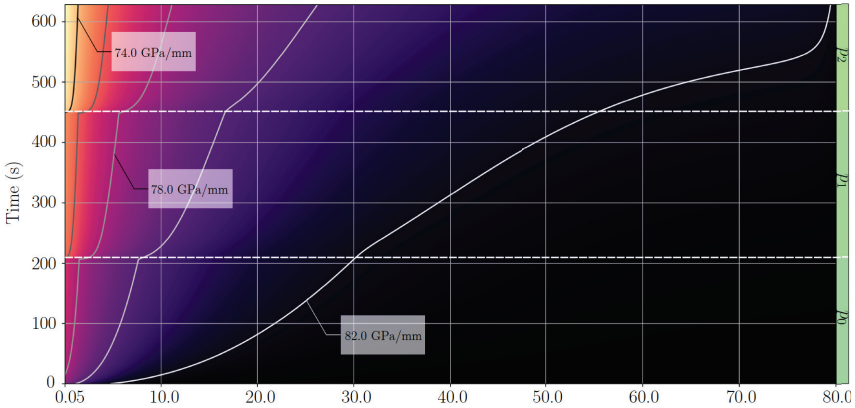


Figure 9: The specific fracture stiffness $\partial\sigma_{N,33.0}^{Fr}/\partial\Delta\delta_{33.0}^{sum}$ of fracture $\Gamma_{33.0}^{Fr}$ is plotted over the local fracture coordinate x^{Fr} and the investigated time range t . The color-map indicates lower values of the specific fracture stiffness by yellow and high values by black. Isolines introduce absolute values of the specific stiffness and visualize the evolution in time.

tion. For stiffness parameters obtained by best numerical fits of the experimental fracture deformation data, the proposed constitutive model converges towards normal stresses for increasing fracture opening which are consistent with findings from effective instantaneous shut-in pressure (ISIP) investigations [53]. The orientation of the investigated

fractures at depth 33.0 m can be assumed to be orthogonal to the orientation of the minimum principal stress. Hence, the normal stresses obtained from the proposed contact model for the limiting case of surface separation should be equal to the measured effective minimum stresses determined from the field data since geometrical stiffness of the investigated fracture has a minor contribution to the total fracture stiffness and can be neglected [175]. Agreement of the proposed effective minimum principal stress calculated by Dutler *et al.* 2020 of $\sigma_3 = 4.5$ MPa with the resulting normal stress obtained by the proposed model of $\sigma_{N,33.0}^{\text{Fr}} = 4.5$ MPa proves the consistency of both studies. Due to the slightly different orientation of the natural fracture at depth 31.8 m, normal stresses are expected to be in the range defined by the effective principal stresses σ_2 and σ_3 where lower indices indicate higher stress magnitudes. In case of fracture surface separation the normal stress acting on the natural fracture surfaces is predicted to be $\sigma_{N,31.8}^{\text{Fr}} = 5.75$ MPa and consistent with the findings of the stress state studies where the effective principal stresses are determined to be $\sigma_2 = 6.7$ MPa and $\sigma_3 = 4.5$ MPa. The consistency with the analysis of the characteristic stress state strengthen the assumptions made to identify the driving forces resulting in eq. (4.57) and especially the quality of the chosen constitutive model [175] for acting normal stresses under in-situ conditions. Besides the validation of the derived hydro-mechanical model, the main outcome of this study is the great influence of volume changes of a fracture on the flow transients and amplitudes due to perturbations of the equilibrium state by hydraulic pressure and vice versa. The split between volumetric compensation of injected fluid volume by fracture deformation and compressibility of the injected fluid introduced by eq. (4.63) allows a distinguished assessment of the driving mechanisms. The good alignment of measured and numerically determined fracture deformations guarantees that not only the fracture stiffness parameter is in a realistic range, but also the transient evolution of the total fracture volume is physically described. The numerically determined fracture lengths are overestimating the expected values from field investigations. Numerical overestimation of the fracture length has mainly two reasons; a) the discussed insensitivity of the numerical analysis to fracture length changes during the analysing of transients containing constant flow/pressure regimes and b) the incorporation of potentially intersecting, highly conductive fractures in a single fracture volume. Nevertheless, the results shown in section 4 clearly identify that injected fluid volume is compensated by fracture deformations, whereas the contribution of the fluid's compressibility is negligible. This statement strongly contradicts most inverse calculations based on pressure diffusion models and might be questioned, but is consistent with the experimental deformation transients. To better understand why diffusion-based approaches provide promising results, even though the physical assumptions made are not consistent with the experimental findings of this study, the hybrid-dimensional flow eq. (4.54) is conducted. Regarding the compressibility-related transient term i) and the deformation-related volumetric coupling term v) it could be observed that both possess the same mathematical characteristics since they are first derivatives in time and might potentially provide identical transient responses when parameters are chosen accordingly. This becomes obvious by assuming rather small constant pressure perturbations of the equilibrium state, guaranteeing minor alterations of characteristic flow parameters such as permeability. For these cases, diffusion-based models reproduce the transient characteristic of the flux response well by fitting a constant fracture aperture. Nevertheless, in

order to shift the results in their magnitude, the fracture volume needs to be modified by means of its length, respectively total initial fluid volume. This modification results in an overestimation of the initial fracture volume since neglect of deformation must be compensated by compression of an artificially enlarged initial fluid volume. Consulting the comparison of the hydro-mechanical model a) with the diffusion-based model b) shown in section 4 and focusing on the first pressure step the introduced scenario is reproduced by the numerical findings. Throughout the first pressure increase, the almost aligning flux solutions of both models provide fits of the same quality. Nevertheless, the predicted fracture length of the diffusion-based model is four times as large as the fracture length obtained from simulations with the hydro-mechanical approach. In order to reduce the introduced error in the context of diffusion-based models, the use of outflow boundary conditions might artificially compensate for the incorrect neglect of fracture deformation. In a second step, large perturbations of the equilibrium state causing non-negligible changes of the hydro-mechanical properties are investigated. Under such conditions, purely diffusion-based models fail since the formulation does not consistently account for the interaction of mechanical changes of the fracture geometry and flow processes in the fracture domain. Conducting the results shown in section 4 and focusing on the second and third pressure step, the results of the diffusion-based model b) clearly demonstrate the failure of the model for transient changes of the characteristic fracture properties. Nevertheless, extended diffusion-based models [139] capture local volumetric changes by means of local fracture storativity without explicitly modeling the deformation of the surrounding bulk matrix. This approach introduces another constitutive relation between pressure and fracture aperture on the material point; i.e., a local level to fit experimental data with non-negligible mechanical perturbations. Still, local relations between fracture deformation and pressure are not consistent in the context of fractures since fluid pressures act in an integral nature on the fracture surfaces resulting in non-local volume changes. Results from literature [206] indicate that the non-local deformation effect is not captured by models based on local pressure-deformation assumptions and introduces errors regarding the spatial resolution and temporal evolution of volumetric changes. A prominent example where such models fail to reproduce experimental findings is the phenomenon of reverse water-level fluctuations throughout the testing of fractures. In contrast, the hydro-mechanical model is able to reproduce this phenomenon since it is capable to consider fracture opening in regions that have not been reached by pressure diffusion. Non-local deformations can implicitly be found in the results shown in section 4 when investigating the evolution of iso-lines introduced for the specific stiffness related to normal contact $K^{\text{Fr}} = \partial\sigma_N^{\text{Fr}}/\partial\delta$ since the evolution does not correlate with the local pressure state, but the non-local fracture opening in Figs. 8 and 9. Comprehensive studies on the relationship between acting normal stresses and non-local deformations of tested fractures using the applied hydro-mechanical model exceed the scope of this work and might be content of following studies.

6 Conclusion

The presented work discusses the importance of hydro-mechanical coupling under in-situ conditions conducting the introduced hydro-mechanical model and a consistent set

of pressure, flux and deformation data obtained from field experiments at the Grimsel Test Site. The introduced constitutive relationship based on fracture surface contact and normal stresses related to fracture orientation and position captures in-situ normal stress conditions well and strengthens the assumptions made for the identified driving forces during flow processes in deformable fractures below the limit of fracture separation. Nevertheless, the main outcome of this study is the identification of fracture deformation as the dominant mechanism throughout injection of a weakly compressible fluid into fractures for small to moderate fluid pressure amplitudes. Based on the experimental and numerical results, the limitations of diffusion based models could be discussed and the importance of mechanical responses could be shown by a split of contributing deformation and compressibility related volumetric changes. The study emphasizes the importance of hydro-mechanical coupling in the context of characteristic fracture flow phenomena in the reversible regime and its necessity to extend the understanding of the investigated mechanisms to more complex fracture systems.

7 Acknowledgments

Holger Steeb and Patrick Schmidt gratefully acknowledge the funding provided by the German Federal Ministry of Education and Research (BMBF) for the GeomInt (I & II) project (Grant Numbers 03A0004E and 03G0899E) in the BMBF Geoscientific Research Program “Geo:N Geosciences for Sustainability”. Holger Steeb thanks the DFG for supporting this work under Grant No. SFB 1313 (Project No. 327154368).

Simulation of flow in deformable fractures using a quasi-Newton based partitioned coupling approach

Patrick Schmidt, Alexander Jaust, Holger Steeb, Miriam Schulte, Comput Geosci, November 2021, DOI:10.1007/s10596-021-10120-8

Abstract We introduce a partitioned coupling approach for iterative coupling of flow processes in deformable fractures embedded in a poro-elastic medium that is enhanced by interface quasi-Newton (IQN) methods. In this scope, a unique computational decomposition into a fracture flow and a poro-elastic domain is developed, where communication and numerical coupling of the individual solvers are realized by consulting the open-source library preCICE. The underlying physical problem is introduced by a brief derivation of the governing equations and interface conditions of fracture flow and poro-elastic domain followed by a detailed discussion of the partitioned coupling scheme. We evaluate the proposed implementation and undertake a convergence study to compare a classical interface quasi-Newton inverse least-squares (IQN-ILS) with the more advanced interface quasi-Newton inverse multi-vector Jacobian (IQN-IMVJ) method. These coupling approaches are verified for an academic test case before the generality of the proposed strategy is demonstrated by simulations of two complex fracture networks. In contrast to the development of specific solvers, we promote the simplicity and computational efficiency of the proposed partitioned coupling approach using preCICE and FEniCS for parallel computations of hydro-mechanical processes in complex, three-dimensional fracture networks.

1 Introduction

Modeling of transient flow processes in deformable high-aspect ratio fractures (length \gg aperture) embedded in a poro-elastic medium is a non-trivial task. Complex discretization of the fracture(-network) geometry and stiff numerical coupling of the surrounding poro-elastic and fracture-flow domain require specific implementations to guarantee stability and efficiency of the designed solver. In this work, we propose a highly efficient, straightforward implementation of the governing partial differential equations (PDEs) of each domain using the open-source package FEniCS [7] and realizing the numerical coupling process, its acceleration via quasi-Newton methods and inter-solver communication by the open-source library preCICE [31].

Phenomena such as the occurrence of reverse water-level fluctuations in distant monitoring wells during hydraulic testing of fractured reservoirs indicate the importance of hydro-mechanical interaction throughout fracture-flow processes [69, 185]. Perturbations of the reservoir's equilibrium state result in immediate non-local fracture deformations and time delayed pressure diffusion with distinct characteristic time scales, which highly affect the measured pressure transients. Once the fracture deformation influences the pressure evolution, traditional [60, 133] and extended [139] diffusion-based models fail and the necessity of consistent hydro-mechanical simulations arises [206]. Creeping flow conditions in high-aspect ratio fractures motivate to simplify the balance equations based

on pressure-driven, Poiseuille-type flow formulations [121, 216] to capture flow processes in deformable fractures. The resulting fracture-flow equation leads to a reduction of space dimension of the computational domain by one. Equivalently, the numerical implementation is introduced as a hybrid-dimensional model [206, 208], which can be simplified to the lubrication equation [16] by dimensional analysis considering the specific case of high-aspect ratio geometries [206].

The numerical approaches to solve the strongly coupled hydro-mechanical fracture-flow problem addressed in literature can be divided in two groups: (i) monolithic and (ii) partitioned schemes. Monolithic approaches introduce the fracture-flow domain by zero-thickness interface elements [98, 180, 181, 183] and mostly require direct solution strategies to guarantee high numerical stability since distinct characteristic properties of both domains lead to poor conditioning of the global system [177]. In general, tailored meshing and integration strategies are required to discretize the fracture domain by interface elements. The complexity dramatically increases in the presence of intersecting fractures or regions containing fracture tips. In contrast, partitioned schemes allow the individual treatment of the subdomain and, in particular, the use of non-conformal meshes [177]. However, iterative coupling of both domains is required to ensure global equilibrium for each conducted time step, which potentially makes this approach computationally more expensive. Therefore, stabilization and acceleration methods are used to keep the number of coupling iterations needed low. In the literature, numerical convergence and stability of the equilibrium iterations have been achieved by adapting physics-based preconditioning of unfractured [104, 105] to the specific case of fractured poro-elastic media [18, 38, 72, 73, 103]. Nevertheless, parallel communication within the proposed staggered algorithms is nontrivial, but required to solve large systems in reasonable time. Therefore, we propose an easily accessible, efficient and fully parallelized deformable fracture-flow implementation introducing a unique computational split of the fracture-flow and poro-elastic domain. It uses advanced quasi-Newton schemes for stabilization and acceleration of the coupling.

More specifically, we employ two separate solvers for (i) flow and mechanical deformation of the porous structure and (ii) flow in the fracture itself. This allows for the use of available, highly efficient and parallel solvers for each of these two subdomains. We avoid assembling the ill-conditioned monolithic system of equations. The coupling library preCICE [31] is used to establish and steer the iterative coupling between the two solvers. preCICE provides a generic coupling solution interface, that is not tailored to a specific use case. Its library approach makes it simple to use with a large variety of solvers. It comes with adapter codes for popular simulation software and a high-level interface for many popular programming languages. Additionally, it has been optimized for high computational efficiency by implementing several acceleration methods, including a number of interface quasi-Newton methods [171], parallel data communication [118, 120], and sophisticated data mapping techniques including radial basis function mapping [118, 119] for the use with non-matching grids. This sets preCICE apart from commercial or closed sourced alternatives such as MpCCI¹ [100], where one cannot access or change the implementa-

¹www.mpcci.de

tion. Other open-source alternatives such as ADVENTURE² [102], the Data Transfer Kit³ [186] or OpenPALM⁴ [30], e.g., are either lacking the high-level programming interface or combined implementation of highly-parallel data communication, coupling steering, sophisticated data mapping, and coupling acceleration. Combining the efficient iterative solvers in the subdomains with preCICE to realize the iterative coupling of both domains yields a fast and efficient overall solution technique. It eliminates the need to develop a specialized solver or preconditioner, respectively, for the corresponding monolithic system. Thus, our simulations of hydro-mechanical processes at high resolution and accuracy can be performed by simple high-level solvers written in Python based on the finite-element library FEniCS. We use the Python interface of preCICE since the recently developed FEniCS-preCICE adapter [160] had not been available and was lacking some functionality needed for the applications presented during the preparation of our work.

After briefly deriving the governing equations, see Sec. 2, and introducing the coupling scheme, see Sec. 3, we verify and investigate the proposed coupling approach for an academic test case (single fracture embedded in a three-dimensional poro-elastic domain) at high resolution. The results obtained by the staggered scheme are compared to a monolithic approach to proof consistency of both strategies in Sec. 4.1. Afterwards, we conduct a case study investigating the convergence behavior of different interface quasi-Newton schemes and their dependency on coupling specific parameters, see Sec. 4.1.1. We demonstrate the ability of this approach for large problems for three different meshes ranging from tens of thousands to several million degrees of freedom (DoF), see Sec. 4.1.2. Subsequently, the relevance of the proposed method for more complex applications is shown by two more challenging test cases. The first case focuses on flow processes in complex fracture networks on a short (minutes) time-scale, see Sec. 4.2, while, in the second case, flow through fractured porous media on a large time-scale (days up to years) is investigated, see Sec. 4.3. In summary, this work introduces a stable implementation for fully coupled, parallelized three-dimensional simulations of flow processes in deformable fractures, using an unique split of the computational fracture-flow and poro-elastic domain.

2 Governing Equations

We introduce the governing equations for both parts of our fracture system, the fracture(s) Γ^{Fr} and the surrounding poro-elastic \mathcal{B}^{Pe} domain, resulting in a coupled formulation capturing solid deformation and fluid flow in fractured porous media. For the fracture domain, we base our derivation on the observation that (i) deformation induced volume changes of high-aspect ratio fractures have a strong impact on the flow solution and require an implicit coupling to the surrounding solid domain; (ii) explicit three-dimensional modeling of flow processes in such fracture systems is challenging and leads to poor results in case of insufficient mesh quality.

We overcome these challenges by lower dimensional modeling of the fracture flow domain where the fracture aperture is implicitly treated as a function on a two-dimensional man-

²<https://adventure.sys.t.u-tokyo.ac.jp/>

³<https://ornl-cees.github.io/DataTransferKit/>

⁴<https://www.cerfacs.fr/globc/PALM.WEB/>

ifold. The value of this function is given by an initial opening value and the poro-elastic deformation of the surrounding porous medium.

2.1 Flow in a deformable fracture Γ^{Fr}

In the following, we derive a hybrid-dimensional model [206, 208] governing the flow processes in deformable high-aspect ratio fractures by evaluation of the balance of mass and momentum within the fracture domain Γ^{Fr} . Equilibrium conditions of the fluid and the biphasic porous medium are enforced in terms of fracture aperture δ and fluid pressure p .

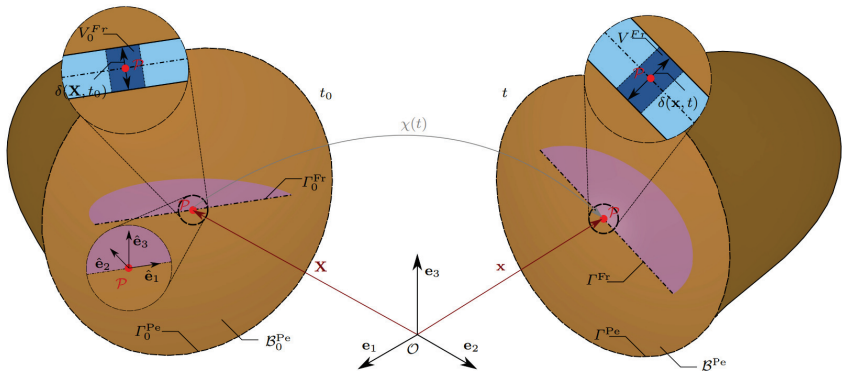


Figure 1: Three dimensional representation of an embedded fracture characterized by its surface Γ^{Fr} in a deformable poro-elastic body \mathcal{B}^{Pe} with its boundary Γ^{Pe} . A local coordinate system $\hat{\mathbf{e}}_i$ at the fracture level is introduced, where $\hat{\mathbf{e}}_3$ is pointing in the direction of the fracture surface normal \mathbf{n}^{Fr} . The volume V^{Fr} and aperture δ changes of the fracture between the reference configuration \mathbf{X} at time t_0 and the current configuration \mathbf{x} at time t of a material point \mathcal{P} are implicitly coupled to the poro-elastic deformations expressed by the unique motion function $\mathcal{X}(t)$.

2.1.1 Balance of Momentum

In our fracture model, the balance of momentum equation can be simplified drastically compared to the full Navier-Stokes equations for viscous and compressible fluids. Studies on flow processes in hydraulically transmissive fractures with low contact areas motivate the simplification to a pressure-driven Poiseuille-type flow between two parallel plates [206, 216] under creeping flow conditions. Assuming a quasi-static, deformation dependent fracture aperture

$$\delta = \mathbf{u}^+ \mathbf{n}_+^{\text{Fr}} + \mathbf{u}^- \mathbf{n}_-^{\text{Fr}}, \quad (4.64)$$

the geometrical characteristics of high-aspect-ratio fractures lead to predominant flow within the fracture plane. In eq. (4.64), we construct the effective fracture aperture δ based

on the jump \mathbf{u}^\pm in normal deformation over the fracture surface, where we introduced the fracture normal vector \mathbf{n}_\pm^{Fr} (see Fig. 2). Integration of the velocity profile of the respective Poiseuille-type (assuming no-slip boundary conditions at the fracture surfaces) yields the relative fluid velocity

$$\hat{\mathbf{w}}_f = -\frac{\delta^2(\mathbf{x}, t)}{12 \eta^{fR}} \hat{\text{grad}} \hat{p} = -\frac{k_{Fr}^s(\mathbf{x}, t)}{\eta^{fR}} \hat{\text{grad}} \hat{p}, \quad (4.65)$$

where η^{fR} denotes the fluid's effective dynamic viscosity and $k_{Fr}^s(\mathbf{x}, t) := \delta^2(\mathbf{x}, t)/12$ the space and time resolved effective fracture permeability⁵. Variables and mathematical operations defined by means of the fracture domain Γ^{Fr} are denoted with $\hat{\square}$ to avoid confusion with quantities and higher dimensional operations defined in the poro-elastic domain \mathcal{B}^{Pe} .

2.1.2 Balance of Mass

Mass conservation has to take into account volumetric changes and fluid compressibility β^f . For a given fluid compressibility $\beta^f = 1/K^f$ with respect to the fluid's bulk modulus K^f , the local mass balance reads

$$\frac{\partial(\rho^{fR} \delta)}{\partial t} + \hat{\text{div}}(\hat{\mathbf{w}}_f \rho^{fR} \delta) = w_f^N, \quad (4.66)$$

where w_f^N is the leak-off triggered seepage velocity of the porous domain normal to the fracture domain.

2.1.3 Governing Equations

The governing equation for the flow in deformable fractures is obtained by combining eq. (4.65) with the balance of mass in eq. (4.66). To close the set of governing equations, we introduce a linear equation of state for the fluid pressure $p \propto \rho^{fR}$

$$p = K^f \left[\frac{\rho^{fR}}{\rho_0^{fR}} - 1 \right]$$

where ρ_0^{fR} is the effective density at $t = 0$. This results in the governing equation

$$\underbrace{\delta \frac{\partial \hat{p}}{\partial t}}_{\text{I)}} - \underbrace{\frac{\delta^3}{12 \eta^{fR}} \hat{\text{grad}} \hat{p} \cdot \hat{\text{grad}} \hat{p}}_{\text{II)}} - \underbrace{\frac{\delta^2}{12 \eta^{fR} \beta^f} \hat{\text{grad}} \delta \cdot \hat{\text{grad}} \hat{p}}_{\text{III)}} - \underbrace{\frac{1}{12 \eta^{fR} \beta^f} \hat{\text{div}}(\delta^3 \hat{\text{grad}} \hat{p})}_{\text{IV)}} + \underbrace{\frac{1}{\beta^f} \frac{\partial \delta}{\partial t}}_{\text{V)}} = \underbrace{w_f^N / \beta^f}_{\text{VI)}}. \quad (4.67)$$

⁵Geometrical characteristics such as the fracture surface roughness can be governed by adaption of the proportionality factor $1/12$ [159].

Note that eq. (4.67) establishes a lower-dimensional non-linear partial differential equation for the pressure \hat{p} in the fracture, i.e., for a scalar unknown function. It consists of a transient term I), a quadratic term II), a convection term III), a diffusion term IV), a volumetric coupling term V) and a leak-off term VI). The leak-off term $\hat{q}_{lk} = w_f^N / \beta^f$ is related to the leak-off triggered seepage velocity w_f^N .

The authors of [206] have shown via a dimensional analysis, that the terms II) and III) can be neglected in the regime of high aspect-ratio fractures due to their minor contribution to the overall solution. Thus, the final form of the fracture flow equation reads

$$\delta \frac{\partial \hat{p}}{\partial t} - \frac{1}{12 \eta^{iR} \beta^f} \operatorname{div} \left(\delta^3 \operatorname{grad} \hat{p} \right) + \frac{1}{\beta^f} \frac{\partial \delta}{\partial t} = w_f^N / \beta^f \quad \text{in } \Gamma^{\text{Fr}}. \quad (4.68)$$

The reduced form introduced by this governing equation still consists of the pressure diffusion term II) and the volumetric coupling term V) which require an implicit, non-trivial coupling to the deformation state of the biphasic material. In case of fracture intersections, the lower dimensional formulation induces moderate inaccuracies of the flow field in limited regions close to the intersection [150]. In case of high aspect ratio fractures with apertures in the micrometer range, the deviating flow field in the intersection area on the overall solution is expected to be negligible and is, therefore, not considered in this work. Still, we compare the two resulting apertures at fracture intersections and choose the larger value considering that the fluid follows the path of highest permeability.

2.2 Partial Differential Equations in the Poro-Elastic Domain \mathcal{B}^{Pe}

Our fracture equation derived above calculates the pressure evolution for a given deformation and seepage velocity of the porous matrix. In this section, we present the respective biphasic poro-elastic formulation [20, 158, 211] for the porous medium. As the main emphasis of this work is on the hybrid-dimensional fracture flow formulation and its coupling to the porous medium, we introduce and explain the governing equations without any explicit derivation of the balance equations. A more detailed derivation of the poro-elastic formulation can be found in [177].

2.2.1 Governing Equations

The governing equations of the poro-elastic mixture consisting of a solid and a pore-fluid constituent that are studied under quasi-static conditions. The unknown functions are the pore-fluid pressure p and the solid displacement \mathbf{u}_s given by the following equations:

$$\left. \begin{aligned} -\operatorname{div}(\boldsymbol{\sigma}_E^s - \alpha p \mathbf{I}) &= \rho \mathbf{b}, \\ \frac{1}{M} \frac{\partial p}{\partial t} - \frac{k^f}{\gamma_0^{iR}} \operatorname{div} \operatorname{grad} p &= -\alpha \operatorname{div} \frac{\partial \mathbf{u}_s}{\partial t}, \end{aligned} \right\} \quad \text{in } \mathcal{B}^{\text{Pe}} \quad (4.69)$$

with

$$\boldsymbol{\sigma}_E^s = 3K \operatorname{vol}(\boldsymbol{\varepsilon}_s) + 2G \operatorname{dev}(\boldsymbol{\varepsilon}_s) + (1 - \alpha) p \mathbf{I}.$$

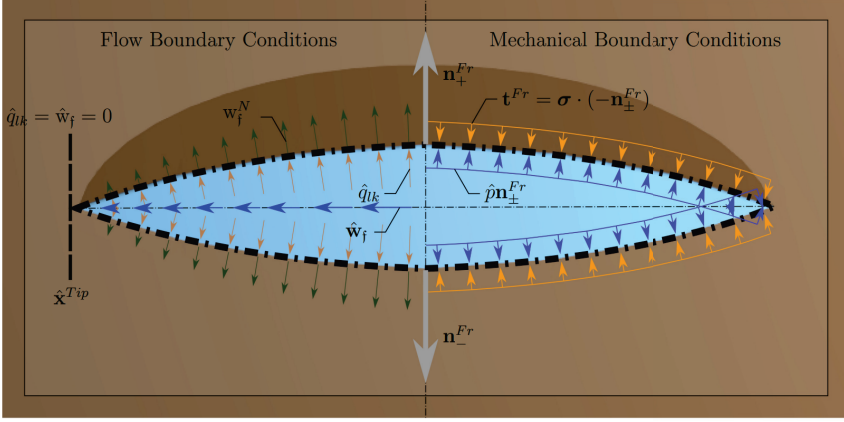


Figure 2: Representation of flow and mechanical coupling conditions along the fracture surface Γ^{Fr} . Fracture normal vectors $\mathbf{n}_{\pm}^{\text{Fr}}$ are introduced and can vary along the fracture surface dependent on the evaluation position $\hat{\mathbf{x}}$. Flow coupling conditions are characterized by the outflow $\hat{q}_{lk} = w_f^N / \beta^f$ and normal seepage velocity w_f^N in combination with a no-flow requirement at the fracture tips $\hat{\mathbf{x}}^{\text{Tip}}$. Mechanical coupling conditions are described with respect to the fracture surface traction \mathbf{t}^{Fr} and the acting fluid pressure \hat{p} [176].

The parameters are the Biot parameter $\alpha = 1 - K/K^s$, where K is the dry bulk modulus of the solid skeleton, K^s the bulk modulus of the compressible grains forming the skeleton and \mathbf{b} are the body forces. The (local) storativity or inverse storage capacity is defined by $1/M = \phi_0/K^f + (\alpha - \phi_0)/K^s$ with the bulk modulus K^f of the pore fluid and the porosity in the initial configuration $\phi_0 = \phi(t_0)$ of the mixture relating the partial and effective densities of the constituents. k^f is the Darcy permeability or hydraulic conductivity, γ_0^{FR} the effective weight at $t = t_0$, $\boldsymbol{\varepsilon}_s$ the elastic strain (split into a volumetric $\text{vol}(\boldsymbol{\varepsilon}_s)$ and a deviatoric $\text{dev}(\boldsymbol{\varepsilon}_s)$ part) and G the dry shear modulus of the skeleton [190, 211].

Compressibility of the porous material is modeled following the assumption of linear poroelasticity [20]. Fluid-flow processes and solid deformations within the fracture and porous domain are now governed by eq. (4.68) and eq. (4.69).

2.3 Coupling Conditions

For a consistent coupling of the fracture and the poro-elastic domain, the system needs to be closed by coupling conditions along the fracture surface. The respective equilibrium conditions along the fracture surface Γ^{Fr} as displayed in Fig. 2 extend eq. (4.68) and eq. (4.69) to a well-defined system of equations for the whole simulation domain comprising fractures and surrounding porous matrix. The equilibrium state of the fluid flow is reached, once equivalent exchange between the fracture zone and the poro-elastic matrix becomes apparent and no-flow boundary conditions at the fracture tips $\hat{\mathbf{x}}^{\text{Tip}}$ are

met. Flow exchange between both domains is governed by leak-off flow \hat{q}_{lk} within the fracture domain and the normal seepage velocity w_f^N within the poro-elastic matrix.

The equilibrium conditions of the mechanical state are met once surface traction $\mathbf{t}^{\text{Fr}} = -\boldsymbol{\sigma} \cdot \mathbf{n}_{\pm}^{\text{Fr}}$, defined by the total stresses $\boldsymbol{\sigma}$, and the fluid pressure \hat{p} acting normal to the fracture surface are balanced. Despite this definition of the coupled system's equilibrium state via surface terms, the physical nature of the coupling is volumetric. This is due to the fluid pressure \hat{p} being relevant for both, the fluid and mechanical boundary conditions. It is defined by the evolution equation eq. (4.68) consisting of the volumetric coupling term V). In conclusion, the necessary boundary conditions along the coupling interface are

$$\hat{q}_{lk} = w_f^N / \beta^f \text{ on } \Gamma^{\text{Fr}} \text{ and } \hat{w}_s = \hat{w}_f = 0 \text{ at } \hat{\mathbf{x}}^{\text{Tip}}, \quad (4.70a)$$

$$\mathbf{t}^{\text{Fr}} = -\hat{p} \mathbf{n}_{\pm}^{\text{Fr}} \text{ on } \Gamma^{\text{Fr}} \text{ and } \hat{p} = p \quad \text{on } \Gamma^{\text{Fr}}. \quad (4.70b)$$

2.4 Weak formulation of governing equations

We employ a Bubnov-Galerkin finite element scheme to introduce a spatial discretization to governing equations (4.67) and (4.69). Therefore, the weak form for each domain is introduced based on the principal of virtual work [e.g., 17].

2.4.1 Deformable fracture Γ^{Fr}

The weak form governing flow processes within the fracture domain Γ^{Fr} is introduced considering a trial function \hat{p}_t and a test function $w_{\hat{p}}$ for the fluid pressure \hat{p} , both required to be smooth enough for the applied mathematical operations. Further, the trial function \hat{p}_t must be suitable to reproduce the applied boundary conditions and the test function $w_{\hat{p}}$ needs to vanish in regions where Dirichlet boundary conditions are defined. Reduction of the smoothness demand on the trial function \hat{p}_t in the second term of eq. (4.67) is achieved by Green's first identity resulting in the implemented weak form

$$\int_{\Gamma^{\text{Fr}}} \left[\delta w_{\hat{p}} \frac{\partial \hat{p}_t}{\partial t} + \frac{\delta^3}{12 \eta^{\text{FR}} \beta^f} \hat{\text{grad}} w_{\hat{p}} \cdot \hat{\text{grad}} \hat{p}_t + w_{\hat{p}} \frac{1}{\beta^f} \frac{\partial \delta}{\partial t} \right] da + \int_{L_{Ne}^{\text{Fr}}} \frac{\delta}{\beta^f} w_{\hat{p}} \hat{\mathbf{w}}_f \cdot \mathbf{n}_{Ne}^f dl = \int_{\Gamma^{\text{Fr}}} w_{\hat{p}} \hat{q}_{lk} da. \quad (4.71)$$

In the presence of a lower-dimensional formulation evaluation of Green's first identity introduces a Neumann boundary term along a line segment L_{Ne}^{Fr} in eq. (4.71) which requires a brief discussion. Contrary to the leak-off term, which considers the fluid exchange with the surrounding poro-elastic domain regarding the normal seepage velocity, the introduced

Neumann boundary condition defined on $L_{N_e}^{Fr}$ considers the fluid exchange in longitudinal flow direction, i.e., relevant once the fracture domain is intersected by a borehole. The line segment $L_{N_e}^{Fr}$ then results from the intersection of the fracture domain with the intersecting geometry, where $\mathbf{n}_{N_e}^l$ introduces the outward pointing normal corresponding to the intersection area. On a side note, in many applications the explicit dependency of the boundary term on the fracture aperture δ vanishes, since it is implicitly considered by the Neumann boundary condition, i.e., when volumetric flow rate protocols are applied.

2.4.2 Poro-Elastic Domain \mathcal{B}^{Pe}

The weak form of the governing equations describing the hydro-mechanical response within the poro-elastic domain \mathcal{B}^{Pe} is introduced considering the test $w_{\mathbf{u}_s}$ and trial functions $\mathbf{u}_{s,t}$ for the solid deformation \mathbf{u}_s and the test w_p and trial p_t functions for the pore fluid pressure p . Their requirements regarding mathematical smoothness and fulfillment of boundary conditions are similar to those required from the test and trial functions introduced for the fracture domain. Evaluation of Green's first identity leads to the implemented weak form

$$\int_{V^{Pe}} \left(\boldsymbol{\sigma}_t^{E,s} - \alpha p_t \mathbf{I} \right) : \text{grad } w_{\mathbf{u}_s} \, dv = \int_{\Gamma_{N_e}^a} \bar{\mathbf{t}} \cdot w_{\mathbf{u}_s} \, da, \quad (4.72)$$

$$\int_{V^{Pe}} \left[w_p \frac{1}{M} \frac{\partial p_t}{\partial t} - \frac{k^f}{\gamma_0^{fR}} \text{grad } w_p \cdot \text{grad } p_t + w_p \alpha \text{div} \frac{\partial \mathbf{u}_{s,t}}{\partial t} \right] dv = \int_{\Gamma_{N_e}^f} w_p \bar{w}_f^N \, da.$$

In eq. (4.72) the seepage velocity \bar{w}_f^N represents normal flow conditions on the total Neumann boundary region of the poro-elastic domain $\Gamma_{N_e}^f$. The total Neumann boundary region includes the fracture surface specific region where the normal seepage velocity w_f^N is evaluated to describe the fluid exchange between fracture and poro-elastic domain. Further, we employ a mixed element formulation for the poro-elastic domain, namely Taylor-Hood elements, by introducing linear, first order elements for the pore fluid pressure and quadratic, second order elements for the solid deformation to guarantee numerical stability [28].

2.4.3 Fluid exchange boundary condition

Considering the fluid exchange of the biphasic poro-elastic domain with the fracture domain, the normal seepage velocity is constructed based on the residual state of the poro-elastic domain obtained for a prescribed fluid pressure along the fracture surface matching the fluid pressure state of the fracture domain. Under the consideration of Green's theorem, the reconstruction is given by inserting the obtained solution fields into the right

hand side of

$$\int_{\Gamma^{\text{Fr}}} w_p w_f^N da = \int_{V^{\text{Pe}}} \left[w_p \frac{1}{M} \frac{\partial p_t}{\partial t} - \frac{k^f}{\gamma_0^{\text{fR}}} \text{grad } w_p \cdot \text{grad } p_t + w_p \alpha \text{div} \frac{\partial \mathbf{u}_{s,t}}{\partial t} \right] dv \quad (4.73)$$

When considering a finite element discretization we refer to [e.g., 214, sec. 1.2.] for the node wise evaluation of eq. (4.73). The obtained normal seepage velocity can then be applied within the fracture domain in terms of the right hand side of eq. (4.71) where we account for the leak-off term by $\hat{q}_{lk} = w_f^N / \beta^f$ like introduced in eq. (4.70a).

2.4.4 Treatment of the Poro-Elastic Response on Different Time Scales

Investigations of systems involving (crystalline) rock characterized by a low permeability, perturbations in the low frequency range ($\ll 100$ Hz), under undrained conditions, and with a low viscous pore fluid motivate the application of Gassmann's effective low-frequency result [66, 127]. Considering pore pressure effects by effective parameters in a single-phase, solid formulation introduces two major numerical advantages since a) the number of degrees of freedom considered in the rock domain is reduced and b) numerical instabilities due to distinct diffusion times of the rock and the fracture domain can be avoided. Still, investigation periods must be considerably small compared to the characteristic diffusion time of the rock matrix to ensure the negligible contribution of leak-off effects. The effective parameters based on Gassmann's effective low-frequency result are determined by

$$K_{\text{eff}} = \frac{\phi_0 \left(\frac{1}{K^s} - \frac{1}{K^f} \right) + \frac{1}{K^s} - \frac{1}{K}}{\frac{\phi_0}{K} \left(\frac{1}{K^s} - \frac{1}{K^f} \right) + \frac{1}{K^s} \left(\frac{1}{K^s} - \frac{1}{K} \right)}, \quad (4.74)$$

$$G_{\text{eff}} = G.$$

Here, K_{eff} is the effective bulk and G_{eff} the effective shear modulus. The poro-elastic effects are governed by the effective Gassman modulus K_{eff} . In this work, we assume isotropic linear elasticity of the surrounding bulk material (with effective elastic parameters K_{eff} and G_{eff}) to avoid numerical instabilities in the pore pressure solution once the introduced coupling conditions eq. (4.70) are fulfilled.

3 Partitioned coupling

The coupling of the poro-elastic medium and the fracture flow is realized using partitioned coupling methods instead of a monolithic solver, i.e., we solve the equations for the fracture domain Γ^{Fr} eq. (4.68) and poro-elastic domain \mathcal{B}^{Pe} Alex eq. (4.69) separately. The coupling conditions eq. (4.70a) and eq. (4.70b) are then enforced via suitable boundary conditions for the subdomains, see Fig. 2, and iterative exchange of the respective boundary values within a time step.

We use a fracture solver F that maps a seepage velocity w_f^N and an aperture δ to a pressure p by executing a discrete time step for eq. (4.68). The corresponding porous

medium solver S maps the pressure p at the fractures back to a seepage velocity w_f^N and an aperture δ by executing a time step for eq. (4.69) while deriving w_f^N and δ via eq. (4.73) and the difference between displacements \mathbf{u}^\pm at both sides of the fracture. This can be considered equivalent to the typical approach in classical fluid-structure interactions (FSI) with elastic solid structures as Dirichlet-Neumann domain decomposition approach [47, 58, 130]. Note that there are two major differences compared to classical FSI: (i) the fluid domain is modeled with a lower-dimensional simplified equation and, thus, the transferred aperture and seepage velocities are not boundary conditions in the strict sense; (ii) the fluid exchange between porous matrix and fractures and the compressibility of the porous structure and the fluid might be a factor that makes our problem less prone to instabilities than FSI, in particular with incompressible fluids. A potential third point are the relatively large fracture aperture changes that appear in the first time step for most applied boundary conditions. This makes the coupled problem hard to solve in the very beginning which is also the case for the studied test cases in this work.

By iteratively solving one of the fixed-point equations

$$S \circ F(\delta, w_s^N) = (\delta, w_s^N) \quad \text{or} \quad (4.75a)$$

$$\begin{pmatrix} F(\delta, w_s^N) \\ S(p) \end{pmatrix} = \begin{pmatrix} p \\ (\delta, w_s^N) \end{pmatrix}, \quad (4.75b)$$

we, thus, ensure fulfilment of all equations and coupling conditions at the new time step. In this formulation, input and output of F and S refer to the end point of the respective time step.

One of the main advantages of the approach presented here is that it allows for “black box” coupling, i.e., we can reuse existing solvers that have been tailored for the problems in the subdomains. If we can provide an efficient iterative scheme to solve eq. (4.75), we do not have to develop a dedicated solver for the overall highly ill-conditioned system of equations that arises from the monolithic approach, either. Note that, despite of the equilibrium state definition for the coupled system via the fracture surface, the nature of the coupling from the point of view of the fracture domain Γ^{Fr} is volumetric. This is due to the involvement of the fluid pressure \hat{p} in both, the fluid and mechanical boundary conditions, which is defined by evolution equation eq. (4.67) incorporating the volumetric coupling term V).

3.1 Iterative Coupling

We present different options to solve eq. (4.75) within each time step. These options have been presented before in [31, 45, 46, 171] and evaluated for classical FSI problems. In this work, we analyze their potential for the lower-dimensional fracture flow problem. The cheapest version in terms of cost per time step, but in general known to generate unstable time stepping is the *explicit coupling* where each solver is executed only once per

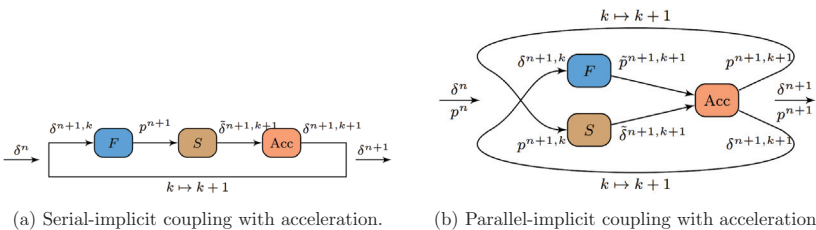


Figure 3: Sketch of the used coupling schemes. For the sake of readability, we display the case without the normal seepage velocity w_s^N .

time step, i.e.,

$$(\delta^{(n+1)}, w_s^{N,(n+1)}) = S \circ \underbrace{F(\delta^{(n)}, w_s^{N,(n)})}_{=: p^{(n+1)}} \quad \text{or} \quad (4.76a)$$

$$\begin{pmatrix} p^{(n+1)} \\ (\delta^{(n+1)}, w_s^{N,(n+1)}) \end{pmatrix} = \begin{pmatrix} F(\delta^{(n)}, w_s^{N,(n)}) \\ S(p^{(n)}) \end{pmatrix}, \quad (4.76b)$$

where the superscript (n) denotes the discrete solution at time t_n . Note that the first option in eq. (4.76b) implies a sequential one-after-the-other execution of the two solvers F and S , where S already uses the “new” pressure $p^{(n+1)}$ as an input, whereas, in the second option, both solvers can be executed simultaneously. Explicit coupling cannot capture the strong physical interaction between the fracture and porous matrix and is not considered further.

Implicit coupling can be achieved via fixed point iterations

$$(\delta^{(n+1),i+1}, w_s^{N,(n+1),i+1}) = S \circ \underbrace{F(\delta^{(n+1),i}, w_s^{N,(n+1),i})}_{=: p^{(n+1),i+1}} \quad \text{or} \quad (4.77a)$$

$$\begin{pmatrix} p^{(n+1),i+1} \\ (\delta^{(n+1),i+1}, w_s^{N,(n+1),i+1}) \end{pmatrix} = \begin{pmatrix} F(\delta^{(n+1),i}, w_s^{N,(n+1),i}) \\ S(p^{(n+1),i}) \end{pmatrix}. \quad (4.77b)$$

The first equation refers to a *serial-implicit*, cf. 3a, and the second equation to a *parallel-implicit* coupling, cf. 3b. In the figures, an additional element, the so-called acceleration scheme, is shown. This numerical component generates an improved next iterate based on the output of the respective fixed-point iteration either by under-relaxation or interface quasi-Newton (IQN) methods. To simplify the notation in the following, we use the general formulation

$$H(a) = a \quad (4.78)$$

with a vector of unknowns $a \in \mathbb{R}^m$ at the fractures and the fixed-point operator $H : \mathbb{R}^m \mapsto \mathbb{R}^m$ for both variants of fixed-point equations in eq. 4.75.

We write the general accelerated version of the fixed-point iterations in eq. (4.77b) as

$$a^{i+1} = \mathcal{A}(H(a^i)),$$

with the acceleration operator \mathcal{A} . A straight-forward option to realize the acceleration is to use underrelaxation,

$$a^{i+1} = \omega H(a^i) + (1 - \omega)a^i, \omega \in]0; 1], \quad (4.79)$$

e.g., based on a dynamic Aitken scheme [113]. A more advanced approach is to reuse past iterates to establish quasi-Newton iterations [45, 46, 84]⁶:

$$a^{i+1} = \tilde{a}^i + \Delta \tilde{a}^i \quad \text{with} \quad \Delta \tilde{a}^i = J_{\tilde{R}}^{-1}(\Delta \tilde{a}^i) \tilde{R}(\Delta \tilde{a}^i),$$

with $\tilde{a}^i := H(\tilde{a}^i)$, the modified residual $\tilde{R}(\tilde{a}) := \tilde{a} - H^{-1}(\tilde{a})$, and $J_{\tilde{R}}^{-1}(\tilde{a}^i)$ as an approximation of the inverse of the Jacobian of \tilde{R} .

To compute $J_{\tilde{R}}^{-1}(\tilde{a}^i)$, we collect input-output information from past iterates of H in tall and skinny matrices $V_i, W_i \in \mathbb{R}^{m \times i}$, $m \gg i$,

$$\begin{aligned} V_i &= \left[\tilde{R}(\tilde{a}^1) - \tilde{R}(\tilde{a}^0), \tilde{R}(\tilde{a}^2) - \tilde{R}(\tilde{a}^1), \dots, \tilde{R}(\tilde{a}^i) - \tilde{R}(\tilde{a}^{i-1}) \right], \\ W_i &= \left[\tilde{a}^1 - \tilde{a}^0, \tilde{a}^2 - \tilde{a}^1, \dots, \tilde{a}^i - \tilde{a}^{i-1} \right]. \end{aligned}$$

The matrices V_i and W_i define the multi-secant equations for the inverse Jacobian

$$J_{\tilde{R}}^{-1}(\tilde{a}^i) V_i = W_i. \quad (4.80)$$

To get the classical interface quasi-Newton inverse least-squares (IQN-ILS) method [45, 46], we close eq. (4.80) by

$$\|J_{\tilde{R}}^{-1}(\tilde{a}^i)\|_{F \rightarrow \min}.$$

For time-dependent problem, we have to solve the coupling problem for every time step n . We can extend the notation of V_i and W_i to V_i^n and W_i^n to emphasize the collection of differences in the current time step. In this case, the convergence of the quasi-Newton method can be improved by additionally consider information of previous time steps, i.e. to use $V_i^{n-1}, V_i^{n-2} \dots$ and $W_i^{n-1}, W_i^{n-2} \dots$. This is referred to as *reuse* of time steps method. However, we cannot store information from an infinite amount of time due to memory restrictions and since information can be outdated. Thus, we define a reuse parameter m that defines for how long information is retained, i.e., we keep $V_i^{n-1}, V_i^{n-2}, \dots, V_i^{n-m}$ and $W_i^{n-1}, W_i^{n-2}, \dots, W_i^{n-m}$. If there are many coupling iterations per time step and, thus, the matrices V_i^n and W_i^n are very large, this can lead to excessive memory requirements as well. To avoid storing the information of too many time steps, we also define the iteration reuse parameter M that limits how many data pairs over previous coupling iterations and time steps may be kept in total.

An alternative to IQN-ILS is based on the multi-vector (MV) approach [24]. The multi-secant equation eq. (4.80) is closed by

$$\|J_{\tilde{R}}^{-1}(\tilde{a}^i) - J_{\tilde{R}}^{-1}(\tilde{a}^{\text{prev}})\|_{F \rightarrow \min}$$

⁶To avoid linear dependencies between information from previous iterations, modified Newton iterations starting from the result of the pure fixed-point iteration are used (for details, see [203]).

where $J_{\tilde{R}}^{-1}(\tilde{a}^{\text{prev}})$ is the approximation of the inverse Jacobian from the previous time step. The method is also referred to as interface quasi-Newton inverse multi-vector Jacobian (IQN-IMVJ) method [171]. In contrast to the IQN-ILS method, we do not need to store information from previous time steps explicitly, since the information is kept by the explicit incorporation of $J_{\tilde{R}}^{-1}(\tilde{a}^{\text{prev}})$ in the minimization condition. However, this also leads to increased memory and runtime requirements for an increasing number of time steps, as the amount of information stored in $J_{\tilde{R}}^{-1}(\tilde{a}^i)$ and, thus, its size increases. Therefore, we use a IMVJ flavor with periodic restart to reduce runtime complexity and storage requirements.

After number η time steps, the method computes a singular value decomposition (SVD) of the approximated Jacobian and drops all information connected to singular values smaller than a user-specified threshold ε_{SVD} . We refer to this restart method as RS-SVD (restarted via singular value decomposition). For a detailed derivation and analysis of this restarted method, we refer to [171]. Main advantages over the ILS method are the low number of parameters and that it showed less dependency on the choice of coupling parameters.

Both quasi-Newton methods may suffer from a lack of stability, if the columns in V_i become (nearly) linearly dependent. Therefore, additional stabilization of the numerical method is achieved by filtering to remove such nearly linearly dependent columns. In this work, we use a QR filter, also called QR2 filter, which constructs the QR decomposition $QR = V_i$ and drops columns that do not add sufficiently much new information to the problem based on a user-defined filter limit ε_{F} . A detailed description of this filtering technique and a comparison with other filter techniques can be found in literature such as [83, 171].

All grids used in this work are generated such that the location of the degrees of freedom in both domains matches on the coupling interface, i.e., the grids are matching. In general, preCICE also allows for non-matching meshes by mapping data between the meshes. A variety of different mapping methods such as low order nearest-neighbor projection or higher-order approaches using radial basis functions are available for the mapping. However, the introduction of data mapping increases the parameter space for the evaluation of the numerical stability and efficiency of the investigated coupling approach. Therefore, we limit this work to matching grids and leave the study of different data mapping methods and their influence on the coupling for future work. Implementation details of the partitioned coupling methods, including the efficient parallelization, data-mapping techniques etc., are out of the scope of this work. Instead, we refer to the reference paper of preCICE [31] and the references therein.

4 Numerical results

Computational efficiency and flexibility of the proposed partitioned coupling algorithm allow numerical investigations of non-trivial flow processes in deformable, arbitrarily fractured porous media in three dimensions for realistic initial aperture openings in the micrometer range. The capacity of the proposed method is shown throughout a number of numerical studies. First, the implementation of the partitioned scheme is verified by

Table 4.17: Parameters defining the validation boundary value problem.

Quantity	Value	Unit	Quantity	Value	Unit
Numerical parameters					
solid depth $d_{\mathcal{B}_s^{\text{Pe}}}$	10.0	[m]	solid width $w_{\mathcal{B}_s^{\text{Pe}}}$	10.0	[m]
solid height $h_{\mathcal{B}_s^{\text{Pe}}}$	10.0	[m]	fracture radius $r_{\Gamma_s^{\text{Fr}}}$	1.25	[m]
well diameter d_w	0.28	[m]	solid vertices part.	$8.3 \cdot 10^4$	[-]
fracture vertices part.	$3.8 \cdot 10^3$	[-]	solid vertices mono.	$4.4 \cdot 10^4$	[-]
fracture vertices mono.	$1.0 \cdot 10^3$	[-]	time step size Δt	0.1	[sec]
Rock parameters					
dry frame bulk modulus K	8.0	[GPa]	grain bulk modulus K^s	33.0	[GPa]
shear modulus G	15.0	[GPa]	initial porosity ϕ_0	0.01	[-]
intrinsic permeability k^s	$1.1 \cdot 10^{-19}$	[m ²]	fluid compressibility β^f	0.45	[1/GPa]
effective bulk modulus K_{eff}	29.1	[GPa]	effective shear modulus G_{eff}	15.4	[GPa]
Fracture parameters					
initial aperture δ_0	50.0	[μm]	effective fluid viscosity η^{fR}	0.001	[Pa·s]
fluid compressibility β^f	0.45	[1/GPa]	injection pressure \tilde{p}_i^s	200.0	[kPa]
Coupling Parameters					
coupling	serial-implicit		quasi-Newton	ILS	
filter	QR2		initial relaxation ω	0.001	[-]
rel. convergence	10^{-6}	[-]			

a comparison to a reference solution (computed by a monolithic approach) for a simple boundary value problem consisting of a single embedded fracture. Afterwards, the efficiency and robustness of the method is explored carrying out a study on the convergence behavior of the interface quasi-Newton schemes and their dependence on coupling parameters such as reuse m , restart η , and filter limit ε_F . The mesh dependency of the solution is investigated via parallel computations on meshes ranging from tens of thousand to several million degrees of freedom. The work is closed by demonstrating the potential of the approach to answer relevant questions in a broad range of fields including the inverse analysis of pumping operations and investigations related to nuclear waste disposal; two fields that clearly require computations with distinct boundary conditions and time scales.

The implementation of the proposed strategy uses the open-source libraries preCICE and FEniCS to couple flow processes in the fracture domain Γ_s^{Fr} governed by eq. (4.68) with responses of the poro-elastic domain $\mathcal{B}_s^{\text{Pe}}$ defined by eqs. (4.69), resulting in a non-linear system. In both domains, the governing equations are solved by standard continuous Galerkin methods [e.g., 17] and the grids at the coupling interface match.

4.1 Verification of the partitioned implementation

Closed form solutions for non-linear flow processes in deformable fractures are not known to exist. Thus, the partitioned approach is verified by comparison to a monolithic scheme. Focusing on the hydro-mechanical interaction within the fracture domain, the surrounding bulk material is assumed to be linear-elastic where poro-elastic effects are transferred to the material parameters using Gassmann's effective low-frequency result, see eq. (2.46). The numerical stiffness of the coupled system of governing equations mainly scales with

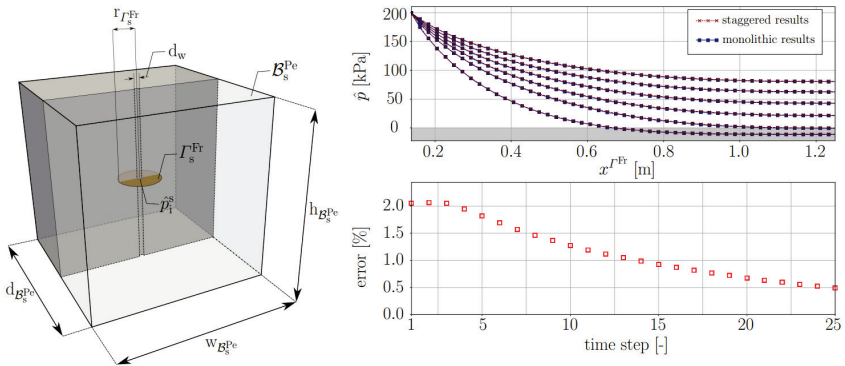


Figure 4: **Left:** Sketch of a single fracture embedded in a solid matrix used for comparisons of the monolithic and the partitioned scheme. **Top Right:** Pressure results obtained from both methods plotted over the fracture radius for time steps t_i with $i = 1, 5, 10, 15, 20, 25$. **Bottom Right:** Relative error plots based on the deviation between solutions obtained from the monolithic and the partitioned scheme.

(i) the compressibility of the fluid β^f and (ii) the initial fracture aperture δ_0 . For the limiting case of $\beta^f \rightarrow 0$ and $\delta_0 \rightarrow 0$, the fracture flow formulation (4.68) reduces to the volumetric coupling term V and the leak-off term VI leading to a non-unique solution in case of partitioned coupling approaches due to the reduction to Neumann boundary condition terms. Nevertheless, such a combination of compressibility and initial fracture aperture is non-physical and has no relevance for experimental investigations. As we use implicit coupling based on sophisticated quasi-Newton iterations, we did not observe numerical instabilities, but an increase in equilibrium iterations for decreasing values of initial fracture aperture δ_0 and fluid compressibility β^f , where the number of coupling iterations increased stronger with decreasing initial fracture aperture than with decreasing fluid compressibility. For the evaluation of the proposed coupling strategy, we therefore consider a numerically challenging set of parameters in terms of a low compressible fluid with properties comparable to those of water under 20°C and an initial fracture aperture in the micrometer range. The chosen parameters have a high relevance for hydraulic testing operations under in-situ conditions [e.g., 175, 176].

The parameters used in the investigated boundary value problem are presented in Tab. 4.17 and the geometrical set up is given in 4. Throughout all numerical studies, Dirichlet deformation boundary conditions are applied to the poro-elastic domain \mathcal{B}^{Pe} by setting deformations on the outer surfaces in normal direction equal to zero. Within the fracture domain Γ_s^{Fr} , pressure Dirichlet conditions \hat{p}_i^s are applied at the intersection of fracture and well. In 4, we compare the monolithic and partitioned solutions. We exploit the radial-symmetric characteristic of the boundary value problem and plot the pressure over the fracture radius at six different times. We observe very good agreement of the pressure for the monolithic and partitioned approach for all time steps. Additionally, we give the

Table 4.18: Coupling parameters used in the study of quasi-Newton methods.

Quantity	Value	Unit	Quantity	Value	Unit
Coupling Parameters					
coupling	{serial-implicit, parallel-implicit}		quasi-Newton	{ILS, IMVJ}	
filter	QR2		initial relaxation ω	0.1	[-]
filter limit ε_F	$\{10^{-4}, 10^{-3}, 10^{-2}, 10^{-1}\}$		relative convergence	10^{-3}	[-]
ILS parameters					
Reuse parameter m	{0, 8, 16, ∞ }	[-]			
IMVJ parameters					
SVD threshold ε_{SVD}	$\{10^{-4}, 10^{-3}, 10^{-2}, 10^{-1}\}$	[-]	Restart parameter η	8	[-]

deviations between both strategies evaluated by a relative error

$$\text{error} = \frac{\sum_{i=1}^{N_c} |\hat{p}_i^m - \hat{p}_i^p|}{\sum_{i=1}^{N_c} |\hat{p}_i^m|} \cdot 100 \quad (4.81)$$

The pressure solution of both approaches has been interpolated to $N_c = 50$ control points equally distributed over the fracture radius. The monolithic approach is based on quad meshes, while the partitioned approach is based on tetrahedral (porous matrix) and triangular (fracture) meshes. 3 808 degrees of freedom (DoF) were used in the fracture and 83 109 DoF in the solid domain for the partitioned approach and 44 418 DoF for the monolithic approach, where the fracture flow domain consists of 952 DoF. Due to this, the elements and vertices of the monolithic and the partitioned coupling strategy do not match and a comparison of the obtained solutions can not be expected to result in perfect agreement. Nevertheless, the results given by 4 show reasonably small errors below 2.5% and decrease over time.

From a physical perspective, the obtained results are sound and the expected response in form of reverse water level fluctuations can be observed at an early stage, where negative pressure values are induced by non-local volumetric deformations of the fracture. Summarizing, the verification indicates the convergence of both coupling approaches towards the same solution.

4.1.1 Investigation of interface quasi-Newton schemes

To verify the suitability of the partitioned coupling approach, we run a parameter study with the same settings as in Tab. 4.17 for the physical setup and coupling parameters as given in Tab. 4.18. All simulations are run in serial-implicit mode, i.e., we iterate in every time step until we fulfill the first fixed-point equation in eqs. 4.75. The initial relaxation is $\omega = 0.1$ and we use the QR2 filter. In order to keep the simulation feasible, we use a somewhat coarse mesh with 3 292 degrees of freedom in the fracture domain and 68 853 degrees of freedom in the porous-medium domain. If the reuse parameter is set to $m = \infty$, we allow the ILS method to keep information from all time steps. In this case, information from the current or previous time step is only dropped due to the QR2 filter.

In eq. (4.75), we have formulated the coupling in terms of the aperture δ . We refer to this as “pre-accumulated” case here as it uses $\delta = \mathbf{u}^+ \mathbf{n}_+^{Fr} + \mathbf{u}^- \mathbf{n}_-^{Fr}$ in the coupling. An

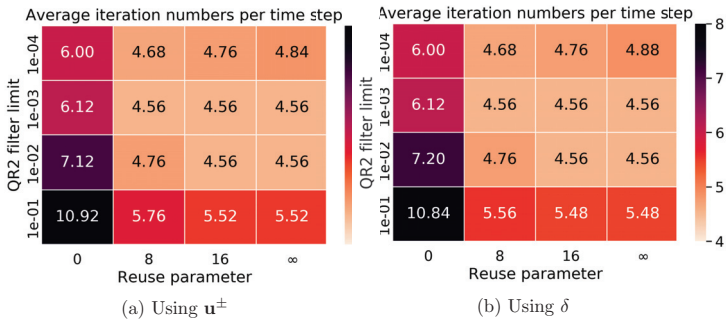


Figure 5: Average number of coupling iterations per time step. The serial-implicit coupling and the IQN-ILS quasi-Newton method are used. The initial relaxation parameter is $\omega = 0.1$, the filter limit and the reuse parameter are varied.

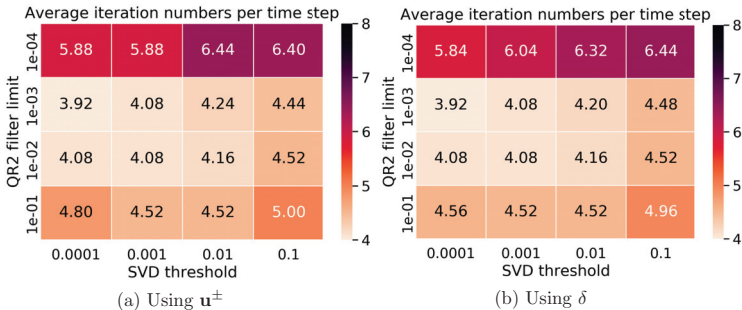


Figure 6: Average number of coupling iterations per time step. The serial-implicit coupling and the IQN-IMVJ quasi-Newton method are used. The initial relaxation parameter is $\omega = 0.1$, the filter limit and the reuse parameter are varied.

alternative way, that we have studied is the explicit use of the displacements \mathbf{u}^\pm instead. We refer to this as “post-accumulated” approach. In the latter case, summation of the displacements to obtain the aperture is done in the fluid solver and the amount of data has to be exchanged between the solvers is increased. The latter case was straightforward to couple in preCICE as it could rely on already implemented features. We do not expect, that the different approaches affect the obtained solution, but rather influence the coupling iteration convergence. Minimal deviations can be expected as the definition of the coupling residual differs slightly as it depends on δ in the pre-accumulated case and on \mathbf{u}^\pm otherwise.

In Figs. 5 and 6, the average number of coupling iterations per time step using the serial-implicit approach is given for the IQN-ILS and the IQN-IMVJ quasi-Newton method, while the filter limit and the quasi-Newton method-specific parameters are varied. The coupling works for all parameter settings investigated.

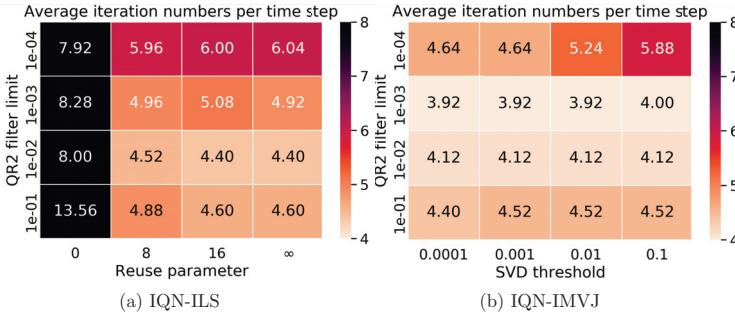


Figure 7: Average number of coupling iterations per time step. The parallel-implicit coupling and both quasi-Newton methods are used. The initial relaxation parameter is $\omega = 0.1$ and the filter limit and quasi-Newton specific parameters are varied.

The IQN-ILS method, see Fig. 5, requires the largest number of coupling iterations, when no information from previous time steps is kept, i.e., the reuse parameter is 0, and the filter limit is too large, i.e., 10^{-1} . Consequently, the largest time-averaged number of coupling iterations is observed, when the reuse parameter is $m = 0$ and the filter limit is $\varepsilon_F = 10^{-1}$. All other cases need an average of approximately 4.5 coupling iterations per time step, which is reasonably small.

For the IQN-IMVJ method, see Fig. 6, we observe only weak dependence on the SVD truncation threshold ε_{SVD} , but stronger dependence on the filter limit. In contrast to the IQN-ILS method, the average number of iterations increases for larger ($\varepsilon_F = 10^{-1}$) and smaller filter limits ($\varepsilon_F = 10^{-4}$). Bad choices of coupling parameters lead to approximately 6 coupling iterations per time step, while, in the ideal cases, only 4 iterations per time step are needed. This is even less than for the best cases of the ILS method.

The effect of the coupling parameters is very similar to what is reported in [171], where a study of different quasi-Newton methods was carried out for fluid-structure interaction test cases. The authors also observed, that the IQN-ILS method with $m = 0$ performs worst and it depends stronger on the actual choice of parameters than the IQN-IMVJ method.

Using the pre- or post-accumulation approach has barely any effect in the current setting. In the observed time frame, the time-averaged number of coupling iterations are nearly identical. However, using the aperture δ in the coupling instead of the displacements \mathbf{u}^\pm reduces the amount of data, that needs to be exchanged. Additionally, we observed strongly improved coupling stability for the fracture networks using the pre-accumulated coupling approach and, thus, it has been used in all following test cases.

In Fig. 7, we show the average number of coupling iterations per time step when a parallel-implicit coupling method is used. The coupling behavior is really similar to the serial-implicit approach, see Figs. 5 and 6. The IQN-IMVJ method needs less iterations than the IQN-ILS method and shows less dependency on the coupling parameters. For the IQN-ILS, one needs most coupling iterations, again, for very small filter limits and especially

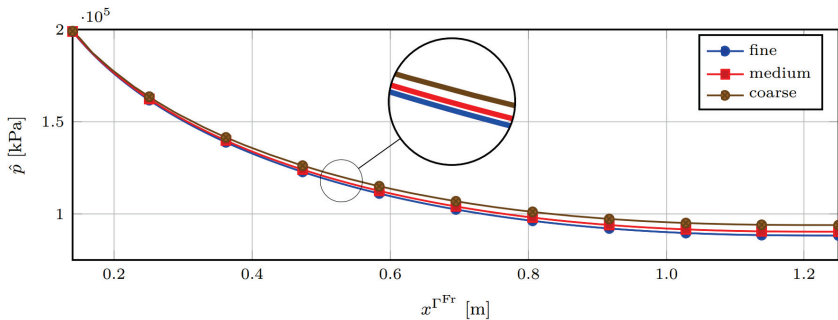


Figure 8: Mesh convergence study for different mesh sizes. We plot the pressure over the fracture radius at time $t = 2.5$ similar to Fig. 4.

when $m = 0$. Surprisingly, the parallel-implicit even beats the serial-implicit coupling in terms of coupling iterations needed. This was not expected as the parallel-implicit approach is weaker and thus normally needs more iterations to recover the strong coupling behavior of the underlying physical problem. It is not clear what causes this and should be investigated further.

4.1.2 Mesh convergence study

For the numerical investigation of mesh convergence, we use three meshes for the fluid and the poro-elastic subdomain with different resolution: (i) (68 853, 3 292) degrees of freedom (coarse, the same mesh as in the parameter study), (ii) (447 816, 24 188) degrees of freedom (medium), and (iii) (6 586 770, 323 976) degrees of freedom (fine) in the porous matrix and fluid domain.

In 8, we present the pressure over the fracture radius at the final time $t = 2.5$ for the different meshes. In all cases, a reasonable pressure curve is obtained. On the coarsest mesh, the pressure is highest. On the medium mesh, the pressure is clearly lower than on the coarse mesh. Thus, the predicted pressure tends to get lower for higher mesh resolution. This is confirmed by the solution on the finest mesh where the pressure is again lower than on the medium mesh. At the same time, the pressure difference between the fine and the medium mesh is smaller than between the medium and the coarse mesh although the difference in grid points increased severely. This indicates that the simulations converges toward a grid-converged solution.

The simulation setup was tested on shared-memory and distributed-memory systems with up to 256 cores. No adjustments had to be made to the code as the parallelization is handled internally via FEniCS and preCICE. However, parallel efficiency is not the focus of this work, but the simplicity of the current approach to realize solvers and couplings that can be executed on parallel computers. Therefore, we do not report scaling results and instead leave it for future work.

Table 4.19: Parameters defining the injection-production boundary value problem.

Quantity	Value	Unit	Quantity	Value	Unit
Numerical parameters					
solid depth $d_{\mathcal{B}_{\text{NW}}^{\text{Pe}}}$	50.0	[m]	solid width $w_{\mathcal{B}_{\text{NW}}^{\text{Pe}}}$	50.0	[m]
solid height $h_{\mathcal{B}_{\text{NW}}^{\text{Pe}}}$	50.0	[m]	small fracture radius $r_{\Gamma_{\text{Fr}}^{\text{NW}}}^{\text{sm}}$	2.0	[m]
large fracture radius $r_{\Gamma_{\text{Fr}}^{\text{NW}}}^{\text{la}}$	4.5	[m]	solid DoF $\mathcal{B}_{\text{NW}}^{\text{Pe}}$	$9.5 \cdot 10^5$	[-]
fracture DoF $\Gamma_{\text{Fr}}^{\text{NW}}$	$5.0 \cdot 10^4$	[-]	time step size Δt	5.0	[sec]
Rock parameters					
dry frame bulk modulus K	8.0	[GPa]	grain bulk modulus K^s	33.0	[GPa]
shear modulus G	15.0	[GPa]	initial porosity ϕ_0	0.01	[-]
intrinsic permeability k^s	$1.1 \cdot 10^{-19}$	[m ²]	fluid compressibility β^f	0.45	[1/GPa]
effective bulk modulus K_{eff}	29.1	[GPa]	effective shear modulus G_{eff}	15.4	[GPa]
Fracture parameters					
initial aperture δ_0	75.0	[μm]	effective fluid viscosity η^{FR}	0.001	[Pa·s]
fluid compressibility β^f	0.45	[1/GPa]	injection pressure \hat{p}_i^{NW}	200.0	[kPa]
production pressure \hat{p}_p^{NW}	-200.0	[kPa]			
Coupling Parameters					
coupling	serial-implicit		quasi-Newton	ILS	
filter	QR2		initial relaxation ω	0.001	[-]
rel. convergence	10^{-5}	[-]			

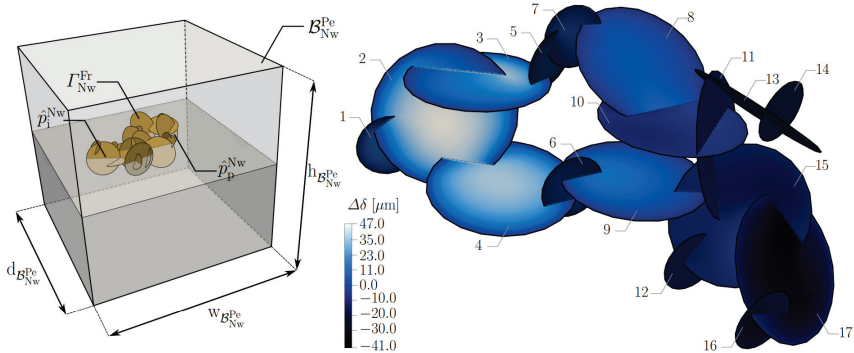


Figure 9: **Left:** Sketch of the connected fracture network $\Gamma_{\text{Fr}}^{\text{NW}}$ embedded in a solid matrix $\mathcal{B}_{\text{NW}}^{\text{Pe}}$. **Right:** Change of fracture aperture after $t = 900$ secs including numbering of the embedded fractures.

4.2 Injection and production in an arbitrarily fractured reservoir

Transient flow and pressure data obtained by experimental field operations on fractured reservoirs provide information of their storage capacity, when evaluated by best numerical fits. Computational effort might be reduced for specific investigations on circular fractures by using two dimensional radial-symmetric models, but most field settings require

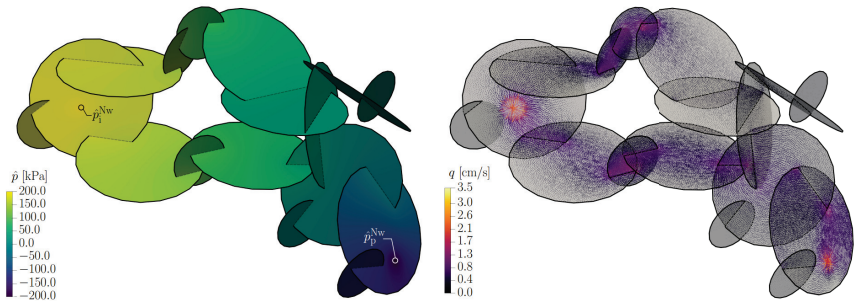


Figure 10: **Left:** Pressure state at time $t = 900$ secs highlighting positions of pressure injection \hat{p}_i^{NW} and production \hat{p}_p^{NW} . **Right:** Post-processed fluid flow field obtained by inserting pressure and aperture solutions into the balance of momentum eq. (4.65) at time $t = 900$ secs.

consideration of several interacting fractures and three-dimensional modeling.

Due to the low permeability of the surrounding bulk matrix, experimental pumping operations are often performed on fractured granite reservoirs. Such a problem setting might lead to instabilities throughout the numerical analysis, since characteristic pressure diffusion times of fracture network and granite bulk material greatly differ. Based on the short experimental execution time, outflow into the surrounding bulk material can be neglected and effective material parameters can be introduced based on Gassmann's solution defined by eq. (2.46). This reduces the matrix response to linear-elastic behavior. Hence, the hydro-mechanically coupled system consists of the hybrid-dimensional flow eq. (4.68) and the linear-elastic response of eq. (4.69), similar to the problem solved in section 4.

Here, we demonstrate the capability of the proposed method to solve flow problems in fracture networks embedded in a low permeable porous bulk material. Therefore, we test our approach on an arbitrarily generated fracture network containing 17 fractures by inducing injection and production Dirichlet pressure boundary conditions in the fracture domain $\Gamma_{\text{PN}}^{\text{Fr}}$, see 9. The regions of injection and production are highlighted. The parameters describing the boundary value problem and the coupling parameters are given in Tab. 4.19.

The applied coupling strategy shows a convergence behavior, which is characteristic for quasi-Newton schemes. Convergence in the first, critical time step is reached within 27 iterations, before the required number of iterations reduces to 14 in the second time step and reaches its minimum of 4–5 iterations for later time steps. The characterization of the tested network is carried out by investigations on the preferential flow path through the network connecting the injection with the production well. The chosen time step size resolves the fracture aperture evolution and allows to study transient hydro-mechanical effects such as the inverse pressure response at an early stage of the simulation. Nevertheless, the results are evaluated at time $t = 900$ sec to focus on a solution close to the quasi-static equilibrium.

In 9, the aperture changes of the fracture network indicate strong hydro-mechanical inter-

Table 4.20: Parameters defining the fractured porous media boundary value problem.

Quantity	Value	Unit	Quantity	Value	Unit
Numerical parameters					
solid depth $d_{\text{PN}}^{\text{se}}$	30.0	[m]	solid size $w_{\text{PN}}^{\text{se}}$	30.0	[m]
solid height $h_{\text{PN}}^{\text{se}}$	20.0	[m]	smallest fracture are $A_{\text{PN}}^{\text{sm}}$	240.5	[m ²]
largest fracture area $A_{\text{PN}}^{\text{la}}$	4.9	[m ²]	solid DoF $\text{DoF}_{\text{PN}}^{\text{se}}$	$6.0 \cdot 10^5$	[-]
fracture DoF $\text{DoF}_{\text{PN}}^{\text{fr}}$	$3.2 \cdot 10^4$	[-]	time step width Δt	200.0	[sec]
Rock parameters					
dry frame bulk modulus K	8.0	[GPa]	grain bulk modulus K^s	33.0	[GPa]
shear modulus G	15.0	[GPa]	initial porosity ϕ_0	0.01	[-]
intrinsic permeability k^s	$1.0 \cdot 10^{-17}$	[m ²]	fluid compressibility β^f	0.45	[1/GPa]
effective bulk modulus K_{eff}	29.1	[GPa]	effective shear modulus G_{eff}	15.4	[GPa]
applied pressure p_0^{PN}	200.0	[kPa]	applied pressure p_1^{PN}	0.0	[kPa]
Fracture parameters					
initial aperture δ_0	75.0	[μm]	effective fluid viscosity η^{fR}	0.001	[Pa·s]
fluid compressibility β^f	0.45	[1/GPa]			
Coupling Parameters					
coupling	serial-implicit		quasi-Newton	ILS	
filter	QR2		initial relaxation ω	0.001	[-]
rel. convergence	10^{-5}	[-]			

action showing, that fractures with dominant opening behavior are closing fractures with similar orientations by reallocation of the surrounding bulk material. This phenomenon is evident when looking at the aperture change distribution of fractures 9 and 10 and to some extend for fractures 1 and 2, or 15 and 17, respectively.

The pressure distribution in 10 shows a smooth pressure field, where pressure drops between fractures are highest, when large fractures are connected by small fractures which is due to their lower cross-section area and higher geometrical stiffness. The phenomenon is demonstrated best by the pressure drop between large fractures 3 and 8 interconnected by the small fractures 5 and 7.

The calculated flow solution shown in 10 visualizes the preferential flow path of the system through fractures 2, 4, 6, 9, 15 and 17 and confirms that the dominant opening of fracture 9 leads to the reduction of the flow through fracture 10. Regions of high flow rates are small connecting fractures and regions close to the injection or production area, which is consistent with the investigated pressure and aperture distributions. The study is representative for hydro-mechanical investigations on tested networks embedded in low permeable rock at a short time scale. It emphasizes the numerical capacity of the proposed approach and its relevance for detailed investigations of research questions in the field of experimental pumping operations.

4.3 Flow through fractured porous media

Approximations of preferential flow patterns through fractured poro-elastic media are of high interest in the field of nuclear waste disposal to reduce the risk of potential pollution by leak-off of contaminated matter. In contrast to the previous test case, an entirely

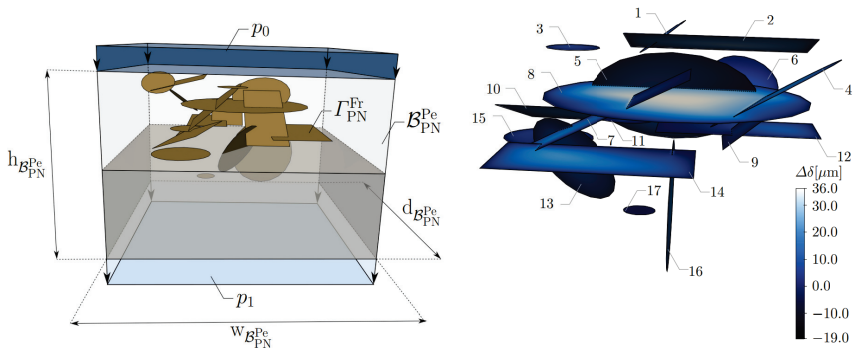


Figure 11: **Left:** Sketch of an arbitrarily chosen fracture network Γ_{PN}^{Fr} embedded within a poro-elastic matrix highlighting the fluid pressure boundary conditions p_0 and p_1 applied to the poro-elastic domain \mathcal{B}_{PN}^{Pe} . **Right:** Change of fracture aperture after $t = 1.65$ days including numbering of the embedded fractures.

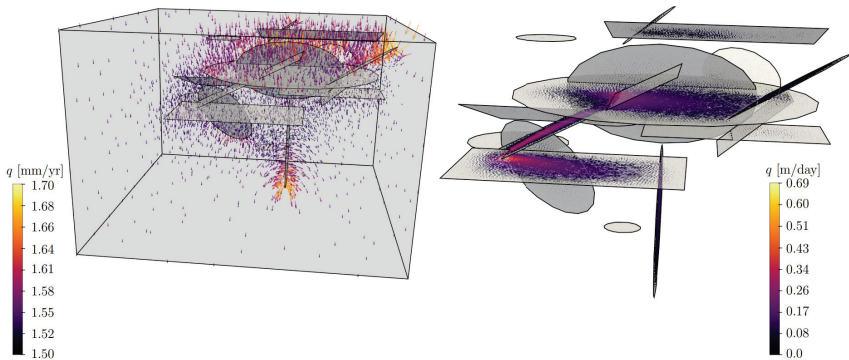


Figure 12: **Left:** Post-processed fluid-flow field in the poro-elastic domain \mathcal{B}_{PN}^{Pe} after $t = 1.65$ days obtained by inserting the pressure solution into the governing equation eq. (4.69) and neglecting of time dependent terms by assuming quasi static conditions. **Right:** Post-processed fluid-flow field within the fracture domain Γ_{PN}^{Fr} after $t = 1.65$ days obtained by inserting the pressure and aperture solutions into the balance of momentum eq. (4.65).

different time scale is required, since investigation periods might last up to a million years. Discrete fracture networks influence the effective transport characteristics of a reservoir and even slight hydro-mechanically induced changes of the fractures' permeability have an immediate impact on its final characteristic diffusion time.

The following boundary value problem investigates fractures embedded in a poro-elastic matrix with a low permeability. Here, we solve the fully coupled system consisting of

the hybrid-dimensional flow eq. (4.68) and the set of poro-elastic governing eqs. (4.69), where fluid exchange between fracture and poro-elastic domain is considered by evaluating eq. (4.73). We induce a pressure gradient on the poro-elastic domain by prescribing the fluid pressure p_0 and p_1 at the top and bottom, see 11. The parameters defining the boundary value problem and the numerical coupling are given in Tab. 4.20, the geometrical set up is shown in 11. The embedded fractures can be grouped into three single fractures (fractures 3, 15 and 17), a small fracture network consisting of fractures 1 and 2 and a large fracture network formed by the remaining fractures (4–14 and 16). The position, shape and orientation of the fractures is chosen arbitrarily to demonstrate the flexibility of the method.

The applied coupling parameters result in a stable convergence behaviour. Convergence is reached within 31 iterations in the first, critical time step, 15 iterations in the following step and 4–5 iterations for later time steps.

Investigations on the impact of hydraulically highly conductive deformable fractures on the transport characteristic of the tested reservoir are evaluated by means of the preferential flow pattern in the poro-elastic and the fracture domain. Results are displayed for a stage close to the converged quasi-static equilibrium after $t = 1.65$ days, see Figs. 11 and 12. Similar to the findings of the previous study, hydro-mechanical interactions are evident in the fracture aperture change distribution displayed, where the fracture pairs 7 and 8, 9 and 14 and 4 and 8 have the strongest interactions, see 11. The interaction results in opening or closing of the involved fractures, which has an immediate impact on the local conductivity of the network.

The post-processed flow solutions in the poro-elastic $\mathcal{B}_{\text{PN}}^{\text{Pe}}$ and in the fracture domain $\Gamma_{\text{PN}}^{\text{Fr}}$ are presented in 12. Depending on the fracture orientation and the fracture connectivity, embedded fractures have a distinct impact on the flow through the poro-elastic medium. Related to the orientation orthogonal to the pressure gradient and the lack of connectivity, the embedded single fractures 3, 15 and 17 have a minor contribution. At the same time, the fluid is strongly attracted by the small and large fracture network. The fluid mainly enters the networks through fractures 1, 4, 5 and 7 which are closest to the pressure boundary p_0 and is released back into the poro-elastic matrix through fractures 13 and 16 which are closest to the applied pressure boundary p_1 . The impact of the fracture network on the transport characteristic of the studied poro-elastic domain is evident in terms of the distinct difference of flow rates in both domains. The hydro-mechanical interaction between the fracture and the poro-elastic domain has shown the potential of the method to consider flow through deformable fractures embedded in a hydro-mechanically interacting poro-elastic medium throughout long term investigations with a relevance for fields such as nuclear waste disposal.

5 Conclusion

We proposed a new partitioned coupling approach for hydro-mechanical flow processes in deformable fractures embedded in a poro-elastic medium. Implicit coupling of the decomposed fracture flow and poro-elastic domain under consideration of the introduced interface conditions was realized by an iterative approach. The latter solves the underlying

fixed-point problem using interface quasi-Newton methods. It was implemented using the open-source computing platform FEniCS to solve the individual systems of PDEs and the open-source coupling library preCICE to realize the implicit coupling.

We showed, that the proposed coupling strategy enables straight-forward usage of parallel computations throughout solution and coupling steps. This allows to study complex fracture systems in three dimensions with a high computational resolution. Evaluation of the proposed implementation against solutions obtained from a monolithic approach showed good agreement in terms of the transient pressure evolution in a single deformable fracture. Throughout a coupling convergence study, we showed the slightly better performance of the advanced IQN-IMVJ quasi-Newton scheme in comparison to the performance of the classical IQN-ILS quasi-Newton scheme, which is in good agreement with results on classical fluid-structure interaction problems in [171].

The generality of the proposed strategy and its relevance for research topics such as modeling of injection and production in fractured reservoirs and the flow through a fractured poro-elastic domain was demonstrated throughout two numerical studies of complex fracture networks in three dimensions. We emphasized the advantage of the fracture and poro-elastic domain decomposition in terms of the creation of complex networks and straight forward post-processing of the numerical solutions in each computational region to identify preferential flow paths through the fracture network and the poro-elastic medium, respectively.

Future work can focus on the extension of the physical models to include temperature, e.g., extension of the partitioned coupling schemes, and the investigation of other discretization methods in for the subproblems. Considering additional physics in the model opens new application such as heat related energy production relevant for geothermal applications. The partitioned coupling schemes, especially in the black-box setting of preCICE, can be improved by developing more sophisticated start-up strategies to reduce the number of coupling iterations in the first time steps and by new data mapping and communication concepts. The mixed-dimensional modeling leads to several challenges on how to communicate data between the different models, especially at fracture intersections, where the dominant deformation has to be identified.

Acknowledgments

Holger Steeb and Patrick Schmidt gratefully acknowledge the funding provided by the German Federal Ministry of Education and Research (BMBF) for the GeomInt (I & II) project (Grant Numbers 03A0004E and 03G0899E) in the BMBF Geoscientific Research Program “Geo:N Geosciences for Sustainability”. Alexander Jaust, Miriam Schulte, and Holger Steeb thank the German Research Foundation (DFG) for supporting this work under Grant No. SFB 1313 (Project No. 327154368). We thank the preCICE developers for their support, especially B. Uekermann.

Assessing the role of non-linear contact mechanics for flow in fractures

Patrick Schmidt, Holger Steeb, Jörg Renner, *Geophys Res Lett - Geophysical Research Letters*, Submitted July 2022

- harmonic pumping tests exhibit a unique diagnostic potential for the occurrence of hydro-mechanical effects, systematic overtones in response spectra
- fractured rocks but also granular porous media exhibit non-linear effects for excitations typically applied in pumping tests
- non-dimensional formulation of the hydrodynamic problem yields a “regime map” that allows for (a-priori) analysis of the significance of hydro-mechanical coupling

Abstract

Hydro-mechanically induced transient changes in fracture volume elude an analysis of pressure and flow rate transients by conventional diffusion-based models. We used a previously developed fully coupled, inherently non-linear numerical simulation model to demonstrate that harmonic hydraulic excitation of fractures leads to systematic overtones in the response spectrum that can thus be used as a diagnostic criterion for hydro-mechanical interaction. We therefore investigated the response spectra of data obtained from harmonic testing in four different subsurface scenarios for the occurrence of overtones and thereby assessed their potential for the hydro-mechanical characterization of tested reservoirs further. Our non-dimensional analysis identified relative aperture change as the critical system parameter. Harmonic pumping tests exhibit a strong diagnostic potential for hydro-mechanical interaction, the crucial prerequisite to account for it in the analysis of pumping tests to overcome the limitations of purely diffusion-based models.

Plain Language Summary

A reliable hydraulic characterization of the subsurface is important for the recovering of fluid resources but also for the subsurface storage of heat or waste. In pumping tests, the hydraulic state of the subsurface is perturbed by injection or production of fluid into or from boreholes; hydraulic parameters of the subsurface are conventionally inverted from observed pressure and flow rate relying on diffusion models. When hydraulic conduits deform due to the changes in fluid pressure, the conventional analyses based on diffusion equations becomes questionable. Our numerical study demonstrates that pumping with a harmonic excitation allows the operator to assess the significance of these so-called hydro-mechanical effects, e.g., widening of fractures due to an increase of pressure along them. The response to a harmonic excitation will not be truly harmonic but exhibit systematic overtones. We demonstrate that significant hydro-mechanical coupling is expected for typical fracture deformation characteristics. An analysis of previously reported results

from field tests confirms our numerical findings for fractured rocks but also for a gravel aquifer, typically considered the prototypical scenario for a diffusion-based analysis. We provide a dimensionless framework that allows for an assessment of the role of hydro-mechanical effects using a regime map.

Introduction

The pressure and flow transients in fractures and fractured rocks are affected by hydro-mechanical coupling, the influence that changes fluid pressure exert on fracture geometry. The deformation of fractures may significantly affect their effective hydraulic properties [207]. Non-local deformation, induced by fluid pressure variations, has an instantaneous impact on the fracture volume, in contrast to the time-delayed change in fluid pressure caused by diffusion. For example, the direct pressure-induced mechanical response of fractures may result in inverse pressure fluctuations at some distance from the perturbation's source [206], a phenomenon similar to the Noordbergum effect known for poro-elastic media [107, 162]. In addition to these non-local phenomena, local changes in fracture permeability may be significant due to changes in fracture aperture, related to fluid injection, as demonstrated by field [52, 164, 165, 175] and laboratory studies [115, 122, 219]. The identified changes in the fracture's transport characteristics induced by fluid injection, attributable to non-linear fracture stiffness-permeability relationships, are relevant for fault reactivation and seismicity in general [33, 51, 78–80]. Fracture stiffness and permeability are both closely related to measures of fracture aperture, albeit not necessarily the same, because hydraulic and mechanical responses to changes in fluid pressure along a fracture might be governed by different aspects of the fracture geometry [209].

Pumping tests constitute the primary option for determining hydro-mechanical properties of fractures and fractured rocks on field-scale. Periodic pumping tests, exhibiting technical and analytical advantages compared to conventional constant-rate testing regarding signal separation from noise or from prevailing transients due to previous or ongoing pumping operations in nearby boreholes [154, 157], characterization of flow regimes [39, 89], and identification of subsurface heterogeneity [3, 36, 63, 89, 157], also promise a substantial sensitivity to hydro-mechanical effects since conduit deformation causes changes in permeability and storage capacity in every period, i.e., repeatedly, as previously demonstrated for open radial fractures [208]. We discuss the role of hydro-mechanical coupling for the occurrence of overtones observed in the response spectrum of transients recorded during in-situ tests on different scales in the light of the results of numerical simulations of a harmonic pressure excitation applied to a single mechanically closed but fluid-filled and permeable radial fracture for two distinctly different fracture domains under a range of normal stress conditions. Introducing dimensionless properties allows us to compare the influence of hydro-mechanical coupling on the response spectrum observed for the numerical model to that of experimentally recorded transients.

Methods

Our numerical approach employs an implicitly coupled, non-linear, time-domain formulation of a hybrid-dimensional model [177, 208] including fluid pressure-induced changes of local permeability and fracture volume overcoming the limitations of purely diffusion-based models (for details see Text S1). The opening and closing of fractures is controlled by two “stiffnesses”, one related to their overall geometry and the bulk elastic properties of the medium embedding the “void”, and one representing the contact mechanics of the touching fracture surfaces. When a fracture is fully open, i.e., the two surfaces loose contact, e.g., due to fluid pressure on it, solely the geometrical stiffness determines their deformation; when they are mechanically closed, the contact stiffness tends to dominate their deformation [e.g., 175]. The deformation characteristics of individual asperities forming the contact may be approximated by that of Hertzian contacts. Such non-linear behavior particularly predicts “relatively large” aperture changes and associated changes in effective hydraulic properties of fractures for modest changes in normal stresses, when the effective normal stresses on the fracture are small.

The chosen constitutive model for the fracture deformation (see Text S3, eq. 4) accounts for the strong non-linearity between changes in normal stress and fracture aperture characteristic for mechanically closed fractures in rocks [e.g., 12, 145] but might be replaced by alternative models to match experimental observations for specific rock samples. We adopt a sign convention, according to which compressive stresses are negative as are reductions in aperture. The (stress dependent) specific fracture stiffness C^{Fr} , the change in normal stress σ_N required for a change in effective fracture aperture $\Delta\delta = \delta - \delta_0$ relative to the initial (mean) aperture δ_0 at zero stress, reads

$$C^{\text{Fr}} = \frac{\partial\sigma_N}{\partial\Delta\delta} = \frac{E^{\text{Fr}}}{\delta_0 - \delta_{\text{min}}} \left(1 - \frac{\sigma_N}{E^{\text{Fr}}}\right)^2 \quad (4.82)$$

with the minimum effective fracture aperture δ_{min} reached for $\sigma_N \rightarrow -\infty$ and E^{Fr} the fracture Young’s modulus [70, 180]. The specific effective fracture stiffness C^{Fr} increases non-linearly with an increasing magnitude of compressive normal stresses σ_N .

In our modelling, we assume the “global” constitutive relation (4.82) to apply locally and identify the normal stress σ_N as an effective normal stress $\sigma_N \rightarrow \sigma_N - p$, calculated as the unweighted difference between normal stress and the (local, time-dependent) fluid pressure. A numerical simulation is performed in three steps; first, the fracture is subjected to a normal stress; then a uniform fluid pressure p^{eq} is applied in the fracture domain leading to the mechanical equilibrium state assumed to be characterized by an effective stress of $\sigma_N^{\text{eq}} = \sigma_N - p^{\text{eq}}$. Finally, sinusoidal pressure perturbations are imposed at the fracture’s center. The flow into a “rigid fracture” is simulated using a conventional pressure-diffusion model to illustrate the effects of fracture deformation by a direct comparison of results from the two models.

Dimensionless properties quantifying the hydro-mechanical interaction throughout harmonic testing

A dimensionless formulation seems mandated for a meaningful comparison of results from different experiments because of the multitude of parameters describing the hydro-mechanical system. Several important system parameters, for example fracture permeability, vary spatially and temporally once fluid pressure is harmonically perturbed. Thus, we represent them by their values for equilibrated fluid pressure at a given normal stress, as denoted by a superscript “eq”. Specifically, we introduce the characteristic time of pressure diffusion in a fracture

$$\tau^d = \frac{(l^{\text{Fr}})^2 \eta^{iR} \beta^f}{k^{\text{Fr,eq}}}, \quad (4.83)$$

which constitutes an approximate measure of the time it takes for the pressure perturbation to reach a characteristic diffusion distance l^{Fr} [e.g., 212], here corresponding to the fracture radius or length, η^{iR} and β^f viscosity and compressibility of the fluid, and $k^{\text{Fr,eq}} = (\delta^{\text{eq}})^2/12$ is the intrinsic permeability of the fracture in the equilibrated yet unperturbed state, characterized by a constant aperture δ^{eq} . Furthermore, we characterize a rock domain of height h and a Young’s modulus E by a nominal domain stiffness $C = E/h$. The employed four dimensionless parameters are

- a) the dimensionless characteristic diffusion time $\tau = \tau^d/T$, a normalization of the characteristic diffusion time τ^d (4.83) by the testing period T ,
- b) the dimensionless domain stiffness $\Gamma = C/C^{\text{Fr,eq}}$ that normalizes the nominal domain stiffness C by the specific equilibrium fracture stiffness $C^{\text{Fr,eq}}$, i.e., (4.82) evaluated for σ_N^{eq} ,
- c) the dimensionless domain length $\Lambda = r/r_b$, where we normalize the domain radius r by the borehole radius r_b and
- d) the dimensionless aperture-change $\Omega = p_A s$, for which we multiply the amplitude of the applied fluid pressure p_A with the relative sensitivity of aperture changes to perturbations in effective normal stress $s = \partial \ln(\delta)/\partial \sigma_N = \partial \ln(\delta)/\partial p = 1/(\delta C^{\text{Fr}})$.

Hydro-mechanical characteristics of the numerically investigated fracture domains

We employ experimental observations on single fractures embedded in granite rock samples [145] to determine the parameters, fracture Young’s modulus E^{Fr} and the initial fracture aperture δ_0 , of the proposed constitutive relation (eq. 4.82; eq. 4 in SI). Specifically, we fit two sets of data for fracture deformation $\Delta\delta$ and specific fracture stiffness C^{Fr} as a function of normal stress σ_N , documented in Pyrak-Nolte *et al.* 1987 and Gale 1987 (Fig. 1), assuming $\delta_{\text{min}} = 0$, i.e., the fracture reaches a hydraulically closed state for infinitely high normal stress. One of the two domains, B₁, corresponds to a fracture with a “stiff” response, whereas the other fracture is compliant for low normal stresses and converges to the stiff response of the first domain only for high normal stress.

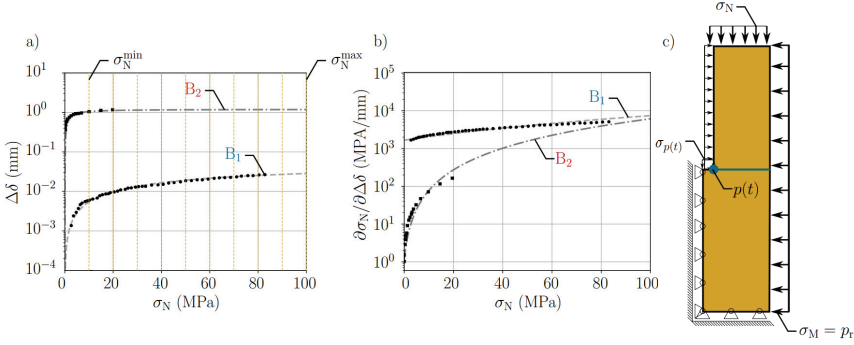


Figure 1: Numerical fits of the dependence of fracture deformation $\Delta\delta$ a) and fracture-specific stiffness $\partial\sigma_N/\partial\Delta\delta$ b) on the acting total normal stresses for samples B₁ and B₂ [145]. The total normal stress values 10, 20, ... 100 MPa applied in our numerical study are indicated by the orange vertical dashed lines in a). The numerical boundary conditions of the axisymmetric model c) comprise lateral stress σ_M on the outer sample surface related to radial pressure p_r , axial or normal stress σ_N , normal stress on the injection borehole wall $\sigma_{p(\tau)}$, and the Dirichlet boundary condition associated with the fluid pressure $p(\tau)$ at the intersection between fracture and injection borehole.

To express their stress dependence, we denote properties evaluated at minimum $\hat{\sigma}_N^{\text{eq}} = \sigma_N^{\text{min}} - p^{\text{eq}} = 5$ MPa and maximum $\hat{\sigma}_N^{\text{eq}} = \sigma_N^{\text{max}} - p^{\text{eq}} = 95$ MPa effective normal stress by $\hat{\square}$ and $\hat{\square}$, respectively (see also Fig. 1 and Text S4, Table S1). The equilibrium fracture apertures are moderately sensitive to applied normal stress for B₁ ($\hat{\delta}_{B_1}/\hat{\delta}_{B_1} \approx 2$) but highly sensitive for B₂ ($\hat{\delta}_{B_2}/\hat{\delta}_{B_2} \approx 15$); the associated stiffnesses stay within half an order of magnitude for B₁ but vary non-linearly over about two orders of magnitude for B₂ and reach the high values of B₁ only at the highest imposed normal stress values of 100 MPa. The domain stiffness C_{B_i} indicates a stiffer characteristic for the smaller sample B₁, though the same Young's modulus E_{sat} is used, because it scales with cumulative height of the rock cylinders h_{B_i} . The normalized radius Λ indicates distinctly different fracture lengths for the two numerically investigated domains ($\Lambda_{B_2}/\Lambda_{B_1} = 10$).

The stress state-dependent, dimensionless domain quantities of B₁ evolve more with stress than those of B₂ over the range of investigated effective stresses. The dimensionless domain stiffness is insensitive to changes in stress for B₁ but decreases significantly for B₂ with increasing normal stress. For domain B₁, the fracture is persistently less compliant than the rock matrix. For domain B₂, the fracture is more compliant than the rock matrix for the minimum applied normal stress and significantly stiffer at the maximum normal stress. The relative aperture sensitivity s , determined from initial fracture aperture and fracture Young's modulus, evolves distinctly different with increasing normal stress for the two numerical domains (Fig. 3 c, d); s is low and constant for B₁, while, for domain B₂, it is high at low normal stress and decreases to the insensitive response of domain B₁ at high normal stress.

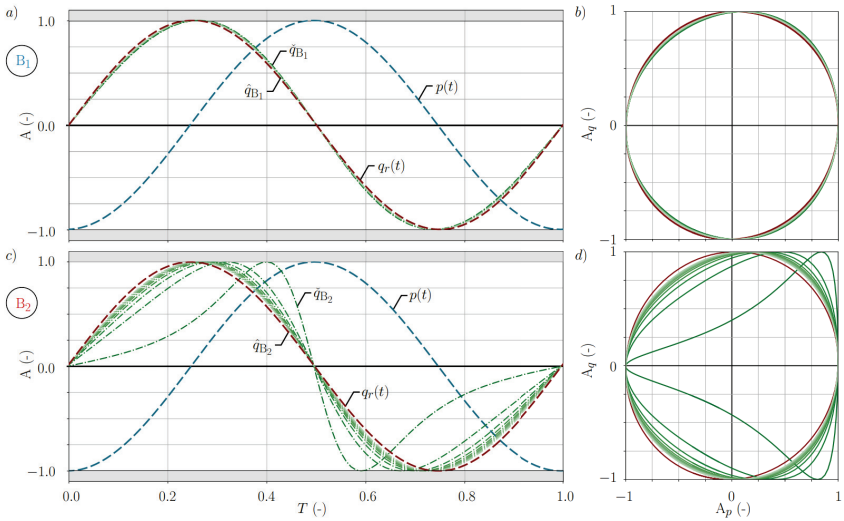


Figure 2: Variation of pressure p (blue, imposed boundary condition) and flow rate q at the fracture mouth, normalized by their maximum values, during an oscillation period T a) and c) and corresponding hysteresis plots b) and d) for samples B_1 a) and b) and B_2 c) and d). The red dashed lines give the reference solutions for pure radial diffusion $q_r(\tau)$ in the absence of fracture deformation. Flow solutions q_{B_i} for deformable fractures are shown in shades of green for normal stress σ_N ranging between the minimum of 10 MPa and the maximum of 100 MPa in steps of 10 MPa.

The diffusion time (4.83) varies modestly for B_1 ($\tilde{\tau}_{B_1}^d/\tilde{\tau}_{B_1}^d \approx 4$), but significantly for B_2 ($\tilde{\tau}_{B_2}^d/\tilde{\tau}_{B_2}^d \approx 225$) over the range of applied normal stresses (Text S4, Table S1). While the characteristic diffusion times of the two considered fracture scenarios are of comparable magnitude at the minimum effective equilibrium normal stress ($\tilde{\tau}_{B_2}^d/\tilde{\tau}_{B_1}^d = 6$), they differ by more than two orders of magnitude at the maximum stress state ($\tilde{\tau}_{B_2}^d/\tilde{\tau}_{B_1}^d = 360$). At all stress conditions, the characteristic diffusion times are, however, significantly smaller than the selected period T of the pressure perturbation ($\tau^d/T \sim 10^{-7}$). The similarity of characteristic times at minimum stress and its relation to the excitation period mean that, if deformation were absent, a) pressure diffusion would take place on a similar time scale in the two fractures and b) pressure would be almost equilibrated along the fractures and thus close to the excitation pressure at all times. With the selection of the two samples, we thus ensure that differences in the hydraulic response of the two fractures to the periodic excitation are dominated by deformation characteristics and that the potential effect of fracture deformation on the flow process is maximized.

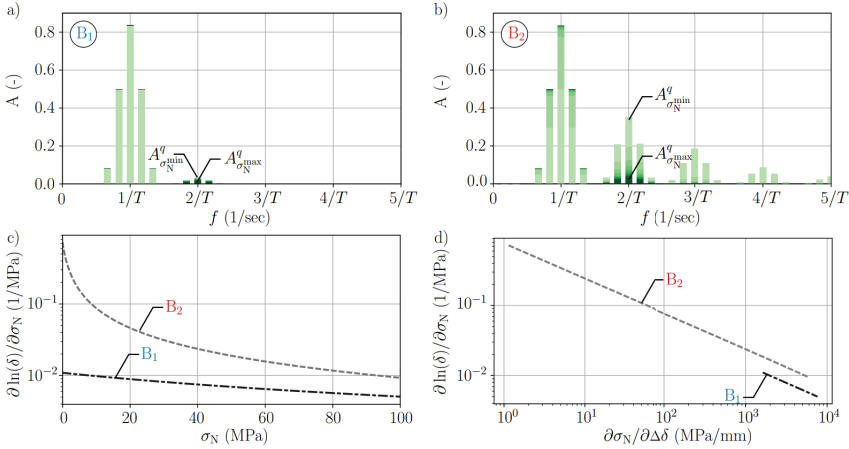


Figure 3: Amplitude spectra of flow q for sample B_1 a) and B_2 b) normalized by their maximum value. Amplitudes of the flow solutions (\bar{q}_{B_1} and \bar{q}_{B_2}) for the minimum and maximum normal stress are represented by different shades of green. Plots of the relative aperture change sensitivity regarding the acting normal stress c) and specific normal stiffness d) for samples B_1 and B_2 .

Results

Evaluation of the numerical pressure and flow transients in the time domain reveals distinctly different responses of the two modeled domains to the harmonic pressure excitation. For the “stiff” fracture B_1 , maxima in pressure and flow exhibit a phase shift close to $T/4$ irrespective of normal stress, as expected for a purely diffusion-based model, corresponding to a circular $p - q$ hysteresis loop (Fig. 2). In contrast, the flow response is visibly non-harmonic for the compliant domain B_2 , with increasing deviations from a phase shift of $T/4$ with decreasing normal stress. The variably distorted $p - q$ hysteresis loops visualize the underlying shift of the flow maxima towards the pressure minimum. The deviations of the flow responses from a harmonic signal observed for the compliant domain B_2 lead to systematic overtones in the spectra at integer multiples of the excitation frequency. The overtones exhibit decreasing amplitudes with increasing frequency at a given normal stress and with increasing normal stress at a given frequency (Fig. 3).

Discussion

Diagnostic potential of overtones for hydro-mechanical interaction during harmonic excitation

Our numerical simulations indicate that overtones in the frequency domain of the flow response permit inferring the relevance of hydro-mechanical interaction and thus assess the

validity of a diffusion approach to go beyond the conventional determination of effective hydraulic parameters [61, 82, 153, 157] and provide constraints on hydro-mechanical properties. The hydro-mechanical response is controlled by a) the intrinsic “responsiveness” of the fracture in terms of the dimensionless aperture-change Ω and b) the actual extent of the excitation characterized by the dimensionless characteristic diffusion time τ^d (4.83) as a measure for the hydraulic penetration depth. The relation between changes in effective aperture and effective normal stress controls the hydro-mechanical responsiveness of the fracture and thus will be examined in detail.

In the numerical model, we assume the local mechanical equilibrium of a fluid-filled fracture under normal stress to be constrained by the stress balance

$$\sigma_N = \sigma_N^{\text{Fr}} + \sigma_{\text{St}} + p, \quad (4.84)$$

i.e., the acting normal stresses σ_N are in equilibrium with the sum of fluid pressure p , normal contact stresses σ_N^{Fr} , and stress σ_{St} related to the deformation of the surrounding bulk material, typically characterized by a structural or geometrical fracture stiffness [131, 175]. In our numerical approach, however, we neglected this geometrical stiffness, because the applied pressure amplitudes remained well below the acting normal stresses and therefore the limit of fracture-surface separation. Hence, variations in effective normal stress $\sigma_N - p$ are exclusively compensated by contact normal stresses σ_N^{Fr} and thus the numerical simulations correspond to an upper bound for the contact-related deformation of a tested fracture.

The amplitudes of overtones observed for the two domains correlate with their different dimensionless aperture-change values Ω ; overtones in the frequency domain are prominent for high dimensionless aperture-change values. Thus, we identify the amplitude of overtones as a measure for changes in flow characteristics of a tested fracture due to hydro-mechanical interaction. The relation between transient changes of the mechanical fracture-surface contact response and the resulting fracture flow induced by harmonic excitation is in agreement with the qualitative specific fracture stiffness-flow relation introduced for quasi-static conditions in Pyrak-Nolte & Morris 2000 and Pyrak-Nolte & Nolte 2016.

Interpretation of overtones in the response spectra of previously reported experimental data

We investigate the records of four field studies that employed harmonic excitation (Text S5, Fig. 5), namely in the Reiche Zeche underground-research laboratory (RZ), Freiberg, Germany [23], at the Terrieu karstic field (TER) near Montpellier, France [61], at the Altona Flat Rock Site (AFR) in Clinton County, NY, USA [82], and at the Boise Hydrogeophysical Research Site in Boise (BHR), ID, USA [153]. The study conducted at BHR comprised tests in a gravel aquifer, while the three other studies represent tests on fractured rock masses. The amplitude spectra of the recorded pressure transients can be classified into three groups: overtones occur (i) at local maxima at multiples of the excitation frequency (RZ, BHR), (ii) at maxima at uneven multiples of the excitation frequency (AFR), and (iii) unsystematically (TER). We compare the overtone observations with estimates of the introduced dimensionless properties to assess the role of hydro-mechanical

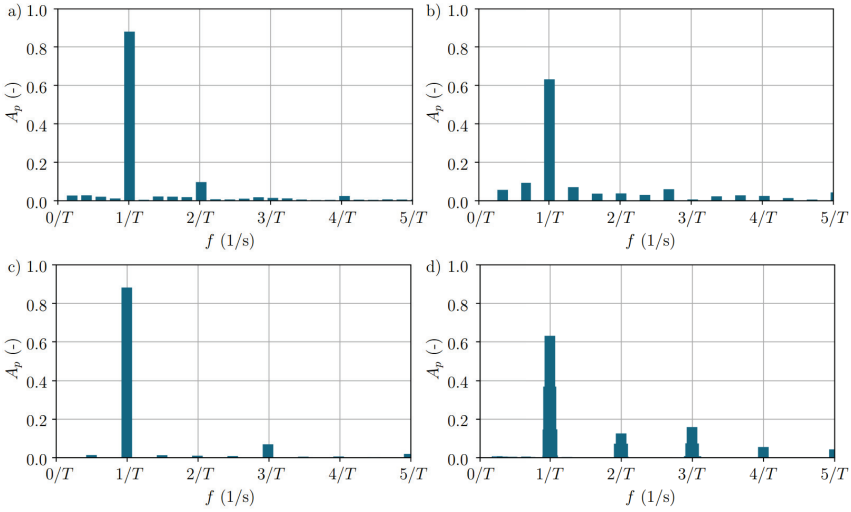


Figure 4: Pressure response spectra recorded during harmonic measurements at a) RZ, b) TER, c) AFR and d) BHR. The amplitudes are normalized by their maximum value.

interaction for their occurrence (Figure 5). Qualitatively, we expect the fields of strong and weak hydro-mechanical interaction to correspond to combinations of low and high specific fracture stiffness with low and high diffusion times. Hydro-mechanical coupling is expected to increase with increasing fracture deformability and applied pressure amplitudes corresponding to increasing dimensionless aperture changes and decreasing pressure diffusion times corresponding to increasing hydraulic penetration depths.

The placement of the different field studies in the “regime diagram” and the occurrence of overtones are consistent and show a significantly higher sensitivity of the magnitude of hydro-mechanical interaction to the dimensionless aperture change than to the characteristic pressure diffusion time:

- The dimensionless properties indicate a high dimensionless aperture-change and a moderate penetration depth for RZ. The similarity between dimensionless parameters and overtone characteristics for RZ with B2 strongly suggest that hydro-mechanical coupling is the cause for the non-linear response.
- The AFR experiments are characterized by a low to moderate dimensionless aperture-change and a high penetration depth in agreement with the amplitude of observed overtones at uneven multiples of the excitation frequency. The absence of even multiples of the excitation frequency remains unclear and might be related to additional effects, such as non-laminar flow, not considered by the present model.
- The combination of low values of dimensionless aperture change and a moderate

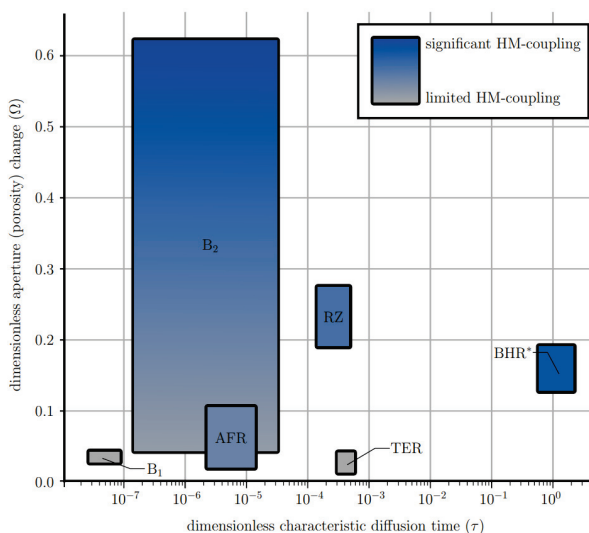


Figure 5: Classification of tests regarding hydro-mechanical interaction, based on the relation between the dimensionless characteristic diffusion time as a measure for the expected hydraulic penetration depth and relative aperture change.

penetration depth indicating negligible hydro-mechanical interactions is in agreement with the inconsistent occurrence of local maxima in the amplitude spectra of the TER response data. Frequencies exceeding the nominally excited one seem related to the insufficient time resolution of the data.

- The amplitude of observed overtones in the response spectrum of the BHR exceed overtones of the three field studies involving fractured rocks indicating significant hydro-mechanical interaction. The pronounced overtones correlate well with the high dimensionless porosity change estimated based on the Kozeny-Carman permeability-porosity relation for granular media (SI, section 2), in lieu of a dimensionless aperture change.

Conclusions

We identified overtones in the response spectrum of harmonic testing as an indicator of hydro-mechanical interaction. Overtones observed in field tests correlate with the sensitivity of fracture aperture (or generally porosity) changes to perturbations in fluid pressure that controls the degree of non-linearity of fracture flow. Hence, overtones observed during harmonic hydraulic testing should not per-se be discarded as measurement imperfections,

but bear the potential to characterize the fracture's stress state and mechanical properties, such as the specific normal stiffness.

An account of hydro-mechanics will improve the inverse analysis of experimental field and laboratory data by separating hydro-mechanical phenomena from undesired measurement artefacts. Improved estimates of hydro-mechanical properties of a tested region then bear a significant potential to optimize the design of energy-storage and/or geothermal systems. An improved (quantitative) understanding of hydro-mechanical properties of fractures and fractured rocks on field scale is also essential for a substantiation of analyses in fields such as seismic [e.g., 29] and volcanic [e.g., 4] tremor, and tidal signals in boreholes [e.g., 220].

Open Research

We used the modular toolbox DUNE, a free software licensed under the GPL (version 2), for solving partial differential equations (PDEs) with grid-based methods to perform the numerical simulations: <https://www.dune-project.org/>. The Git-repository: <https://github.com/PatrickSchm/Assessing-the-role-of-non-linear-contact-mechanics-for-flow-in-fractures---Code> contains our DUNE implementation of the hybrid dimensional interface elements, the files for compilation, the input and mesh files as well as the python script that generates the characteristic, dimensionless properties.

Acknowledgments

The authors gratefully acknowledge the funding provided by the German Federal Ministry of Education and Research (BMBF) for the STIMTEC-X project (subproject SPATZ, Grant Number 03G0901A) and the GeomInt (I & II) project (Grant Numbers 03A0004E and 03G0899E), in the BMBF Geoscientific Research Program "Geo:N Geosciences for Sustainability". Holger Steeb thanks the Deutsche Forschungsgemeinschaft (DFG) for supporting this work under Grant No. SFB 1313 (Project No. 327154368) and under Germany's Excellence Strategy (EXC2075-390740016). Jörg Renner thanks Felix Becker, Gerd Klee, and Florian Seebald of Solexperts GmbH for their expertise brought to the field testing at RZ-URL.

Supporting Information for ”Assessing the role of non-linear contact mechanics for flow in fractures”

Introduction Text S1 to S3 provide details on the governing equations for fluid flow in deformable fractures, their numerical implementation, the considered fracture geometry and constitutive assumptions. Text S4 presents the properties of the numerically investigated fractured domains; their absolute values are compiled in Table S1. Text S5 introduces the aspects of four in-situ experiments that are relevant for our analysis of the role of hydro-mechanical effects. Tables S2 and S3 give the material properties and excitation characteristics of the numerical experiments and the four field experiments in absolute and dimensionless values, respectively.

Text S1. Governing Equations

We incorporate the geometrical assumption of parallel plates for high-aspect ratio fractures and assume creeping flow conditions ($Re \ll 1$) in the derivation of the balance equations. Evaluation of the balance of momentum for weakly compressible, viscous fluids in hydraulic transmissive fracture results in a Poiseuille-type formulation [177, 206]. Then, the relative fluid velocity \mathbf{w}_f is proportional to the pressure gradient $\text{grad } p$; the cubic law [e.g., 216] is evaluated at each material point $\mathcal{P}(\mathbf{x}, \tau)$ along the planar fracture

$$\mathbf{w}_f = -\frac{\delta(\mathbf{x}, \tau)^2}{12 \eta^{fR}} \text{grad } p =: -\frac{k^{\text{Fr}}}{\eta^{fR}} \text{grad } p, \quad (4.85)$$

where $k^{\text{Fr}}(\mathbf{x}, \tau) = \delta(\mathbf{x}, \tau)^2/12$ denotes the space- and time-dependent permeability, \mathbf{x} the current position vector along the fracture, τ time, η^{fR} the dynamic viscosity of the fluid, and $\delta(\mathbf{x}, \tau)$ the space- and time-dependent local fracture aperture.

Using (4.85) in the evaluation of the balance of mass for the fluid and considering a mean velocity averaged over the fracture aperture δ results in a hybrid dimensional formulation [206–208]

$$\underbrace{\delta \frac{\partial p}{\partial \tau}}_{\text{i)}} - \underbrace{\frac{\delta^3}{12 \eta^{fR}} \text{grad } p \cdot \text{grad } p}_{\text{ii)}} - \underbrace{\frac{\delta^2}{12 \eta^{fR} \beta^f} \text{grad } \delta \cdot \text{grad } p}_{\text{iii)}} - \underbrace{\frac{\delta^3}{12 \eta^{fR} \beta^f} \text{Div}(\text{grad } p)}_{\text{iv)}} + \underbrace{\frac{1}{\beta^f} \frac{\partial \delta}{\partial \tau}}_{\text{v)}} = \underbrace{\frac{q_{lk}}{\beta^f}}_{\text{vi)}}, \quad (4.86)$$

where β^f is the fluid compressibility and q_{lk} accounts for leak-off, despite its facile connotation here meant to encompass all fluid exchange between the fracture and the surrounding rock, from here on addressed as matrix. Dimensional analysis of the governing equation (4.86) motivates to neglect the quadratic term ii) and the convection term iii) for problems involving high-aspect ratio fractures [206]. Thus, the hybrid dimensional description comprises a transient i), a diffusion iv), a coupling v), and a leak-off vi) part. Fracture deformation modifies the fracture aperture $\delta(\mathbf{x}, \tau)$ and thus contributes to the fracture-flow solution via the diffusion term iv) and the volumetric coupling term v).

In general, evolution of the deformation of the rock embedding the fracture and the pore pressure in it had to be analyzed relying on a poro-elastic theory, such as Biot’s theory [20, 177]. In this work, however, we focus on the specific case of highly conductive fractures in poorly permeable rocks and thus leak-off driven dissipation is neglected allowing for a

single phase, linear elasticity formulation for the surrounding rock

$$\text{Div}(\boldsymbol{\sigma}^s) = 0, \text{ with } \boldsymbol{\sigma}^s = 3 K_{\text{eff}} \text{vol}(\boldsymbol{\varepsilon}_s) + 2 \mu_{\text{eff}} \text{dev}(\boldsymbol{\varepsilon}_s), \quad (4.87)$$

where $\boldsymbol{\sigma}^s$ and $\boldsymbol{\varepsilon}_s$ are the stress and strain tensor of the solid and $\text{vol}(\boldsymbol{\varepsilon}_s)$ and $\text{dev}(\boldsymbol{\varepsilon}_s)$ the volumetric and deviatoric part of the solid's strain tensor. In equation (4.87), we introduced the effective shear modulus μ_{eff} and the effective bulk modulus K_{eff} of the poro-elastic medium, here derived from Gassmann's 1951 low-frequency result.

Text S2. Implementation

The non-linear system of partial differential equations is solved by an extended Dune-PDELab finite element implementation [15]. Discretization of the hybrid-dimensional flow model is realized by double-node zero-thickness elements, and the set of equations formed by monolithic assembly is solved by a direct solver in parallel. Averaging of balance of mass and momentum in the fracture domain is numerically realized by averaging the fluid pressure of facing fracture surfaces at aligning nodes of the implemented zero-thickness interface elements [177, 180, 181]. Numerical integration of the fracture-flow formulation is then performed on auxiliary lower dimensional elements. The auxiliary elements are used for integration purposes only, do not introduce additional degrees of freedom and therefore contribute to an increase in computational efficiency [177, 181]. Fracture aperture $\delta(\mathbf{x}, \tau)$ is handled on integration-point level accounting for the deformation of the zero-thickness elements. The framework uses a Newton-Raphson-based strategy to reach quadratic convergence of the equilibrium iterations.

Text S3. Model geometry and constitutive assumptions

We envision a harmonic excitation in fluid pressure at the center of a circular planar interface, the fracture, between two cylindrical domains. We investigate fractures in their post setting state [12, 14], i.e., fracture deformation is considered to be reversible for the investigated effective stress states. We assume a uniform initial fracture aperture and homogeneous properties of the solid cylinders to allow for a two dimensional, radial symmetric formulation of the governing equations (4.86) and (4.87). The modeled fractures do not have physical ends, thus their *geometrical stiffness* [131, 175] is not considered in this study; an assumption valid for fluid pressure amplitudes below the acting normal stresses, i.e., much smaller than the fluid pressures required for fracture-surface separation [175]. Yet, we imposed a no-flow boundary at the end of the fractures.

Opposing fracture surfaces are locally in contact for a finite stress normal to the fracture surface, σ_N [40, 77], leading to the *contact stiffness*. Shear deformations are insignificant when, as is typically the case in hydraulic tests, the fluid pressure remains well below the jacking pressure, i.e., the pressure causing fracture surface separation, and we therefore neglect the contribution of shear stress induced fracture dilation [173, 175]. We describe the contact mechanics on the continuum scale by an empirical, hyperbolic evolution law [12, 75]

$$\Delta\delta = (\delta_0 - \delta_{\min}) \frac{\sigma_N}{E^{\text{Fr}} - \sigma_N}, \quad (4.88)$$

where the changes in effective fracture aperture $\Delta\delta$ relative to the initial aperture δ_0 at zero stress are incorporated in the effective fracture aperture $\delta = \delta_0 + \Delta\delta$, δ_{\min} is the minimum effective fracture aperture reached for $\sigma_N \rightarrow -\infty$ and E^{Fr} the fracture Young's modulus [70, 180].

Text S4. Properties of the numerically investigated fractures

In Table 4.21, we use a notation that reflects the minimum $\hat{\sigma}_N^{\text{eq}} = \sigma_N^{\text{min}} - p^{\text{eq}} = 5$ MPa and maximum $\hat{\sigma}_N^{\text{eq}} = \sigma_N^{\text{max}} - p^{\text{eq}} = 95$ MPa effective normal stresses, and define properties evaluated at these range boundaries by $\hat{\square}$ and $\hat{\square}$.

At RZ-URL, harmonic testing was performed with a double-packer probe (Solexperts GmbH, Bochum, Germany) installed at a distance of 40.6 m from the head of a 63 m long borehole drilled dipping downwards 15° to NNE from a tunnel about 130 m below the surface. The interval enclosed between the two packers had a length of 0.7 m; the injection system had a storage capacity of 1×10^{-12} m³/Pa. Stimulation preceding the harmonic testing lead to a pair of axial fracture traces at the borehole wall, complementing a pre-existing circumferential fracture trace, as revealed by televiwer-logging and impression-packer testing [2]. The data used here represent a sinusoidal variation in flow rate with a period of 65 s and an amplitude of 1.25 l/min around a constant flow rate of 3.85 l/min for a total of 5 periods. Pressure in the borehole exhibited a periodic response with an amplitude of 0.3 MPa and a mean value of 4.9 MPa. We approximate fracture properties based on results of a numerical hydro-mechanical characterization of step-rate tests performed at six fractured intervals of the same borehole at different depths [175].

Considering the estimated hydro-mechanical properties gained from preceding investigations for different intervals of the same borehole [175], apertures are approximated to range between 120 to 220 μm under an estimated effective normal stress of 1.1 to 1.6 MPa, and potential effective fracture lengths are expected to be approximately 10 m [175]. The fracture geometry is characterized by an estimated dimensionless domain length Λ_{RZ} of 100 and is slightly larger than the fracture domain investigated for domain B₂. The dimensionless characteristic diffusion time τ_{RZ} ranges from $2.0 \cdot 10^{-4}$ to $5.1 \cdot 10^{-4}$ indicating slightly slower pressure diffusion than investigated for the numerical domains but still rapid compared to the excitation period. The dimensionless domain stiffness of 16 to 42 indicates a compliant fracture response, and a relative aperture-change of $\Omega_{\text{RZ}} = 0.27$, comparable to values obtained for domain B₂ at 5 to 15 MPa effective normal stress. Characteristic occurrence of multiples of the excitation frequency are similar to those observed for the numerical domain B₂ are present in the spectrum of the measurement data (main paper Fig. 4 a).

The harmonic pumping tests at the Altona Flat Rock Site (AFR) in Clinton County were performed near the surface (7.6 m depth) on a single, hydraulically dominant bedding plane fracture with a length of approximately 10 m, embedded in a low-permeability sandstone [82]. With a dimensionless domain length of 200 the tested region is moderately larger than the ones numerically investigated. For characterization purposes, four monitoring boreholes were installed in a distance of 5 m to the excited borehole (radius 0.05 m) intersecting the fracture, too. Effective hydraulic apertures between 717 to 951 μm were estimated based on the measured fracture transmissivity [82]. Pressure responses below the excited amplitude measured in the monitoring boreholes indicate non-equilibrated fluid pressure in the tested volume below the ones typically expected for radial symmetric flow, contradicting with the approximated characteristic diffusion time of $2.3 \cdot 10^{-6}$ to $1.6 \cdot 10^{-5}$, which is comparable to the lower limit investigated for the numerical domains. Considering that pumping was performed near the surface we estimate a

compliant fracture response based on fracture stiffness-depth correlations investigated for fractured granite reservoirs [64, 164]. The resulting dimensionless aperture-change of 0.01 to 0.1 indicates moderate hydro-mechanical interaction comparable to the lower range of numerical domain B_2 . The pressure response to harmonic flow excitation exhibits a dominant frequency, but shows additional amplitudes at uneven multiples of the excitation frequency (main paper Fig. 4 c).

The harmonic pumping at the Terrieu karstic field tested a highly conductive limestone aquifer with conduits of an estimated effective hydraulic aperture of 111 μm to 350 μm . From complementary experimental investigations it is known that apertures can locally reach 20 to 50 cm [61] suggesting that parts of the conduits are not in mechanical contact. The connected hydraulic pathways span a network extending over a total area of approximately 2500 m^2 . Monitoring wells are positioned at distances between 8 to 24 m to the pumping borehole. The dimensionless domain length of 1000 is significantly larger than for the numerical studies and the dimensionless characteristic diffusion time of $3.4 \cdot 10^{-4}$ to $3.4 \cdot 10^{-3}$ indicates slower pressure diffusion processes than for numerical domains B_1 and B_2 . Despite a characteristic diffusion time that is three to four orders of magnitude smaller than the applied period, pressure responses are below the excited amplitude measured in monitoring boreholes, i.e., fluid pressure is not equilibrated in the tested volume. Considering the absence of mechanical contact in large parts of the karstic, we assume that changes in fracture volume are purely induced by deformation of the surrounding bulk material and therefore assume that changes in fracture aperture are directly related to the domain stiffness. Overtones in the recorded data (main paper Fig. 4 b) are not consistently occurring at multiples of the excitation frequency but at arbitrary frequencies.

Harmonic tests at the Boise Hydrogeophysical Research Site (BHR) aimed at the characterization of a gravel aquifer. The gravel reservoir is tested close to the surface under low normal stress conditions where single contacts between cobbles are expected to react compliant to changes in effective stress. Conductivity-based estimates of an equivalent fracture aperture range between 16 and 29 μm . The dimensionless domain length of 1000 translates to a larger tested region than numerically investigated. The high dimensionless characteristic diffusion times, ranging between 0.6 and 2.1 are in good agreement with the non-equilibrated pressure responses indicated by amplitude ratios between 0.004 to 0.037 measured in the monitoring boreholes [153]. The pronounced dimensionless characteristic diffusion time translates to a low penetration depth. Here, we consider deformation induced hydraulic changes of the investigated region in terms of the Kozeny-Carman equation which correlates porosity changes to changes in permeability for granular media [37]. The initial porosity of the gravel aquifer ranges between 0.17 to 0.24 [153]. Similar to the dimensionless aperture-change we therefore introduce the dimensionless porosity change $\Omega^* = p_A \partial \ln(\phi) / \partial p$ to quantify the hydro-mechanical interaction expected throughout a testing period where ϕ is the porosity and where we assumed that changes in effective stress are exclusively related to changes in fluid pressure. We estimated the dimensionless porosity change based on investigated density changes of gravel samples under low perturbations of compression forces [166] resulting in a range of 0.13 to 0.19. The occurrence of overtones in the spectra of the pressure response (main paper Fig. 4 d) show close

similarities to that found for the responses of numerical domain B_2 (main paper Fig. 3 b). The authors stated that the occurrence of overtones scaled with the applied excitation period where longer periods resulted in higher pressure amplitudes, but did not provide any further explanation [153].

Table 4.21: Parameters used for the numerical simulation of periodic hydraulic testing experiments on the two model domains B_1 and B_2 .

Sym.	Quantity	Value	Unit	Sym.	Quantity	Value	Unit
Geometry and hydraulic testing							
<i>B_1 and B_2</i>							
r_b	borehole radius	3.0	(mm)	T	testing period	10.0	(s)
p^{eq}	equilibrium pressure	5.0	(MPa)	p_A	pressure amplitude	4.0	(MPa)
p^c	confining pressure	20.0	(MPa)	$\Delta\sigma_N$	normal stress increment	10.0	(MPa)
σ_N^{\min}	minimum normal stress	10.0	(MPa)	σ_N^{\max}	maximum normal stress	100.0	(MPa)
$\hat{\sigma}_N^{eq}$	minimum equ. normal stress	5.0	(MPa)	$\hat{\sigma}_N^{eq}$	maximum equ. normal stress	95.0	(MPa)
B_1	domain height	7.5	(cm)	r_{B_1}	domain radius	1.5	(cm)
B_2	domain height	1.0	(m)	r_{B_2}	domain radius	0.15	(m)
Rock matrix							
<i>B_1 and B_2</i>							
K	dry frame bulk modulus	37.0	(GPa)	K^g	grain bulk modulus	43.2	(GPa)
G	shear modulus	17.7	(GPa)	ϕ	porosity	0.01	(-)
k^s	intrinsic permeability	$5.0 \cdot 10^{-19}$	(m ²)	β^f	fluid compressibility	0.417	(1/GPa)
calculated effective parameters							
E_{sat}	Gassmann bulk modulus	39.8	(GPa)	G_{sat}	Gassmann shear modulus	17.7	(GPa)
E_{sat}	Gassmann Young's modulus	46.2	(GPa)	ν_{sat}	Gassmann Poisson's ratio	0.3	(-)
B_1				B_2			
$C_{B_1}^1$	specific domain stiffness	616	(MPa/mm)	$C_{B_2}^1$	specific domain stiffness	46	(MPa/mm)

(continued on next page)

(continued from previous page)

Fluid domain **B_1 and B_2**

β^f	fluid compressibility	0.417	(1/GPa)	ρ^f	fluid density	997.0	(kg/m ³)
η^{fR}	effective fluid viscosity	1.0	(mPa s)	δ_{\min}	minimum fracture aperture	0.0	(μm)
B_1	fracture Young's modulus	90.0	(MPa)	δ_{0,B_1}	initial fracture aperture	55.0	(μm)
$E_{B_1}^{\text{Fr}}$							
B_2	fracture Young's modulus	1.4	(MPa)	δ_{0,B_2}	initial fracture aperture	1.2	(cm)
$E_{B_2}^{\text{Fr}}$							
$\delta_{B_2}^{\text{Fr}}$	fracture aperture at σ_N^{eq}	262.5	(μm)		fracture aperture at σ_N^{eq}	17.4	(μm)

Normalized parameters

B_1							
$\tilde{\Gamma}_{B_1}$	specific domain stiffness at σ_N^{eq}	0.34	(-)	$\tilde{\Gamma}_{B_1}$	specific domain stiffness at σ_N^{eq}	0.09	(-)
$\tilde{\tau}_{B_1}$	characteristic diffusion time at σ_N^{eq}	$2.7 \cdot 10^{-8}$	(-)	$\tilde{\tau}_{B_1}$	characteristic diffusion time at σ_N^{eq}	$1.0 \cdot 10^{-7}$	(-)
$\tilde{\Omega}_{B_1}$	relative aperture-change at σ_N^{eq}	0.04	(-)	$\tilde{\Omega}_{B_1}$	relative aperture-change at σ_N^{eq}	0.02	(-)
Λ_{B_1}	domain radius	5	(-)				
B_2							
$\tilde{\Gamma}_{B_2}$	specific domain stiffness at σ_N^{eq}	1.9	(-)	$\tilde{\Gamma}_{B_2}$	specific domain stiffness at σ_N^{eq}	$8.3 \cdot 10^{-3}$	(-)
$\tilde{\tau}_{B_2}$	characteristic diffusion time at σ_N^{eq}	$1.6 \cdot 10^{-7}$	(-)	$\tilde{\tau}_{B_2}$	characteristic diffusion time at σ_N^{eq}	$3.6 \cdot 10^{-5}$	(-)
$\tilde{\Omega}_{B_2}$	relative aperture-change at σ_N^{eq}	0.63	(-)	$\tilde{\Omega}_{B_2}$	relative aperture-change at σ_N^{eq}	0.04	(-)
Λ_{B_2}	domain radius	50	(-)				

Table 4.22: Numerical and experimental characteristic properties. Here, we replace the fracture length l^F by the more general domain size a and introduce the hydraulic conductivity K_{hyd} .

Exp.	a (m)	h (m)	r_b (cm)	T (s)	p_A (MPa)	K_{hyd} (m/s)	δ (μm)	E (GPa)	C (MPa/mm)	C^{Fr} (MPa/mm)
B_1	0.015	0.075	0.3	3.8	4.0	$5.7 \cdot 10^{-4t} - 2.2 \cdot 10^{-3t}$	26.6 – 52.0	46.2	616	1800 – 7000
B_2	0.15	1.0	0.3	10.0	4.0	$2.4 \cdot 10^{-4t} - 5.6 \cdot 10^{-2t}$	17.4 – 262.5	46.2	46	24 – 5549
RZ	~ 10	~ 0.2	~ 4	65.0	0.3	$1.2 \cdot 10^{-2t} - 3.9 \cdot 10^{-2t}$	121.9 – 218.2	42.0	210	5 – 13
TER	~ 50	~ 10	~ 5	300.0	$1.7 \cdot 10^{-2}$	$1.0 \cdot 10^{-2} - 1.0 \cdot 10^{-1}$	110.8 ^t – 350.3 ^t	40.0	4	4
AFR	~ 10	7.6	~ 5	61.0 – 243.0	$1.5 \cdot 10^{-3}$	$4.2 \cdot 10^{-1t} - 7.4 \cdot 10^{-1t}$	716.7 [†] – 950.5 [†]	10.0	1.3	0.02 – 0.1
BHR	~ 50	~ 10	~ 5	24.0	$0.3 \cdot 10^{-3}$	$2.0 \cdot 10^{-4} - 7.0 \cdot 10^{-4}$	-	0.1	0.01	-

† calculated based on $K_{\text{hyd}} = T_{\text{hyd}}/\delta$

‡ calculated based on $\delta = \sqrt[3]{12\gamma^{\text{Fr}}T_{\text{hyd}}/(\rho^{\text{Fr}}g)}$ [95] with $T_{\text{hyd}} = 3.0 - 7.2 \cdot 10^{-4} \text{ m}^2/\text{s}$ [82]

T calculated based on $\delta = \sqrt[2]{12\gamma^{\text{Fr}}K_{\text{hyd}}/(\rho^{\text{Fr}}g)}$, [95] considering $T_{\text{hyd}} = K_{\text{hyd}}\delta$

Table 4.23: Numerical and experimental dimensionless properties.

Exp.	Λ	τ	Γ	Ω
B ₁	5	$2.7 \cdot 10^{-8} - 1.0 \cdot 10^{-7}$	0.09 – 0.34	0.02 – 0.04
B ₂	50	$1.6 \cdot 10^{-7} - 3.6 \cdot 10^{-5}$	1.89 – 0.01	0.04 – 0.63
RZ	100	$1.6 \cdot 10^{-4} - 5.1 \cdot 10^{-4}$	16.0 – 41.6	0.19 – 0.27
TER	1000	$3.4 \cdot 10^{-4} - 3.4 \cdot 10^{-3}$	1.0	0.01 – 0.04
AFR	200	$2.3 \cdot 10^{-6} - 1.6 \cdot 10^{-5}$	13.2 – 65.8	0.01 – 0.10
BHR	1000	0.6 – 2.1	-	0.13 – 0.19 [†]

[†] dimensionless porosity change

Chapter 5:

Summary and outlook

5.1 Summary

Detailed knowledge about the underground characteristics of fractured reservoirs increases the efficiency of energy production based on natural resources. Inverse analysis of the measurement data has proven to be of great importance when sophisticated numerical models have been used for detailed investigations. The demands on the consulted model are defined by hydro-mechanical phenomena found in experimental transient data sets indicating the strong dependence of the fracture flow on the deformation state of the surrounding reservoir and the characteristic high-aspect ratio fracture geometry which introduces some limitations to the numerical discretization. Considering these limiting conditions this work has been concerned with the derivation of a consistent hydro-mechanical model for flow in deformable fractures below the limit of seismic actions by consulting the framework of continuum-mechanics.

Capturing hydro-mechanical phenomena throughout perturbations of the fractured reservoir's equilibrium state has been achieved by introducing distinct models for the porous and fracture domain along with consistent transition boundary conditions defined on the fracture surface. Responses of the surrounding porous matrix have been considered by means of a biphasic poro-elastic model accounting for a barotropic fluid and linear-elastic material response. Characteristics of flow processes in deformable fractures have been governed by a dimensionally reduced hybrid-dimensional model. To close the continuum-mechanical description governing the behaviour of hydro-mechanically interacting fractured porous media, hydraulic and mechanical transition boundary conditions have been defined along the fracture surface.

Numerical coupling of the fracture and poro-elastic domain requires special treatment to guarantee stability and computational efficiency. In the scope of this work three different coupling strategies have been investigated. Monolithic coupling of both domains has been achieved by introducing a zero-thickness element formulation by consulting an averaging procedure of the balance equations. The advantage of the monolithic coupling scheme has been identified to be the numerical stability of the method quantified by the convergence rate determined throughout a number of numerical studies. Nevertheless, parallel computing using iterative linear solvers would require the implementation of specific preconditioning and has not been considered throughout this work. Alternatively two partitioned coupling schemes have been investigated. The fixed-stress coupling enforces constant stress-rates throughout the calculation of the flow processes to guarantee numerical stability. It has been found that its implementation requires a reasonable number of iterations to meet the convergence criterion. Coupling in a less specific sense has been studied by using a number of advanced quasi-Newton coupling schemes consulting the coupling library preCICE. Studies on the convergence behaviour proved satisfying con-

vergence behaviour throughout a number of test cases in three dimensions. Besides the implemented numerical coupling schemes, another advantage when consulting preCICE is the fully parallelized infrastructure for communication between different domains which drastically increases the computational efficiency and is of interest for large-scale problems.

In a subsequent step the proposed model has been used to investigate hydro-mechanical effects throughout stimulations of fractured porous media. To capture the mechanical interaction of both fracture surfaces in terms of contact, assumptions for investigations below the limit of seismic actions have been discussed to introduce a normal fracture stiffness model under in-situ conditions. Based on a consistent set of hydro-mechanical measurement data obtained from field experiments under in-situ conditions the importance of deformation related volume changes of fractures throughout flow processes could then consistently be proven by a split of contributing compressible fluid volume and fracture aperture changes. Another study was concerned with the identification of hydro-mechanical effects throughout harmonic fluid pressure excitations of a single fracture. The study could consistently correlate additional frequencies in the flow response not to measurement imperfections, like assumed in the known literature, but to transient changes of the hydro-mechanical fracture characteristics within one stimulation period.

5.2 Outlook

At this stage, the proposed model has been shown to consider hydro-mechanical effects throughout flow processes under the limit of seismic actions in a fulfilling manner. Nevertheless, once the field of investigations might be extended it is of importance to introduce certain modifications to the existing model. Thinking about re-activation of existing faults, experimental operations are performed at high stimulation pressures that potentially induce seismic actions in the sense of fracture shearing [33, 78–80]. Determination of seismic actions requires the consideration of shear stresses to evaluate the friction state of the fracture surfaces. Consistent extension of the normal stiffness constitutive relation to a model considering frictional behaviour would require, e.g. a Mohr-Coulomb type formulation capable of determining potential areas of fracture shearing. Taking the proposed zero-thickness element formulation into consideration the assumption of static fracture networks might be extended to fracture propagation by cohesive element formulations to potentially investigate phenomena related to hydraulic fracturing [e.g., 117]. Extension of the existing model by means of consideration of convection and diffusion effects of temperature exchange between the fracture domain and the porous media would allow for studies on geothermal energy production [e.g., 167].

Besides extension of the existing model to investigate phenomena in varying fields of fractured porous media, harmonic experiments on the laboratory scale might be performed to better understand hydro-mechanical characteristics occurring throughout harmonic fluid pressure excitation of a single horizontal fracture. The knowledge gained by the numerical investigations could then be used throughout the design and execution of experimental studies to generate consistent sets of pressure, flow and deformation data. Comparison of the numerical and experimental findings could be used to determine a relation between

the fracture stiffness and the occurrence of additional overtones in the flow, respectively pressure response.

Bibliography

- [1] Adachi, J.; Siebrits, E.; Peirce, A. & Desroches, J.: Computer simulation of hydraulic fractures. *International Journal of Rock Mechanics and Mining Sciences* **44** (2007), 739 – 757.
- [2] Adero, B. A.: Experimental investigations of mechanical anisotropy of Freiberg gneiss: implications for hydraulic stimulation. *Dissertation, Ruhr-Universität Bochum* (2020).
- [3] Ahn, S.; Hammond, P. S. & Gringarten, A. C.: Estimating permeability distributions from pressure pulse testing. In *SPE Annual Technical Conference and Exhibition*, Society of Petroleum Engineers 2010.
- [4] Aki, K. & Koyanagi, R.: Deep volcanic tremor and magma ascent mechanism under Kilauea, Hawaii. *Journal of Geophysical Research: Solid Earth* **86** (1981), 7095–7109.
- [5] Alnæs, M.; Blechta, J.; Hake, J.; Johansson, A.; Kehlet, B.; Logg, A.; Richardson, C.; Ring, J.; Rognes, M. E. & Wells, G. N.: The FEniCS project version 1.5. *Archive of Numerical Software* **3** (2015).
- [6] Alnæs, M. S.; Blechta, J.; Hake, J.; Johansson, A.; Kehlet, B.; Logg, A.; Richardson, C.; Ring, J.; Rognes, M. E. & Wells, G. N.: The FEniCS project version 1.5. *Archive of Numerical Software* **3** (2015).
- [7] Alnæs, M. S.; Blechta, J.; Hake, J.; Johansson, A.; Kehlet, B.; Logg, A.; Richardson, C.; Ring, J.; Rognes, M. E. & Wells, G. N.: The fenics project version 1.5. *Archive of Numerical Software* **3** (2015).
- [8] Altmann, J.; Müller, B.; Müller, T.; Heidbach, O.; Tingay, M. & Weißhardt, A.: Pore pressure stress coupling in 3D and consequences for reservoir stress states and fault reactivation. *Geothermics* **52** (2014), 195 – 205.
- [9] Amann, F.; Gischig, V.; Evans, K.; Doetsch, J.; Jalali, R.; Valley, B.; Krietsch, H.; Dutler, N.; Villiger, L.; Brixel, B.; Klepikova, M.; Kittilä, A.; Madonna, C.; Wiemer, S.; Saar, M. O.; Loew, S.; Driesner, T.; Maurer, H. & Giardini, D.: The seismo-hydromechanical behavior during deep geothermal reservoir stimulations: open questions tackled in a decameter-scale in situ stimulation experiment. *Solid Earth* **9** (2018), 115–137, ISSN 1869-9529.
- [10] Babazadeh, M. & McClure, M.: Coupling fluid flow and geomechanics in a three-dimensional discrete fracture network simulator. *49th U.S. Rock Mechanics/Geomechanics Symposium* (2015).

- [11] Bakhos, T.; Cardiff, M.; Barrash, W. & Kitanidis, P. K.: Data processing for oscillatory pumping tests. *Journal of Hydrology* **511** (2014), 310 – 319, ISSN 0022-1694.
- [12] Bandis, S.; Lumsden, A. & Barton, N.: Fundamentals of rock joint deformation. In *International Journal of Rock Mechanics and Mining Sciences & Geomechanics Abstracts*, Pergamon 1983, vol. 20, pp. 249–268.
- [13] Barker, J. A.: A generalized radial flow model for hydraulic tests in fractured rock. *Water Resour Res* **24** (1988), 1796–1804.
- [14] Barton, N.; Bandis, S. & Bakhtar, K.: Strength, deformation and conductivity coupling of rock joints. *International Journal of Rock Mechanics and Mining Sciences & Geomechanics Abstracts* **22** (1985), 121 – 140, ISSN 0148-9062.
- [15] Bastian, P.; Heimann, F. & Marnach, S.: Generic implementation of finite element methods in the distributed and unified numerics environment (DUNE). *Kybernetika* **46** (2010), 294–315.
- [16] Batchelor, G. K.: *An Introduction to Fluid Dynamics*. Cambridge Mathematical Library, Cambridge University Press 2000.
- [17] Belytschko, T.; Liu, W. K.; Moran, B. & Elkhodary, K.: *Nonlinear Finite Elements for Continua and Structures*. John Wiley & Sons 2013.
- [18] Berge, R. L.; Berre, I.; Keilegavlen, E.; Nordbotten, J. M. & Wohlmuth, B.: Finite volume discretization for poroelastic media with fractures modeled by contact mechanics. *International Journal for Numerical Methods in Engineering* **121** (2020), 644–663.
- [19] Berre, I.; Doster, F. & Keilegavlen, E.: Flow in fractured porous media: A review of conceptual models and discretization approaches. *Transport in Porous Media* **130** (2019), 215–236.
- [20] Biot, M. A.: General theory of three-dimensional consolidation. *Journal of Applied Physics* **12** (1941), 155–164.
- [21] Blöcher, G.; Kluge, C.; Milsch, H.; Cacace, M.; Jacquy, A. B. & Schmittbuhl, J.: Permeability of matrix-fracture systems under mechanical loading – constraints from laboratory experiments and 3-D numerical modelling. *Advances in Geosciences* **49** (2019), 95–104.
- [22] Blok, K.; Williams, R.; Katofsky, R. & Hendriks, C. A.: Hydrogen production from natural gas, sequestration of recovered CO₂ in depleted gas wells and enhanced natural gas recovery. *Energy* **22** (1997), 161–168.
- [23] Boese, C.; Renner, J. & Dresen, G.: The STIMTEC experiment at the Reiche Zeche Ulab. Paper presented at the EGU General Assembly, Vienna 2020, no. EGU2020-14117.

- [24] Bogaers, A. E. J.; Kok, S.; Reddy, B. D. & Franz, T.: Quasi-Newton methods for implicit black-box FSI coupling. *Computer Methods in Applied Mechanics and Engineering* **279** (2014), 113–132, ISSN 0045-7825, URL <http://www.sciencedirect.com/science/article/pii/S0045782514002199>.
- [25] Bourdet, D.; Ayoub, J. & Pirard, Y.: Use of pressure derivative in well test interpretation. *SPE Formation Evaluation* **4** (1989), 293–302.
- [26] Brace, W. F.: *Pore Pressure in Geophysics*, American Geophysical Union 2013. ISBN 9781118664063, pp. 265–273.
- [27] Brenner, K.; Hennicker, J.; Masson, R. & Samier, P.: Gradient discretization of hybrid-dimensional darcy flow in fractured porous media with discontinuous pressures at matrix - fracture interfaces. *IMA Journal of Numerical Analysis* **37** (2017), 1551–1585.
- [28] Brezzi, F. & Fortin, M.: *Mixed and Hybrid Finite Element Methods*, vol. 15. Springer Science & Business Media 2012.
- [29] Brown, K. M.; Tryon, M. D.; DeShon, H. R.; Dorman, L. M. & Schwartz, S. Y.: Correlated transient fluid pulsing and seismic tremor in the Costa Rica subduction zone. *Earth and Planetary Science Letters* **238** (2005), 189–203.
- [30] Buis, S.; Piacentini, A. & Déclat, D.: Palm: A computational framework for assembling high-performance computing applications. *Concurrency and Computation: Practice and Experience* **18** (2006), 231–245.
- [31] Bungartz, H.-J.; Lindner, F.; Gatzhammer, B.; Mehl, M.; Scheufele, K.; Shukaev, A. & Uekermann, B.: preCICE – A fully parallel library for multi-physics surface coupling. *Computers and Fluids* **141** (2016), 250–258, ISSN 0045-7930.
- [32] Bungartz, H.-J.; Lindner, F.; Gatzhammer, B.; Mehl, M.; Scheufele, K.; Shukaev, A. & Uekermann, B.: preCICE – A fully parallel library for multi-physics surface coupling. *Computers & Fluids* **141** (2016), 250 – 258, ISSN 0045-7930, advances in Fluid-Structure Interaction.
- [33] Cappa, F.; Guglielmi, Y.; Nussbaum, C. & Birkholzer, J.: On the relationship between fault permeability increases, induced stress perturbation, and the growth of aseismic slip during fluid injection. *Geophysical Research Letters* **0** (2018).
- [34] Cappa, F.; Guglielmi, Y.; Rutqvist, J.; Tsang, C.-F. & Thoraval, A.: Hydromechanical modelling of pulse tests that measure fluid pressure and fracture normal displacement at the Coaraze Laboratory site, France. *International Journal of Rock Mechanics and Mining Sciences* **43** (2006), 1062 – 1082.
- [35] Cappa, F.; Guglielmi, Y.; Rutqvist, J.; Tsang, C.-F. & Thoraval, A.: Estimation of fracture flow parameters through numerical analysis of hydromechanical pressure pulses. *Water Resources Research* **44** (2008).

- [36] Cardiff, M.; Barrash, W. & Kitanidis, P. K.: Hydraulic conductivity imaging from 3-D transient hydraulic tomography at several pumping/observation densities. *Water Resources Research* **49** (2013), 7311–7326.
- [37] Carman, P.: *Flow of Gases through Porous Media*. Academic Press Inc. 1956.
- [38] Castelletto, N.; White, J. A. & Tchelepi, H. A.: Accuracy and convergence properties of the fixed-stress iterative solution of two-way coupled poromechanics. *International Journal for Numerical and Analytical Methods in Geomechanics* **39** (2015), 1593–1618.
- [39] Cheng, Y. & Renner, J.: Exploratory use of periodic pumping tests for hydraulic characterization of faults. *Geophysical Journal International* **212** (2018), 543–565.
- [40] Cook, N.: Natural joints in rock: Mechanical, hydraulic and seismic behaviour and properties under normal stress. *International Journal of Rock Mechanics and Mining Sciences & Geomechanics Abstracts* **29** (1992), 198 – 223.
- [41] Coussy, O.: *Poromechanics*. John Wiley & Sons 2004.
- [42] Daniel, D. E.: *Geotechnical Practice for Waste Disposal*. Springer Science & Business Media 2012.
- [43] David, C.: Geometry of flow paths for fluid transport in rocks. *Journal of Geophysical Research: Solid Earth* **98** (1993), 12267–12278.
- [44] Davies, S. J.; White, C. M. & Appleton, E. V.: An experimental study of the flow of water in pipes of rectangular section. *Proceedings of the Royal Society of London. Series A, Containing Papers of a Mathematical and Physical Character* **119** (1928), 92–107.
- [45] Degroote, J.; Bruggeman, P.; Haelterman, R. & Vierendeels, J.: Stability of a coupling technique for partitioned solvers in FSI applications. *Computers & Structures* **86** (2008), 2224–2234, ISSN 0045-7949.
- [46] Degroote, J.; Haelterman, R.; Annerel, S.; Bruggeman, P. & Vierendeels, J.: Performance of partitioned procedures in fluid–structure interaction. *Computers & Structures* **88** (2010), 446 – 457, ISSN 0045-7949.
- [47] Deparis, S.; Discacciati, M.; Fourestey, G. & Quarteroni, A.: Fluid–structure algorithms based on Steklov-Poincaré operators. *Computer Methods in Applied Mechanics and Engineering* **195** (2006), 5797–5812, ISSN 0045-7825, John H. Argyris Memorial Issue. Part II.
- [48] Doe, T. W. & Korbin, G. E.: A Comparison Of Hydraulic Fracturing And Hydraulic Jacking Stress Measurements. *The 28th U.S. Symposium on Rock Mechanics (US-RMS), Tucson, 29 June - 1 July 1987* (1987), 283–290.
- [49] Doré, A. & Sinding-Larsen, R.: *Quantification and Prediction of Hydrocarbon Resources*. Elsevier Science 1996, ISBN 9780080540092.

- [50] Dresen, G.; Renner, J.; Bohnhoff, M.; Konietzki, H.; Kwiatek, G.; Plenkers, K.; Klee, G. & Backers, T.: T. STIMTEC – a mine-back experiment in the Reiche Zeche underground laboratory. *Geophysical Research Abstracts vol 21, EGU2019-9357, EGU General Assembly, Vienna* (2019).
- [51] Duboeuf, L.; De Barros, L.; Cappa, F.; Guglielmi, Y.; Deschamps, A. & Seguy, S.: Aseismic motions drive a sparse seismicity during fluid injections into a fractured zone in a carbonate reservoir. *Journal of Geophysical Research: Solid Earth* **122** (2017), 8285–8304.
- [52] Dutler, N.; Valley, B.; Gischig, V.; Villiger, L.; Krietsch, H.; Doetsch, J.; Brixel, B.; Jalali, M. & Amann, F.: Hydraulic fracture propagation in a heterogeneous stress field in a crystalline rock mass. *Solid Earth* **10** (2019), 1877–1904.
- [53] Dutler, N.; Valley, B.; Gischig, V. S.; Jalali, M.; Brixel, B.; Krietsch, H.; Roques, C. & Amann, F.: Hydromechanical insight of fracture opening and closure during in-situ hydraulic fracturing in crystalline rock. *Int. J. Rock Mech. Min. Sci.* **135** (2020), 104450.
- [54] Ehlers, W. & Bluhm, J.: *Porous Media: Theory, Experiments and Numerical Applications*. Springer Science & Business Media 2002.
- [55] Ehlers, W.; Ellsiepen, P.; Blome, P.; Mahnkopf, D. & Markert, B.: *Theoretische und numerische Studien zur Lösung von Rand- und Anfangswertproblemen in der Theorie Poröser Medien. Abschlußbericht zum DFG-Forschungsvorhaben Eh 107/6-2*. Berichte aus dem Institut für Mechanik (Bauwesen) 1999.
- [56] Evans, K.; Kohl, T.; Rybach, L. & Hopkirk, R.: The effects of fracture normal compliance on the long term circulation behavior of a hot dry rock reservoir: A parameter study using the New fully-coupled code 'Fracture'. *Geothermal Resources Council, Davis, CA(USA)*. **16** (1992), 449–456.
- [57] Eymard, R.; Gallouët, T. & Herbin, R.: Finite volume methods. *Handbook of numerical analysis* **7** (2000), 713–1018.
- [58] Farhat, C.: *CFD-Based Nonlinear Computational Aeroelasticity*, John Wiley & Sons 2004, chap. 13. ISBN 9780470091357.
- [59] Felsenthal, M.: Step-rate tests determine safe injection pressures in floods. *Oil & Gas Journal* **72** (1974).
- [60] Fetter, C. W.: *Applied Hydrogeology*. Waveland Press 2018.
- [61] Fischer, P.; Jardani, A.; Cardiff, M.; Lecoq, N. & Jourde, H.: Hydraulic analysis of harmonic pumping tests in frequency and time domains for identifying the conduits networks in a karstic aquifer. *Journal of Hydrology* **559** (2018), 1039 – 1053, ISSN 0022-1694.

- [62] Flemisch, B.; Berre, I.; Boon, W.; Fumagalli, A.; Schwenck, N.; Scotti, A.; Stefansson, I. & Tatomir, A.: Benchmarks for single-phase flow in fractured porous media. *Advances in Water Resources* **111** (2018), 239 – 258.
- [63] Fokker, P. A.; Renner, J. & Verga, F.: Applications of harmonic pulse testing to field cases. In *SPE Europec/EAGE Annual Conference*, Society of Petroleum Engineers 2012.
- [64] Fransson, Å.: *Literature survey: Relations between stress change, deformation and transmissivity for fractures and deformation zones based on in situ investigations*. Skb rapport r-09-13, Swedish Nuclear Fuel and Waste Management Co, Box 250, SE-101 24 Stockholm 2009, iSSN 1402-3091.
- [65] Gale, J. E.: Comparison of coupled fracture deformation and fluid flow models with direct measurements of fracture pore structure and stress-flow properties. *American Rock Mechanics Association* (1987).
- [66] Gassmann, F.: *Über die Elastizität poröser Medien: Vierteljahrsschrift der Naturforschenden Gesellschaft in Zürich*. 1951.
- [67] Ge, S.: A governing equation for fluid flow in rough fractures. *Water Resources Research* **33** (1997), 53–61.
- [68] Geertsma, J. & De Klerk, F.: A rapid method of predicting width and extent of hydraulically induced fractures. *Journal of Petroleum Technology* **21** (1969), 1–571.
- [69] Gellasch, C. A.; Wang, H. F.; Bradbury, K. R.; Bahr, J. M. & Lande, L. L.: Reverse water-level fluctuations associated with fracture connectivity. *Groundwater* **52** (2014), 105–117.
- [70] Gens, A.; Carol, I. & Alonso, E.: A constitutive model for rock joints formulation and numerical implementation. *Computers and Geotechnics* **9** (1990), 3 – 20, special Issue on Soil-Structure Interaction.
- [71] Geuzaine, C. & Remacle, J.-F.: Gmsh: A 3-D finite element mesh generator with built-in pre- and post-processing facilities. *International Journal for Numerical Methods in Engineering* **79** (2009), 1309–1331.
- [72] Girault, V.; Kumar, K. & Wheeler, M. F.: Convergence of iterative coupling of geomechanics with flow in a fractured poroelastic medium. *Computational Geosciences* **20** (2016), 997–1011, ISSN 1573-1499.
- [73] Girault, V.; Wheeler, M. F.; Ganis, B. & Mear, M. E.: A lubrication fracture model in a poro-elastic medium. *Mathematical Models and Methods in Applied Sciences* **25** (2015), 587–645.
- [74] Gleeson, T.; Wada, Y.; Bierkens, M. F. & Van Beek, L. P.: Water balance of global aquifers revealed by groundwater footprint. *Nature* **488** (2012), 197–200.

- [75] Goodman, R. E.: *Methods of Geological Engineering in Discontinuous Rocks*. West Publishing Company 1976.
- [76] Gothäll, R. & Stille, H.: Fracture–fracture interaction during grouting. *Tunnelling and Underground Space Technology* **25** (2010), 199 – 204.
- [77] Greenwood, J. A.; Williamson, J. B. P. & Bowden, F. P.: Contact of nominally flat surfaces. *Proceedings of the Royal Society of London. Series A. Mathematical and Physical Sciences* **295** (1966), 300–319.
- [78] Guglielmi, Y.; Cappa, F. & Amitrano, D.: High-definition analysis of fluid-induced seismicity related to the mesoscale hydromechanical properties of a fault zone. *Geophysical Research Letters* **35** (2008).
- [79] Guglielmi, Y.; Cappa, F.; Avouac, J.-P.; Henry, P. & Elsworth, D.: Seismicity triggered by fluid injection–induced aseismic slip. *Science* **348** (2015), 1224–1226, ISSN 0036-8075.
- [80] Guglielmi, Y.; Elsworth, D.; Cappa, F.; Henry, P.; Gout, C.; Dick, P. & Durand, J.: In situ observations on the coupling between hydraulic diffusivity and displacements during fault reactivation in shales. *Journal of Geophysical Research: Solid Earth* **120** (2015), 7729–7748.
- [81] Guiducci, C.; Collin, F.; Radu, J.-P.; Pellegrino, A. & Charlier, R.: Numerical modeling of hydro-mechanical fracture behaviour. *NUMOG VIII* (2003), 293–299.
- [82] Gultinan, E. & Becker, M. W.: Measuring well hydraulic connectivity in fractured bedrock using periodic slug tests. *Journal of Hydrology* **521** (2015), 100–107, ISSN 0022-1694.
- [83] Haelterman, R.; Bogaers, A.; Scheufele, K.; Uekermann, B. & Mehl, M.: Improving the performance of the partitioned QN-ILS procedure for fluid–structure interaction problems: Filtering. *Computers & Structures* **171** (2016), 9 – 17, ISSN 0045-7949.
- [84] Haelterman, R.; Degroote, J.; Van Heule, D. & Vierendeels, J.: The quasi-newton least squares method: A new and fast secant method analyzed for linear systems. *SIAM Journal on Numerical Analysis* **47** (2009), 2347–2368.
- [85] Haimson, B.; Fairhurst, C. *et al.*: Hydraulic fracturing in porous-permeable materials. *Journal of Petroleum Technology* **21** (1969), 811–817.
- [86] Hanowski, K. K. & Sander, O.: Simulation of Deformation and Flow in Fractured, Poroelastic Materials. *ArXiv e-prints* (2016).
- [87] Hartmaier, H.; Doe, T. & Dixon, G.: Evaluation of Hydrojacking Tests for an Unlined Pressure Tunnel. *Tunnelling and Underground Space Technology* **13** (1998), 393–401.
- [88] Haupt, P.: *Continuum Mechanics and Theory of Materials*. Springer Science & Business Media 2013.

- [89] Hollaender, F.; Hammond, P. S. & Gringarten, A. C.: Harmonic testing for continuous well and reservoir monitoring. In *SPE Annual Technical Conference and Exhibition*, Society of Petroleum Engineers 2002.
- [90] Holloway, S.: Underground sequestration of carbon dioxide - a viable greenhouse gas mitigation option. *Energy* **30** (2005), 2318–2333.
- [91] Holzapfel, G. A.: *Nonlinear Solid Mechanics: A Continuum Approach for Engineering Science*. John Wiley & Sons 2000, ISBN 9780471823193.
- [92] Horne, R. N.: *Modern Well Test Analysis*. Petroway Inc. 1995.
- [93] Hubbert, M. K. & Willis, D. G.: Mechanics of hydraulic fracturing. *Transactions of the AIME* **210** (1957), 153–168.
- [94] Hughes, T. J.: *The Finite Element Method: Linear Static and Dynamic Finite Element Analysis*. Dover Publications Inc. 2000.
- [95] Hyman, J. D.; Aldrich, G.; Viswanathan, H.; Makedonska, N. & Karra, S.: Fracture size and transmissivity correlations: Implications for transport simulations in sparse three-dimensional discrete fracture networks following a truncated power law distribution of fracture size. *Water Resources Research* **52** (2016), 6472–6489.
- [96] Iwai, K.: *Fundamental Studies of Fluid Flow Through a Single Fracture*. University of California at Berkeley 1976.
- [97] Jiang, X.-W.; Wan, L.; Wang, X.-S.; Liang, S.-H. & Hu, B. X.: Estimation of fracture normal stiffness using a transmissivity-depth correlation. *International Journal of Rock Mechanics and Mining Sciences* **46** (2009), 51–58, ISSN 1365-1609.
- [98] Jin, L. & Zoback, M. D.: Fully coupled nonlinear fluid flow and poroelasticity in arbitrarily fractured porous media: A hybrid-dimensional computational model. *Journal of Geophysical Research: Solid Earth* **122** (2017), 7626–7658.
- [99] Johnson, C. R.; Greenkorn, R.; Woods, E. *et al.*: Pulse-testing: A new method for describing reservoir flow properties between wells. *Journal of Petroleum Technology* **18** (1966), 1–599.
- [100] Joppich, W. & Kürschner, M.: MpCCI — a tool for the simulation of coupled applications. *Concurrency and Computation: Practice and Experience* **18** (2006), 183–192.
- [101] Kamal, M.; Brigham, W. E. *et al.*: Pulse-testing response for unequal pulse and shut-in periods. *Society of Petroleum Engineers Journal* **15** (1975), 399–410.
- [102] Kataoka, S.; Minami, S.; Kawai, H.; Yamada, T. & Yoshimura, S.: A parallel iterative partitioned coupling analysis system for large-scale acoustic fluid–structure interactions. *Computational Mechanics* **53** (2014), 1299–1310, ISSN 1432-0924.

- [103] Keilegavlen, E.; Berge, R.; Fumagalli, A.; Starnoni, M.; Stefansson, I.; Varela, J. & Berre, I.: PorePy: An open-source simulation tool for flow and transport in deformable fractured rocks. *Computational Geosciences* **25** (2021), 243–265, ISSN 1573-1499.
- [104] Kim, J.; Tchelepi, H. & Juanes, R.: Stability and convergence of sequential methods for coupled flow and geomechanics: Drained and undrained splits. *Computer Methods in Applied Mechanics and Engineering* **200** (2011), 2094 – 2116.
- [105] Kim, J.; Tchelepi, H. & Juanes, R.: Stability and convergence of sequential methods for coupled flow and geomechanics: Fixed-stress and fixed-strain splits. *Computer Methods in Applied Mechanics and Engineering* **200** (2011), 1591 – 1606.
- [106] Kim, J.; Tchelepi, H. A.; Juanes, R. *et al.*: Stability, accuracy and efficiency of sequential methods for coupled flow and geomechanics. In *SPE Reservoir Simulation Symposium*, Society of Petroleum Engineers 2009.
- [107] Kim, J.-M. & Parizek, R. R.: Numerical simulation of the Noordbergum effect resulting from groundwater pumping in a layered aquifer system. *Journal of Hydrology* **202** (1997), 231 – 243.
- [108] Klimczak, C.; Schultz, R. A.; Parashar, R. & Reeves, D. M.: Cubic law with aperture-length correlation: implications for network scale fluid flow. *Hydrogeol J* **18** (2010), 851–862.
- [109] Kohl, T. & Hopkirk, R.: “FRACure” — A simulation code for forced fluid flow and transport in fractured, porous rock. *Geothermics* **24** (1995), 333 – 343, ISSN 0375-6505, hot Dry Rock (HDR) Reservoir Modelling Activities within Europe.
- [110] Kolditz, O.; Fischer, T.; Frühwirt, T.; Görke, U.-J.; Helbig, C.; Konietzky, H.; Maßmann, J.; Nest, M.; Pötschke, D.; Rink, K.; Sattari, A.; Schmidt, P.; Steeb, H.; Wuttke, F.; Yoshioka, K.; Vowinkel, B.; Zieffe, G. & Nagel, T.: *GeomInt: geomechanical integrity of host and barrier rocks—experiments, models and analysis of discontinuities. Environmental Earth Sciences* **80** (2021).
- [111] Kurzeja, P. S. & Steeb, H.: About the transition frequency in Biot’s theory. *The Journal of the Acoustical Society of America* **131** (2012), EL454–EL460.
- [112] Kurzeja, P. S.; Steeb, H. & Renner, J.: *The Critical Frequency in Biphase Media: Beyond Biots Approach*. pp. 2361–2370.
- [113] Küttler, U. & Wall, W.: Fixed-point fluid-structure interaction solvers with dynamic relaxation. *Computational Mechanics* **43** (2008), 61–72.
- [114] Küttler, U. & Wall, W. A.: Fixed-point fluid–structure interaction solvers with dynamic relaxation. *Computational Mechanics* **43** (2008), 61–72.
- [115] Lamur, A.; Kendrick, J.; Eggertsson, G.; Wall, R.; Ashworth, J. & Lavallée, Y.: The permeability of fractured rocks in pressurised volcanic and geothermal systems. *Scientific Reports* **7** (2017), 6173.

- [116] Li, X.; Zhong, L. & Pyrak-Nolte, L. J.: Physics of partially saturated porous media: Residual saturation and seismic-wave propagation. *Annual Review of Earth and Planetary Sciences* **29** (2001), 419–460.
- [117] Li, Y.; Deng, J.; Liu, W. & Feng, Y.: Modeling hydraulic fracture propagation using cohesive zone model equipped with frictional contact capability. *Computers and Geotechnics* **91** (2017), 58 – 70.
- [118] Lindner, F.: *Data transfer in partitioned multi-physics simulations : interpolation & communication*. Ph.D. thesis, University of Stuttgart (2019).
- [119] Lindner, F.; Mehl, M. & Uekermann, B.: Radial basis function interpolation for black-box multi-physics simulations. In *Conference Proceedings at the ECCOMAS Coupled Problems 2017*, 2017.
- [120] Lindner, F.; Totounferoush, A.; Mehl, M.; Uekermann, B.; Pour, N. E.; Krupp, V.; Roller, S.; Reimann, T.; C. Sternel, D.; Egawa, R.; Takizawa, H. & Simonis, F.: ExaFSA: Parallel Fluid-Structure-Acoustic Simulation. In Bungartz, H.-J.; Reiz, S.; Uekermann, B.; Neumann, P. & Nagel, W. E. (eds.): *Software for Exascale Computing - SPPEXA 2016-2019*, Cham 2020, ISBN 978-3-030-47956-5, pp. 271–300.
- [121] Louis, C.: A study of groundwater flow in jointed rock and its influence on the stability of rock masses. *Rock Mechanics Research Report* **10** (1969), 1–90.
- [122] Makurat, A.: The measurement of the mechanical and hydraulic properties of rock joints at different scale in the Stripa project. In *Proc. Int. Symp. Rock Joints, 1990*, Balkema 1990, pp. 541–548.
- [123] Malvern, L. E.: *Introduction to the Mechanics of a Continuous Medium*. 1969.
- [124] Martin, V.; Jaffré, J. & Roberts, J. E.: Modeling fractures and barriers as interfaces for flow in porous media. *SIAM Journal on Scientific Computing* **26** (2005), 1667–1691.
- [125] Matthews, C.: Analysis of pressure build-up and flow test data. *Journal of Petroleum Technology* **13** (1961), 862–870.
- [126] Matthews, C. S. & Russell, D. G.: *Pressure Buildup and Flow Tests in Wells*, vol. 1. Society of Petroleum Engineers 1967.
- [127] Mavko, G.; Mukerji, T. & Dvorkin, J.: *The Rock Physics Handbook: Tools for Seismic Analysis of Porous Media*. Cambridge University Press 2009.
- [128] Mays, L. W.: *Water Resources Engineering*. John Wiley & Sons 2010.
- [129] McClure, M.; Babazadeh, M.; Shiozawa, S. & Huang, J.: Fully coupled hydromechanical simulation of hydraulic fracturing in three-dimensional discrete fracture networks. *SPE Hydraulic Fracturing Technology Conference* **21** (2015), 1302–1320.

- [130] Monge, A. & Birken, P.: On the convergence rate of the Dirichlet-Neumann iteration for unsteady thermal fluid-structure interaction. *Computational Mechanics* **62** (2018), 525–541, ISSN 1432-0924.
- [131] Murdoch, L. C. & Germanovich, L. N.: Analysis of a deformable fracture in permeable material. *International Journal for Numerical and Analytical Methods in Geomechanics* **30** (2006), 529–561.
- [132] Murdoch, L. C. & Germanovich, L. N.: Storage change in a flat-lying fracture during well tests. *Water Resources Research* **48** (2012).
- [133] Muskat, M. & Wyckoff, R.: *The Flow of Homogeneous Fluids Through Porous Media*. International series in physics, McGraw-Hill 1937.
- [134] Nordgren, R. *et al.*: Propagation of a vertical hydraulic fracture. *Society of Petroleum Engineers Journal* **12** (1972), 306–314.
- [135] Oliver, D. S. & Chen, Y.: Recent progress on reservoir history matching: A review. *Computational Geosciences* **15** (2011), 185–221.
- [136] Oron, A. P. & Berkowitz, B.: Flow in rock fractures: The local cubic law assumption reexamined. *Water Resources Research* **34** (1998), 2811–2825.
- [137] Ortiz R., A. E.; Jung, R. & Renner, J.: Two-dimensional numerical investigations on the termination of bilinear flow in fractures. *Solid Earth* **4** (2013), 331–345.
- [138] Ortiz R., A. E.; Jung, R. & Renner, J.: Two-dimensional numerical investigations on the termination of bilinear flow in fractures. *Solid Earth* **4** (2013), 331–345.
- [139] Ortiz R., A. E.; Renner, J. & Jung, R.: Hydromechanical analyses of the hydraulic stimulation of borehole Basel 1. *Geophysical Journal International* **185** (2011), 1266–1287.
- [140] Ortiz R., A. E.; Renner, J. & Jung, R.: Hydromechanical analyses of the hydraulic stimulation of borehole Basel 1. *Geophysical Journal International* **185** (2011), 1266–1287.
- [141] Peirce, A. P. & Siebrits, E.: A dual mesh multigrid preconditioner for the efficient solution of hydraulically driven fracture problems. *International Journal for Numerical Methods in Engineering* **63** (2005), 1797–1823.
- [142] Perkins, T.; Kern, L. *et al.*: Widths of hydraulic fractures. *Journal of Petroleum Technology* **13** (1961), 937–949.
- [143] Petrovitch, C. L.; Nolte, D. D. & Pyrak-Nolte, L. J.: Scaling of fluid flow versus fracture stiffness. *Geophysical Research Letters* **40** (2013), 2076–2080.
- [144] Preisig, G.; Joel Cornaton, F. & Perrochet, P.: Regional flow simulation in fractured aquifers using stress-dependent parameters. *Groundwater* **50** (2012), 376–385.

- [145] Pyrak-Nolte, L. & Morris, J.: Single fractures under normal stress: The relation between fracture specific stiffness and fluid flow. *International Journal of Rock Mechanics and Mining Sciences* **37** (2000), 245 – 262, ISSN 1365-1609.
- [146] Pyrak-Nolte, L. J.; Cook, N. G. W. & Nolte, D. D.: Fluid percolation through single fractures. *Geophysical Research Letters* **15** (1988), 1247–1250.
- [147] Pyrak-Nolte, L. J.; Myer, L. R.; Cook, N. G. & Witherspoon, P. A.: Hydraulic and mechanical properties of natural fractures in low permeability rock. *International Society for Rock Mechanics and Rock Engineering* (1987).
- [148] Pyrak-Nolte, L. J. & Nolte, D. D.: Approaching a universal scaling relationship between fracture stiffness and fluid flow. *Nature Communications* **7** (2016), ISSN 2041-1723.
- [149] Quintal, B.: Frequency-dependent attenuation as a potential indicator of oil saturation. *Journal of Applied Geophysics* **82** (2012), 119 – 128, ISSN 0926-9851.
- [150] Quintal, B.; Caspari, E.; Holliger, K. & Steeb, H.: Numerically quantifying energy loss caused by squirt flow. *Geophysical Prospecting* **67** (2019), 2196–2212.
- [151] Quintal, B.; Germán Rubino, J.; Caspari, E. & Holliger, K.: A simple hydromechanical approach for simulating squirt-type flow. *Geophysics* **81** (2016), 335–344.
- [152] Quirion, M. & Tournier, J.-P.: Hydraulic jacking tests in crystalline rocks for hydroelectric projects in Quebec, Canada. *ISRM International Symposium on In-Situ Rock Stress* (2010).
- [153] Rabinovich, A.; Barrash, W.; Cardiff, M.; Hochstetler, D. L.; Bakhos, T.; Dagan, G. & Kitanidis, P. K.: Frequency dependent hydraulic properties estimated from oscillatory pumping tests in an unconfined aquifer. *Journal of Hydrology* **531** (2015), 2 – 16, groundwater flow and transport in aquifers: Insights from modeling and characterization at the field scale.
- [154] Rasmussen, T. C.; Haborak, K. G. & Young, M. H.: Estimating aquifer hydraulic properties using sinusoidal pumping at the Savannah River site, South Carolina, USA. *Hydrogeology Journal* **11** (2003), 466–482.
- [155] Raven, K. & Gale, J.: Water flow in a natural rock fracture as a function of stress and sample size. *International Journal of Rock Mechanics and Mining Sciences & Geomechanics Abstracts* **22** (1985), 251–261, ISSN 0148-9062.
- [156] Renner, J.: STIMTEC – A mine-scale hydraulic stimulation experiment of anisotropic metamorphic rock with evaluation by mine-back drilling. *ARMA Newsletter* (2020).
- [157] Renner, J. & Messar, M.: Periodic pumping tests. *Geophysical Journal International* **167** (2006), 479–493.

- [158] Renner, J. & Steeb, H.: *Modeling of Fluid Transport in Geothermal Research*, Springer Berlin Heidelberg, Berlin, Heidelberg 2015. pp. 1443–1500.
- [159] Renshaw, C. E.: On the relationship between mechanical and hydraulic apertures in rough-walled fractures. *Journal of Geophysical Research: Solid Earth* **100** (1995), 24629–24636.
- [160] Rodenberg, B.; Desai, I.; Hertrich, R.; Jaust, A. & Uekermann, B.: Fenics-precice: Coupling fenics to other simulation software (2021).
- [161] Rodrigues, J.: The Noordbergum effect and characterization of aquitards at the Rio Maior mining project. *Ground Water* **21** (1983), 200–207.
- [162] Rodrigues, J. D.: The Noordbergum effect and characterization of aquitards at the Rio Maior mining project. *Groundwater* **21** (1983), 200–207.
- [163] Rutqvist, J.: Determination of hydraulic normal stiffness of fractures in hard rock from well testing. *International Journal of Rock Mechanics and Mining Sciences and* **32** (1995), 513–523.
- [164] Rutqvist, J.: Fractured rock stress-permeability relationships from in situ data and effects of temperature and chemical-mechanical couplings. *Geofluids* **15** (2015), 48–66.
- [165] Rutqvist, J.; Tsang, C.; Ekman, D. & Stephansson, O.: Evaluation of in situ hydro-mechanical properties of rock fractures at Laxemar in Sweden. *Proceedings of 1st Asian Rock Mechanics Symposium ARMS* **97** (1997), 619–624.
- [166] Rücknagel, J.; Götze, P.; Hofmann, B.; Christen, O. & Marschall, K.: The influence of soil gravel content on compaction behaviour and pre-compression stress. *Geoderma* **209–210** (2013), 226–232, ISSN 0016-7061.
- [167] Salimzadeh, S. & Nick, H.: A coupled model for reactive flow through deformable fractures in enhanced geothermal systems. *Geothermics* **81** (2019), 88 – 100.
- [168] Sandve, T.; Berre, I. & Nordbotten, J.: An efficient multi-point flux approximation method for discrete fracture–matrix simulations. *Journal of Computational Physics* **231** (2012), 3784 – 3800, ISSN 0021-9991.
- [169] Sandve, T. H.; Keilegavlen, E. & Nordbotten, J. M.: Physics-based preconditioners for flow in fractured porous media. *Water Resources Research* **50** (2014), 1357–1373.
- [170] Schenk, O.; Gärtner, K.; Fichtner, W. & Stricker, A.: PARDISO: A High-Performance Serial and Parallel Sparse Linear Solver in Semiconductor Device Simulation. *Future Gener. Comput. Syst.* **18** (2001), 69–78.
- [171] Scheufele, K. & Mehl, M.: Robust multiseant quasi-newton variants for parallel fluid-structure simulations and other multiphysics applications. *SIAM Journal on Scientific Computing* **39** (2017), S404–S433.

- [172] Schild, M.; Siegesmund, S.; Vollbrecht, A. & Mazurek, M.: Characterization of granite matrix porosity and pore-space geometry by in situ and laboratory methods. *Geophysical Journal International* **146** (2001), 111–125.
- [173] Schmidt, P.; Dutler, N. & Steeb, H.: Importance of fracture deformation throughout hydraulic testing under in situ conditions. *Geophysical Journal International* **228** (2021), 493–509.
- [174] Schmidt, P.; Holger & Renner, J.: Assessing the role of non-linear contact mechanics for flow in fractures. *Nature Geoscience* **submitted** (2021).
- [175] Schmidt, P.; Holger & Renner, J.: Investigations into the opening of fractures during hydraulic testing using a hybrid-dimensional flow formulation. *Environmental Earth Sciences* **80** (2021).
- [176] Schmidt, P.; Jaust, A.; Steeb, H. & Schulte, M.: Simulation of flow in deformable fractures using a quasi-Newton based partitioned coupling approach. *Computational Geosciences* **26** (2022), 381–400.
- [177] Schmidt, P. & Steeb, H.: Numerical aspects of hydro-mechanical coupling of fluid-filled fractures using hybrid-dimensional element formulations and non-conformal meshes. *International Journal on Geomathematics* **10** (2019), 14, ISSN 1869-2680.
- [178] Schuite, J.; Longuevergne, L.; Bour, O.; Guihéneuf, N.; Becker, M. W.; Cole, M.; Burbey, T. J.; Lavenant, N. & Boudin, F.: Combining periodic hydraulic tests and surface tilt measurements to explore in situ fracture hydromechanics. *J Geophys Res Solid Earth* **122** (2017), 6046–6066.
- [179] Segura, J. M. & Carol, I.: On zero-thickness interface elements for diffusion problems. *International Journal for Numerical and Analytical Methods in Geomechanics* **28** (2004), 947–962.
- [180] Segura, J. M. & Carol, I.: Coupled HM analysis using zero-thickness interface elements with double nodes. Part I: Theoretical model. *International Journal for Numerical and Analytical Methods in Geomechanics* **32** (2008), 2083–2101.
- [181] Segura, J. M. & Carol, I.: Coupled HM analysis using zero-thickness interface elements with double nodes—Part II: Verification and application. *International Journal for Numerical and Analytical Methods in Geomechanics* **32** (2008), 2103–2123.
- [182] Selvadurai, P.; Selvadurai, P. A. & Nejati, M.: A multi-phasic approach for estimating the biot coefficient for grimsel granite. *Solid Earth* **10** (2019), 2001–2014.
- [183] Settigast, R. R.; Fu, P.; Walsh, S. D.; White, J. A.; Annavarapu, C. & Ryerson, F. J.: A fully coupled method for massively parallel simulation of hydraulically driven fractures in 3-dimensions. *International Journal for Numerical and Analytical Methods in Geomechanics* **41** (2017), 627–653.

- [184] Shen, B.; Stephansson, O. & Rinne, M.: *Hydro-Mechanical Coupling*, Springer Netherlands, Dordrecht 2014. pp. 77–82.
- [185] Slack, T. Z.; Murdoch, L. C.; Germanovich, L. N. & Hisz, D. B.: Reverse water-level change during interference slug tests in fractured rock. *Water Resources Research* **49** (2013), 1552–1567.
- [186] Slattery, S. R.; Wilson, P. P. H. & Pawlowski, R. P.: The Data Transfer Kit: A geometric rendezvous-based tool for multiphysics data transfer. In *Proceedings of the 2013 International Conference on Mathematics and Computational Methods Applied to Nuclear Science and Engineering - M and C 2013*, 2013.
- [187] Sneddon, I. N. & Elliot, H. A.: The opening of a griffith crack under internal pressure. *Quarterly of Applied Mathematics* **4** (1946), 262–267.
- [188] Sokolova, I.; Bastisyra, M. G. & Hajibeygi, H.: Multiscale finite volume method for finite-volume-based simulation of poroelasticity. *Journal of Computational Physics* **379** (2019), 309–324.
- [189] Steeb, H.; Kurzeja, P. S.; Fehner, M. & Schmalholz, S. M.: Phase velocity dispersion and attenuation of seismic waves due to trapped fluids in residual saturated porous media. *Vadose Zone Journal* **11** (2012), ISSN 1539-1663.
- [190] Steeb, H. & Renner, J.: Mechanics of poro-elastic media: A review with emphasis on foundational State variables. *Transport in Porous Media* **130** (2019), 437–461.
- [191] Stegemeier, G. L.: Interwell pressure testing for field pilots. In *SPE Annual Technical Conference and Exhibition*, Society of Petroleum Engineers 1982.
- [192] Stober, I. & Bucher, K.: *Geothermie*. Springer 2012.
- [193] Suttera, S. P. & Skalak, R.: The history of Poiseuille’s law. *Annual Review of Fluid Mechanics* **25** (1993), 1–20.
- [194] Tadmor, E. B.; Miller, R. E. & Elliott, R. S.: *Continuum Mechanics and Thermo-dynamics: From Fundamental Concepts to Governing Equations*. Cambridge University Press 2011.
- [195] Taleghani, A. D.: *Analysis of hydraulic fracture propagation in fractured reservoirs: an improved model for the interaction between induced and natural fractures*. The University of Texas at Austin 2009.
- [196] Tao, Q.; Ghassemi, A. & Ehlig-Economides, C. A.: A fully coupled method to model fracture permeability change in naturally fractured reservoirs. *International Journal of Rock Mechanics and Mining Sciences* **48** (2011), 259–268, ISSN 1365-1609.
- [197] Timoshenko, S. P. & Goodier, J. N.: *Theory of Elasticity*. Engineering societies monographs, McGraw-Hill 1987, ISBN 9780070701229.

- [198] Toselli, A. & Widlund, O.: *Domain Decomposition Methods-Algorithms and Theory*, vol. 34. Springer Science & Business Media 2006.
- [199] Truesdell, C.: *Rational Thermodynamics*. Springer New York 1984.
- [200] Tunc, X.; Faille, I.; Gallouët, T.; Cacas, M. C. & Havé, P.: A model for conductive faults with non-matching grids. *Computational Geosciences* **16** (2012), 277–296, ISSN 1573-1499.
- [201] Ucar, E.; Berre, I. & Keilegavlen, E.: Three-dimensional numerical modeling of shear stimulation of fractured reservoirs. *Journal of Geophysical Research: Solid Earth* **123** (2018), 3891–3908.
- [202] Ucar, E.; Keilegavlen, E.; Berre, I. & Nordbotten, J. M.: A finite-volume discretization for deformation of fractured media. *Computational Geosciences* **22** (2018), 993–1007.
- [203] Uekermann, B.: *Partitioned Fluid-Structure Interaction on Massively Parallel Systems*. Ph.D. thesis, Institut für Informatik, Technische Universität München (2016), URL <https://mediatum.ub.tum.de/doc/1320661/document.pdf>.
- [204] Versteeg, H. K. & Malalasekera, W.: *An Introduction to Computational Fluid Dynamics: The Finite Volume Method*. Pearson education 2007.
- [205] Vinci, C.: *Hydro-mechanical coupling in fractured rocks: modeling and numerical simulations*. Ph.D. thesis, Ruhr-University Bochum (2014).
- [206] Vinci, C.; Renner, J. & Steeb, H.: A hybrid-dimensional approach for an efficient numerical modeling of the hydro-mechanics of fractures. *Water Resources Research* **50** (2014), 1616–1635.
- [207] Vinci, C.; Renner, J. & Steeb, H.: On attenuation of seismic waves associated with flow in fractures. *Geophysical Research Letters* **41** (2014), 7515–7523.
- [208] Vinci, C.; Steeb, H. & Renner, J.: The imprint of hydro-mechanics of fractures in periodic pumping tests. *Geophysical Journal International* **202** (2015), 1613–1626.
- [209] Vogler, D.; Settgest, R. R.; Annavarapu, C.; Madonna, C.; Bayer, P. & Amann, F.: Experiments and simulations of fully hydro-mechanically coupled response of rough fractures exposed to high-pressure fluid injection. *Journal of Geophysical Research: Solid Earth* **123** (2018), 1186–1200.
- [210] Walsh, J.: Effect of pore pressure and confining pressure on fracture permeability. *International Journal of Rock Mechanics and Mining Sciences & Geomechanics Abstracts* **18** (1981), 429 – 435, ISSN 0148-9062.
- [211] Wang, H. F.: *Theory of Linear Poroelasticity*. Princeton University Press, Princeton & Oxford 2000.

- [212] Weir, G. J.: Single-phase flow regimes in a discrete fracture model. *Water Resources Research* **35** (1999), 65–73.
- [213] Wenning, Q. C.; Madonna, C.; de Haller, A. & Burg, J.-P.: Permeability and seismic velocity anisotropy across a ductile–brittle fault zone in crystalline rock. *Solid Earth* **9** (2018), 683–698.
- [214] Widlund, O. & Toselli, A.: *Domain decomposition methods - algorithms and theory*, Springer 2004, vol. 34.
- [215] Witherspoon, P. A.; Amick, C. H.; Gale, J. E. & Iwai, K.: Observations of a potential size effect in experimental determination of the hydraulic properties of fractures. *Water Resources Research* **15** (1979), 1142–1146.
- [216] Witherspoon, P. A.; Wang, J. S. Y.; Iwai, K. & Gale, J. E.: Validity of cubic law for fluid flow in a deformable rock fracture. *Water Resources Research* **16** (1980), 1016–1024.
- [217] Woodbury, A. & Zhang, K.: Lanczos method for the solution of groundwater flow in discretely fractured porous media. *Advances in Water Resources* **24** (2001), 621 – 630, ISSN 0309-1708.
- [218] Yew, C. H. & Weng, X.: *Mechanics of Hydraulic Fracturing*. Gulf Professional Publishing 2014.
- [219] Zangerl, C.; Evans, K.; Eberhardt, E. & Loew, S.: Normal stiffness of fractures in granitic rock: A compilation of laboratory and in-situ experiments. *International Journal of Rock Mechanics and Mining Sciences* **45** (2008), 1500 – 1507, ISSN 1365-1609.
- [220] Zeumann, S.; Weise, A. & Jahr, T.: Tidal and non-tidal signals in groundwater boreholes in the KTB area, Germany. *Journal of Geodynamics* **48** (2009), 115–119, ISSN 0264-3707.
- [221] Zhang, M.; Ambastha, A. *et al.*: New insights in pressure-transient analysis for stress-sensitive reservoirs. In *SPE Annual Technical Conference and Exhibition*, Society of Petroleum Engineers 1994.
- [222] Zheltov, A. K.: Formation of vertical fractures by means of highly viscous liquid. In *4th World Petroleum Congress*, World Petroleum Congress 1955.
- [223] Zienkiewicz, O. C.; Taylor, R. L.; Taylor, R. L. & Taylor, R. L.: *The Finite Element Method: Solid Mechanics*, vol. 2. Butterworth-Heinemann 2000.
- [224] Zimmerman, R. W.; Al-Yaarubi, A.; Pain, C. C. & Grattoni, C. A.: Non-linear regimes of fluid flow in rock fractures. *International Journal of Rock Mechanics and Mining Sciences* **41** (2004), 163 – 169, proceedings of the ISRM SINOROCK 2004 Symposium.

- [225] Zimmerman, R. W. & Yeo, I.-W.: *Fluid Flow in Rock Fractures: From the Navier-Stokes Equations to the Cubic Law*, American Geophysical Union (AGU) 2013. ISBN 9781118669662, pp. 213–224.
- [226] Zoback, M. D.: *Reservoir Geomechanics*. Cambridge University Press 2007.

Curriculum Vitae

Personal data:

Name: Patrick Schmidt
Date of birth: April 8, 1988
Place of birth: Hagen, Germany
Nationality: German
Parents: Klaus and Jutta Schmidt
Siblings: -
Marital status: unmarried
Children: -

Education:

09/1994 – 06/1998 elementary school “Grundschule Breckerfeld”,
Breckerfeld, Germany
06/1998 – 06/2000 secondary school “St. Jacobus-Schule Breckerfeld”,
Breckerfeld, Germany
09/2000 – 06/2007 secondary school “Anne-Frank Gymnasium”,
Halver, Germany
06/2007 degree: “Allgemeine Hochschulreife” (high school diploma)
10/2008 – 04/2012 studies in mechanical engineering
at Ruhr-Universität Bochum, Germany
09/2006 degree: “Bachelor of Science (B.Sc.) Maschinenbau”
04/2012 – 10/2013 studies in mechanical engineering
at Ruhr-Universität Bochum, Germany
09/2006 degree: “Master of Science (M.Sc.) Maschinenbau”

Civilian service:

10/2007 – 06/2008 civilian service (reintegration facility Gebal),
Gevelsberg, Germany

Foreign Studies:

04/2013 – 10/2013 semester abroad (master thesis),
at the University of Queensland, Australia

10/2014 – 12/2016 PhD candidate at the
School of Civil Engineering at the
University of Queensland, Australia

Professional occupation:

03/2014 – 10/2014 occupational trainee at the
School of Civil Engineering at the
University of Queensland, Australia

01/2016 – 12/2016 visiting scholar at the
Institute of Applied Mechanics (Civil Engineering) at the
University of Stuttgart, Germany

01/2017 – 01/2022 teaching assistant and research associate at the
Institute of Applied Mechanics (Civil Engineering) at the
University of Stuttgart, Germany



Underground flow processes in fractured porous media possess a great significance regarding the optimization of energy production based on natural resources. Energy is stored in form of liquids, respectively heat in the underground and its excavation is highly impacted by discontinuities of the porous medium's transport characteristics such as induced by discrete fractures or fracture networks. Throughout the exploitation flow processes might become fairly complex, since fractures do not simply increase the permeability and induce preferential flow paths within the reservoir, they also reduce the stiffness of the surrounding rock mass.

Therefore, the objective of this thesis is to derive a numerically efficient hydro-mechanical model for flow in fractured porous media in which the reduction of the fracture flow domain by one dimension increases the computational performance. The derived model is then applied to data obtained from field-scale pumping operations in fractured reservoirs to contribute to a better understanding of hydro-mechanical processes under in-situ conditions.